

5/1/01  
AFRL-MN-EG-TR-2002-7001

## Dynamic Testing of Materials

---

**Stanley E. Jones**  
University of Alabama  
Tuscaloosa, AL

**Peter P. Gillis**  
University of Kentucky  
Lexington, KY



CONTRACT NO. F08630-96-K-0014

October 2001

FINAL REPORT FOR PERIOD APRIL 1996 – MAY 2001

**DISTRIBUTION** – Approved for public release

**AIR FORCE RESEARCH LABORATORY, MUNITIONS DIRECTORATE**

Air Force Materiel Command ■ United States Air Force ■ Eglin Air Force Base

20030613 053

## NOTICE

When Government drawings, specifications, or other data are used for any purpose other than in connection with a definitely Government-related procurement, the United States Government incurs no responsibility or any obligation whatsoever. The fact that the Government may have formulated or in any way supplied the said drawings, specifications, or other data, is not to be regarded by implication, or otherwise in any manner construed, as licensing the holder, or any other person or corporation; or as conveying any rights or permission to manufacture, use, or sell any patented invention that may in any way be related thereto.

This technical report is releasable to the National Technical Information Services (NTIS). At NTIS it will be available to the general public, including foreign nations.

Contract Number: F08630-96-K-0014

Contractor: University of Alabama

This technical report has been reviewed and is approved for publication.

FOR THE COMMANDER

Paul K. Laird  
PAUL K. LAIRD  
Technical Director, Ordnance Division

Joel W. House  
JOEL W. HOUSE, Ph.D.  
Program Manager

Kirk E. Herzog  
KIRK E. HERZOG  
Tech Advisor, Damage Mechanisms Branch

Anyone having need for a copy of this report should first contact the Defense Technical Information Center (DTIC) at the address shown below. If you are a registered DTIC User, DTIC can provide you with a copy. Please do not request copies from the Air Force Research Laboratory, Munitions Directorate. Requests for additional copies should be directed to:

Defense Technical Information Center (DTIC)  
8725 John J. Kingman Road, Ste 0944  
Ft Belvoir, VA 22060-6218

This report is published in the interest of the scientific and technical information exchange. Publication of this report does not constitute approval or disapproval of the ideas or findings

If your address has changed, if you wish to be removed from our mailing list, or if your organization no longer employs the addressee, please notify AFRL/MNMN, Eglin AFB FL 32542-6810, to help us maintain a current mailing list. Do not return copies of this report unless contractual obligations or notice on a specific document requires that it be returned.

# REPORT DOCUMENTATION PAGE

Form Approved  
OMB No. 0704-0188

Public reporting burden for this collection of information is estimated to average 1 hour per response, including the time for reviewing instructions, searching existing data sources, gathering and maintaining the data needed, and completing and reviewing the collection of information. Send comments regarding this burden estimate or any other aspect of this collection of information, including suggestions for reducing this burden, to Washington Headquarters Services, Directorate for Information Operations and Reports, 1215 Jefferson Davis Highway, Suite 1204, Arlington, VA 22202-4302, and to the Office of Management and Budget, Paperwork Reduction Project (0704-0188), Washington, DC 20503.

1. AGENCY USE ONLY (Leave blank)			2. REPORT DATE Oct 2001	3. REPORT TYPE AND DATES COVERED Final Report, April 1998 – May 2001
4. TITLE AND SUBTITLE Dynamic Testing of Materials			5. FUNDING NUMBERS Contract #:F08630-96-K-0014 JON: 2502 PE: 62602F PR: 2502 TA: 06 WU: 98	
6. AUTHOR(S) Stanley E. Jones and Peter P. Gillis			8. PERFORMING ORGANIZATION REPORT NUMBER	
7. PERFORMING ORGANIZATION NAME(S) AND ADDRESS(ES) University of Alabama Aerospace Engineering and Mechanics Tuscaloosa, Alabama 335487-0280			University of Kentucky Chemical and Materials Engineering Lexington, Kentucky 40506	
9. SPONSORING/MONITORING AGENCY NAME(S) AND ADDRESS(ES) (Program Mgr Name & Ph #) Air Force Research Laboratory, Munitions Directorate Ordnance Division Damage Mechanisms Branch (AFRL/MNMW) 101 W. Eglin Blvd., Ste 135 Eglin AFB, FL 32542-6810			10. SPONSORING/MONITORING AGENCY REPORT NUMBER AFRL-MN-EG-TR-2002-7001	
11. SUPPLEMENTARY NOTES <del>SUBJECT TO EXPORT CONTROL LAWS.</del> <del>Availability of this report is specified on the front cover and its reverse.</del>				
12a. DISTRIBUTION/AVAILABILITY STATEMENT DISTRIBUTION Public release authorized.			12b. DISTRIBUTION CODE (Leave this block blank)	
13. ABSTRACT: The subject of this project was dynamic testing of materials at high strain rates. Most of the effort was directed toward the Taylor impact test. The Taylor Test is important because it helps bridge the gap between the split-Hopkinson pressure bar and flyer plate experiments. Another important feature of the Taylor test is the very large compressive strains that are achieved. New analytical tools were devised to reduce data from the Taylor test and a number of experiments were performed at the University of Alabama. To reduce the effect of radial inertia, new low caliber launcher was built and 0.164 inch diameter specimens were tested. Taylor tests of viscoelastic materials, for which a recovered deformed specimen was not possible, were also performed. In this case, a high speed film record of the impact event was substituted instead. Some progress was also made on quantifying the high rate behavior of some materials that are not candidates for the Taylor test. The mechanical properties of geologically based materials are often deduced from penetration tests where the appropriate rates and pressures are available. Improvements and modifications of existing one-dimensional hard target penetration models were undertaken.				
14. SUBJECT TERMS: Dynamic Properties, Taylor Impact testing, Cylinder Impact Testing, High Strain Rate, Plasticity			15. NUMBER OF PAGES 242	
			16. PRICE CODE	
17. SECURITY CLASSIFICATION OF REPORT UNCLASSIFIED	18. SECURITY CLASSIFICATION OF THIS PAGE UNCLASSIFIED	19. SECURITY CLASSIFICATION OF ABSTRACT UNCLASSIFIED	20. LIMITATION OF ABSTRACT SAR	

## ACKNOWLEDGEMENT

The principal investigators would like to acknowledge the many contributions of our collaborators and students at the University of Alabama and the University of Kentucky. We also wish to acknowledge the support of the Mechanical Shop in the College of Engineering at the University of Alabama. It is safe to say that without their capable effort much of this work would not have been done.

The contributions of our many Air Force collaborators must also be recognized. In particular, the advice and council of Dr. Joseph C. Foster, Jr. and Mr. Leonard L. Wilson on the Taylor test facility at the University of Alabama cannot be overestimated. Without drawing from their vast experience, we could never have accomplished what we did.

Finally, we were fortunate to have Dr. Joel House as our program manager. He made many important contributions to the technical effort and assisted us in every way.

## Table of Contents

Section	Title	Page
1.	Executive Summary	1
2.	Introduction	4
3.	Taylor Testing	7
3.1	Reduction of Taylor Test Data	8
3.2	The Revised Johnson-Cook Strength Model	11
3.3	High Speed Film Data Reduction	13
4.	Taylor Test Results	14
4.1	Mechanical Characterization of Astralloy-V	14
4.2	Mechanical Characterization of High Strength Steels	14
4.3	Mechanical Characterization of Dense Urethane (Adiprene-100)	15
4.4	Mechanical Characterization of PVC and of PET	15
5.	Quasi-Static Yield Strength Estimates	17
6.	Penetration Testing	19
7.	Conclusions	23
8.	References	26
Appendix A	Radial Inertia in the Taylor Test	A-1
Appendix B	An Elementary Theory for the Taylor Impact Test	B-1
Appendix C	A Revised Form for the Johnson-Cook Strength Model	C-1
Appendix D	Mechanical Characterization of Hardened Astralloy-V® Using the Taylor Impact Test	D-1
Appendix E	Film Data Reduction from Taylor Impact Tests	E-1

<b>Appendix F</b>	<b>Validating the High Strain-Rate Strength Estimates Generated from High-Speed Film Data and a Revised Elementary Theory For the Taylor Test</b>	<b>F-1</b>
<b>Appendix G</b>	<b>An Estimate for Strain-Rate in the Taylor Impact Test</b>	<b>G-1</b>
<b>Appendix H</b>	<b>Optimizing Material Strength Constants Numerically Extracted From Taylor Impact Test Data</b>	<b>H-1</b>
<b>Appendix I</b>	<b>Taylor Impact Testing of High Strength Steels</b>	<b>I-1</b>
<b>Appendix J</b>	<b>Taylor Test Analysis of an Unconventional Material</b>	<b>J-1</b>
<b>Appendix K</b>	<b>Relationship Between Strain Rate, Temperature, and Impact Failure Mechanism for Poly (vinyl chloride) and Poly (ethylene Terephthalate)</b>	<b>K-1</b>
<b>Appendix L</b>	<b>Testing Machines and Strain Sensors</b>	<b>L-1</b>
<b>Appendix M</b>	<b>An Engineering Analysis of Normal Rigid Body Penetration into Concrete</b>	<b>M-1</b>
<b>Appendix N</b>	<b>On the Optimal Nose Geometry for a Rigid Penetrator</b>	<b>N-1</b>
<b>Appendix O</b>	<b>On the Optimal Geometry for a Rigid Penetrator, Including the Effects of Pressure-Dependent Friction</b>	<b>O-1</b>
<b>Appendix P</b>	<b>Some Remarks on the Optimal Geometry of a Rigid Penetrator In the Presence of Friction</b>	<b>P-1</b>
<b>Appendix Q</b>	<b>An Analytical Estimate for Mass Loss from a High Velocity Rigid Penetrator</b>	<b>Q-1</b>
<b>Appendix R</b>	<b>An Estimate for Mass Loss from High Velocity Steel Penetrators</b>	<b>R-1</b>
<b>Appendix S</b>	<b>Normal Penetration of Semi-Infinite Targets by Ogive-Nose Projectiles, Including the Effects of Blunting and Erosion</b>	<b>S-1</b>
<b>Appendix T</b>	<b>An Analysis of Rod Penetration of Semi-Infinite Targets Using An Average Pressure Estimate</b>	<b>T-1</b>

## **1. EXECUTIVE SUMMARY**

The proposal for this project set forth a comprehensive plan to perform research in three areas:

- (i) Taylor testing of conventional materials
- (ii) Taylor testing of unconventional materials
- (iii) Biaxial testing under combined tension and torsion.

This report documents the progress that was made in developing the analytical tools to reduce the data from Taylor cylinder tests. Also included in the report are the results of our efforts to deduce the mechanical properties of some unconventional materials, such as concrete, that are ill suited for Taylor impact testing. Some progress was made on testing and analysis of data from biaxial tests under combined tension and torsion, but items (i) and (ii) were deemed of higher priority by the Air Force. Thus, we have more accomplishments to report in these areas.

Regarding the first of our objectives, we achieved a major milestone with the development of an elementary one-dimensional theory for estimating the state of stress of ductile materials at strain-rates that exceed  $10^4 / s$ . The theory could be applied to post-test cylinder data or to a high-speed film record of a Taylor cylinder test. References to both applications are included in the report.

Also referring to the first objective, a modification to the Johnson-Cook Strength Model was devised by including additional terms to more accurately account for high strain-rate behavior. The new material model is called the Revised Johnson-Cook

Strength Model (RJC). To evaluate all of the parameters in the model, only Taylor cylinder data and the results of quasi-static, uniaxial stress tests are required. There is remarkable agreement between the RJC strength model and the one-dimensional theory mentioned in the previous paragraph, although they are completely independent of one another. References are provided in the report and the results of a number of Taylor cylinder tests are included.

Regarding the second of our objectives, references are provided for data reduction of Taylor cylinder tests of dense urethane (Adiprene-100). The one-dimensional analysis was used in conjunction with a high-speed film record of the test to deduce the mechanical properties of the viscoelastic material. This was a novel application of the theory because there was no perceptible deformation of the recovered specimen to measure. A reference to these results is included in the report.

Another class of materials that are poor candidates for conventional Taylor testing are those that are geologically based. Many of them, especially concrete, are very brittle with very low tensile and shear strengths. Yet, it is exactly these material properties that are presently of interest to code developers for design purposes. Although mechanical testing of these materials has been carried out for years, there is very little known about their response to loads that produce strain-rates in excess of  $10^3 / s$ . Under high-pressure loading when the material is confined, even less is known. As indicated before, the brittle nature of these materials prevents many of them from being tested by any of the usual laboratory methods. One of the most common methods for deducing the properties of geological target materials is interpretative analysis of penetration test data. This has the advantage of subjecting the target to the highest strain-rates and pressures, but

requires the use of an accurate penetration theory for the results to have any value.

Several improvements to classical penetration theories were proposed in order to more accurately reflect the mechanical properties of hard targets. References to these results are included in the report.

The work on biaxial testing led to publication of a general treatise on testing machines and strain sensors. This appeared as a chapter in the most recent edition of the ASM Metals Handbook. It is included as an Appendix to this report.

## **2. INTRODUCTION**

This report documents our efforts to quantify the state of stress for materials at high rates of strain. Dynamic testing of materials at strain rates higher than  $10^4/s$  has been a subject of considerable interest for many years. The split-Hopkinson pressure bar is capable of testing at high strains, but the rates are limited to less than  $10^4/s$  in practice. Flyer plate experiments are capable of reaching ultra high strain rates in excess of  $10^6/s$  but only at very low strains. Specimen design and interpretation of the results is critical and argumentative in both of these tests.

Our efforts have been concentrated on the Taylor impact test. The Taylor test is capable of very large strains and strain rates in excess of  $10^4/s$  even for relatively low impact velocities. Beginning with these advantages, we sought improvements in the Taylor test and new methods for reducing data from the test. The results we achieved are useful and important for understanding material behavior and quantifying this behavior into computational mechanics codes.

There are several new results presented in this report. They fall into three categories, with some natural overlap. The three categories are: improvements in the experimental design, analytical modeling to support data reduction, and computational modeling to refine constitutive behavior and to support code calculations.

In the course of the project, a Taylor test facility was constructed at The University of Alabama. The purpose of this facility was to investigate some aspects of the test for potential improvements. One of the objectives was to demonstrate to the technical community that the Taylor test could occupy a position of importance in the laboratory like any other piece of materials testing equipment. In this context, we tried to

demonstrate that worthwhile and sensible conclusions about the state of stress in the specimen could be drawn from the test without the use of expensive camera equipment. The reliance on a recovered specimen is consistent with ordinary laboratory capability and Taylor's original intention. However, our objective is to use the recovered specimen to gain more than a simple estimate for "dynamic yield stress," which does not provide us with information that has the same value it once did. Most of our innovations are directed to this end.

To reduce the effects of radial inertia and make the propagation of plastic waves more truly one-dimensional, experimentation with sub-scale 4 mm (0.164 inch) diameter Taylor cylinders was investigated. These cylinders are difficult to test because of their very low mass and their extremely small cross-sectional area. They have a propensity for dynamic buckling and many of the recovered specimens have no value. This difficulty is generally not shared by the larger specimens. These sub-scale specimens also present a challenge to measure. With an initial diameter of only 4 mm, a one percent longitudinal strain corresponds to a change in specimen diameter of only about 20  $\mu$ m. This is less than one thousandth of an inch and a source of tremendous uncertainty in experimental results. However, the data from these tests is excellent and worth the patience required to obtain it.

An elementary one-dimensional theory was devised to reduce the data from recovered Taylor specimens. The fundamental basis for this theory was confirmed through direct measurement of high-speed films and a comparison with code calculations. In both procedures, the comparison was very favorable. This theory was successfully applied to several specimen materials. One of the most interesting applications of the

theory is to the estimation of the quasi-static yield stress for the specimen material. This result offers additional confirmation for the basis of the theory.

Over the past thirty years, a number of constitutive models have been devised to describe the high strain-rate behavior of materials with varying degrees of success. Some of the relations are based on fundamental physics, while others are *ad hoc*. One of the most widely used constitutive equations is the Johnson-Cook. The advantage to this relation is its simplicity. Traditionally, it requires only five free parameters to relate the effective stress to the effective strain, effective strain rate and temperature. The methods used to evaluate these parameters are well documented. However, this relation tends to underestimate the effect of strain-rate at higher rates. To make the Johnson-Cook strength model apply to higher rate cases, three constants were added. The new relation is called the Revised Johnson-Cook strength model. The new constants adjust the behavior at high rates to accommodate the sudden strengthening that many materials experience when a critical strain-rate is reached. All of the constants can be evaluated from a quasi-static strength test and recovered Taylor cylinders. The results provide for estimates of critical strain-rate and ultimate dynamic stress. Both are important in ultra high rate processes, such as impact, penetration, and warhead collapse problems.

### **3. TAYLOR TESTING**

A large number of Taylor cylinder tests were performed. The purpose of these tests was to support the development of new analytical and computational constitutive models that can account for high rate behavior. In both cases, the objective was to utilize recovered specimen data to the maximum extent possible. As indicated in the introduction, the analysis of specimen behavior in the radial direction (Gillis and Jones [5], see Appendix A) indicated that the lowest caliber specimen should be used whenever possible. The lowest caliber smooth bore launch tube that we could purchase commercially, without a retooling fee, was 0.167 caliber. The effect of radial inertia is nearly absent from these cylinders. All impacts occurred against composite targets with hardened Astralloy-V® faces. Astralloy-V® is a high strength steel that is carbonitride treated to a hardness of  $R_C$  60-65.

A number of tests were performed on a variety of materials. Data from all of these tests is not included in this report. Data on OFHC copper and wrought iron 0.164 caliber specimens is reported in Jones, Drinkard, Rule, and Wilson [13] (Appendix B). Data from 7075-T6 aluminum, OFHC copper, wrought iron, and Astralloy-V® is contained in Rule and Jones [20] (Appendix C). Astralloy-V® data from 0.164" diameter specimens is reported in Jones, Barkey, Rule and Huber, [13] (Appendix D). These data consist of cylinder profile measurements, undeformed section length measurements, and overall length measurements for a wide range of impact velocities.

The materials mentioned above were relatively straightforward to test and to evaluate. One class of materials that turns out to be difficult to test is high strength steels other than Astralloy-V®. In the process of hardening the steel to produce high strength,

there may be such a loss of ductility that the strain to failure is very low, even in compression. For such specimens, there is a very narrow window in which data can be collected. The reason for this is that the specimens shatter on impact at moderately high velocities and sustain little deformation at low velocities. This magnifies the uncertainties in the measurement of recovered specimens and their effect on data reduction.

### **3.1 REDUCTION OF TAYLOR TEST DATA**

#### **3.1.1 An Elementary One-Dimensional Theory for the Taylor Test**

The requirements for Taylor testing have changed. The earliest theories concentrated on taking measurements from a recovered specimen and using them to produce an estimate for the dynamic yield stress. High-speed photography has improved the analysis because instead of giving us only the data discernible from a recovered specimen it provides sequential, specimen profiles during the deformation process. One accomplishment of the research program was to document processes for the determination of strain and strain rate from high-speed films (see House, Aref, Foster, and Gillis [8] (Appendix E) and Cinnamon, Jones, House, and Rule [2] (Appendix F)). In the first reference, an elementary estimate of local stress was obtained using an impulse-momentum balance. The approach taken in the second reference is somewhat different. The elementary one-dimensional theory mentioned earlier was applied to a specimen by analyzing the high-speed film record of a single Taylor test.

In Taylor's theory of the impact test some average value of flow stress was obtained from the post-test measurements. This stress was not associated with a particular strain and only marginally associated with an average strain rate. Contemporary

constitutive modeling requires the state of stress of the specimen material. This presents a new challenge.

Most materials laboratories will not be equipped with high-speed camera capability. Recognizing this, one of the objectives of this modeling was to devise a method for reducing Taylor cylinder data to estimate the state of stress in the specimen material using only the post-test specimens. A very satisfactory theory was devised that is capable of estimating the state of stress at strain rates usually exceeding  $10^4 / s$  and requiring only a few specimens over a range of specimen impact velocities (see Jones, Drinkard, Rule, and Wilson [13], Appendix B).

This theory relies upon the assumption that the particle velocity of the material behind the deformation front is proportional to the velocity of the undeformed section. This is a very reasonable assumption that has been computationally verified. The result is an estimate for compressive dynamic stress  $\sigma$  at strain  $e$

$$\sigma = (1+e) \left[ \sigma_0 + \frac{(1-\beta)^2}{e} \rho v^2 \right]. \quad (1)$$

In this equation,  $e$  is the constant strain at which the deformation wave propagates in the specimen,  $\rho$  is the specimen density,  $\sigma_0$  is a reference stress related to the quasi-static yield stress for the specimen material,  $\beta$  is the dimensionless constant of proportionality, and  $v$  is the current velocity of the undeformed section. Once  $\beta$  and  $\sigma_0$  have been determined, the dynamic flow stress for the specimen material at strain  $e$  can be estimated with Equation (1).

To complete the description of the mechanical behavior of the material, we require an estimate for the strain rate at the deformation front. A very useful estimate for the

maximum strain rate after initial transient behavior is completed was given earlier by Jones, Maudlin, and Foster [16]

$$\dot{\epsilon} = \frac{-v_0}{L_0 - \bar{\ell}} \quad (2)$$

where  $v_0$  is the impact velocity,  $L_0$  is the original specimen length, and  $\bar{\ell}$  is the undeformed section length at the completion of initial transient behavior. In the course of the project, several other estimates for strain rate were developed and used in constitutive modeling. In Jones, Wilson and Rule [19] (Appendix G), an estimate based on conservation of energy across the deformation front was given

$$\dot{\epsilon} = -\frac{1}{(1+e)\bar{\ell}} \frac{v \exp \left\{ \frac{\rho(1-\beta)}{2e\sigma_0} (v_0^2 - v^2) \right\}}{1 + \frac{(1-\beta)^2}{e\sigma_0} \rho v^2}. \quad (3)$$

Equations (1) and (3) are an implicit constitutive equation for the specimen material. In this case, the parameter that connects the two equations is  $v$ , the undeformed section velocity. Another velocity dependent strain rate estimate was given by Cinnamon, et al [2] (Appendix F)

$$\dot{\epsilon} = \frac{-v}{L_0 - \bar{\ell} \exp \left\{ \frac{\rho(1-\beta)}{2e\sigma_0} (v^2 - v_0^2) \right\}}. \quad (4)$$

This estimate was used effectively in film data reduction. Each of these strain rate estimates has some value in the context in which it was used. In any event, the state of stress for the specimen material can be estimated from post-test measurements once  $\beta$ ,  $\sigma_0$ , and  $\bar{\ell}$  have been determined. Finding suitable estimates for these parameters, was the

subject of Jones, Drinkard, Rule, and Wilson [14]. Using some of the fundamental equations from the analysis and a new definition of undeformed section length at strain  $\epsilon$ , we were able to connect  $\beta$  to post-test measurements. The details of this analysis are contained in Appendix B. The reader should consult Figures 3 and 4 in Appendix B.

### 3.2 The Revised Johnson-Cook Strength Model

Another method for reducing data from Taylor impact tests was introduced by Rule and Jones [20] (Appendix C) in the course of examining low caliber cylinders. The thinking that led to the development of this method was presented by Allen, Rule and Jones [1] (Appendix H). A new constitutive model was devised that accounts for the extreme rate sensitivity that some materials exhibit when a critical strain rate is approached. With this model we accomplish several things. The analysis provides for estimates for the critical strain rate and the ultimate dynamic strength of the material. Both of these are important issues to material scientists involved in design problems in which ultra high strain rates are possible.

Many ductile metals display an enormous increase in yield stress for strain rates in excess of  $10^3 / s$ . This observed behavior provided the motivation for the Revised Johnson-Cook strength model. The goal was to retain the simplicity and convenience of the original Johnson-Cook strength model, while accommodating this extraordinary behavior. This was accomplished with the addition of three new parameters to the Johnson-Cook model. The new constitutive model has the form

$$\sigma = (C_1 + C_2 \epsilon^N) \left[ 1 + C_3 \ln \epsilon^* + C_4 \left( \frac{1}{C_5 - \ln \epsilon^*} - \frac{1}{C_5} \right) \right] (1 - T^*^M) \quad (5)$$

where  $\sigma$  is the equivalent yield strength of the material,  $\varepsilon$  is the equivalent plastic strain,  $\varepsilon^*$  is the dimensionless equivalent plastic strain rate (made dimensionless by dividing by a unit plastic strain rate),  $T^*$  is a non-dimensional temperature, and  $C_1$ ,  $M$ , and  $N$  are empirical coefficients and exponents. There are seven constants in Equation (5). An eighth constant  $C_6$  is added to account for the peak strain rate sensitivity that satisfies the inequality

$$\left[ 1 + C_3 \ln \varepsilon^* + C_4 \left( \frac{1}{C_5 - \ln \varepsilon^*} - \frac{1}{C_5} \right) \right] \leq C_6. \quad (6)$$

A method for estimating the values of all eight constants using only quasi-static yield strength data and Taylor cylinder data is presented in Rule and Jones [20] (Appendix C). The rationale behind this method is also discussed as some consider the use of such data to be inappropriate. In general, the results are very satisfactory, achieving good agreement with the one-dimensional analysis presented earlier. A comparison between the Revised Johnson-Cook and the one-dimensional theory is given for Astralloy V®, a high strength steel designed for applications requiring wear resistance, in Appendix C, Figure 7. The comparison is very favorable. The data reduction for this type of material is difficult and subject to some of the uncertainties mentioned earlier. Nevertheless, the results show strong correlation. The same is true of OFHC copper in the as received condition, see Appendix C, Figure 5. The copper is more ductile and there is less uncertainty in the measurements. There is less scatter in the data and the agreement is very good.

### **3.3 High Speed Film Data Reduction**

High-speed film data provides dynamic Taylor cylinder data. Instead of having only a recovered specimen to analyze, we have a film record that gives us a sequence of images of the specimen at known times relative to the time of impact. Effectively, each of the frames of the film record is a deformed Taylor cylinder that can be measured for mechanical characterization of the specimen material. In this project, the data from the film record was used in two distinct ways. First, Cinnamon, Jones, House and Rule [2] (Appendix F) used the images to confirm the fundamental assumption behind the development of the one-dimensional model. Second, House, Aref, Foster and Gillis [9] (Appendix E) measured the film record directly to estimate the state of stress in the specimen material. Each of these approaches has merit and the results confirm the state of stress estimates from the two theories presented earlier.

#### **4. TAYLOR TEST RESULTS**

Taylor testing of a number of important materials took place over the life of the project. The results of some of the testing have already been mentioned. However, there are several materials that deserve special mention. These are listed below.

##### **4.1 Mechanical Characterization of Astralloy-V®**

Astralloy-V® is a high strength steel manufactured and marketed by a firm in Birmingham, AL. The product is intended for use in applications in which high wear is anticipated. The Taylor target face is made from this material because it can be case hardened to 60-65 on the Rockwell C scale either by carburizing or by carbo-nitriding. The material appears to be ideal for hard target penetration applications. The material was tested and the results reported by Jones, et al [12] (Appendix D) and later by Rule and Jones [20] (Appendix C), where a comparison between the estimates obtained with the elementary theory were compared to those obtained with the Revised Johnson-Cook Strength Model. There was remarkable agreement (see Figure 7 of Appendix C).

##### **4.2 Mechanical Characterization of High Strength Steels**

High strength steels generally present a challenge for Taylor testing. The reason for this is that the specimens do not deform very much at low impact velocities. At higher impact velocities, the specimens fail because the strain-to-failure is very low for most of the alloys. Astralloy-V® is a special case because it retains some ductility in spite of the fact that its compressive yield stress is around 1800 MPa.

Several candidate hard steel casing materials were tested during the course of this project. The purpose of the tests was to provide high strain-rate behavior to code

developers and to attempt to correlate mechanical response to penetration performance. Several materials were tested. The results are contained in Jones, Ahearn, Taylor and Rule [11] (Appendix I).

#### **4.3 Mechanical Characterization of Dense Urethane (Adiprene-100)**

All of the materials described above shared one thing in common. There was a recovered specimen for each successful test. There are a number of important ductile materials whose high rate behavior is required for which the recovered specimen provides no information. Dense urethane (Adiprene-100) is such a material. The specimen undergoes large deformation during the test, but recovers immediately, before any measurements can be made. In this case, a high-speed film record can provide us with the specimen behavior. Wilson, Foster, Jones and Gillis [25] (Appendix J) showed how the elementary theory described earlier could be used in conjunction with a high-speed film record to deduce the mechanical properties of dense urethane.

Data from selected frames of the film record was digitized and the plot of the normalized, undeformed section length vs. normalized overall length data was a linear relation from which the slope and intercept could be found. As observed earlier for recovered metallic cylinders, this information is all that is necessary to estimate the state of stress for the material. The slopes and intercepts of the lines were then used to estimate the key parameters in the one-dimensional model and very reasonable estimates for the state of stress at strain-rates in excess of  $10^4 / s$  were made.

#### **4.4 Mechanical Characterization of PVC and of PET**

One approach to the purification of recycled thermoplastic mixtures is selective grinding to induce differences in size and shape between polymers of different chemical

compositions. These mixtures could then be separated using one of several technologies including conventional sieving or hydrocyclones. The trick here is to select the grinding temperature. An investigation of mechanical properties, with emphasis on fracture behavior, was conducted on the polymers PVC and PET (see Green, Petty, Gillis, and Grulke [6], Appendix K). The Taylor impact test facility at the University of Alabama performed experiments which showed that, at room temperature and high strain rates, PVC deformed plastically while PET exhibited brittle fracture.

## **5. QUASI-STATIC YIELD STRENGTH ESTIMATES**

One of the most interesting results that stems from the elementary analysis is an estimate for quasi-static yield strength. We can use the Taylor impact test to estimate the quasi-static stress/strain curve for the specimen material. The fundamental equation comes directly from the theory and takes the form

$$\sigma_s(e) = \frac{\rho(1+e)(1-\beta)v_0^2}{2eln(\bar{\ell}/\ell_f)} \quad (7)$$

where  $\rho$  is the specimen density,  $e$  is the mean engineering strain,  $\bar{\ell}$  is the undeformed section length at the end of initial transient behavior,  $\ell_f$  is the undeformed section length at the end of the event,  $\beta$  is a dimensionless constant determined from experimental data, and  $v_0$  is the impact velocity of the specimen. If an estimate for  $\bar{\ell}$  can be found, then Equation (7) can be used to estimate the quasi-static yield stress for the specimen material at specific compressive strains  $e$ . A very simple estimate was provided by Jones, et al [13, p.11] (Appendix B). This estimate is based on modeling the deformed and undeformed regions of the Taylor specimen as concentric cylinders. The estimate takes the form

$$\frac{\bar{\ell}}{L_0} = \frac{b}{\beta} - \frac{(1-\beta)}{\beta} \frac{(1+e)}{e} \quad (8)$$

where  $L_0$  is the initial specimen length and  $b$  is a parameter that is determined from recovered Taylor cylinder data. Equations (7) and (8) produce remarkably accurate compressive stress/strain diagrams, in spite of the fact that no load cell is involved at all. Figures 10 and 11 of Appendix B show the comparison between experimentally determined quasi-static stress/strain diagrams and the estimates using Taylor cylinder data for two different materials. Obviously, the comparisons are very favorable, with the

discrepancies being attributable to uncertainties introduced by the theory and specimen measurement. This aspect of the analysis provides us with some confirmation and confidence for the theory.

There is very little material data reported at strain-rates of  $10^4$  / s and higher, so a direct comparison of the elementary theory with the results of some other test is impossible. However, quasi-static testing, in either tension or compression, can be accurately performed for any materials (see House and Gillis (Appendix L)). The comparisons that the theory gives us in this case are very significant. Also, the theory can now be applied to a series of Taylor tests of the same material and data reduction can be performed and the stress/strain-rate diagrams can be drawn without relying on data from any other test.

## **6. PENETRATION TESTING**

There are classes of materials for which there are presently no reliable methods for acquiring material properties at high strain rates. Among these are brittle geological materials, such as concrete or rock. In spite of the fact that these materials have been studied for dozens of years, there is very little known about their behavior at strain rates consistent with penetration tests. Specimen size and the brittle nature of these materials has limited laboratory testing. Most of the information that has been reported about these materials at ultra high strain-rates comes from penetration tests. The free constants in penetration models can be used to estimate the material properties of the target from penetration depth after the test is completed. The results are only as good as the penetration theory used to acquire them. In this context, any improvements to the accepted theories that can be made, may offer an improvement in the estimate of the mechanical properties of the target.

The most reliable one-dimensional theories for rigid body penetration of hard targets are those that stem from cavity expansion models. These theories produce estimates of pressure on the nose of the penetrator that is dependent on the square of the current velocity of the penetrator. Such pressures are usually referred to as Poncelet pressures and they lead directly to logarithmic penetration depth estimates. Nose geometry, penetrator mass loss, and assumptions about friction and shear can all have an influence on the results. These are the subjects of a series of papers devoted to improving and amplifying the one-dimensional penetration models with velocity-squared target pressure.

A very simple theory was developed by Jones, Jerome, Wilson, and Christopher [15] (Appendix L) to estimate the depth of penetration of hard concrete targets. This theory was used to estimate the time of penetration and can be used to find the target properties algebraically.

The noses of rigid penetrators can have a considerable influence on performance at high velocities. In order to investigate this influence, an analysis of nose geometry was performed by Jones, Rule, Jerome, and Klug [17] (Appendix M). A product of the analysis is an analytical formulation of a nose shape that minimizes the net force on the penetrator due to a Poncelet normal pressure. The solution is explicit and in the form of a perturbation series in powers of the nose ratio  $\alpha = a/b$ , where  $a$  is the shank radius and  $b$  is the nose length. This result avoids the use of more complicated means to satisfy the boundary conditions (e.g., see R. L. Halfman [7, pp. 466-469]) and alternative constraints on the nose, such as volume or surface area. The results are given in Appendix M, Figure 3 for several different nose shapes. The nose factor  $N$  governs the penetration capability for a fixed nose ratio, with the smallest values of  $N$  providing for the deepest penetration, assuming no mass loss or change in shape occurs.

The results presented by Jones, Rule, Jerome, and Klug [17] reflect the possibilities for penetration modeling of geological targets without friction. The blunting and erosion of some penetrator noses indicates that this approximation may not be entirely appropriate. This issue was addressed by Jones and Rule [10] (Appendix N) and Rule and Jones [21] (Appendix O) for some very simple frictional models. In the first case, pressure-dependent friction proportional to the pressure was used with reasonable success. In the second case, constant friction was used. Constant friction can be interpreted as maximum

target shear under high pressure. Estimating this material property at high strain-rates for geological materials is very difficult because the sample sizes must be very large and the material is brittle. Laboratory tests to estimate these material properties have yet to be devised and penetration data was effectively used to find them here.

One of the factors that influences the use of elementary penetration models to deduce the mechanical properties of geological target materials at high strain-rates and pressures is the loss of mass and blunting of the noses that occurs during very high speed penetration. These effects are not included in the penetration modeling discussed in the previous paragraphs, but they can obviously influence the results. To address these questions, an elementary analysis of nose erosion and mass loss was presented by Foster, Jones, Toness, DeAngelis, and Rule [4] (Appendix P). The principle behind the modeling is that erosion is the result of surface melting of the penetrator nose due to friction acting on the nose. The result is the very simple estimate for mass loss given below.

$$\Delta m = \frac{\pi a^2 \tau_0 M z}{k \int C_p dT} \quad (9)$$

In this equation,  $k$  is the mechanical equivalent of heat equal to 4.18 joules/calorie,  $\pi a^2$  is the cross-sectional area of the penetrator at the shank,  $\tau_0$  is the maximum dynamic shear strength of the target,  $M$  is the cross-sectional area of the nose,  $k \int C_p dT = 1032 J/g$  for steel, and  $z$  is the length of the tunnel. Equation (9) agrees very well with experimental observations. Figures 2 and 3 of Appendix P show the correlation for mass loss of steel penetrators impacting high strength concrete targets. In Figure 2, the penetrators are 4340 steel with ogive noses. In Figure 3, the penetrators are AerMet100 steel, also with ogive noses.

Equation (9) is a very interesting and useful relationship. By examining it, we see that mass loss is proportional to the length of the tunnel that the projectile makes in the target and inversely proportional to the heat required to melt the steel. Mass loss is also proportional to the product  $\pi r^2 M$ , which is roughly equivalent to the surface area of the nose. These are all very reasonable conclusions.

In Foster, Jones, Toness, DeAngelis, and Rule [4] many of the details required to derive Equation (9) were omitted. Another paper followed (Jones, Foster, Toness, DeAngelis, and Rule [14]) that was devoted to filling all of the gaps and presenting as complete a picture of the assumptions that were made in the process of arriving at Equation (9). This paper is included in the report as Appendix Q.

The effect of friction between the target and the projectile was assessed by Jones, Toness, Jerome and Rule [19] (Appendix R) for several different steels against the same concrete target.

Finally, work continued on penetration of metallic targets by metallic projectiles in Cinnamon and Jones [3]. The objective was to correlate penetration performance to the dynamic mechanical properties of the target and the projectile. It should be noted that there is substantial correlation between strength, crater diameter and penetration depth. The details of this work are contained in Appendix S.

## **7. CONCLUSIONS**

On this project, we successfully reached a number of important conclusions. We concentrated on the high rate response of materials and produced several methods for deducing the state of stress in a significant range of strain-rates between the limits of the Split-Hopkinson Pressure Bar and Flyer Plate experiments. The significance of these results reflect the need for reasonable constitutive modeling of warhead candidate materials in the critical strain-rate regime of  $10^4 - 10^6 / s$ .

For high rate behavior of metals and some other materials, we devised an elementary, one-dimensional theory for estimating the state of stress. This theory is versatile enough that an estimate for quasi-static stress was produced that was remarkably close to that achieved by means of a load frame and load cell. This provided confirmation for the theory, while a direct comparison with high rate results was not possible.

In the context of modeling the flow stress of materials in the neighborhood of  $10^4 - 10^6 / s$  strain-rate, an alternative to the conventional Johnson-Cook Strength Model, the RJC Model, was offered. Terms were added to the relation to account for high strain-rate behavior. This required the evaluation of three additional constants. A scheme for finding all eight of the adjustable parameters in the model using only quasi-static and Taylor test data was given. Comparison between the RJC model and the elementary theory was very favorable.

The elementary theory for reducing Taylor test data from experiments on an unconventional material, that is one for which the recovered specimen showed no deformation, was successfully applied to film data from tests on dense urethane. The

results of the application are very promising and suggest that the theory may have widespread use. Everything that was observed in the application of the theory to recovered metallic specimens was also present for the film record.

Air Force priorities dictated that some effort be directed toward characterizing geological materials for hard target penetrator applications. The difficulty here is no laboratory tests have been devised to date for testing these materials at strain-rates and pressures comparable to those observed in the penetration process. As a result, we have to rely on the free parameters in penetration models to provide us with constitutive behavior of the geological target materials. Naturally, any improvements or modifications to existing models may refine the estimates for material behavior. There were several papers published on hard target penetration on this project. Included in the results are estimates for shear stress in hard targets under high pressure.

The objectives of the project were largely fulfilled. But, in a project of this nature that crosses several disciplines and a wide variety of material problems, there are a number of important issues that remain to be addressed.

In the course of the investigation of hard target penetration modeling, it was clear that friction acting on the nose of the penetrator nose was inadequately modeled by any of the usual methods. High-speed friction is a very complex phenomenon that may have no simple explanation. Historically, the dependence of friction on pressure and velocity is vague because most of the testing was done at relatively low velocities. In order to model hard target penetration events successfully, we will have to devise some new and accurate friction laws.

Constitutive modeling with the Taylor test could be accomplished if a completely reliable estimate for strain-rate could be found. Although three different estimates for strain-rate were proposed in this project, all have some weaknesses. Work should continue in this area because the results have such important implications.

Finally, mass loss and blunting of high steel penetrators has serious consequences for performance. We gave an analysis that accounted for mass loss due to surface melting of the nose. This produced a very reasonable estimate that agreed fairly well with experimental observations. However, there are a few things that should be looked into. The changing geometry of the nose was not included in the analysis and this is one reason for the discrepancy between the predictions and the experimental evidence. Another area that should be explored further is the heat required to melt the steel penetrator material. We used the heat required to melt iron to make the estimates. This problem will be studied in the coming years.

## **8. REFERENCES**

1. Allen, D. J., Rule, W. K., and Jones, S. E., "Optimizing Material Strength Constants Numerically Extracted from Taylor Impact Test Data," *Experimental Mechanics*, 37, 3, 333 (1997).
2. Cinnamon, J. D., Jones, S. E., House, J. W., and Rule, W. K., "Validating the High Strain-Rate Strength Estimates Generated from High-Speed Film Data and a Revised Elementary Theory for the Taylor Test," in *Structures Under Extreme Loading Conditions-2000*, H. Levine, ed, 2000 ASME Pressure Vessels and Piping Conference, Seattle, WA, August (2000).
3. Cinnamon, John D. and Jones, S. E., "An Analysis of Rod Penetration of Semi-Infinite Targets Using an Average Pressure Estimate," in *Structures Under Extreme Loading Conditions-1999*, D. M. Jerome, ed, 1999 ASME Pressure Vessels and Piping Conference, Boston, MA, pp. 19-35 (1999).
4. Foster, J. C., Jr., Jones, S. E., Toness, O., De Angelis, R. J., and Rule, William K., "An Analytical Estimate for Mass Loss from a High Velocity Rigid Penetrator," *Proceedings of the 1999 APS Topical Conference on Shock Compression of Condensed Matter*, Snowbird, UT (1999).
5. Gillis, Peter P. and Jones, S. E., "Radial Inertia in the Taylor Test," in *Constitutive and Damage Modeling of Inelastic Deformation and Phase Transformation*, A. S. Khan, ed., pp. 647-650, Proceedings of Plasticity '99, The Seventh International Symposium on Plasticity, Cancun, Mexico, January (1999).
6. Green, Janet L., Petty, Charles A., Gillis, Peter P., and Grulke, Eric A., "Relationship Between Strain Rate, Temperature, and Impact Failure Mechanism for Poly(Vinyl

Chloride) and Poly(Ethylene Terephthalate)," *Polymer Engineering and Science*, **38**, 194 (1998).

7. Halfman, Robert L., *Dynamics: Systems, Variational Methods, and Relativity, Volume II*, Addison-Wesley Publishing Co., Reading, PA (1962).
8. House, J. W., Aref, B., Foster, J. C., Jr., and Gillis, P. P., "Film Data Reduction from Taylor Impact Tests," *Journal of Strain Analysis for Engineering Design*, **34**, 337 (1999).
9. House, Joel W. and Gillis, Peter P., "Testing Machines and Strain Sensors," in *Metals Handbook*, 10<sup>th</sup> ed., Volume 8, *Mechanical Testing and Evaluation*, ASM International, pp. 79-92, (2000).
10. Jones, S. E. and Rule, William K., "On the Optimal Geometry for a Rigid Penetrator, Including the Effects of Pressure-Dependent Friction," *International Journal of Impact Engineering*, **24**, 403 (2000).
11. Jones, S. E., Ahern, David, Taylor, Marcus A., and Rule, William K., "Taylor Impact Testing of High Strength Steels," submitted for publication.
12. Jones, S. E., Barkey, M. E., Rule, W. K., and Huber, E., "Mechanical Characterization of Hardened Astralloy-V® Using the Taylor Impact Test," Proceedings of the AIAA Symposium on Orbital Debris, Huntsville, AL (1996).
13. Jones, S. E., Drinkard, J. A., Rule, W. K., and Wilson, L. L., "An Elementary Theory for the Taylor Impact Test," *Int. J. Impact Engng.*, **21**, 1 (1998).
14. Jones, S. E., Foster, J. C., Jr., Toness, O., De Angelis, R. J., and Rule, W. K., "An Estimate for Mass loss from High Velocity Steel Penetrators," submitted for publication in the *International Journal of Impact Engineering*.

15. Jones, S. E., Jerome, D. M., Wilson, L. L., and Christopher, F. R., "An Engineering Analysis of Normal Rigid Body Penetration into Concrete," in *Structures Under Extreme Loading Conditions*, H. S. Levine, ed, PVP-VOL. 361, pp. 63-67, ASME Pressure Vessels and Piping Conference, San Diego, CA (1998).

16. Jones, S. E., Maudlin, P. J., and Foster, J. C., Jr., "Constitutive Modeling Using the Taylor Impact Test," in *High Strain Rate Effects in Polymer, Metal and Ceramic Matrix Composites and Other Advanced Materials*, Y. D. S. Rajapakse and J. R. Vinson, eds., ASME Winter Annual Meeting, San Francisco, CA (1995).

17. Jones, S. E., Rule, William K., Jerome, D. M., and Klug, R. T., "On the Optimal Nose Geometry for a Rigid Penetrator," *Computational Mechanics*, **22**, 413 (1998). A six page summary of this paper appears in *Modeling and Simulation Based Engineering, Vol. II*, S. N. Atluri and P. E. O'Donoghue, eds., Tech Science Press, Palmdale, CA, pp. 1120-1125 (1998).

18. Jones, S. E., Toness, O. A., Jerome, D. M., and Rule, William K., "Normal Penetration of Semi-Infinite Targets by Ogive-Nose Projectiles, Including the Effects of Blunting and Erosion," in *Thermal Hydraulics, Liquid Sloshing, Extreme Loads, and Structural Response, 2001*, F. J. Moody, ed., ASME-PVP (2001).

19. Jones, S. E., Wilson, L. L., and Rule, William K., "An Estimate for Strain-Rate in the Taylor Impact Test," in *Constitutive and Damage Modeling of Inelastic Deformation and Phase Transformation*, A. S. Kahn, ed. Proceedings of Plasticity '99, The Seventh International Symposium on Plasticity, Cancun, Mexico, January (1999).

20. Rule, W. K. and Jones, S. E., "A Revised Form for the Johnson-Cook Strength Model," *Int. J. Impact Engng.*, **21**, 609 (1998).

21. Rule, William K. and Jones, S. E., "Some Remarks on the Optimal Geometry of a Rigid Penetrator in the Presence of Friction," in *Structures Under Extreme Loading Conditions-1999*, D. M. Jerome, ed, 1999 ASME Pressure Vessels and Piping Conference, Boston, MA, pp. 11-17 (1999).

22. Wilson, L. L., Foster, J. C., Jr., Jones, S. E., and Gillis, P. P., "Taylor Test Analysis of an Unconventional Material," Proceedings of the Third International Conference on Composite Materials, New Orleans, LA (1996).

## **APPENDIX A**

## RADIAL INERTIA IN THE TAYLOR IMPACT TEST

Peter P. Gillis<sup>1</sup> and S. E. Jones<sup>2</sup>

1. Department of Chemical and Materials Engineering, University of Kentucky, Lexington, KY 40506, 2. U. S. Air Force Research Laboratory, MNMW, Eglin AFB, FL 32542 (on leave from the University of Alabama)

**ABSTRACT-** In this paper, we examine the effect of radial inertia on the axial stress distribution during axisymmetric constant-volume deformation. In place of the frequently used assumption that at each axial position the axial stress is constant, we assume that plane cross-sections remain plane. It is shown that both the radial and circumferential stress components will be compressive if only strain-rate effects are considered. Strain-acceleration must be taken into account in order to have radial tension, as would be expected in a dynamic tension test. Results of this analysis are applied to the Taylor impact test.

**INTRODUCTION:** As an aid to visualization, the present analysis is framed in terms of a Taylor impact test. However, it is equally applicable to any axially symmetric, dynamic deformation.

In the discussion of radial inertia, one expects that under dynamic tension a tensile radial stress would be required to move material radially inwards towards the axis of symmetry. In analyses that neglect strain-acceleration, the radial stress is compressive. Under dynamic compression, a compressive radial stress would be expected, to move material outwards from the axis of symmetry. In analyses that neglect strain-acceleration, the magnitude of this radial stress is significantly underestimated. The present analysis rectifies these problems by accounting for the strain-acceleration. The ensuing results are applied to the Taylor impact test.

**THEORY:** Consider the normal impact of a Taylor [1948] cylinder against a massive anvil and assume that the subsequent deformation of the cylinder is axisymmetric. The natural coordinate system to describe the deformation is polar coordinates  $r, \theta, z$ . The prescribed symmetry obviates displacements in the circumferential direction; displacements in the radial and axial directions are denoted by  $\eta$  and  $\zeta$ , respectively as shown in the appended drawing. The axial displacement  $\zeta$  is assumed independent of  $r$ . ("Plane cross-sections remain plane.") The radial displacement  $\eta$  must be an odd function of radial position. To lowest order terms

$$\eta(r, z, t) = N(z, t)r \quad (1)$$

where  $N(z, t)$  is a dimensionless function to be determined. For isochoric deformation,  $N$  has the form

$$N = (1 + e)^{-1/2} - 1 \quad (2)$$

where  $e$  is the engineering axial strain.

Let the normal stress components  $\sigma_r, \sigma_\theta, \sigma_z$  express the force intensity with respect to the deformed configuration. Assume that the shear stress can be neglected and  $\sigma_r \equiv \sigma_\theta$ . Then, assuming that a von Mises type of yield criterion is obeyed, it follows that

$$\sigma_r - \sigma_z = \sigma \quad (3)$$

where  $\sigma$  is the flow stress (positive).

Simplified by all of the foregoing assumptions, the differential equation of motion for the radial direction is

$$\partial \sigma_r / \partial t = \rho \partial^2 \eta / \partial t^2 \quad (4)$$

where  $\rho$  is the mass density of the specimen material. Integrating Equation (4) partially with respect to  $r$  leads to

$$\sigma_r = -(1/2) \rho \partial^2 N / \partial t^2 [R^2 - r^2] \quad (5)$$

where  $R$  is radius of the specimen.  $R$  can be expressed as

$$R = R_0 (1 + N) = R_0 (1 + e)^{-1/2} \quad (6)$$

where  $R_0$  is the initial specimen radius. It is also possible, using Equation (2), to express  $\partial^2 N / \partial t^2$  in terms of strain  $e$ , strain-rate  $\dot{e}$ , and strain-acceleration  $\ddot{e}$

$$\partial^2 N / \partial t^2 = [3\dot{e}^2 - 2(1 + e)\ddot{e}] / 4(1 + e)^{5/2}. \quad (7)$$

In the one-dimensional analysis of Taylor [1948], the axial stress  $\sigma_r$  and the effective stress  $\sigma$  coincide; at least in magnitude. Furthermore, the Taylor axial stress must be the average value over the cross-section because he used it in the sense that  $\sigma_r A$  equaled the axial force. The present approximate analysis requires equal strain and strain-rate components at every point in a given cross-section. Consequently, most constitutive relations would require a constant effective stress.

Assume that  $\hat{\sigma}_s$  represents the average axial stress as determined from the Taylor equations or some other one-dimensional analysis of the test. To find the effective stress  $\sigma$ , the relation

$$\hat{\sigma}_s A = \int \sigma_s dA = -\sigma A + \int \sigma_s dA \quad (8)$$

is first employed. Here  $A = \pi R^2$  is the current, local, cross-sectional area and the integration is performed over it. Now,  $\sigma_s$  is given in Equation (5). Substituting into Equation (8) and performing the integration, leads to

$$\hat{\sigma}_s = -\sigma - (1/4) \rho \partial^2 N / \partial t^2 R^2 = -\sigma - \rho \partial^2 N / \partial t^2 R_0^2 / 4(1+e). \quad (9)$$

This equation shows that the radial inertia correction can be either positive or negative depending upon the sign of the radial acceleration. In turn, Equation (7) shows that the sign of the radial acceleration depends upon the sign and magnitude of the effective strain-acceleration  $\dot{e}$ . Equation (9) can be rearranged to provide a dynamic, compressive equivalent of the static, tensile Bridgman [1952] correction factor

$$\sigma = -\hat{\sigma}_s [1 + \rho \partial^2 N / \partial t^2 R_0^2 / 4\hat{\sigma}_s (1+e)]. \quad (10)$$

The factor in the brackets is the ratio of the magnitude of effective stress to average axial stress.

**SOME OBSERVATIONS:** In the Taylor analysis, both strain-rate and strain-acceleration are unbounded at the location to which Equation (7) should be applied. This has long been recognized as a defect of the Taylor analysis: although it yields a dynamic flow strength, there is no estimate of the corresponding strain-rate prevailing in each test.

In the present analysis, in order to assess the relative magnitudes of the two terms in Equation (7), the strain-acceleration will be related to the strain-rate using the mean value theorem:  $\dot{e} = \int_0^t (\partial^2 e / \partial t^2) dt = at$ . Here  $a$  is the time average value of the strain-acceleration during the interval 0 to  $t$  when the strain-rate,  $\partial e / \partial t$ , changes from 0 to  $\dot{e}$ . It also represents some actual value if the strain-acceleration is continuous during the interval. Thus,  $a = \dot{e}/t$  can be used to replace  $\partial^2 e / \partial t^2$  in Equation (7), which now becomes

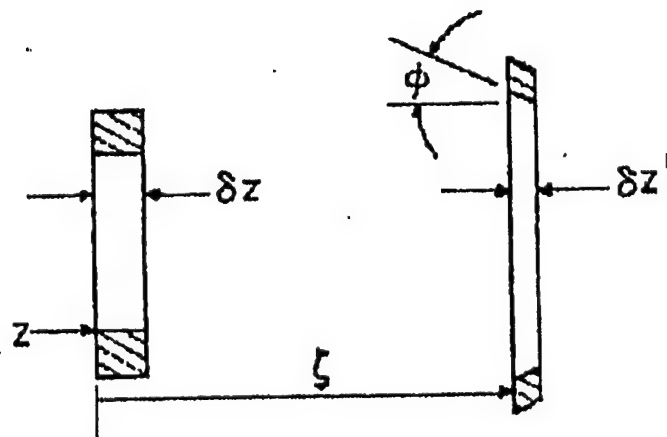
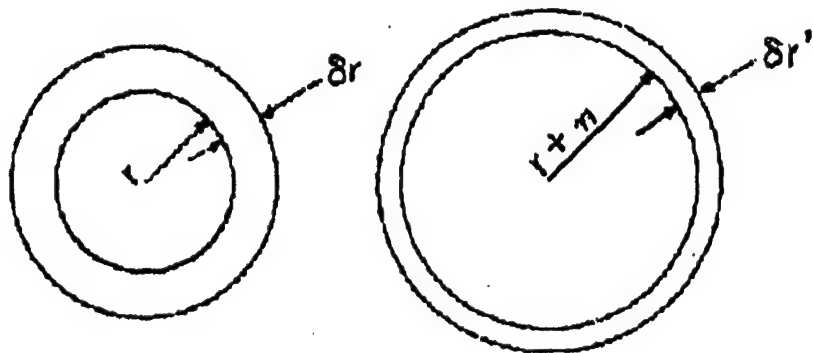
$$\frac{\partial^2 N}{\partial t^2} = \frac{3\dot{e}^2}{4(1+e)^{5/2}} \left[ 1 - \frac{2(1+e)}{3\dot{e}t} \right] \quad (11)$$

where the second term in the brackets represents the relative magnitude of the strain-acceleration in comparison to unity.

Suppose that the Taylor test maximum strain-rate  $\dot{\epsilon}$  is in the range (minus)  $10^3 - 10^4 / s$ . and the rise time of the plastic wave front is in the range  $1-10 \mu s$ . Then, omitting the value of  $\epsilon$  from Equation (11), the maximum relative effect of the strain-acceleration is over 600 while the minimum is about 6. Evidently, the strain-acceleration term can dominate under some circumstances and must always be retained.

#### REFERENCES:

Bridgman, P. W. (1952), Large Plastic Flow & Fracture, McGraw-Hill, New York.  
 Jones, S. E., et al (1991), *J. Engr. Mats. Tech. (Trans. ASME)* 113, 228.  
 Taylor, G. I. (1948), *Proc. Roy. Soc. (London) Ser. A* 194, 289.



## **APPENDIX B**

## AN ELEMENTARY THEORY FOR THE TAYLOR IMPACT TEST

S. E. JONES\*, JEFFREY A. DRINKARD\*, W. K. RULE\* and L. L. WILSON†

\*College of Engineering, The University of Alabama, Tuscaloosa, AL 35487, U.S.A.  
 †SAIC, Shalimar, FL 32542, U.S.A.

(Received 10 January 1997; in revised form 6 June 1997)

**Summary**—There is a linear relationship between certain normalized lengths in recovered Taylor Impact specimens. This observation seems to have first been made by J. W. House, although G. I. Taylor and A. C. Whiffen both produced graphs involving these same scaled variables. However, no explanation was given for this scaling and it was not used for any specific purpose. In this paper, a theoretical basis for the linearity is established and the slope and intercept are used to determine several important physical parameters. These parameters are then used to determine the state of stress at strain-rates exceeding  $10^4/s$ . This information is useful because it helps to bridge the strain-rate gap between Split-Hopkinson pressure bar testing and the ultra-high rates achieved with plate impact experiments. © 1997 Elsevier Science Ltd.

### INTRODUCTION

The Taylor test [1, 2] is a useful high rate materials test in which strain-rates of  $10^4$ – $10^5\text{ s}^{-1}$  can be easily realized for even relatively low velocity impacts. Higher rates are possible, but often they are found during the initial transient stage of deformation [3]. This stage is difficult to analyze because of the shock at impact and the effects of shock hardening on the specimen material [4]. However, this stage attenuates rapidly into quasi-steady wave propagation followed by specimen deceleration during the terminal transient. Although the strain-rates are somewhat lower during these stages, the behavior of the undeformed section of the specimen can be accurately predicted with an elementary mathematical model. The strain-rates achieved during these latter stages are still above the limit of the Split-Hopkinson pressure bar and its many variants.

After the initial transient, the motion of the undeformed section can be described by a one-dimensional analysis. Several one-dimensional analyses for the Taylor test have been proposed (e.g. [5–10]). However, these analyses do not address the highly nonlinear front motion during the initial transient or do not offer a very precise estimate of the state of stress in the specimen at any specific time during the deformation. Recently, an analysis of plastic wave propagation was presented that effectively excludes the initial transient [11–13]. This paper provides an alternative to the method used to evaluate the key parameters in [12].

### AN ELEMENTARY THEORY

Taylor [1] and Whiffen [2] observed the relationship between certain normalized lengths in a recovered Taylor specimen. House [3] later confirmed that one of these relationships is linear. There are other scalings (e.g. [14]), but this is the most useful to date.

A very simple theory can be developed with some of the observations presented in [12]. After the initial transient at impact has attenuated, we assume that the particle velocity,  $u$ , for the plastic material behind the plastic wave front and the undeformed section speed,  $v$ , are approximately proportional to each other [11]:

$$u = \beta v. \quad (1)$$

Justification for this relationship is given in [12] and it appears to persist throughout the quasi-steady and terminal transient stages of the deformation. The initial transient refers to nonlinear time-dependent behavior of the deformation front following impact of the specimen. Now, conservation of mass across the plastic wave front leads to

$$e\dot{\ell} = v - u = (1 - \beta)v, \quad (2)$$

where  $e$  is the compressive engineering strain on the plastic side of the wave front and  $\ell$  is the current undeformed section length, see Fig. 1. Dots over variables denote time differentiation. As observed before [1, 10],  $e = (A_0/A) - 1$ , where  $A_0$  and  $A$  are the initial and current cross-sectional areas of the specimen, respectively.

For a plastic wave moving with constant strain away from the impact face, the variables in Eqn (2) may be separated:

$$d\ell = \frac{1 - \beta}{e} ds, \quad (3)$$

where Eqn (3) applies to the behavior of the undeformed section after the initial transient and may be directly integrated to give

$$\ell - \bar{\ell} = \frac{1 - \beta}{e} (s - \bar{s}). \quad (4)$$

Bars over variables are used to denote the values of the indicated variables at the end of the initial transient stage.

If Eqn (4) applies until the end of the event, then it becomes

$$\ell_f - \bar{\ell} = \frac{1 - \beta}{e} (s_f - \bar{s}), \quad (5)$$

where  $\ell_f$  and  $s_f$  are the final undeformed section length and the final displacement of the undeformed section, respectively. These quantities can be determined from post-test measurement of a ductile metal Taylor cylinder, as shown in Fig. 2.

Dividing Eq (5) by  $L_0$ , the original length of the cylinder, and noting that  $s_f = L_0 - L_f$  allows us to express Eq (5) in the following form:

$$\frac{\ell_f}{L_0} = -\frac{1 - \beta}{e} \frac{L_f}{L_0} + \frac{\bar{\ell}}{L_0} + \frac{1 - \beta}{e} - \frac{1 - \beta}{e} \frac{\bar{s}}{L_0}. \quad (6)$$

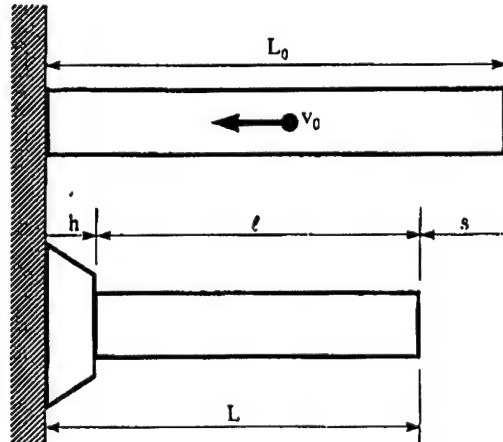


Fig. 1. A uniform cylinder of length  $L_0$  impacts an uncompliant target with velocity  $v_0$ . Subsequent deformation of the specimen can be successfully modeled in terms of deformed and undeformed regions  $h$  and  $\ell$ .  $L$  is the current overall specimen length and  $s$  is the displacement of the back end of the specimen.

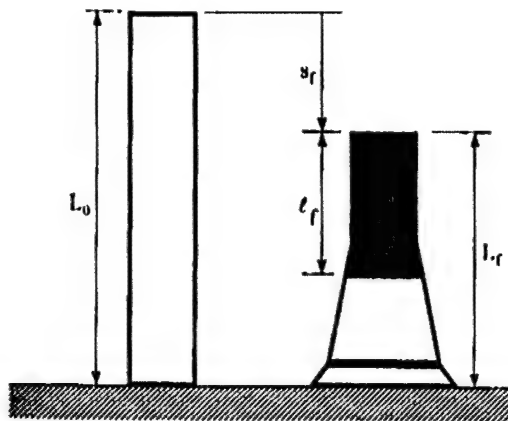


Fig. 2. Undeformed and deformed Taylor specimens. The final undeformed section length  $l_f$  is the distance from the back of the specimen to the cross section with area  $A = A_0/(1 + e)$ .  $L_f$  is the final overall length of the deformed specimen.

This equation expresses a linear relationship between  $l_f/L_0$  and  $L_f/L_0$ . This relationship, which has been observed experimentally by House [3], is the basis for the remainder of this paper.

#### THE LINEARITY BETWEEN $l_f/L_0$ AND $L_f/L_0$

Cylindrical specimens of OFHC copper and wrought iron were impacted against an Astralloy-V<sub>6</sub> Steel target. The Astralloy V<sub>6</sub> was hardened to Rockwell C 58 and presented a very uncompliant surface. To reduce the effects of friction, the target was lapped and polished to a mirror like finish. 17 Caliber specimens were impacted against this target and the target was rotated after each impact to assure that conditions were the same for each test. By 17 caliber, we refer to a bore diameter of 0.170 in. for the launch tube. The test results are shown for various strain levels as plots of  $l_f/L_0$  and  $L_f/L_0$  in Figs 3 and 4.  $l_f$  is the distance from the back end of the specimen to the cross-section with area  $A = A_0/(1 + e)$  for a prescribed strain  $e$  (see Fig. 2). The area  $A$  is determined from a diameter measurement. There are several methods suitable for this measurement. The best is a diameter guage originally suggested by J. W. House. A hole is drilled in a steel block to the exact diameter required. From the opposite direction, a relief hole of larger diameter is drilled, allowing for clearance of the specimen. Very reasonable estimates of undeformed section length can be made using this device. There is a level of uncertainty with all measurement techniques and it is difficult to assess the degree of uncertainty. In fact, it may not be worthwhile to focus on any specific source of error when it is impossible to make the same assessment of the theory itself.

Equation (6) predicts a linear relationship between  $l_f/L_0$  and  $L_f/L_0$ :

$$\frac{l_f}{L_0} = m \frac{L_f}{L_0} + b, \quad (7)$$

where

$$m = -\frac{1 - \beta}{e} \quad (8)$$

and

$$b = \frac{\bar{l}}{L_0} + \frac{1 - \beta}{e} - \frac{1 - \beta}{e} \frac{\bar{s}}{L_0}. \quad (9)$$

For a given strain level, the slope and intercept values of Eqn (7) can be obtained by conducting a series of Taylor tests over a range of impact velocities. However, often a single

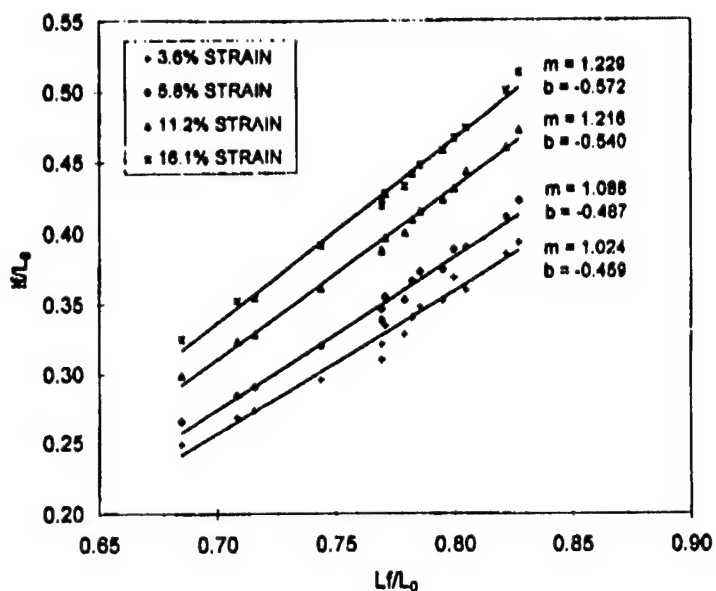


Fig. 3. The results of 17-caliber OFHC copper impact tests. The lines were drawn using the data reduction technique described by Eqns (10)–(12).

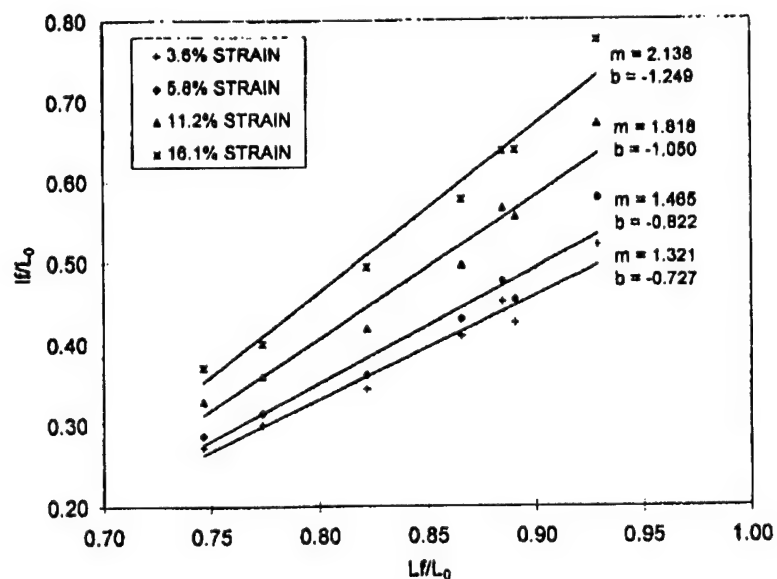


Fig. 4. The results of 17-caliber wrought iron impact tests. The lines were drawn using the data reduction technique described by Eqns (10)–(12).

Taylor test can be used to obtain data at several strain levels. Equation (8) suggests that the slope might decrease with increasing compressive strain. This is not the case because  $\beta$  decreases with increasing compressive strain.

There are two basic methods for obtaining the slope and intercept values for each strain level from this data. A classical least squares approach can be used repeatedly (operating on one set of constant strain data at a time) to obtain the sets of slope and intercept data for each strain level. However, this approach does not allow for the fact that the sets of constant strain data are actually coupled to each other since each Taylor specimen is used to obtain data at several strain levels.

A more consistent approach would entail using the entire data set at once to determine the slope and intercept values as a function of strain. This can be simply accomplished by assuming quadratic forms for the slope and intercept functions:

$$m = m_0 + m_1|e| + m_2|e|^2, \quad (10)$$

$$b = b_0 + b_1|e| + b_2|e|^2, \quad (11)$$

where  $|e|$  is the magnitude of the plastic strain and the  $m_i$  and  $b_j$  are coefficients to be determined from the data. Accordingly, the least squares quantity to be minimized,  $\Delta$ , for this application is

$$\Delta = \sum_{i=1}^N \left\{ \left( \frac{L_f}{L} \right)_i - \left[ (m_0 + m_1|e_i| + m_2|e_i|^2) \left( \frac{L_f}{L} \right)_i + (b_0 + b_1|e_i| + b_2|e_i|^2) \right] \right\}^2, \quad (12)$$

where  $N$  is the number of measured data points, and  $(L_f/L)_i$  and  $(L_f/L_0)_i$  indicate measured values of these parameters. An optimizer is used to adjust the  $m_i$  and  $b_j$  coefficients of Eqn (12) to minimize the fit error  $\Delta$ . In this paper, it was found for wrought iron and OFHC copper data that the slope and intercept functions of Eqns (10) and (11) were almost linear in strain. Thus the form of these equations appears to be of a sufficiently high order to obtain a good fit.

There are two advantages in fitting all the data at once using Eqn (12) as opposed to doing a separate least-squares fit for each strain level. Firstly, the error associated with the inherently more inaccurate low strain data is reduced since slope and intercept functions are fit in a manner that forces them to be consistent with the more accurate high strain data. Secondly, sets of constant strain data are not required for use in Eqn (12). This provides for more flexibility in the deformed specimen measurement techniques.

At high impact velocities [(low  $(L_f/L_0)$ )] specimen failure (void nucleation and fracture) can occur. Also, at low impact velocities [high  $(L_f/L_0)$ ] quasi-steady-state plastic flow may not occur. Both of these effects are not accounted for by the theory presented here and thus produce nonlinearities in plots of Eqn (7). Accordingly, it is recommended that obviously nonlinear high- and low-velocity data points be excluded from the least-squares calculations of Eqn (12).

### ESTIMATION OF STRESS

The dynamic stress  $\sigma$  at the strain  $e$  has been shown to take the form

$$\sigma = (1 + e) \left[ \sigma_0 + \frac{(1 - \beta)^2}{e} \rho v^2 \right], \quad (13)$$

where  $\sigma_0$  is a constant reference stress (see [12]). In Eqn (13),  $\rho$  is the constant specimen density and  $\beta$  the particle velocity constant in Eqn (1). The stress  $\sigma_0$  is negative in compression and positive in tension.

The equation of motion of the undeformed section is

$$\rho \ell \dot{v} = \sigma_0 \quad (14)$$

(see [12]). With a change of variables, this equation can be written in the form

$$\rho \ell \frac{d\ell}{dt} \frac{dv}{d\ell} = \sigma_0. \quad (15)$$

Using Eqn (2) to eliminate  $d\ell/dt$ , we find

$$\frac{\rho(1 - \beta)}{e} \ell v \frac{dv}{d\ell} = \sigma_0. \quad (16)$$

The variables in this equation can be separated and the resulting equation can be integrated to give

$$\frac{\rho(1-\beta)}{2e\sigma_0} v^2 = \ln(\ell) + C. \quad (17)$$

The constant of integration  $C$  appearing in Eqn (17) can be evaluated by noting that  $\ell = \bar{\ell}$  when  $v = v_0$ . This leads to

$$\ell = \bar{\ell} \exp \left[ \frac{\rho(1-\beta)}{2e\sigma_0} (v^2 - v_0^2) \right]. \quad (18)$$

The undeformed section no longer deforms at strain  $e$  when a critical velocity, say  $v = v_c$ , is reached. At this point, the final undeformed section length  $\ell = \ell_f$  is reached and

$$\ell_f = \bar{\ell} \exp \left[ \frac{\rho(1-\beta)}{2e\sigma_0} (v_c^2 - v_0^2) \right]. \quad (19)$$

This relation can be used to find the reference stress  $\sigma_0$

$$\sigma_0 = \frac{\rho(1-\beta)(v_0^2 - v_c^2)}{2e \ln(\bar{\ell}/\ell_f)} \quad (20)$$

This stress can be used in Eqn (13) to determine the dynamics stress  $\sigma$ .

In most instances, the critical velocity  $v_c$  can be set to zero, without much loss of accuracy, as the term involving  $v_c^2$  only contributes to the stress when  $v_c$  is fairly large. In this case, Eqn (20) becomes

$$\sigma_0 = \frac{\rho(1-\beta)v_0^2}{2e \ln(\bar{\ell}/\ell_f)}. \quad (21)$$

Equation (13) represents the dynamic stress in the specimen at the plastic wave front. As the velocity of the undeformed section  $v$  approaches  $v_c$ , or in this case zero,  $\sigma$  must approach the compressive quasi-static stress at the compressive strain  $e$ . Denoting the quasi-static stress by  $\sigma_s$ , we see that

$$\sigma_s(e) = (1+e)\sigma_0 = \frac{\rho(1+e)(1-\beta)v_0^2}{2e \ln(\bar{\ell}/\ell_f)}. \quad (22)$$

This relation expresses the quasi-static stress as a function of the strain and the parameters from the Taylor test.

Using a quasi-static stress/strain diagram for the specimen material and Eqn (22), we can find the reference stress  $\sigma_0$ , and the stress provided by Eqn (13) is determined.

## RESULTS

The state of stress in the specimen material can now be estimated. An estimate for the highest strain-rate after the initial transient was given by Jones *et al.* [15]:

$$\dot{e} = \frac{-v_0}{L_0 - \ell_0}. \quad (23)$$

This estimate is based on Taylor's [1] original idea for an average strain-rate over the entire test. In this respect, his estimate is very conservative and generally underestimates the strain-rate by nearly an order of magnitude. Equation (23) applies relatively close to the impact point and provides a more accurate estimate of strain-rate.

As indicated in the previous section, the stress can be evaluated using Eqn (13) once  $\beta$  has been found using Eqn (8) and  $\sigma_0$  has been found using Eqn (22). Quasi-static (compression) stress-strain diagrams for OFHC copper and wrought iron are shown in Figs 5 and 6.  $\sigma_0 = \sigma_s(e)/(1+e)$  can be found for any particular strain from the diagrams.

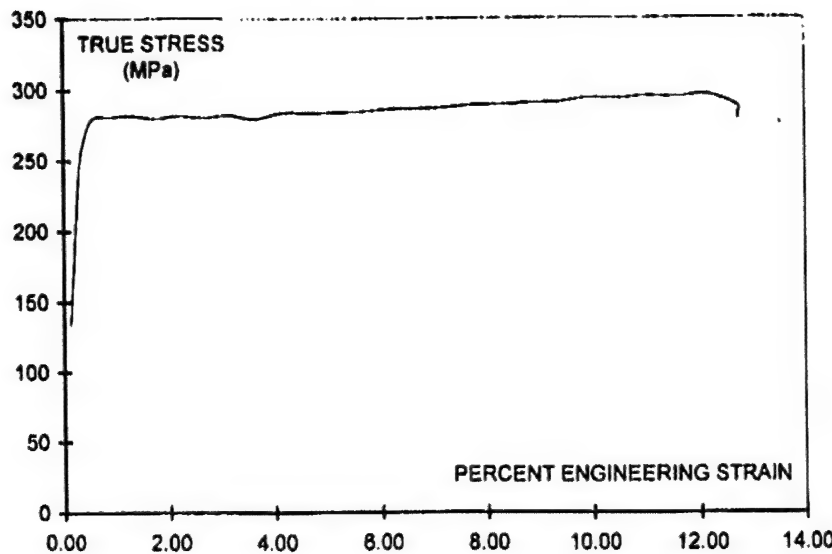


Fig. 5. Quasi-static compression data for OFHC copper.

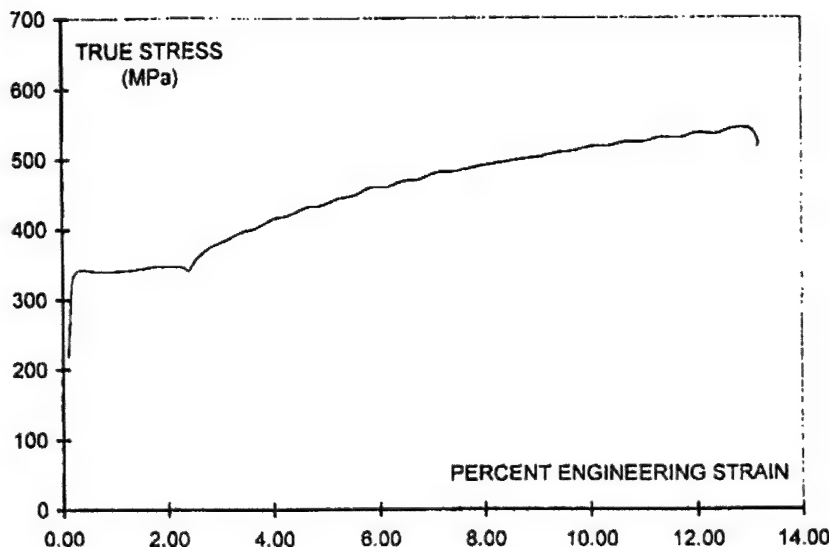


Fig. 6. Quasi-static compression data for wrought iron.

The undeformed section length at the end of the initial transient,  $Z$ , can be found from Eqn (21). Now, the state of stress at a known strain can be predicted by Eqns (13) and (23). Since the strain-rate estimate only applies at the instant when quasi-steady propagation of the plastic wave with strain  $e$  begins, only the stress at this instant should be used. During the initial transient, there is no change in the velocity of the undeformed section [16]. Thus, the stress at the point where Eqn (23) applies is given by

$$\sigma = \sigma_s(e) + \frac{(1+e)(1-\beta)^2}{e} \rho v_0^2. \quad (24)$$

This is the maximum stress in the event for which this analysis applies. We can now plot stress vs. strain-rate at fixed strain. Figures 7 and 8 show the results of numerous Taylor tests of 17 caliber OFHC copper and wrought iron specimens for a series of strains ranging from 3.6% to 16.1%. The choice of these strains was made on the basis of initial specimen

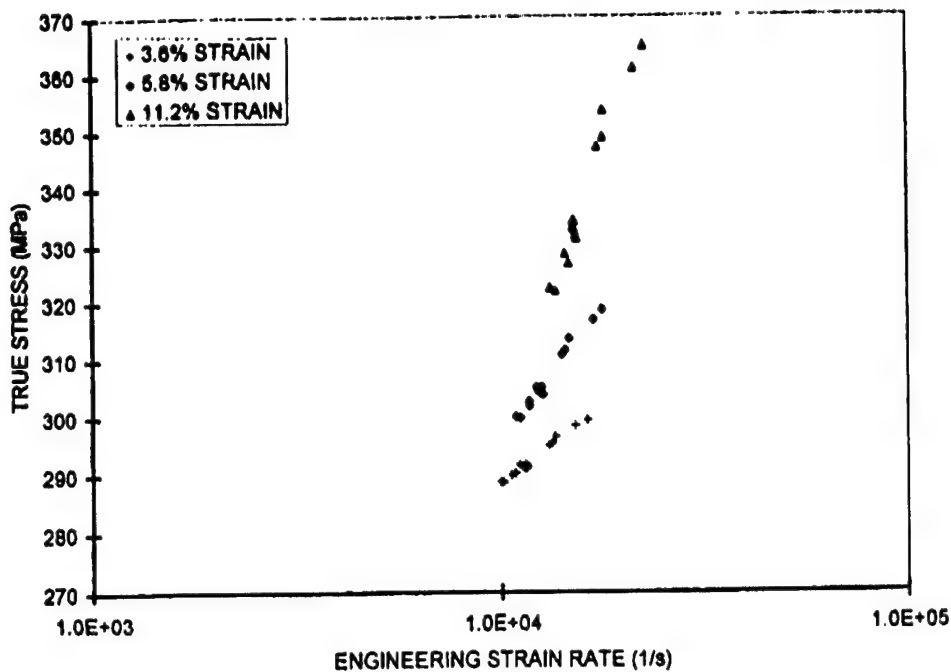


Fig. 7. Dynamic true stress vs. engineering strain-rate for OFHC copper in the "as received" condition.

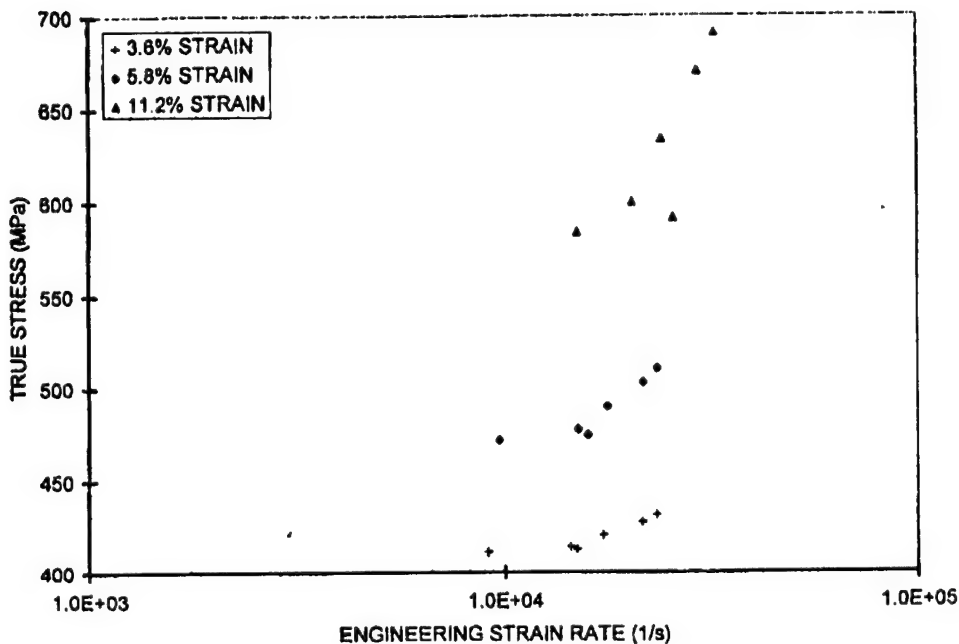


Fig. 8. Dynamic true stress vs. engineering strain-rate for wrought iron.

diameter and measurements of final diameter were made carefully. Low caliber specimens are difficult to measure accurately. Higher caliber tests are feasible and deformed specimen measurements can be made more accurately. However, the effects of radial inertia are more pronounced in higher caliber specimens.

For several reasons, a 17 caliber launch tube provides the lowest practical diameter. Lower caliber specimens may readily buckle under the impact load. Also, very low caliber specimens are difficult to launch as the load that the buck end of the specimen suffers in the launch process deforms it and may cause it to come to rest in the launch tube. This makes testing with these specimens a tedious and often unrewarding task. However, the gain from effectively eliminating radial inertia makes it worthwhile.

### ADDITIONAL RESULTS

Another point regarding the presentation of this theory can be made. The ratio  $\bar{z}/L_0$  is critical to the strain-rate estimate in Eqn (23). In the previous section, this ratio was determined for OFHC copper and wrought iron using Eqn (22) with  $\sigma_s$  taken from the quasi-static stress-strain diagrams given in Figs 5 and 6. Another approach can be adopted which avoids the use of Figs 5 and 6. This alternative allows us to estimate the quasi-static stress-strain diagram from Taylor impact data alone.

Equation (9) provides a relationship between  $\bar{z}/L_0$  and  $\bar{s}/L_0$ . In addition, it is evident that

$$\frac{\bar{z}}{L_0} + \frac{\bar{h}}{L_0} + \frac{\bar{s}}{L_0} = 1. \quad (25)$$

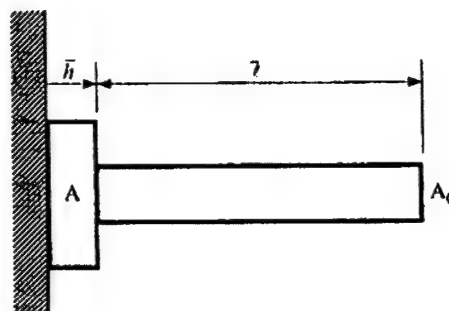


Fig. 9. Elementary mushrooming rod geometry. The mushroom is a cylinder with cross-sectional area  $A = A_0/(1 + e)$ . The undeformed section is a cylinder of length  $\bar{z}$  with cross-sectional area  $A_0$ .

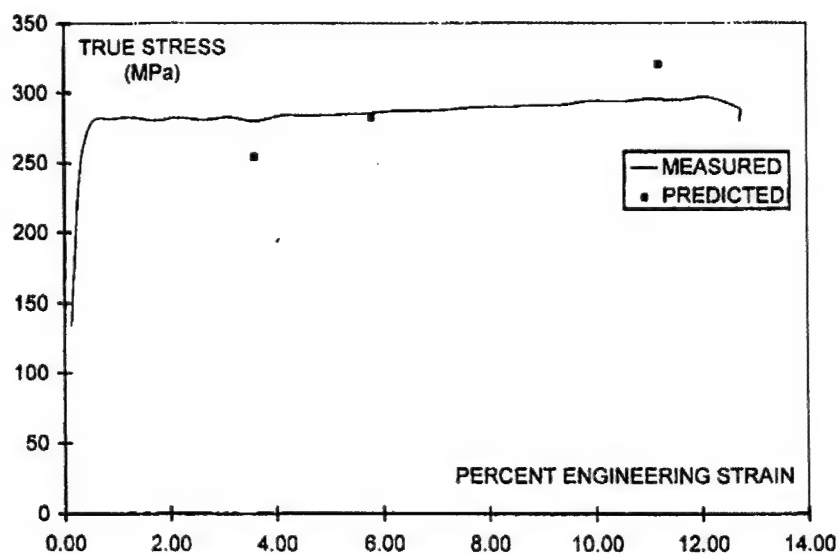


Fig. 10. Comparison of quasi-static OFHC copper stress/strain data given in Fig. 5 with estimates using Eqns (22) and (27).

Table I

Data point (m/s)	Percent comp. strain	Results obtained from quasi-static test data		Predictions obtained from using Taylor test data only		Percentage differences	
		$\bar{z}/L_0$	Quasi-static yield stress (MPa)	$\bar{z}/L_0$	Quasi-static yield stress (MPa)	$\bar{z}/L_0$	Quasi-static yield stress
1 $V_0 = 171$	3.6	0.529	282	0.552	258	4.3	- 8.5
	5.8	0.564	288	0.572	279	1.4	- 3.0
	11.2	0.638	295	0.623	310	- 2.3	5.2
2 $V_0 = 200$	3.6	0.513	282	0.552	252	7.7	- 10.6
	5.8	0.548	288	0.572	270	4.3	- 6.3
	11.2	0.630	295	0.623	300	- 1.1	1.7
3 $V_0 = 212$	3.6	0.503	282	0.552	249	9.7	- 11.7
	5.8	0.542	288	0.572	267	5.6	- 7.1
	11.2	0.622	295	0.623	294	0.2	- 0.3
4 $V_0 = 146$	3.6	0.536	282	0.552	259	3.0	- 8.1
	5.8	0.574	288	0.572	291	- 0.4	1.2
	11.2	0.650	295	0.623	336	- 4.1	13.7
5 $V_0 = 144$	3.6	0.544	282	0.552	270	1.5	- 4.4
	5.8	0.587	288	0.572	312	- 2.5	8.2
	11.2	0.662	295	0.623	359	- 5.8	21.7
6 $V_0 = 174$	3.6	0.515	282	0.552	246	7.2	- 12.9
	5.8	0.558	288	0.572	274	2.5	- 4.9
	11.2	0.634	295	0.623	306	- 1.7	3.6
7 $V_0 = 170$	3.6	0.517	282	0.552	246	6.8	- 12.7
	5.8	0.558	288	0.572	273	2.5	- 5.2
	11.2	0.641	295	0.623	314	- 2.8	6.4
8 $V_0 = 167$	3.6	0.538	282	0.552	266	2.6	- 5.6
	5.8	0.579	288	0.572	296	- 1.1	2.7
	11.2	0.653	295	0.623	329	- 4.5	11.4
9 $V_0 = 153$	3.6	0.541	282	0.552	258	2.0	- 8.4
	5.8	0.593	288	0.572	294	- 3.5	2.0
	11.2	0.683	295	0.623	338	- 8.8	14.5
10 $V_0 = 174$	3.6	0.498	282	0.552	232	10.8	- 17.9
	5.8	0.545	288	0.572	262	4.9	- 9.1
	11.2	0.631	295	0.623	303	- 1.3	2.8
11 $V_0 = 160$	3.6	0.527	282	0.552	253	4.8	- 10.4
	5.8	0.562	288	0.572	276	1.7	- 4.1
	11.2	0.643	295	0.623	319	- 3.1	8.2
12 $V_0 = 203$	3.6	0.513	282	0.552	253	7.7	- 10.3
	5.8	0.548	288	0.572	270	4.4	- 6.2
	11.2	0.635	295	0.623	303	- 1.8	2.8
13 $V_0 = 156$	3.6	0.527	282	0.552	252	4.7	- 10.7
	5.8	0.574	288	0.572	290	- 0.3	0.8
	11.2	0.659	295	0.623	343	- 5.5	16.4
14 $V_0 = 168$	3.6	0.529	282	0.552	257	4.4	- 9.0
	5.8	0.572	288	0.572	288	0.0	- 0.1
	11.2	0.647	295	0.623	322	- 3.8	9.1

If a third relationship can be found, we use Eqs (9) and (25) with this relationship to solve for  $\bar{z}/L_0$ .

A very simple geometry for a mushrooming impact specimen was introduced by Jones et al. [16] and used in a different context. Consider the mushroom to be a cylinder of cross-sectional area  $= A = A_0/(1 + e)$  for a specific, prescribed strain  $e$  (see Fig. 9). Using the geometry in Fig. 9 and noting that the volume of the undeformed rod must equal the

sum of the volumes in Fig. 9 leads to

$$\frac{1}{1+e} \frac{\tilde{h}}{L_0} + \frac{\tilde{z}}{L_0} = 1. \quad (26)$$

Equations (9), (25), and (26) can be solved simultaneously to find

$$\frac{\tilde{z}}{L_0} = \frac{b}{\beta} - \frac{(1-\beta)(1+e)}{\beta} \frac{e}{e}. \quad (27)$$

Table 2

Data point	Results obtained from quasi-static test data		Predictions obtained from using Taylor test data only		Percentage differences	
	Percent comp. strain	$\tilde{z}/L_0$	Quasi-static yield stress (MPa)	$\tilde{z}/L_0$	Quasi-static yield stress (MPa)	$\tilde{z}/L_0$
1 $V_0 = 266$	3.6	0.636	400	0.586	462	- 7.9 15.5
	5.8	0.637	450	0.610	504	- 4.3 12.0
	11.2	0.738	523	0.713	576	- 3.4 10.1
2 $V_0 = 180$	3.6	0.603	400	0.586	451	- 2.9 12.8
	5.8	0.620	450	0.610	499	- 1.6 10.9
	11.2	0.719	523	0.713	564	- 0.8 7.8
3 $V_0 = 216$	3.6	0.603	400	0.586	439	- 2.7 9.8
	5.8	0.612	450	0.610	479	- 0.3 6.4
	11.2	0.713	523	0.713	552	0.0 5.5
4 $V_0 = 249$	3.6	0.631	400	0.586	463	- 7.1 15.8
	5.8	0.633	450	0.610	503	- 3.6 11.8
	11.2	0.730	523	0.713	571	- 2.3 9.2
5 $V_0 = 170$	3.6	0.638	400	0.586	554	- 8.2 38.5
	5.8	0.660	450	0.610	628	- 7.6 39.6
	11.2	0.788	523	0.713	794	- 9.6 51.8
6 $V_0 = 160$	3.6	0.579	400	0.586	401	1.3 0.3
	5.8	0.606	450	0.610	465	0.7 3.3
	11.2	0.745	523	0.713	648	- 4.2 23.9

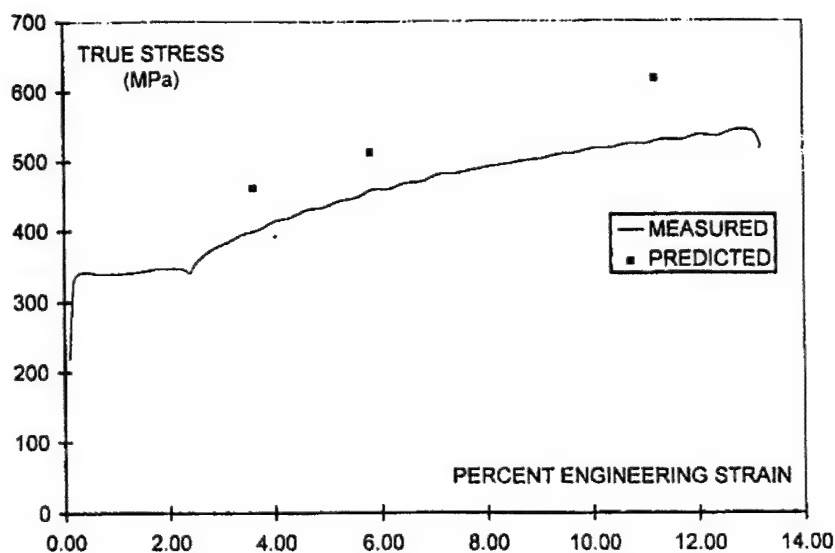


Fig. 11. Comparison of quasi-static wrought iron stress/strain data given in Fig. 6 with estimates using Eqns (22) and (27).

With this estimate for  $Z/L_0$ , we can use Eqn (22) to find  $\sigma_c = \sigma_c(e)$ , without measuring any loads. Notice that the ratio  $Z/L_0$  is independent of impact velocity  $v_0$ . The data from a number of 17 caliber Taylor tests is presented in Tables 1 and 2. For each strain,  $Z/L_0$  is nearly constant. The estimates for the ratio using Eqn (27) are also shown. The differences are very small.

Figures 10 and 11 give the comparison between the compressive stress-strain diagrams for OFHC copper and wrought iron. Considering some of the uncertainties, the comparison is very favorable. It is remarkable that Taylor impact data can be used to generate an estimate for the quasistatic stress-strain diagram for a specimen material. This provides further evidence of the validity of the theory presented in this paper. As it stands, the theory has produced a useful interpretation of impact test data that agrees with existing data to the extent that it is possible to make a comparison. We plan to further strengthen our case with the publication of additional test data.

## CONCLUSIONS

In this paper, we have presented an elementary theory for the Taylor test with which estimates of high strain-rate behavior of ductile metals can be accomplished. The strain-rates exceed  $10^4/s$  which makes it difficult to compare the results to those obtained by alternative methods because none exist at present. However, for OFHC copper data reported by Follansbee [17], the data in this paper correlates very well (see Fig. 12). It should be noted that the copper used by Follansbee [17] may have a different structure than our "as-received" OFHC copper. Also there may be considerable variation between shipments of OFHC Copper in the "as-received" condition.

The Taylor impact test is useful because it provides essential information in the strain-rate regime between the Split-Hopkinson pressure bar and plate impact shear experiments. For this reason it is of considerable interest to the defense community (e.g. see [18]).

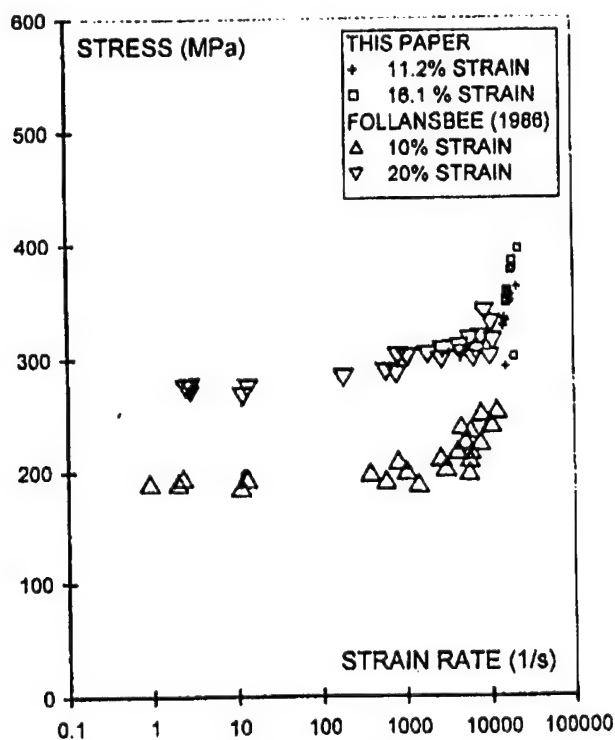


Fig. 12. Comparison of high strain-rate data for OFHC copper at 11.2% and 16.1% compressive strain with data reported by Follansbee in 1986.

Strain-rates of the order of  $10^4$ - $10^5$  per second are usually observed in impact and penetration problems. We will continue to search for interpretations of test data that allow us to model materials behavior in the high strain-rate.

**Acknowledgements**—This work was supported by the U.S. Air Force Armament Directorate at Eglin Air Force Base under contract number F08630 96K0014. Mr. Drinkard gratefully acknowledges the support of the Air Force Office of Scientific Research under an ASSERT grant to the University of Alabama. The authors are grateful to Dr. Mark Barkey for providing them with quasi-static compression data on OFHC copper and wrought iron. The authors are also grateful to Miss Miranda Whitfield for her careful typing of the manuscript. The authors further acknowledge the help of the reviewers with the revision of this paper.

## REFERENCES

1. G. I. Taylor, The use of flat-ended projectiles for determining dynamic yield stress I. Theoretical considerations. *Proc. Roy. Soc. London A* **194**, 289 (1948).
2. A. C. Whifflen, The Use of flat-ended projectiles for determining dynamic yield stress II: Tests on various metallic materials. *Proc. Roy. Soc. London A* **194**, 300 (1948).
3. S. E. Jones, P. J. Maudlin, P. Gillis and J. C. Foster, Jr., An analytical interpretation of high strain rate material behavior during early time plastic deformation in the Taylor impact test. *Computers in Engineering*, Vol. 2, *Proc. 1992 Computers in Engineering Conference and Exposition*, San Francisco, CA, *Trans. ASME* (1992).
4. J. W. House, *Taylor impact testing*, Technical Report, AFATL-TR-89-41, AD-A215 018 (1989).
5. G. I. Barenblatt and A. I. Ishlinskii, On the impact of a viscoplastic bar on a rigid wall. *Prikladnaya Matematika i Mekhanika* **26**, 497 (1962).
6. T. C. E. Ting, Impact of a nonlinear viscoplastic rod on a rigid wall. *J. Appl. Mech. Trans. ASME* **33**, 505 (1966).
7. J. B. Hawkyard, D. Eaton and W. Johnson, The mean dynamic yield strength of copper and low carbon steel at elevated temperatures from measurements of the "mushrooming" of flat-ended projectiles. *Int. J. Mech. Sci.* **10**, 929 (1968).
8. J. B. Hawkyard, A theory for the mushrooming of flat-ended projectiles impinging on a flat rigid anvil, using energy considerations. *Int. J. Mech. Sci.* **11**, 313 (1969).
9. I. M. Hutchings and T. J. O'Brien, Normal impact of metal projectiles against a rigid target at low velocities. *23*, 505 (1981).
10. S. E. Jones, P. P. Gillis and J. C. Foster, Jr., On the equation of motion of the undeformed section of a Taylor specimen. *J. Appl. Phys.* **61**(2), 15 (1987).
11. J. C. Foster, Jr., P. J. Maudlin and S. E. Jones, On the Taylor test: A continuum analysis of plastic wave propagation. *Proc. 1995 APS Topical Conf. on Shock Compression of Condensed Matter*, Seattle, WA (1995).
12. S. E. Jones, P. J. Maudlin and J. C. Foster, Jr., An engineering analysis of plastic wave propagation in the Taylor test. To appear in the *Int. J. Impact Engineering* (1996).
13. P. J. Maudlin, J. C. Foster, Jr. and S. E. Jones, A Continuum Mechanics Code Analysis of Steady Plastic Wave Propagation in the Taylor Test. To appear in the *Int. J. Impact Engineering* (1996).
14. S. E. Jones and P. P. Gillis, An elementary scaling law for rod impact specimens, *Int. J. Impact Engineering* **4**, 195 (1985).
15. S. E. Jones, P. J. Maudlin and J. C. Foster, Jr., Constitutive modeling using the Taylor impact test In *High Strain Rate Effects on Polymer, Metal and Ceramic Matrix Composites and Other Advanced Materials*, edited by Y. D. S. Rajapakse and J. R. Vinson, *ASME Winter Annual Meeting*, San Francisco, CA (1995).
16. S. E. Jones, P. P. Gillis, J. C. Foster, Jr. and L. L. Wilson, A one-dimensional, two phase flow model for Taylor impact specimens. *J. Eng. Mater. Technol. (Trans. ASME)* **113**, 228 (1991).
17. P. S. Follensbee, High-strain-rate deformation of FCC metals and alloys. In: *Metallurgical Applications of Shock-wave and High-Strain-Rate Phenomena* (edited by L. E. Murr *et al.*), (1986).
18. R. L. Woodward, N. W. Burman and B. J. Baxter, An experimental and analytical study of the Taylor impact test. *Int. J. Impact Engineering* **15**, 4 (1994).

## **APPENDIX C**



## A REVISED FORM FOR THE JOHNSON-COOK STRENGTH MODEL

WILLIAM K. RULE\* and S. E. JONES

Department of Aerospace Engineering and Mechanics, University of Alabama, Tuscaloosa,  
AL 35487-0280, U.S.A.

(Received 10 January 1997; in revised form 7 November 1997)

**Summary**—Strength models play a key role in the numerical simulation of impact events. A revised form of the Johnson-Cook strength model is proposed in this paper. The revised model treats the sudden strengthening that many ductile metals exhibit at strain rates greater than  $10^4/s$ . Strain rates of this magnitude are generally considered to be beyond the capability of the split-Hopkinson pressure bar and so such abrupt strengthening behavior is often not observed and reported. A method to economically estimate all eight coefficients of the revised strength model using quasi-static tension data and Taylor impact test data reduced with a modified version of the EPIC finite element code is also described. Revised strength model coefficients were determined for: 7075-T6 aluminum, OFHC copper, wrought iron, and a high-strength steel (Astralloy-V<sup>X</sup>). A good fit to the quasi-static tension data and Taylor impact test results was obtained for these four different metals. The behavior of the revised strength model at high strain rates also compared favorably with independent predictions from an analytical model calibrated with the Taylor impact data. © 1998 Elsevier Science Ltd. All rights reserved

### NOTATION

$C_1$	strength model coefficient
$F$	objective function for optimizer
$F_{QS}$	component of objective function for matching quasi-static tension data
$F_{TI}$	component of objective function for matching Taylor impact data
$M$	strength model exponent
$N$	strength model exponent
$N_{QS}$	number of quasi-static tension data points
$N_{TI}$	number of Taylor impact tests
$T^*$	homologous temperature
$V$	volume of Taylor impact specimen
$V_{ERR,I}$	volume difference (error) between measured and EPIC calculated deformed Taylor impact specimen profile
$V_0$	Taylor cylinder impact velocity
$X$	deformed Taylor cylinder axial dimension
$X_0$	Taylor cylinder initial length
$Y$	deformed Taylor cylinder radial dimension
$Y_0$	Taylor cylinder initial radius
$\alpha$	strength model exponent
$\beta$	weight factor for objective function
$\epsilon$	equivalent plastic strain
$\epsilon'$	equivalent plastic strain rate
$\epsilon^*$	dimensionless equivalent plastic strain rate = $\epsilon'/(1/s)$
$\sigma$	yield strength (flow stress)
$\sigma_{QS,i}$	quasi-static yield stress calculated from revised strength model
$\sigma_{QSM,i}$	quasi-static yield stress measured from tension test

### 1. INTRODUCTION

Finite element modeling of high rate events involving ductile metals requires three basic material models: an equation of state to predict pressures, a failure model to predict loss of load carrying capability, and a strength model to predict the yield strength (flow stress). This paper discusses a proposed revision to the empirical Johnson-Cook (JC) strength

\*Corresponding author. Tel.: 001 205 3481627; e-mail: wrule@coe.eng.ua.edu.

model [1] to more closely match observed material behavior at high strain rates. Further, a practical scheme for evaluating the revised Johnson-Cook (RJC) strength model coefficients by using Taylor impact test results and quasi-static tension data is disclosed.

Although the JC strength model is empirical in nature and simple in form it is the most popular strength model in use today [2]. Simple strength models are popular because of the difficulty in obtaining accurate strength model constants at high strain rates. Complex strength models generally require more, and more sophisticated, test data for coefficient calibration. Strength model coefficients for many common metals are not available from the literature. Also, high rate properties of a given material can vary significantly depending on grain size [3] and processing history. Thus, there is clearly a need for simple strength models that are practical to calibrate.

## 2. THE REVISED JOHNSON-COOK STRENGTH MODEL

The JC strength model was first proposed in 1983 [1]. It has the following form:

$$\sigma = (C_1 + C_2 e^N)(1 + C_3 \ln e^*)(1 - T^{*M}), \quad (1)$$

where  $\sigma$  is the equivalent yield strength,  $e$  is the equivalent plastic strain,  $e^*$  is the dimensionless equivalent plastic strain rate (made dimensionless by dividing the equivalent plastic strain rate by a unit plastic strain rate),  $T^*$  is the homologous temperature, and  $C_1$ ,  $N$ , and  $M$  are empirical coefficients and exponents. The model also provides for setting an upper bound for the yield strength. However, this capability is usually not required in simulations since Eqn (1) assumes that the yield strength varies linearly with the logarithm of the effective strain rate and so  $\sigma$  does not become unrealistically large even for enormous strain rates.

A large number of studies have shown that numerical simulations employing Eqn (1) can produce results of sufficient accuracy for engineering purposes. This is remarkable considering Eqn (1) uses simple scalar expressions to represent the strains and strain rates which are second-order tensors, and also Eqn (1) assumes isotropic hardening. The temperature factor is also quite simple in form. When using such simple models it is important to calibrate the coefficients with experimental data which is similar in nature to the intended application. This point will play a key role in the latter part of this paper where a practical strategy for strength model coefficient estimation is proposed.

For many ductile metals the yield strength increases more rapidly with strain rate than that described by the form of Eqn (1) for strain rates in excess of  $10^3$ /s. To increase the strain rate sensitivity a modified Johnson-Cook (MJC) strength model was proposed [4] with the following form:

$$\sigma = (C_1 + C_2 e^N)(e^{*\alpha})(1 - T^{*M}) \quad (2)$$

where  $\alpha$  is an empirical exponent. However, the MJC strength model does not appear to be widely used today probably because the strain rate sensitivity is not significantly enhanced over that provided by Eqn (1).

Many ductile metals display an enormous increase in yield stress for strain rates in excess of  $10^3$ /s (see Fig. 1 of Ref. [5], for instance). This observed behavior provided the motivation for the revised Johnson-Cook (RJC) strength model proposed here. The goal of this study is to enhance the high strain rate sensitivity of the JC strength model while minimizing changes to the model for those loading regimes where it has clearly been shown to be effective. The proposed form of the RJC strength model is:

$$\sigma = (C_1 + C_2 e^N) \left[ 1 + C_3 \ln e^* + C_4 \left( \frac{1}{C_5 - \ln e^*} - \frac{1}{C_5} \right) \right] (1 - T^{*M}), \quad (3)$$

where  $C_4$  and  $C_5$  are additional empirical coefficients.

The strain rate sensitivity has been enhanced by the term  $1/(C_5 - \ln e^*)$  where  $C_5$  is the natural logarithm of a critical strain rate level. This term tends to infinity as the strain rate

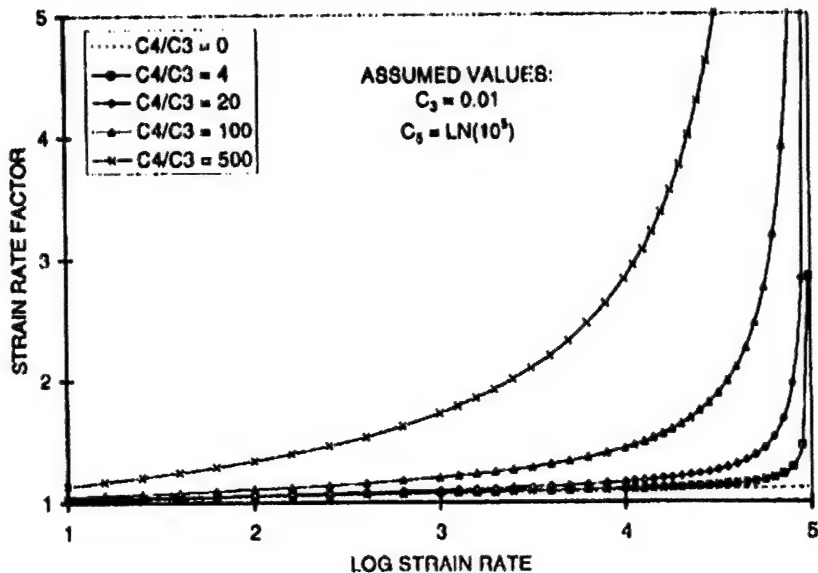


Fig. 1. Illustration of the strain rate factor of the RJC model (Eqn (3)) for various  $C_4/C_3$  ratios.

approaches the critical strain rate. Note that this strain rate sensitivity enhancement term contribution tends toward zero for low strain rates due to the  $-1/C_5$  correction term in Eqn (3). Thus, the RJC model approaches to the original JC model for low strain rates and is identical to the JC model for a strain rate of unit magnitude where  $\ln \epsilon^* = 0$ . Further, the entire strain rate sensitivity enhancement term  $C_4(1/C_5 - \ln \epsilon^*) - 1/(C_5)$  is removed for strain rates of less than unit magnitude. In other words, the RJC model is identical to the JC model for  $\epsilon^*$  values of unity or less.

The amount of deviation of the strain rate behavior of the RJC model from JC model is controlled by the  $C_4$  factor as illustrated in Fig. 1. This provides for the fact that some materials exhibit a very sudden departure of yield strength from linearity with respect to the logarithm of strain rate (see Fig. 1 of Ref. [5], for instance) while others vary more gradually (see Fig. 13.26(b) of Ref. [2], for example).

As stated previously the original JC strength model provides for specifying a maximum value for the yield strength  $\sigma$ . However, a limiting value is usually not required for high strain rate simulations since the sensitivity to strain rate is relatively low (linear logarithmic dependence). However, the RJC strength model as discussed to this point predicts a physically untenable infinite yield strength as  $\ln \epsilon^*$  approaches  $C_5$ . To prevent this unrealistic occurrence the RJC model simply assumes that there exists a maximum value that the strain rate sensitivity factor in Eqn (3) can attain for each material which cannot be exceeded regardless of the prevailing strain and temperature state. The peak strain rate sensitivity factor is defined through the nondimensional constant  $C_6$  as follows:

$$\left[ 1 + C_3 \ln \epsilon^* + C_4 \left( \frac{1}{C_5 - \ln \epsilon^*} - \frac{1}{C_5} \right) \right] \leq C_6. \quad (4)$$

A method for estimating  $C_6$  is discussed in a following section.

The RJC scheme for limiting the strain rate sensitivity factor to physically reasonable values is the simplest possible—it assumes that the peak value is a constant ( $C_6$ ). It is difficult to construct a more elaborate model for peak strain rate sensitivity behavior in the framework of the JC class of strength models due to the lack of accurate test data. It is technically challenging to conduct material tests at strain rates in excess of  $10^4/s$  where  $C_6$  begins to play a role. At these strain rates split-Hopkinson bar results become questionable [6, 7], which leaves mainly flyer plate and Taylor impact testing as alternatives. Flyer plate testing has the advantage of producing reasonably uniform stress and strain states, but

such testing is expensive and the results can exhibit a significant amount of scatter as shown, for instance, in Fig. 7 of Ref. [8]. Taylor testing is relatively inexpensive and data can be obtained from simple post-test measurements. Unfortunately, there is currently some controversy about the results obtained from Taylor tests because of the nonuniform stress and strain fields produced. Thus, considering the available experimental data, there appears to be a large amount of uncertainty about the yield strength of ductile materials at high strain rates.

However, there is some data to suggest that proposing a constant value for the strain rate sensitivity factor is not unreasonable. Steinberg *et al.* [9] assumed that there was a strain rate level beyond which the yield strength was not significantly affected. They were able to obtain some experimental data to validate their assumption. Also, Jones *et al.* [10] state that for dislocation activation energies greater than a critical value plastic flow of f.c.c. crystal metals is independent of strain rate.

The eight RJC strength model coefficients were evaluated for four different metals as is described in the next section.

### 3. RJC STRENGTH MODEL COEFFICIENT EVALUATION FOR FOUR METALS

#### 3.1. *The experimental data*

RJC strength model coefficients were evaluated for the following metals: 7075-T6 aluminum, OFHC copper, wrought iron, and a high-strength steel produced by Astralloy Wear Technology of Birmingham, AL, called Astralloy-V®. These metals have widely varying characteristics and thus should provide a good test of the suitability of the proposed RJC strength model. Quasi-static tensile test data for these four metals is shown in Fig. 2.

Ideally, the strength model should be capable of making accurate predictions over a wide range of strain rates. Accordingly, for this study coefficients were evaluated giving equal weight to quasi-static tensile test data ( $\dot{\epsilon}' \leq 10^{-3}$ ) and Taylor impact test data ( $\dot{\epsilon}' > 10^4$ ). All test data was obtained at the University of Alabama in Tuscaloosa. A conventional, computer controlled, hydraulically actuated, material testing machine was used to acquire the quasi-static tension data. It is assumed that the materials tested exhibit similar yielding behavior in tension and compression.

The Taylor impact testing apparatus developed at the University of Alabama has been described by Allen [11]. Although using the Taylor test to evaluate strength model

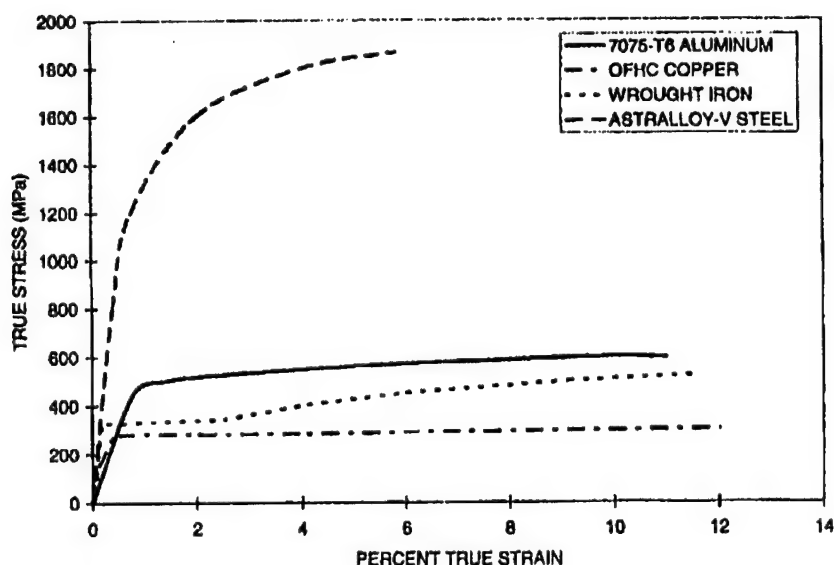


Fig. 2. Quasi-static tensile test data for the four metals tested.

coefficients is currently considered inappropriate by some. Zerilli and Armstrong [3] make the point that "the attempt to model a Taylor cylinder impact can provide a real test of a material model, since conditions of strain and strain rate are achieved which are outside the range of ordinary testing – in particular, strain rates in the range of  $10^4$ – $10^6$  s<sup>-1</sup> and strains in the range of 0–2". Also, Holmquist and Johnson (see Fig. 4 of Ref. [4]) show that strength model coefficients obtained from currently accepted conventional tension and torsion tests often do not produce good Taylor test simulations. Since in many cases the stress, strain, strain rate, and temperature fields of a deforming Taylor specimen are closer in nature to the intended application than that found in conventional tests it may be advisable to give more weight to Taylor impact results while evaluating strength model coefficients. In general, simple empirical models should be calibrated with data that most closely resembles the intended application.

The Taylor specimens used in this study had undeformed diameters slightly in excess of 4 mm, and most had length to diameter ratios of approximately 7.5. The small specimen diameter was used to reduce radial inertia effects after the initial transient at impact was completed. Radial inertia was minimized to improve the accuracy of the one-dimensional Taylor specimen analysis technique introduced in Section 3.4. As will be discussed, the predictions of the one-dimensional analyses were used as an independent check of the RJC results. Impact velocities varied between 140 and 270 m/s. Experimental data on the Taylor specimens are given in Tables 1–4.

### 3.2. RJC model coefficient optimization using the EPIC code

The main purpose for developing strength models and determining their coefficients for different materials is to conduct numerical simulations of high rate events. Many codes for numerical simulations of such events have been developed. The code modified for use in this study was the most recent version of the well-known code EPIC [12]. For some time numerical models have also been used to evaluate the accuracy of the coefficients of their strength models and to adjust the coefficients so that numerical predictions matched observed behavior. This has frequently been done with Taylor test data [1, 3, 4, 13]. Usually, only some of the deformed Taylor specimen dimensions are used to adjust certain strength model coefficients. This approach was extended for this study to include the entire deformed specimen profile and all of the strength model coefficients ( $C_1$ – $C_6$ ,  $N$ ,  $M$ ) were simultaneously determined in the process. In addition, the quasi-static yield strength data was also included in this fitting process as will now be described.

First, the EPIC code was modified to incorporate the RJC strength model of Eqns (3) and (4). The new coding was setup so that only 0.9999 of critical strain rate ( $e^{C_1}$ ) was allowed (for higher strain rates the strain rate sensitivity factor was simply set equal to  $C_6$ ) to avoid an accidental numerical singularity. The proposed RJC strength model was conveniently incorporated into EPIC as strength model type 0, leaving 1 for the JC model, and 2 for the MJC model. Thus, all the original capabilities of the code were retained.

Then, a computer program for strength model coefficient optimization was developed which was designed to successively write out an EPIC input file (with an adjusted set of strength model coefficients), launch the EPIC code, and then post-process the EPIC results to determine the next set of strength model coefficients required to seek a better fit with the quasi-static and Taylor test data. This process was repeated until the specified number of coefficient optimization cycles had been completed. The optimization algorithm used was the well-known, gradient-based, conjugate direction method [14].

The objective function,  $F$ , operated on by the optimizer had two components

$$F = \beta F_{QS} + (2 - \beta) F_{TI} \quad (5)$$

$F_{QS}$  was the component associated with discrepancies between calculated and measured quasi-static yield stress results. Similarly,  $F_{TI}$  treated the Taylor impact data. The factor  $\beta$  in Eqn (5) can be used to weight the relative importance of quasi-static versus the Taylor

Table 1. Experimental data on 7075-T6 Aluminum Taylor specimens

Specimen 1	Specimen 2		Specimen 3		Specimen 4		Specimen 5		Specimen 6		Specimen 7	
	$X_0$ (mm)	$X_0$ (mm)	$X_0$ (mm)	$Y_0$ (mm)	$X_0$ (mm)	$Y_0$ (mm)	$X_0$ (mm)	$Y_0$ (mm)	$X_0$ (mm)	$Y$ (mm)	$X$ (mm)	$Y$ (mm)
0.00	2.29	0.00	2.51	0.00	2.46	0.00	2.36	0.00	2.51	0.00	2.31	0.00
0.71	2.27	0.97	2.43	1.04	2.31	0.97	2.31	1.24	2.39	0.84	2.29	1.19
1.04	2.26	1.80	2.36	1.85	2.29	1.52	2.29	2.03	2.34	1.55	2.26	1.42
1.40	2.25	2.26	2.35	2.67	2.28	2.29	2.26	4.37	2.34	2.54	2.25	2.72
1.98	2.24	4.37	2.35	3.89	2.28	4.65	2.26	6.22	2.26	4.27	2.25	6.10
3.33	2.24	5.46	2.31	5.11	2.26	6.38	2.21	9.37	2.18	6.20	2.21	8.43
4.34	2.24	6.02	2.29	6.83	2.18	7.59	2.18	11.02	2.15	8.31	2.16	12.78
6.55	2.18	9.04	2.21	10.62	2.15	10.36	2.15	11.96	2.12	10.36	2.15	29.77
8.61	2.15	11.30	2.15	11.61	2.12	11.56	2.12	28.70	2.08	11.35	2.12	2.21
10.59	2.12	12.12	2.12	29.03	2.08	29.46	2.08	29.51	2.08	29.51	2.08	2.08
29.79	2.08	28.65	2.08									

Note:  $X_0$  = initial length,  $Y_0$  = impact velocity,  $X$  and  $Y$  are deformed cylinder, axial, and radial dimensions, respectively.

A revised form for the Johnson-Cook strength model

Table 2. Experimental data on OFHC copper Taylor specimens

Specimen 1				Specimen 2				Specimen 3				Specimen 4				Specimen 5				Specimen 6							
$X_0$ (mm)	31.4	$X_0$ (mm)	31.3	$X_0$ (mm)	31.4	$X_0$ (mm)	31.4	$X_0$ (mm)	31.2																		
$Y_0$ (mm)	2.08	$Y_0$ (mm)	2.08	$Y_0$ (mm)	2.08	$Y_0$ (mm)	2.08	$Y_0$ (mm)	2.07																		
$V_0$ (m/s)	171	$V_0$ (m/s)	200	$V_0$ (m/s)	212	$V_0$ (m/s)	145	$V_0$ (m/s)	144	$V_0$ (m/s)	144	$V_0$ (m/s)	173														
$X$ (mm)		$Y$ (mm)		$X$ (mm)	$Y$ (mm)																						
0.00	3.56	0.00	4.04	0.00	4.23	0.00	3.18	0.00	3.15	0.00	3.52	0.00	3.48	0.00	3.12	0.00	3.12	0.00	3.12	0.00	3.12	0.00					
0.76	3.23	0.41	3.81	0.76	3.67	0.64	2.95	0.71	2.92	1.17	2.95	0.76	3.15	0.76	3.15	0.76	3.15	0.76	3.15	0.76	3.15	0.76					
1.27	2.92	0.84	3.43	1.37	3.12	1.30	2.72	1.32	2.69	1.55	2.79	1.30	2.87	1.30	2.87	1.30	2.87	1.30	2.87	1.30	2.87	1.30	2.87				
2.18	2.77	1.35	3.02	1.57	3.02	1.85	2.64	2.06	2.62	2.03	2.76	1.98	2.76	1.98	2.76	1.98	2.76	1.98	2.76	1.98	2.76	1.98	2.76				
2.95	2.78	1.65	2.92	2.29	2.98	2.82	2.65	3.18	2.64	3.10	2.77	2.92	2.76	2.92	2.76	2.92	2.76	2.92	2.76	2.92	2.76	2.92	2.76				
3.99	2.74	2.69	2.92	3.18	2.96	3.20	2.74	4.24	2.59	4.65	2.67	4.34	2.69	4.34	2.69	4.34	2.69	4.34	2.69	4.34	2.69	4.34	2.69				
10.80	2.27	5.26	2.74	11.30	2.27	10.10	2.27	9.80	2.27	10.80	2.27	10.80	2.27	10.80	2.27	10.80	2.27	10.80	2.27	10.80	2.27	10.80	2.27				
11.81	2.21	11.30	2.27	12.10	2.21	11.35	2.21	11.07	2.21	11.81	2.21	11.81	2.21	11.81	2.21	11.81	2.21	11.81	2.21	11.81	2.21	11.81	2.21				
13.00	2.15	12.10	2.21	13.10	2.15	12.90	2.15	12.62	2.15	13.00	2.15	13.00	2.15	13.00	2.15	13.00	2.15	13.00	2.15	13.00	2.15	13.00	2.15				
13.69	2.12	13.30	2.15	13.70	2.12	13.71	2.12	13.53	2.12	13.69	2.12	13.69	2.12	13.69	2.12	13.69	2.12	13.69	2.12	13.69	2.12	13.69	2.12				
24.23	2.08	13.80	2.12	21.50	2.08	25.80	2.08	25.80	2.07	23.98	2.07	24.28	2.07	24.28	2.07	24.28	2.07	24.28	2.07	24.28	2.07	24.28	2.07				
Specimen 8				Specimen 9				Specimen 10				Specimen 11				Specimen 12				Specimen 13				Specimen 14			
$X_0$ (mm)	31.2	$X_0$ (mm)	31.2	$X_0$ (mm)	31.2	$X_0$ (mm)	31.2	$X_0$ (mm)	31.2	$X_0$ (mm)	31.2	$X_0$ (mm)	31.2	$X_0$ (mm)	31.2	$X_0$ (mm)	31.2	$X_0$ (mm)	31.2	$X_0$ (mm)	31.2	$X_0$ (mm)	31.2				
$Y_0$ (mm)	2.07	$Y_0$ (mm)	2.07	$Y_0$ (mm)	2.07	$Y_0$ (mm)	2.07	$Y_0$ (mm)	2.07	$Y_0$ (mm)	2.07	$Y_0$ (mm)	2.07	$Y_0$ (mm)	2.07	$Y_0$ (mm)	2.07	$Y_0$ (mm)	2.07	$Y_0$ (mm)	2.07	$Y_0$ (mm)	2.07				
$V_0$ (m/s)	167	$V_0$ (m/s)	152	$V_0$ (m/s)	174	$V_0$ (m/s)	160	$V_0$ (m/s)	160	$V_0$ (m/s)	160	$V_0$ (m/s)	156														
$X$ (mm)		$Y$ (mm)		$X$ (mm)	$Y$ (mm)																						
0.00	3.47	0.00	3.24	0.00	3.53	0.00	3.35	0.00	4.05	0.00	3.28	0.00	3.45	0.00	3.35	0.00	3.35	0.00	3.35	0.00	3.35	0.00	3.35	0.00			
0.71	3.15	0.79	2.97	1.45	2.95	1.09	2.90	1.04	2.74	1.60	2.96	1.40	2.74	1.52	2.74	1.52	2.74	1.52	2.74	1.52	2.74	1.52	2.74	1.52			
1.37	2.79	1.55	2.72	2.11	2.74	1.55	2.74	2.03	2.69	2.84	2.91	2.06	2.67	2.11	2.67	2.11	2.67	2.11	2.67	2.11	2.67	2.11	2.67	2.11			
1.85	2.73	2.03	2.67	2.74	2.74	2.03	2.69	2.03	2.69	2.83	3.15	2.83	2.83	3.15	2.83	2.83	3.15	2.83	2.83	3.15	2.83	2.83	3.15	2.83			
2.41	2.72	3.35	2.68	3.61	2.76	3.15	2.69	4.14	2.67	5.46	2.72	4.17	2.64	4.17	2.64	4.17	2.64	4.17	2.64	4.17	2.64	4.17	2.64	4.17			
3.43	2.72	4.83	2.59	4.85	2.67	4.11	2.67	5.74	2.54	10.80	2.27	11.81	2.21	11.81	2.21	11.81	2.21	11.81	2.21	11.81	2.21	11.81	2.21	11.81	2.21		
4.27	2.67	10.80	2.27	10.80	2.27	11.81	2.21	10.80	2.27	11.81	2.21	11.81	2.21	11.81	2.21	11.81	2.21	11.81	2.21	11.81	2.21	11.81	2.21	11.81	2.21		
10.80	2.27	11.81	2.21	13.00	2.15	13.00	2.15	11.81	2.21	13.00	2.15	11.81	2.21	13.00	2.15	13.00	2.15	13.00	2.15	13.00	2.15	13.00	2.15	13.00	2.15		
11.81	2.21	13.00	2.15	13.69	2.12	13.69	2.12	13.69	2.07	24.00	2.07	13.69	2.12	22.15	2.07	24.77	2.07	24.77	2.07	24.77	2.07	24.77	2.07	24.77	2.07		
13.00	2.15	13.69	2.12	25.27	2.07	24.00	2.07	24.00	2.07	24.77	2.07	24.77	2.07	24.77	2.07	24.77	2.07	24.77	2.07	24.77	2.07	24.77	2.07	24.77	2.07		
13.69	2.12	24.51	2.07	20.7																							

Note:  $X_0$  = initial length,  $Y_0$  = initial radius,  $V_0$  = impact velocity.  $X$  and  $Y$  are deformed cylinder axial and radial dimensions, respectively.

Table 3. Experimental data on wrought iron Taylor specimens

Specimen 1	Specimen 2			Specimen 3			Specimen 4			Specimen 5			Specimen 6		
	$X_0$ (mm)	$X_0$ (mm)	$X_0$ (mm)	$X_0$ (mm)	$X_0$ (mm)	$X_0$ (mm)	$X_0$ (mm)	$X_0$ (mm)	$X_0$ (mm)	$X_0$ (mm)	$X_0$ (mm)	$X_0$ (mm)	$X_0$ (mm)	$X_0$ (mm)	
$X_0$ (mm)	$Y_0$ (mm)	$V_0$ (m/s)	$X$ (mm)	$Y$ (mm)											
0.00	3.99	0.00	2.93	0.00	3.28	0.00	3.67	0.00	2.87	0.00	2.74	0.00	2.74	0.00	2.74
0.74	3.45	1.02	2.69	0.97	2.87	0.99	3.10	1.12	2.59	1.24	2.54	1.24	2.54	1.24	2.54
1.52	2.90	1.83	2.54	1.50	2.67	1.45	2.84	1.50	2.51	1.73	2.49	1.73	2.49	1.73	2.49
1.98	2.79	2.34	2.50	1.96	2.62	1.83	2.74	2.39	2.44	2.74	2.46	2.74	2.46	2.74	2.46
2.54	2.74	3.38	2.49	2.44	2.58	2.54	2.69	2.90	2.41	3.99	2.44	3.99	2.44	3.99	2.44
3.58	2.74	4.50	2.46	3.43	2.58	3.94	2.67	3.99	2.41	5.08	2.41	5.08	2.41	5.08	2.41
4.83	2.67	5.61	2.41	4.55	2.54	4.88	2.62	6.05	2.34	7.39	2.31	7.39	2.31	7.39	2.31
6.38	2.54	9.10	2.27	6.73	2.41	6.15	2.51	7.90	2.27	10.50	2.27	10.50	2.27	10.50	2.27
11.80	2.27	11.60	2.21	10.30	2.27	8.53	2.41	10.10	2.21	13.90	2.21	13.90	2.21	13.90	2.21
13.20	2.21	13.70	2.15	12.60	2.21	11.70	2.27	12.90	2.15	18.20	2.15	18.20	2.15	18.20	2.15
14.50	2.15	14.30	2.12	14.40	2.15	13.00	2.21	13.70	2.12	19.30	2.12	19.30	2.12	19.30	2.12
14.90	2.12	27.15	2.08	15.00	2.12	14.40	2.15	27.79	2.08	37.08	2.08	37.08	2.08	37.08	2.08
23.47	2.10			25.81	2.08	14.90	2.12		24.31	2.08					

Note:  $X_0$  = initial length,  $Y_0$  = impact velocity,  $X$  and  $Y$  are deformed cylinder axial and radial dimensions, respectively.

Table 4. Experimental data on Astralloy-V\* steel Taylor specimens

Specimen 1	Specimen 2		Specimen 3		Specimen 4		Specimen 5		Specimen 6		Specimen 7	
	$X_0$ (mm)	$X_0$ (mm)	$X_0$ (mm)	$Y_0$ (mm)	$Y_0$ (mm)	$X_0$ (mm)	$Y_0$ (mm)	$X_0$ (mm)	$Y_0$ (mm)	$X_0$ (mm)	$Y_0$ (mm)	
0.00	2.46	0.00	2.71	0.00	2.65	0.00	2.69	0.00	2.36	0.00	2.67	0.00
5.03	2.27	6.12	2.27	5.77	2.27	6.10	2.27	1.57	2.27	5.77	2.27	5.23
6.35	2.21	7.32	2.21	6.99	2.21	7.06	2.21	5.00	2.21	7.01	2.21	6.55
8.56	2.15	9.27	2.15	8.94	2.15	8.94	2.15	7.19	2.15	9.02	2.15	8.76
9.93	2.12	10.19	2.12	10.01	2.12	10.16	2.12	8.36	2.12	10.01	2.12	9.83
29.64	2.08	28.75	2.09	29.06	2.08	28.88	2.08	30.15	2.08	29.24	2.08	29.51

Note:  $X_0$  = initial length,  $Y_0$  = initial radius,  $V_0$  = impact velocity,  $X$  and  $Y$  are deformed cylinder axial and radial dimensions, respectively.

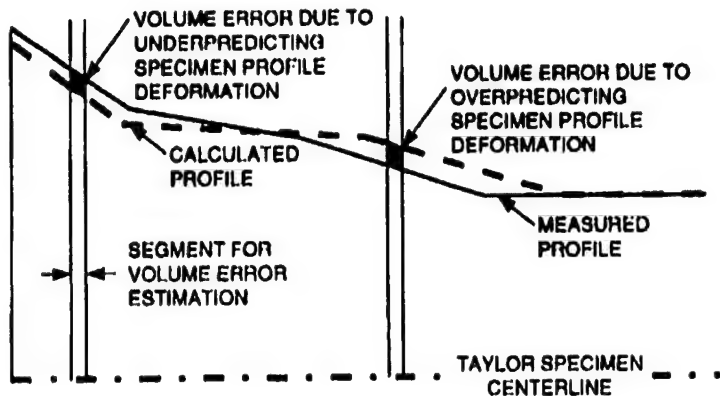


Fig. 3. Schematic cross-sectional drawing of measured and calculated Taylor impact specimen deformed geometries and segments used for profile volume error calculations.

impact results. For this study both sets of data were given even weight and so  $\beta$  was set to unity.  $F_{QS}$  was evaluated from

$$F_{QS} = 100 \frac{\sum_{i=1}^{N_{QS}} \left( \frac{\sigma_{QSC,i} - \sigma_{QSM,i}}{\sigma_{QSM,i}} \right)}{N_{QS}} \quad (6)$$

where  $N_{QS}$  is the number of measured quasi-static stresses under consideration,  $\sigma_{QSM,i}$  is the measured quasi-static yield strength, and  $\sigma_{QSC,i}$  is the calculated quasi-static yield strength obtained from the RJC strength model, Eqn (3). Thus,  $F_{QS}$  is simply the average percentage difference between the calculated and measured quasi-static yield strengths.

Similarly,  $F_{V1}$  is the average percentage volume error between the calculated and measured deformed Taylor impact specimen profiles:

$$F_{V1} = 100 \frac{\sum_{j=1}^{N_{Ti}} \left( \frac{V_{err,j} - V_j}{V_j} \right)}{N_{Ti}} \quad (7)$$

where  $N_{Ti}$  is the number of Taylor specimens,  $V_{err,j}$  is the volume error, and  $V_j$  is the initial Taylor specimen volume. The volume error was considered to be composed of two components. One component was associated with the absolute value of the difference between the measured and calculated deformed specimen overall lengths. This quantity was converted to a volume error (for dimensional homogeneity) by multiplying the length error magnitude by the undeformed specimen cross-sectional area. The other volume error component was associated with volume differences between measured and calculated deformed Taylor impact specimen profile shapes. For determining the profile volume error first the calculated profile was scaled to be the same length as that measured and then each profile was divided into 50 segments. Figure 3 shows a schematic cross-sectional drawing of two typical segments: one where the radial deformation was underestimated and one where it was overestimated. The trapezoidal profile errors of each segment of the cross section (see shaded areas in Fig. 3) can be converted to segmental volume errors by the theorem of Pappus. Note all segmental volume errors were considered positive whether due to underestimating or overestimating the radial deformation. The profile volume error was determined by simply summing together all 50 segmental volume errors.

Thus, as the optimizer drives the two volume error components towards zero the calculated deformed geometry will be made to match that measured. If the numerical model was perfect, and if the deformed specimens were measured exactly, then the volume error could be driven to zero. However, neither of these conditions exist in reality so all specimens produce nonzero volume errors at the end of the optimization process. Volume errors of the

order of 1-3% indicate very good agreement between the measured and calculated deformed Taylor impact specimen geometries.

$F_{T1}$  is dimensionless as is  $F_{QS}$ . Equal values of these quantities indicate approximately the same goodness of fit with their respective measured data sets. As the optimizer seeks to reduce the magnitude of the objective function (Eqn (5)) a conflict arises between satisfying quasi-static and Taylor test behavior requirements. In general, each set of data requires somewhat different strength model coefficients for an optimum fit. If the data are given an equal weight ( $\beta = 1$  in Eqn (5) as was done in this study) then  $F_{QS}$  and  $F_{T1}$  will have approximately the same magnitude when the optimizer has converged.

The coefficient optimization process was entirely automated. Once started the optimizer automatically launched the EPIC code many hundreds of times while seeking to minimize differences between measured and calculated results. It is important to note that a completely seamless computing environment was created. There is no requirement for users of this dynamic material property data reduction technique to be experts in the use of EPIC or numerical optimizers.

For computational efficiency the Taylor specimens were modeled with two-dimensional axisymmetric elements. Three node triangular elements were used. The optimizer code automatically setup the mesh so that sets of four triangular elements occupied approximately square regions of the cross-section model. The initial optimizer run was setup using a very coarse mesh with a single-element spanning the entire radius. This allowed the optimizer to quickly adjust the strength model coefficients to near-optimal values. Then the optimizer was rerun with two-elements spanning the radius. There was no significant difference between the results of these two meshes so further mesh refinement was not required. It is fortunate that computationally intensive fine meshes are not necessary for convergence of the strength model coefficients since the optimizer requires many EPIC runs while seeking to minimize the objective function. A typical data set can be reduced in a few hours on a Pentium Pro class of PC.

### 3.3. RJC strength model coefficient optimization results

The results of the RJC strength model coefficient optimization process for the four metals considered in this study are listed in Table 5. In general, a satisfactory fit was obtained

Table 5. Optimization results and RJC strength model coefficients and exponents for four metals

	7075-T6 Aluminum	OFHC copper	Wrought iron	Astralloy-V <sup>a</sup> steel
No. quasi-static yield stress measurements	3	3	3	3
Ave. quasi-static yield strength percentage error $F_{QS}$ Eqn (6)	1.4	1.0	2.5	4.7
No. Taylor impact specimens	7	14	6	7
Ave. volume percentage error $F_{T1}$ Eqn (7)	1.7	3.4	5.3	2.2
$C_1$ (MPa)	452.4	111.3	251.8	1657
$C_2$ (MPa)	457.1	239.7	584.7	271.5
$N$	0.3572	0.1047	0.3796	0.3334
$C_3$	1.085E-2	8.813E-4	9.681E-7	1.002E-6
$C_4$	0.01114	0.1893	0.1064	0.07431
$C_5$	10.29	10.02	9.268	10.79
(Corresponding critical strain rate = $\dot{\epsilon}^C$ )	(2.94E4)	(2.25E4)	(1.06E4)	(4.85E4)
$M$	-1.131	1.010	0.4974	1.063
$C_6$	2.919	4.741	3.115	1.507
RJC strength model: $\sigma = (C_1 + C_2 \dot{\epsilon}^N) \left[ 1 + C_3 \ln \dot{\epsilon}^* + C_4 \left( \frac{1}{C_5 - \ln \dot{\epsilon}^*} - \frac{1}{C_5} \right) \right] (1 - T^{*M})$				
With $\left[ 1 + C_3 \ln \dot{\epsilon}^* + C_4 \left( \frac{1}{C_5 - \ln \dot{\epsilon}^*} - \frac{1}{C_5} \right) \right] \leq C_6$				

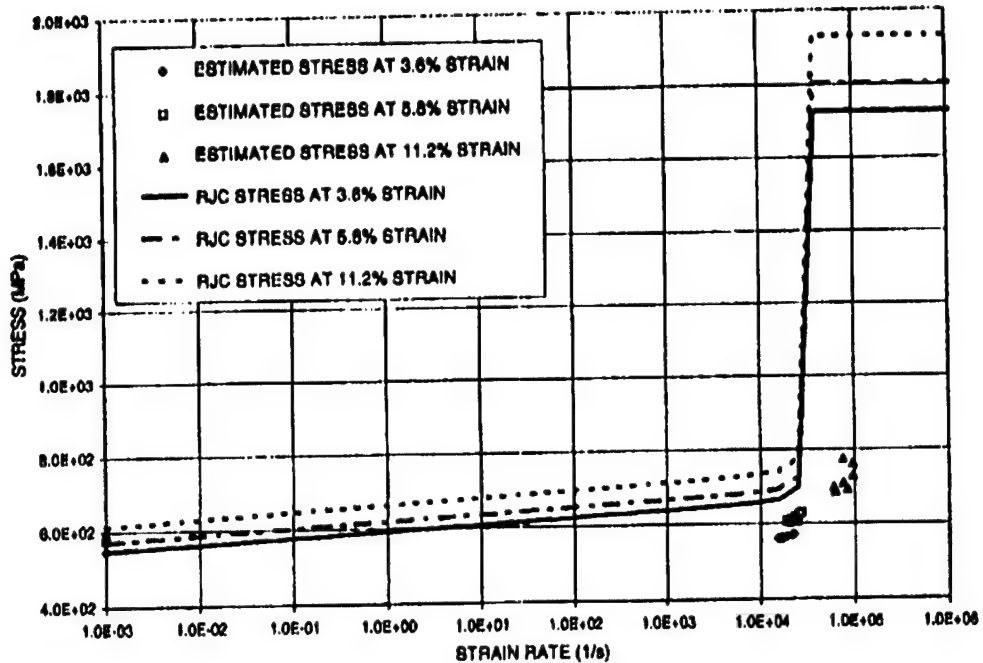


Fig. 4. Plots of yield strength versus strain rate for 7075-T6 aluminum for various strain levels comparing RJC strength model results (Eqns (3) and (4)) with quasi-static measurements and estimates from a one-dimensional Taylor specimen model.

between the measured and calculated results. The strength model coefficients of Table 5 appear to be reasonable when compared with those of other JC models.

It is difficult to compare the results of this study with data obtained from the literature since, in general, common materials are not evaluated. However, a comparison can perhaps be made with some published results on a copper. The predicted yield strength of this study for OFHC copper under conditions of  $\epsilon = 0.4$ ,  $\epsilon' = 6.4E5 \text{ s}^{-1}$ , and  $T = 295 \text{ K}$  is 1560 MPa. This value is significantly larger than the predictions of Clifton ( $\cong 482 \text{ MPa}$ ), and Foliansbee and Kocks ( $\cong 649 \text{ MPa}$ ) for OFE copper (see Fig. 11 of Ref. [5]). Part of this discrepancy can perhaps be explained by the fact that the materials were not identical (OFHC copper versus OFE copper). The range of these predictions in Ref. [5] emphasize the difficulties of determining yield strengths at high strain rates.

The RJC model stress-strain rate curves are plotted in Figs 4-7 for the four metals tested. These plots display the expected behavior. The quasi-static ( $\epsilon^* \cong 10^{-3}$ ) yield stress estimates are indicated with markers on the ordinate axes of Figs 4-7. The markers indicated on the right-hand side of these figures (in the vicinity of the critical strain rate) are discussed in the next section.

As can be seen from Table 5, the wrought iron results produced the poorest fit with respect to the Taylor data, with an average volume percentage error of 5.3%. For the other materials tested, the fit was significantly better. The measured and calculated deformed profiles for the six wrought iron Taylor specimens are compared in Fig. 8. It can be seen from this figure that constraining the optimizer to replicate the quasi-static behavior produced a higher strength material model than that required for a good fit to the Taylor results. However, considering the shape of the wrought iron stress-strain curve (discrete yield plateau and work hardening behavior, Fig. 2), and considering the many other approximations built into the EPIC model, Fig. 8 shows an adequate fit to the Taylor data. It is important to note that the Taylor results of Fig. 8 were obtained while achieving an accurate fit (2.5% average error) to the quasi-static results as can be seen by the data points indicated on the ordinate axis of Fig. 6. Running the optimizer without the quasi-static constraints produced a very high quality fit to the Taylor data (2.3% average volume error). At this level of average error, measured and calculated deformed profiles for most Taylor specimens are virtually identical.

A revised form for the Johnson-Cook strength model

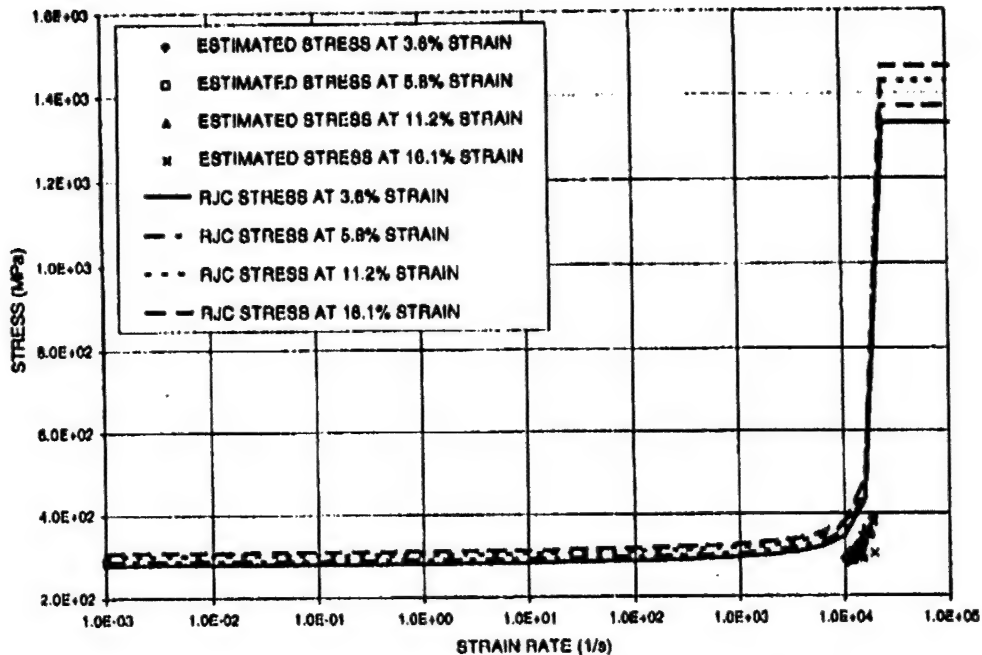


Fig. 5. Plots of yield strength versus strain rate for OFHC copper for various strain levels comparing RJC strength model results (Eqns (3) and (4)) with quasi-static measurements and estimates from a one-dimensional Taylor specimen model.

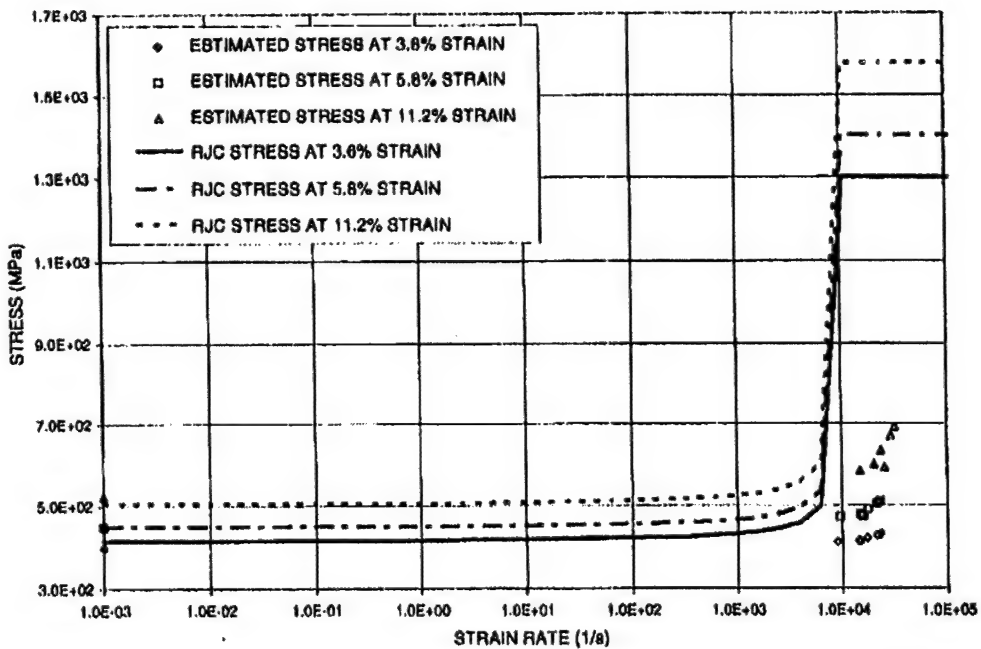


Fig. 6. Plots of yield strength versus strain rate for wrought iron for various strain levels comparing RJC strength model results (Eqns (3) and (4)) with quasi-static measurements and estimates from a one-dimensional Taylor specimen model.

### 3.4. Approximate results from a one-dimensional analytical model

In some respects the Taylor impact test can be approximately treated as a one-dimensional system in order to obtain closed form semi-empirical expressions describing stress-strain rate behavior. Such an expression was recently developed [15, 16] and applied

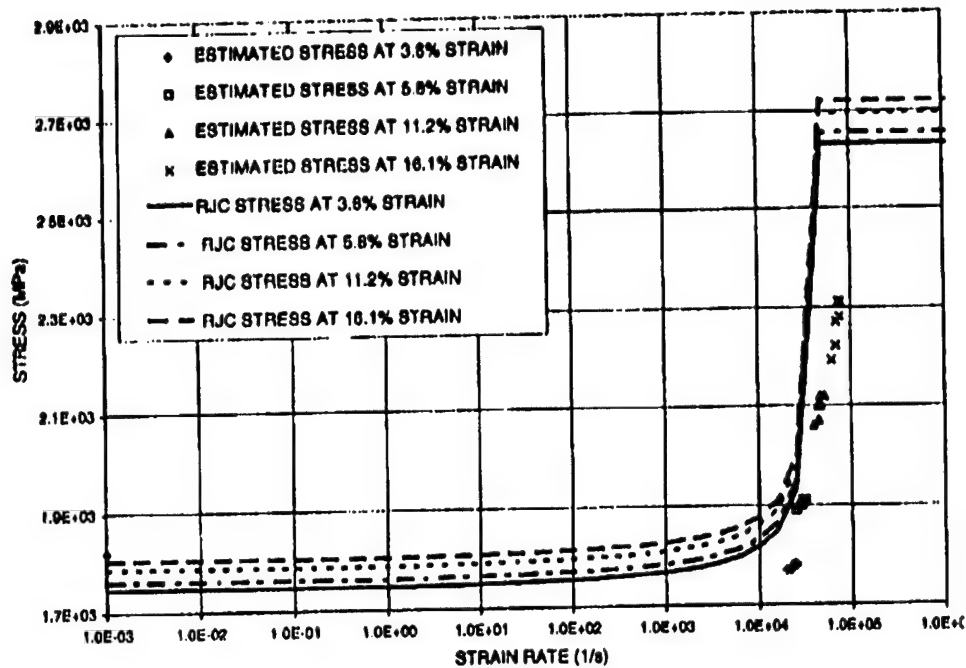


Fig. 7. Plots of yield strength versus strain rate for Astralloy-V<sup>®</sup> steel for various strain levels comparing RJC strength model results (Eqns (3) and (4)) with quasi-static measurements and estimates from a one-dimensional Taylor specimen model.

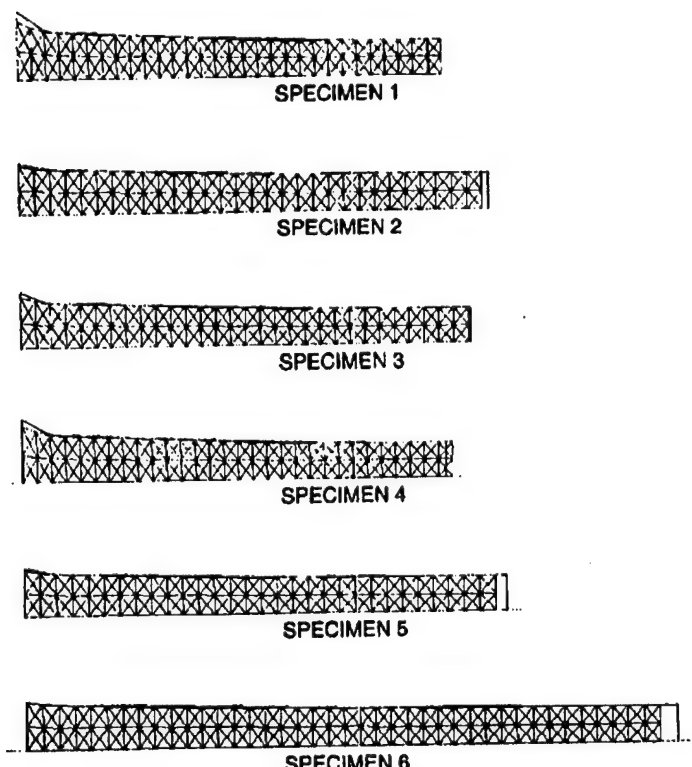


Fig. 8. Comparison of measured (black lines) and calculated (dark gray triangular meshes) deformed geometries of the wrought iron Taylor specimens.

to the metals of this study. These calculations provided estimates for the yield strength at high strain rates where pronounced strengthening was observed, as shown by the data points for various strain levels on the right-hand side of Figs 4-7. Note that these calculations were made without assuming any functional form for stress-strain rate behavior. Thus, they provide an independent check of the optimized results obtained for the RJC strength model as described in the previous section.

There appears to be a reasonable agreement between the RJC and one-dimensional model results. The one-dimensional model tends to over estimate the strain rate to some degree because it assumes a strain rate equal to the average strain rate during the initial transient portion of the impact event [15, 16]. Since the one-dimensional model makes predictions of mechanical behavior just after the initial transient, this may account for some of this strain rate discrepancies shown in Figs 4-7.

#### 4. SUMMARY

The strain rate term of the Johnson-Cook strength model was revised to treat the dramatic increase in yield strength exhibited by some ductile metals at high strain rates. The revised strength model assumes that each material has a maximum strain rate induced increase in yield strength which cannot be exceeded. The RJC strength model has eight material constants that require evaluation. An economical method employing an optimizer was proposed to evaluate the material constants using quasi-static tension test and Taylor impact data. The finite element code EPIC was modified and used to reduce the Taylor impact data for processing by the optimizer. RJC model material constants were evaluated for 7075-T6 aluminum, OFHC copper, wrought iron, and a high-strength steel (Astralloy-V<sup>®</sup>). The RJC model appears to be capable of representing the stress-strain rate behavior of these metals over a wide range of strain rates. The RJC model also correlates reasonably well with yield strength estimates at high strain rates provided by a one-dimensional model for Taylor impact specimens.

**Acknowledgements** —Dr M. Barkey of the Department of Aerospace Engineering and Mechanics at the University of Alabama in Tuscaloosa provided the quasi-static test results for the four metals treated in this paper. Jeffrey A. Drinkard, Vanessa Ennis, and Daniel T. Suggs, students at the University of Alabama, assisted with the Taylor testing and Taylor data reduction. The EPIC source code, which was modified for use in this investigation, was provided by Dr G. R. Johnson of Alliant Techsystems, Incorporated and Dr W. H. Cook of Eglin AFB. This is much appreciated. Ms E. R. Huber of Astralloy Wear Technology kindly provided machined specimens of Astralloy-V<sup>®</sup> steel for quasi-static and Taylor impact testing. The writers are also grateful for the many constructive suggestions provided by the reviewers.

#### REFERENCES

1. G. R. Johnson and W. H. Cook, A constitutive model and data for metals subjected to large strains, high strain rates, and high temperatures. *Proc. 7th Int. Symp. on Ballistics*, Hague, Netherlands, April (1983).
2. M. A. Meyers, *Dynamic Behavior of Materials*. Wiley, New York (1994).
3. F. J. Zerilli and R. W. Armstrong, Dislocation-mechanics-based constitutive relations for material dynamics calculations. *J. Appl. Phys.* **61**(5), 1816-1825 (1987).
4. T. J. Holmquist and G. R. Johnson, Determination of constants and comparison of results for various constitutive models. *J. Phys. I*, C3-853 C3-860 (1991).
5. P. S. Follansbee and U. F. Kocks, A constitutive description of the deformation of copper based on the use of mechanical threshold stress as an internal state variable. *Acta Metall.* **36**(1), 81-93 (1988).
6. U. S. Lindholm, Dynamic deformation of metals. *Proc. Colloquium on Behavior of Materials Under Dynamic Loading at the Winter Annual Meeting of the ASME*, Chicago, Illinois, November 9 (1965).
7. T. Nicholas, Material behavior at high strain rates. *Impact Mechanics*. Krieger Publishing Company, Malabar, FL (1992).
8. R. J. Clifton, *Dynamic Plasticity*. *J. Appl. Mech.* **50**, 941-952 (1983).
9. D. J. Steinberg, S. G. Cochran and M. W. Guinan, A constitutive model for metals applicable at high-strain rate. *J. Appl. Phys.* **51**(3), 1498-1504 (1980).
10. A. H. Jones, C. J. Maiden, S. J. Green and H. Chin, Prediction of elastic-plastic wave profiles in aluminum 1060-0 under uniaxial strain loading. In *Proc. Mechanical Behavior of Materials under Dynamic Loads*, (edited by U. S. Lindholm) Sponsored by Army Research Office and Southwest Research Institute, Springer, New York (1968).

11. D. J. Allen, Use of the Taylor impact test to determine constants for material strength models. Masters Thesis, Department of Engineering Science and Mechanics, University of Alabama, Tuscaloosa (1995).
12. G. R. Johnson, R. A. Stryk, T. J. Holmquist and S. R. Beissel, *User Instructions for the 1996 Version of the EPIC Code*. Alliant Techsystems Inc., March (1996).
13. G. R. Johnson and T. J. Holmquist, Evaluation of cylinder-impact test data for constitutive model constants. *J. Appl. Phys.* **64**(8), 3901-3910 (1988).
14. G. N. Vanderplaats, *Numerical Optimization Techniques for Engineering Design with Applications*. McGraw-Hill, New York (1984).
15. S. E. Jones, M. E. Barkey, and W. K. Rule, Mechanical characterization of hardened Astralloy-V<sup>®</sup> using the Taylor impact test. Paper No. AIAA-96-4294, Space Programs and Technologies Conf., Huntsville, AL (1996).
16. S. E. Jones, J. A. Drinkard, W. K. Rule and L. L. Wilson, An elementary theory for the Taylor impact test. *Int. J. Impact Engng.* accepted for publication.

## **APPENDIX D**

## MECHANICAL CHARACTERIZATION OF HARDENED ASTRALLOY-V® USING THE TAYLOR IMPACT TEST

S. E. Jones, M. E. Barkley, and W. K. Rule

Department of Engineering Science and Mechanics

The University of Alabama, Tuscaloosa, Alabama, 35487

and

Elizabeth R. Huber

Astralloy Wear Technology

Birmingham, AL

### Abstract

Hardened Astralloy-V® is the material from which some armor plates for civilian and military use are made. In order to assess the ballistic performance of this material, we require a mechanical characterization at strain-rates exceeding 10/s. These rates exceed the limits of conventional Split-Hopkinson Bar testing. However, the Taylor impact test achieves these rates with even moderately low impact velocities. Using a new one-dimensional analysis, proposed by one of the authors, a high rate description of material behavior is possible. The results of the one-dimensional analysis are compared with the results obtained by modeling the Taylor specimens with the EPIC finite element analysis code. These methods may be used to find high strain-rate properties for other ductile materials and their ballistic performance investigated in a similar manner.

### Introduction

ASTRALLOY-V® is a high strength and high hardness (477 BHN) steel that is used in a number of applications. Some of the applications involve wear resistance, which is the primary market for this product. However, ASTRALLOY-V® has been used as armor plate in terminal ballistics applications. To understand and interpret the performance of this armor under impact conditions, the constitutive properties of the material at strain-rates comparable to those observed in an impact/penetration event must be determined. This presents an analytical and experimental challenge.

The Split-Hopkinson Pressure Bar is the most reliable method for obtaining high rate properties<sup>1-4</sup>. However, it is difficult to approach strain-rates of the

order of 10<sup>4</sup>/s with this test. The limitation is due to the wave speed in the pressure bars.

Strain-rates exceeding 10<sup>4</sup>/s are easily achieved in the Taylor impact test<sup>5,6</sup>. Even for low impact velocities, relatively high strain-rates can be observed. For this reason, the test is receiving more attention<sup>7,10</sup> from researchers and practicing engineers in the field. However, the difficulty is the interpretation of the results. In this respect, there are two generally accepted methods for interpreting test data: one-dimensional models<sup>5-10</sup> and full scale code calculations<sup>11,12</sup>. There are advantages to both and we will employ both methods to interpret the test data presented in this paper.

### Taylor Impact Tests

There are a number of variants of Taylor test configuration. The one that we will employ is the conventional rod against an uncompliant (very hard, essentially rigid) target. In this test, a cylinder of specimen material is launched from a gun tube and impacted normally against a massive target. For the tests discussed in this paper, the cylinders and target "faces" are Astralloy-V®.

Seventeen-caliber cylinders with length to diameter ratios of 7.5 and 10 were impacted at a variety of speeds ranging from 187 m/s to 232 m/s. The results of these tests are reported in Table 1. The normalized undeformed section lengths  $\xi = \ell_f / L$  are the ratios of undeformed section length,  $\ell_f$ , to initial length, L, for compressive strains of 3.6%, 5.8%, 11.2%, and 16.1%.  $\xi_1$  corresponds to 3.6%,  $\xi_2$  corresponds to 5.8%,  $\xi_3$  corresponds to 11.2%, and  $\xi_4$  corresponds to 16.1%.

$\eta = (L - S_f) / L$  is the normalized deformed length  $L_f / L$  (see Fig. 1).

The theory presented by Jones, et al.<sup>10</sup> predicts that the data presented in Table 1 is linear for  $\xi$  vs.  $\eta$  for sufficiently high impact velocities. Figure 2 demonstrates this linearity. The slope  $m$  and intercept  $b$  of these lines are related to the particle velocity,  $u$ , behind the plastic wave front and the conditions that exist at the end of the initial transient that accompanies the shock at impact of the specimen.

The key parameter in the mathematical model is  $\beta$ , where  $u = \beta v$ . The velocity of the back of the specimen is  $v$ . The modeling process assumes rigid-plastic behavior for the specimen material and the magnitude of  $\beta$  governs the velocity discontinuity at the rigid-plastic interface.

From Jones, et al.<sup>10</sup>, the relationship between the slopes of the lines in Fig. 2 for the constant compressive strains,  $e$ , is

$$m = -\frac{1-\beta}{e} \quad (1)$$

In this equation,  $e = d_0^2/d^2 - 1$  is the longitudinal, compressive strain. The undeformed specimen diameter is  $d_0$  and the deformed specimen diameter is  $d$ . For example, the 17-caliber specimens have an initial diameter  $d_0 = 4.17$  mm. For a compressive strain of 5.8%,  $d = 4.30$  mm. For each slope in Fig. 2, the corresponding value of  $\beta$  can now be calculated directly with Equation (1).

A compression test on Astralloy-V® was performed. The true stress/engineering strain curve is shown in Fig. 3. From the quasi-static yield stresses in Fig. 3, the values of  $\beta$  in Equation (1), and the impact velocities in Table 1, we can estimate the high rate properties of the specimen material.

#### Estimation of Stresses and Strain Rates

After impact, there is a short period of initial transient behavior. The duration of this initial transient is dependent on the strain of the observed wave, or bulge, in the specimen. Lower strain waves move much faster than higher strain waves.

The conditions that exist at the end of the initial transient are denoted by bars over the symbol. It can be shown<sup>10</sup> that the normalized undeformed section length  $\bar{\ell}/L$  achieved at the end of the

initial transient can be related to the final normalized undeformed section length  $\ell_f/L$ :

$$\frac{\bar{\ell}}{L} = \frac{\ell_f}{L} \exp \left\{ \frac{(1+e)(1-\beta)}{2e\sigma_s} \rho v_0^2 \right\}. \quad (2)$$

In this equation,  $\sigma_s = \sigma_s(e)$  is the quasi-static compressive yield stress at the compressive strain  $e$ . The uniform mass density of the specimen is  $\rho$ .

The values of  $\sigma_s(e)$  are given in Table 2. These stresses are taken from the stress-strain diagram in Fig. 3. Using the data in Table 2, Equation (2), and Table 1, the ratios  $\bar{\ell}/L$  are calculated for each experiment. The results are reported in Table 3.

In each instance, note that  $\bar{\ell}/L$  remains virtually constant. This observation has been used to advantage by Jones, et al.<sup>10</sup>, where the quasi-static stress-strain diagram was estimated from Taylor test data.

Now, the maximum stress and maximum strain-rate can be estimated using formulas given by Jones, et al.<sup>13</sup> or Maudlin, et al.<sup>14</sup> and Jones, et al.<sup>15</sup>:

$$\sigma_{\max} = \sigma_s + \frac{(1+e)(1-\beta)^2}{e} \rho v_0^2 \quad (3)$$

and

$$\dot{\epsilon}_{\max} = -\frac{v_0}{L} \frac{1}{\left(1 - \frac{\bar{\ell}}{L}\right)}. \quad (4)$$

The results are given in Fig. 4, where stress is plotted as a function of strain-rate for the constant strains considered in the reduction of the experimental data. The dotted lines on this figure indicate, approximately, stress behavior for lower strain rates. The solid lines on Fig. 4 are predictions made using a Johnson-Cook strength model<sup>16</sup>. These predictions are discussed in the next section.

Astralloy-V® is a high strength steel that has a relatively low strain to failure in tension as is typical of a high strength steel. This lack of ductility is reflected by the minor influence that strain-rate has on the total stress,  $\sigma$ . At the highest strain, 16.1%, the increase in stress at a strain-rate of approximately  $7 \times 10^4/s$  is only 17% greater in magnitude than the quasi-static yield stress at the same strain.

### Constitutive Behavior Using A Computer Code

Validating the high strain rate constitutive results (Equation (3)) obtained from the approach described in the preceding sections of this paper (and shown in Fig. 4) is a difficult but necessary task. The validation approach used here consisted of using an empirical equation to model the constitutive response. The deformed geometries of the Taylor test specimens were used to calibrate the coefficients of the empirical equation. The empirical equation applied here is a commonly used one developed by Johnson and Cook<sup>16</sup>:

$$\sigma = (c_1 + c_2 \varepsilon_p^{c_3}) (1 + c_4 \ln \dot{\varepsilon}_p) (1 - T^{c_5}) \quad (5)$$

where: the  $C_i$  are empirical coefficients,  $\varepsilon_p$  is the equivalent plastic strain,  $\dot{\varepsilon}_p$  is the equivalent plastic strain rate, and  $T'$  is the homologous temperature.

The empirical coefficients,  $C_i$ , of Equation (5) were determined by using an optimizer to drive the well known EPIC finite element code. This involved applying an approach described by Allen et al.<sup>12</sup>, where the coefficients are adjusted in an optimal fashion to minimize the difference between measured and calculated Taylor specimen deformed geometries. Seven Taylor test deformed geometry data sets were used in the coefficient fitting process as shown in Table 4. As indicated in Table 4, average values of the five coefficients of Equation (5) were used for constitutive model validation. The seven Taylor specimens produced quite consistent sets of empirical coefficients as demonstrated by Table 5.

The coefficient fitting process is most sensitive to the impacted end of the Taylor specimen where compressive strains, compressive strain rates, and temperatures are highest. Thus, a severe accuracy test of Equation (5) would be for comparison with quasi-static tension test results, Fig. 5. From this figure it can be seen that, according to Equation (5), the offset yield stress is overestimated, and the ultimate tensile stress underestimated by a remarkably small 14%. Thus, it appears that the coefficients of Table 4 with Equation (5) provides a reasonable representation of the constitutive behavior of the Astralloy-V® material.

For comparison with previously derived constitutive results of Equation (3), Equation (5) is plotted on Fig. 4 (solid lines) for strain values of 3.6% (lowest line), 5.8%, 11.2%, and 16.1% (highest line). Note that the form of Equation (5) is

such that these plots must be linear on a logarithmic strain rate plot and so the abrupt rise in stresses predicted at high strain rates can not be followed. However, it can be seen that Equation (5) (solid lines) attempts to straddle the previously generated constitutive results of Equation (3) (dotted lines) in Fig. 4. Thus, subject to the constraints of the form of the equation, the Johnson-Cook predictions of Equation (5) appear to agree well with the prediction of Equation (3).

### Conclusions

For years the Taylor test has been regarded more for its historical significance than its practical value. The reason for this is that most analyses of the test produced an estimate for the "dynamic yield stress" that was unconnected to accurate estimates for strain and strain-rate. Contemporary design considerations have created a need for accurate estimates of material behavior at strain-rates that are difficult to achieve by any of the accepted methods for mechanical testing. The Taylor test achieves rates that are nearly an order of magnitude higher than those obtained by conventional Split-Hopkinson Pressure Bar testing. Thus, the Taylor test helps to fill the gap between the Split-Hopkinson Pressure Bar and the ultra high strain-rates achieved in plate impact experiments (e.g. Clifton et al.<sup>17</sup>).

A one-dimensional interpretation of the Taylor test has been shown to lead to very satisfactory conclusions regarding the material behavior of Astralloy-V®. This metal is a high strength steel that is suitable for armor applications. In order to understand its behavior in a terminal ballistics environment, however, its high rate constitutive properties are required. Future efforts will concentrate on simulating the terminal ballistic event and on further refining the testing of the material.

### Acknowledgments

Pinson Valley Heat Treating, of Birmingham Alabama, performed all heat treating for this project.

### References

<sup>1</sup>Davies, R. M., "A Critical Study of the Hopkinson Pressure Bar," *Phil. Trans. Roy. Soc. London*, Series A, 240, 376, 1948.

<sup>2</sup>Lindholm, U. S., "Some Experiments with the Split Hopkinson Pressure Bar," *J. Mech. Phys. Solids*, 12, 317, 1964.

<sup>3</sup>Bertholf, L. D., and Karnes, C. H., "Two-Dimensional Analysis of the Split Hopkinson Pressure Bar System," *J. Mech. Phys. Solids*, 23, 1, 1975.

<sup>4</sup>Nicholas, T., "Dynamic Tensile Testing of Structural Materials Using a Split Hopkinson Bar

Apparatus," Technical Paper AFWAL-TR-80-4053, 1980.

<sup>5</sup>Taylor, G. I., "The Use of Flat-Ended Projectiles for Determining Dynamic Yield Stress I: Theoretical Considerations," *Proc Roy. Soc. London*, A 194, 289, 1948.

<sup>6</sup>Whiffen, A. C., "The Use of Flat-Ended Projectiles for Determining Dynamic Yield Stress II: Tests on Various Metallic Materials," *Proc. Royal Soc. London*, A194, 300, 1948.

<sup>7</sup>Hawkyard, J. B., "A Theory for the Mushrooming of Flat-Ended Projectiles Impinging on a Flat Rigid Anvil Using Energy Considerations," *Int. J. Mech. Sci.*, 11, 313, 1969.

<sup>8</sup>Jones, S. E., Gillis, P. P., and Foster, J. C., Jr., "On the Equation of Motion of the Undeformed Section of A Taylor Specimen," *J. Appl. Phys.*, 61, 21, 15, 1987.

<sup>9</sup>Jones, S. E., Gillis, P. P., Foster, J. C., Jr., and Wilson, L. L. "A One-Dimensional, Two-Phase Flow Model for Taylor Impact Specimens," *J. Engr. Mat'l's Tech., Trans. ASME*, 113, 228, 1991.

<sup>10</sup>Jones, S. E., Augustus, S., Drinkard, J. A. and L. L. Wilson, "An Elementary Theory for the Taylor Impact Test," submitted for publication.

<sup>11</sup>Johnson, G. R. and Holmquist, T. J., "Evaluation of Cylinder Impact Test Data for Constitutive Model Constants," *J. Appl. Phys.*, 64, 3901, 1988.

<sup>12</sup>Allen, D. J., Rule, W. K., and Jones, S. E., "Optimizing Material Strength Constants Numerically Extracted from Taylor Test Data," submitted for publication.

<sup>13</sup>Jones, S. E., Maudlin, P. J., and Foster, J. C., Jr., "An Engineering Analysis of Plastic Wave Propagation in the Taylor Test," accepted for publication in the *International Journal of Impact Engineering*.

<sup>14</sup>Maudlin, P. J., Foster, J. C., Jr., and Jones, S. E., "A Continuum Mechanics Code Analysis of Steady Plastic Wave Propagation in the Taylor Test," accepted for publication in the *International Journal of Impact Engineering*.

<sup>15</sup>Jones, S. E., Maudlin, P. J., and Foster, J. C., Jr., "Constitutive Modeling Using the Taylor Impact Test," High Strain Rate Effects on Polymer, Metal and Ceramic Matrix Composites and Other Advanced Materials, Y. D. S. Rajapakse and J. R. Vinson, eds., 1995 ASME International Mechanical Engineering Congress and Exposition, San Francisco, CA, 1995.

<sup>16</sup>Johnson, G. R., and Cook, W., "A Constitutive Model and Data for Metals Subjected to Large Strains, High Strain Rates, and High Temperatures," *Proc. 7<sup>th</sup> Int. Symp. On Ballistics*, The Hague, The Netherlands, 541, 1983.

<sup>17</sup>Clifton, R. J., Gilat, A., and Li, C. H., "Dynamic Plastic Response of Metals Under Pressure-Shear Impact," in *Material Behavior Under High Stress and Ultrahigh Loading Rates*, J. Mescall and V. Weiss, eds., Plenum Press, New York, 1983.

Table 1: Astralloy-V® data for 17 caliber specimens.

$v_0$ (m/s)	L (cm)	$\eta$	$\xi_1$	$\xi_2$	$\xi_3$	$\xi_4$
187	3.142	0.943	0.627	0.671	0.741	0.783
232	3.137	0.917	0.592	0.621	0.683	0.721
216	3.134	0.927	0.608	0.642	0.704	0.743
232	3.137	0.921	0.597	0.636	0.697	0.726
219	3.145	0.930	0.611	0.643	0.707	0.746
198	3.142	0.939	0.627	0.660	0.731	0.773

Table 2: Material parameters.

e	$\sigma_s(e)$ (MPa)	$\beta$	$\rho$ (kg / m <sup>3</sup> )
-0.036	-1750	0.948	7847
-0.058	-1840	0.900	7847
-0.112	-1930	0.760	7847
-0.161	-1970	0.605	7847

Table 3: Normalized undeformed section length after the initial transient.

$v_0$ (m/s)	$\bar{\ell}/L$ ( $\epsilon = 3.6\%$ )	$\bar{\ell}/L$ ( $\epsilon = 5.8\%$ )	$\bar{\ell}/L$ ( $\epsilon = 11.2\%$ )	$\bar{\ell}/L$ ( $\epsilon = 16.1\%$ )
187	0.699	0.757	0.848	0.904
232	0.700	0.748	0.841	0.899
216	0.704	0.754	0.843	0.900
232	0.706	0.766	0.857	0.905
219	0.710	0.759	0.851	0.908
198	0.708	0.756	0.851	0.908

Table 4: Johnson-Cook constitutive model coefficients fit from Taylor test deformed geometries.

VELOCITY (m/s)	CONSTANT 1 (MPa)	CONSTANT 2 (MPa)	CONSTANT 3	CONSTANT 4	CONSTANT 5
152	1333	614.1	0.2301	0.01531	1.094
187	1471	637.3	0.2289	0.01564	1.136
198	1523	642.8	0.2267	0.01571	1.131
216	1490	639.8	0.2261	0.01570	1.119
219	1662	633.7	0.2200	0.01597	1.084
232	1527	628.5	0.2261	0.01580	1.106
232	1662	641.3	0.2217	0.01598	1.151
AVERAGES	1524	633.9	0.2257	0.01573	1.117

Table 5: Variation in Johnson-Cook coefficients from average values.

VELOCITY (m/s)	PERCENTAGE DIFFERENCE FROM AVERAGE				
	CONSTANT 1	CONSTANT 2	CONSTANT 3	CONSTANT 4	CONSTANT 5
152	-12.5	-3.1	2.0	-2.7	-2.1
187	-3.5	0.5	1.4	-0.6	1.7
198	-0.1	1.4	0.5	-0.1	1.2
216	-2.2	0.9	0.2	-0.2	0.2
219	9.1	0.0	-2.5	1.5	-3.0
232	0.2	-0.9	0.2	0.4	-1.0
232	9.1	1.2	-1.8	1.6	3.0

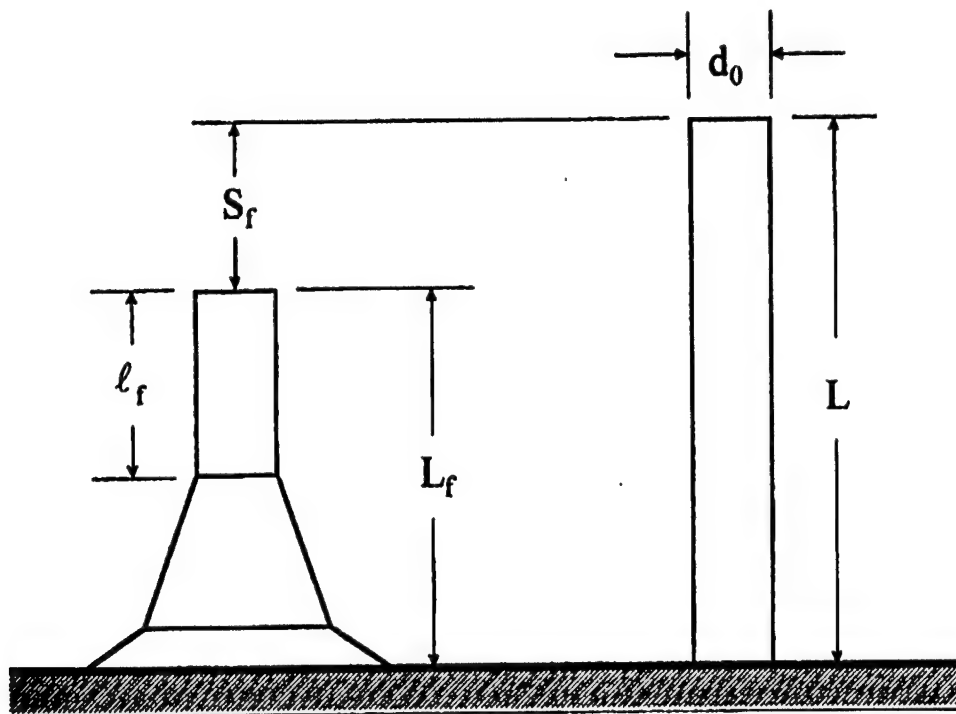


Figure 1: The deformed configuration of a Taylor specimen.

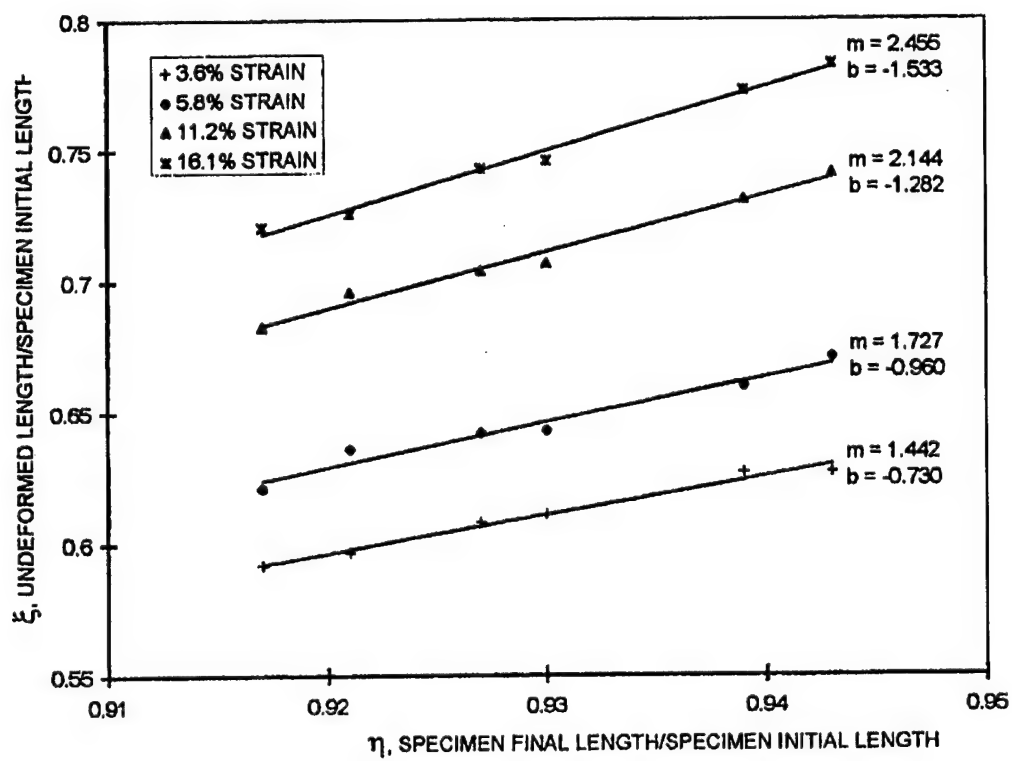


Figure 2: Plots of  $\xi$  versus  $\eta$  for various strain levels.

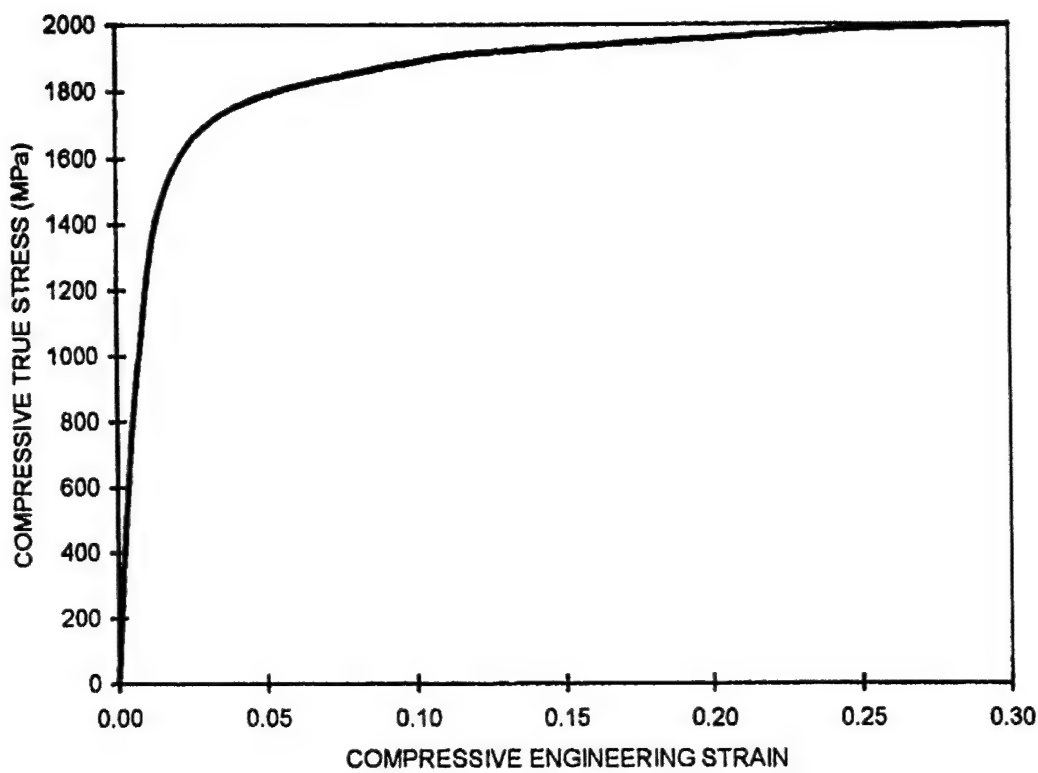


Figure 3: Plot of compressive true stress versus compressive engineering strain.

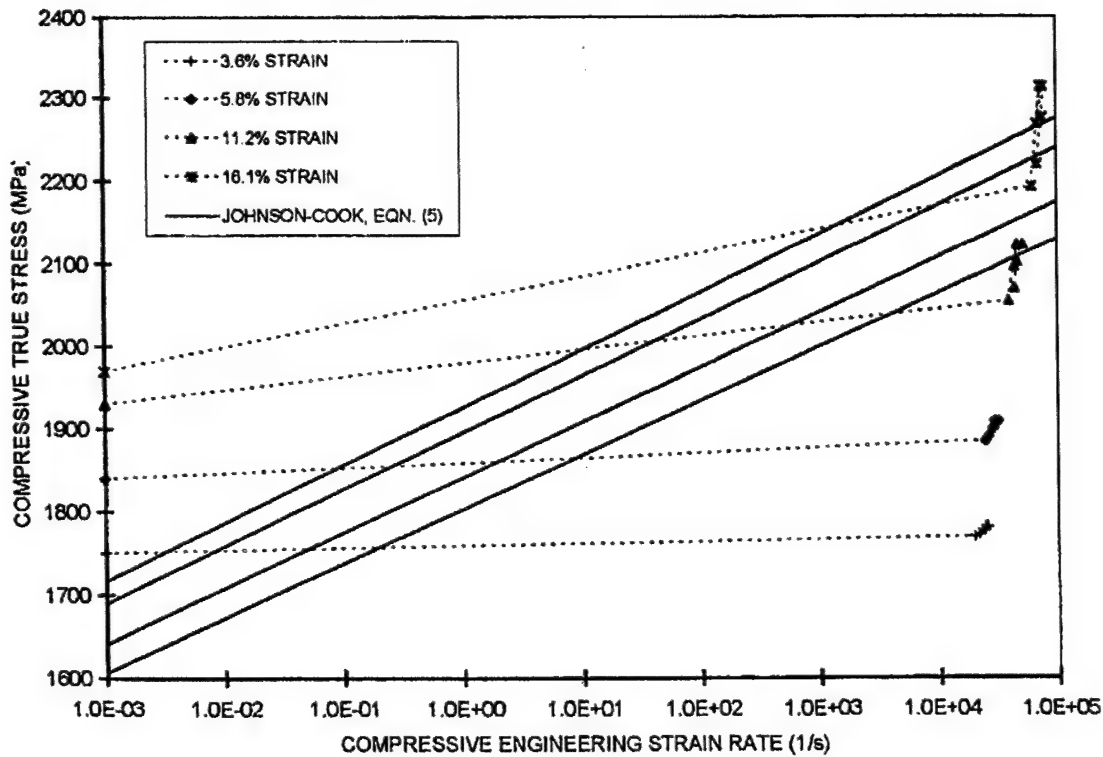


Figure 4: Plot of compressive true stress versus compressive engineering strain rate.

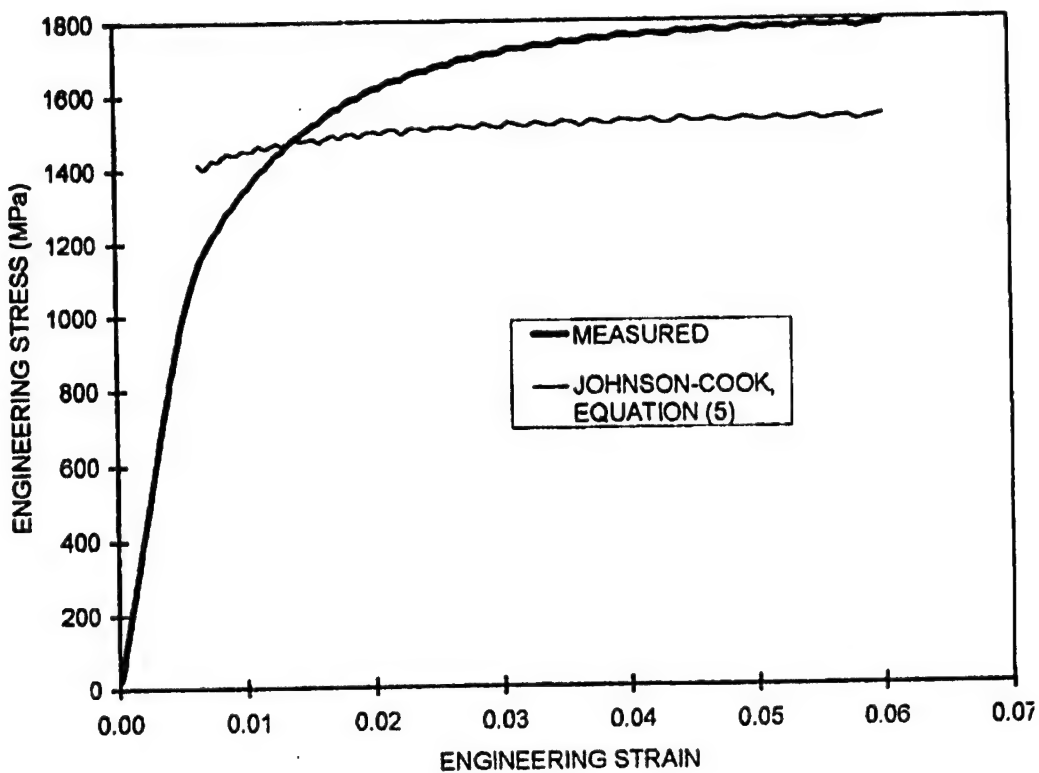


Figure 5: Comparison of Johnson-Cook equation prediction with measured tensile test data.

---

## **APPENDIX E**

# Film data reduction from Taylor impact tests

J W House<sup>1</sup>\*, B Aref<sup>2</sup>, J C Foster Jr<sup>1</sup> and P P Gillis<sup>3</sup>

<sup>1</sup>US Air Force Research Laboratory, Munitions Directorate-AFRL/MNMW, Eglin AFB, Florida, USA

<sup>2</sup>Sverdrup Technologies/TEAS Group, Eglin AFB, Florida, USA

<sup>3</sup>Department of Chemical and Materials Engineering, University of Kentucky, Lexington, Kentucky, USA

**Abstract:** A high-speed photographic film record of a Taylor impact experiment was analysed to determine the strain, strain rate and stress. The stress was calculated on the basis of an interpretive analysis by Taylor involving the motion of a plastic wave in the material. The data on drawn OFE copper produced stresses from 300 to 400 MPa, for strains between 0 and 45 per cent. The strain rate approximation produced a peak value of  $11000 \text{ s}^{-1}$ . The strain rate data showed a wide range of values in the plastically deforming region.

**Keywords:** Taylor impact experiment, dynamic plasticity, strain rate, OFE copper, film analysis

## NOTATION

<i>A</i>	cross-sectional area of the specimen
<i>D</i>	diameter of the specimen
<i>e</i>	areal strain
<i>dot{e}</i>	strain rate
<i>h</i>	current position of the plastic wave front
<i>l</i>	current length of the specimen
<i>t</i>	time
<i>T</i>	temperature
<i>u</i>	current velocity of the back end of the specimen
<i>v</i>	average Eulerian wave speed of the plastic front
<i>epsilon</i>	logarithmic strain
<i>sigma</i>	compressive stress magnitude
<i>rho</i>	mass density

## Subscript

0	initial undeformed geometry
---	-----------------------------

## 1 INTRODUCTION

Continuum models developed to study impact and explosive formation use constitutive relationships to predict the material properties. These material models must be calibrated to a set of data consistent with the problem to be studied, namely large plastic strains and high strain rates. The strain rates found during penetration are  $10^5$ – $10^6 \text{ s}^{-1}$ , whereas the data used to generate constitutive properties

rarely exceed  $10^4 \text{ s}^{-1}$ . Here a technique is described for interpreting a high-deformation-rate experiment that will provide constitutive data closer to the regime of interest.

In 1948, Taylor [1], Whiffen [2] and Carrington and Gayler [3] reported a test aimed at providing flow stress information on materials deformed very rapidly. This high-deformation-rate experiment is performed by striking a cylindrical specimen against a massive anvil. The deformed specimen geometry and striking velocity are processed through an interpretive analysis to give a flow stress estimate. Such experiments are referred to as Taylor impact tests. Taylor's analysis of the experiment employs a rigid-plastic idealization of the material stress-strain curve. His results describe the material response to impulsive loading with a single parameter, the flow stress. Such an analysis lacks the ability to provide a detailed description of material properties since important variables such as strain and strain rate are absent. Other analyses formulated to interpret the experiment have been generated, for example, by Hawkyard [4] and by Jones *et al.* [5]. Yet, these analyses retain the rigid, perfectly plastic idealization found in Taylor's original work.

In the 1980s, the use of high-speed photography significantly expanded the database for these experiments. Photographic records of the deformation process have offered an entirely new method for interpreting the results of the Taylor test. In the present report it is shown how the film record can be analysed to estimate the strain rate and the stress-strain curve for the material tested.

## 2 ANALYSIS

Figure 1 is a schematic representation of three deformation profiles of the same specimen photographed at different times during a Taylor impact test. In Fig. 1a the specimen

The MS was received on 10 November 1998 and was accepted after revision for publication on 15 April 1999.

\*Corresponding author: US Air Force Laboratory Research, Munitions Directorate-AFRL/MNMW, 101 West Eglin Boulevard, Suite 135, Eglin AFB, FL 32542-6810, USA.

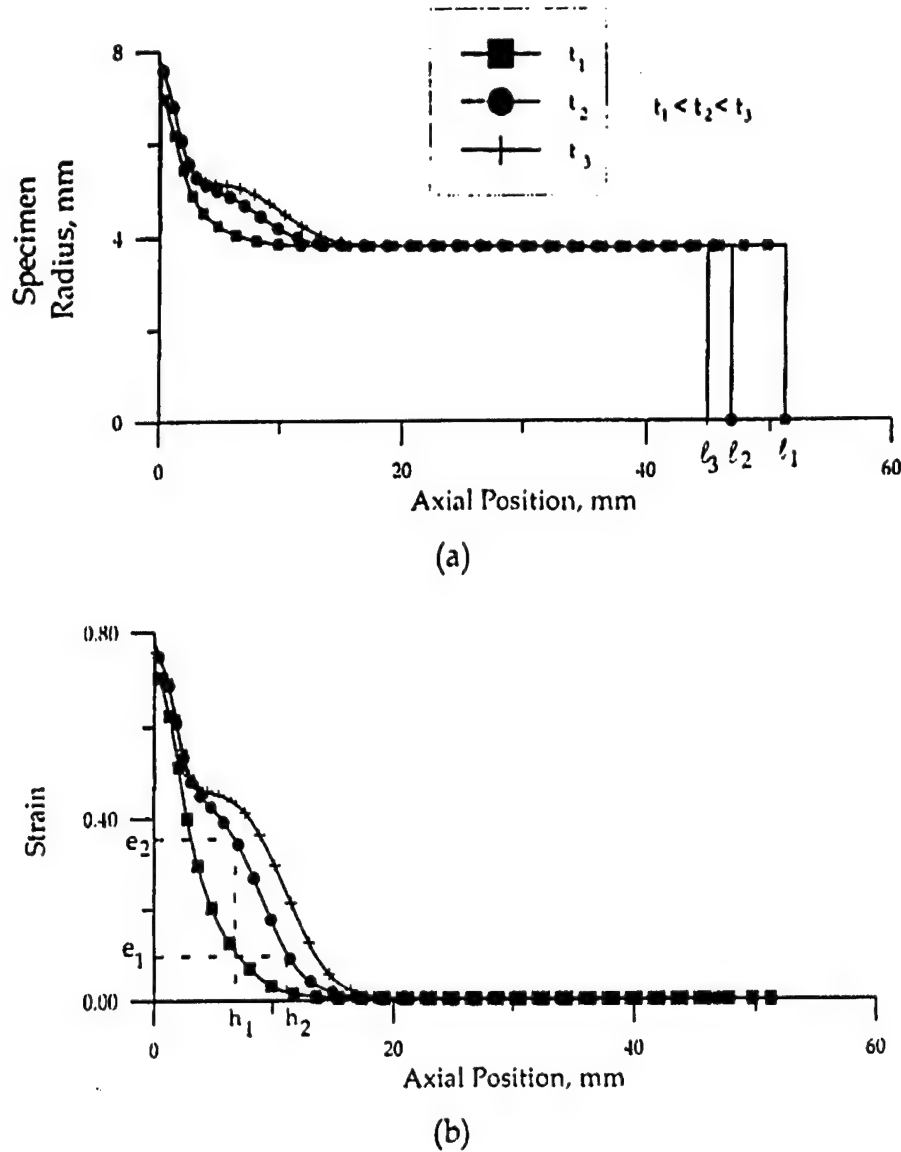


Fig. 1 Specimen radius and strain at three different times: (a) specimen radius versus axial position; (b) specimen strain versus axial position

radius is plotted versus axial position at the times  $t_1$ ,  $t_2$  and  $t_3$ , where  $t_3 > t_2 > t_1$ . Here the axial position is the distance from the anvil (or impact) face. This information can be reduced from corresponding frames of the photographic record of the test using an optical comparator.

The optical comparator, Deltronic model DH214, is designed to illuminate and magnify the profile geometry of an object placed in the lens viewing area. In this case, instead of an object, a strip of 35 mm film is studied. The enlarged image is projected on to a ground glass screen where horizontal and vertical cross-hairs aid in determining spatial information. The film is positioned with stepping motors that control the ram bed of the optical comparator. The current location of the film position identified by the cross-hairs is obtained via a digital read-out integrated with the stepping motor controllers. The optical comparator provides spatial data in increments of  $2.5 \mu\text{m}$  (0.0001 in).

Measurement accuracy for the Taylor impact data will be described in a separate section of the report.

In Fig. 1b the information from Fig. 1a is replotted as the areal strain versus the axial position. Taylor's definition of strain

$$e = 1 - \frac{A_0}{A} \quad (1)$$

is used. Here  $A_0$  is the cross-sectional area of the specimen prior to impact and  $A$  is the current value at the location of  $e$ . Equation (1) is identical with Taylor's equation (10) and defines  $e$  as being positive in compression. For the case of plane cross-sections remaining plane and no change in density,  $e$  equals the axial engineering strain. For actual tests,  $e$  closely approximates the axial strain everywhere except at the anvil face.

Step 1 in the construction of the stress-strain curve is to measure the change in length of the specimen from Fig. 1a. This enables the back end speed  $u$  to be calculated from

$$u = \frac{l_1 - l_2}{t_2 - t_1} \quad (2)$$

where  $l_1$  and  $l_2$  are the specimen lengths at the corresponding times  $t_1$  and  $t_2$ . Equation (2) gives the average value of  $u$  over the interval from  $t_1$  to  $t_2$ . As  $t_2$  is selected to be closer to  $t_1$  the average over the interval approaches the instantaneous value at  $t_1$ . On the other hand, as  $\Delta t$  becomes smaller, the separation between  $l_1$  and  $l_2$  approaches the uncertainty in the spatial measurements. Therefore, some suitable compromise is required in selection of the time interval between profiles.

Step 2 in the construction is to determine a series of plastic wave speeds from Fig. 1b. Select a convenient value of  $e$ , say  $e_1$ , and note the axial positions where that strain occurs in the two profiles at  $t_1$  and  $t_2$ . Denote these locations by  $h_1$  and  $h_2$  respectively. With respect to the anvil face, the strain  $e_1$  has propagated a distance  $h_2 - h_1$  during the time interval  $t_2 - t_1$  and so

$$v = \frac{h_2 - h_1}{t_2 - t_1} \quad (3)$$

Here  $v$  is the average Eulerian wave speed for the strain level  $e_1$  over the interval from  $t_1$  to  $t_2$ .

Another quantity of interest can be calculated from Fig. 1b. By drawing a vertical line through an axial position such as  $h_1$ , the change in strain  $e_2 - e_1$  at this position can be found for the time interval  $t_2 - t_1$ . Thus, some approximation to the strain rate there becomes

$$\frac{de}{dt} \approx \frac{e_2 - e_1}{t_2 - t_1} \quad (4)$$

This is called an approximation rather than an average because  $e$  is a Lagrangian strain measure which is embedded in the material. However, the material located at  $h_1$  at time  $t_2$  is different from that at  $t_1$ .

To obtain the stress associated with the selected strain  $e_1$  and the estimated strain rate requires interpretive analysis. For any constitutive model of material behaviour of the form  $\sigma = f(e, \dot{e}, T)$  the stress can be calculated from the foregoing information. (The logarithmic strain  $e$  is directly calculable from the areal strain  $e$  but, if the temperature is a factor, iteration is required to balance the temperature rise with the plastic work.)

In this paper dealing with the Taylor test, the constitutive approach taken by Taylor in his original analysis of the problem is used. From conservation of mass, Taylor writes

$$A_0(u + v) = Av \quad (5)$$

This is his equation (8). From impulse-momentum considerations

$$\rho A_0(u + v)u = \sigma(A - A_0) \quad (6)$$

which is Taylor's equation (9). Here  $\rho$  denotes the mass density of the material and  $\sigma$  is a compressive stress magnitude. This stress is associated with the strain corresponding to the change from  $A_0$  to  $A$ . Using equation (5) to eliminate  $A$  from equation (6), simplifying and rearranging give

$$\sigma = \rho(u + v)v \quad (7)$$

In combination with equations (2) and (3), equation (7) associates a stress  $\sigma_1$  with each strain  $e_1$ . This stress does not explicitly depend upon the strain rate from equation (4).

To construct a stress-strain curve for the specimen material, first select two frames from the photographic record and determine  $u$  using equation (2) as indicated by Fig. 1a. Then reduce the profile data to a strain plot as in Fig. 1b. From this diagram, several values of  $e$  can be selected, the associated values of  $v$  can be determined using equation (3) and the corresponding values of  $\sigma$  can be calculated from equation (7). These  $(e, \sigma)$  pairs can then be plotted to produce a stress-strain curve appropriate to that particular Taylor impact test.

Application of equation (4) will generally show different strain rates at each of the points plotted. This situation is no different from the ordinary pseudo-static tension test. In that test the strain rate usually increases by at least an order of magnitude at the yield point, varies with the rate of strain hardening during plastic flow and increases further as strain localization occurs during necking. This has been discussed by Hamstad and Gillis [6].

### 3 EXAMPLE

The Taylor test used here as an example, UK-145, is one of a series previously described by House *et al.* [7] in some detail. In short, the specimen is hardened OFE copper initially 7.6 mm (0.299 in) in diameter and 57.1 mm (2.25 in) long. The impact velocity of the specimen was 189 m/s. Figure 2 shows three typical frames of the photographic record. These images are at 33.3, 63.3 and 79.9  $\mu$ s. From these frames the deformed specimen lengths can be measured directly and from their differences the back end speed estimated using equation (2).

The diameter versus axial position data of Fig. 2 has been measured at approximately 1 mm intervals using the previously described technique, reduced to the areal strain  $e$  and plotted in Fig. 3. For each of the three times a relatively smooth curve is drawn through the data set. Using the two curves for 33.3 and 63.3  $\mu$ s, equation (3) is used to find values of  $v$  for each 2 per cent increment of

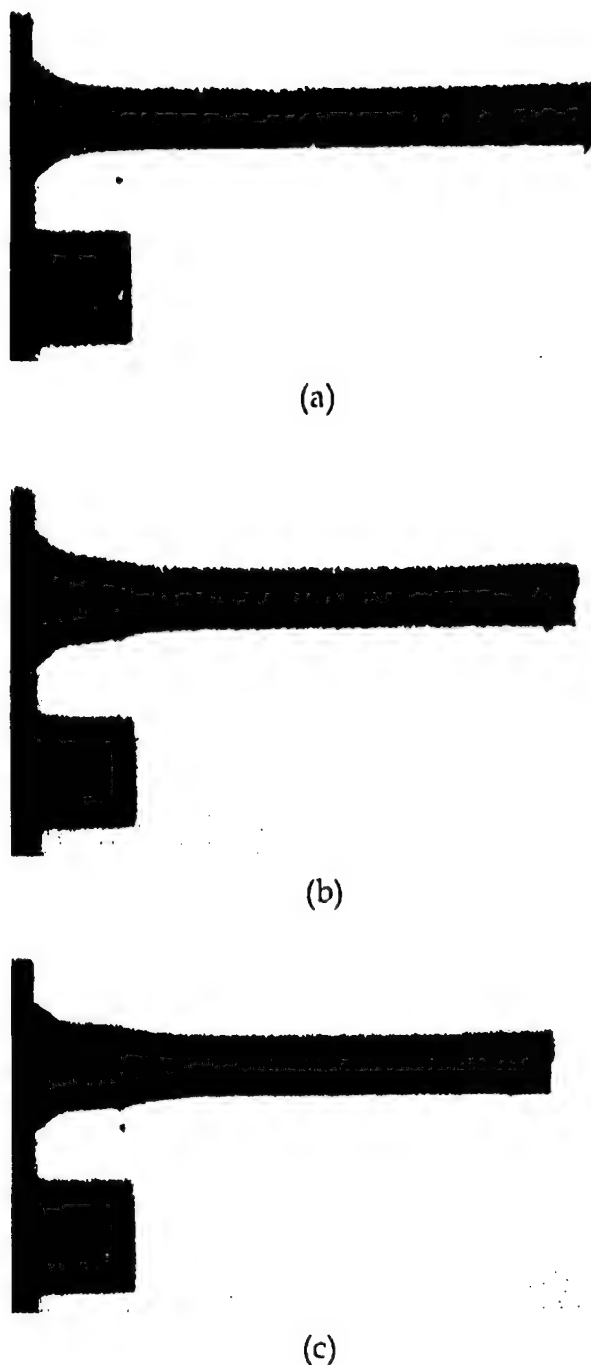


**Fig. 2** Three frames from the photographic record of the Taylor impact test of specimen UK-145. These frames correspond to times of (a) 33.3  $\mu$ s, (b) 63.3  $\mu$ s and (c) 79.9  $\mu$ s. In the photographs the anvil face is to the left and the specimen is moving in that direction. The block (lower left in each picture) is a fiducial establishing horizontal and vertical length scales

strain up to a maximum of 45 per cent. Using  $v$  and the corresponding  $u$  value determined from Fig. 2, the stresses are calculated using equation (7). The set of  $(e, \sigma)$  values obtained in this way are plotted as full squares in Fig. 4.

The strain rate was approximated using equation (4) and

the data in Fig. 3. Using the two curves for 33.3 and 63.3  $\mu$ s, approximate strain rate values were calculated at 0.5 mm increments in the range from 3.5 to 16 mm from the impact face. The strain associated with the approximate strain rate was assumed to be the numerical average of  $e_1$  and  $e_2$ . The set of  $(e, \dot{e})$  values are plotted as full triangles in Fig. 4.

Using the two curves for 63.3 and 79.9  $\mu$ s the process is repeated to generate the other set of  $(e, \sigma)$  and  $(e, \dot{e})$  identified by open symbols in Fig. 4.

The stresses plotted in Fig. 4 are based on two discrete values of back end speed  $u$ . For the two time intervals (33.3–63.3 and 63.3–79.9  $\mu$ s) the values are 145 and 123 m/s respectively. The wavefront speeds  $v$  are listed in Table 1 with the corresponding strain values. The dashed line in Fig. 4 shows the flow stress calculated using Taylor's original theory. The expression used is Taylor's equation (22) involving the initial and final projectile geometries and the initial kinetic energy of the specimen. The development of Taylor's equation (22) is based upon an assumption of constant plastic wave speed. The resultant flow stress is 335 MPa.

#### 4 FILM MEASUREMENT ACCURACY

The camera manufacturer specifies the resolving power of the camera based upon procedures established by the National Bureau of Standards. These test procedures establish distances between the camera and the resolution target consistent with the optics of the camera. The manufacturer's claim for resolving power is 22 line pairs per millimetre, in the transverse direction, and 28 line pairs per millimetre in the dynamic direction. Several factors make it difficult to correlate the accuracy of the film reduction technique with the reported resolving power. These factors include the lens quality, the film granularity and contrast, the film processing, the type of light and how the experiment is illuminated. To assess the accuracy of the film reduction technique a choice is made to present an illustration that gives some practical estimate of what can be expected.

The photographic record of the test SC-06 shows the specimen just rebounding from the anvil. This frame is shown here as Fig. 5. From this frame the specimen profile was measured using the optical comparator. The deformation profile of the recovered specimen was also measured on the optical comparator. These two profiles are superimposed in Fig. 6. Comparison of the measured diameters shows that the film reduction technique is accurate to within about 0.17 mm (0.007 in). The overall length of the specimen from the film data reduction is 15.2 mm (0.598 in), compared with the recovered specimen length of 14.8 mm (0.583 in). On the whole, these comparisons are considered to show good agreement.

Based upon the uncertainty in the data of Fig. 6 an analysis of the potential error in the strain measurement,

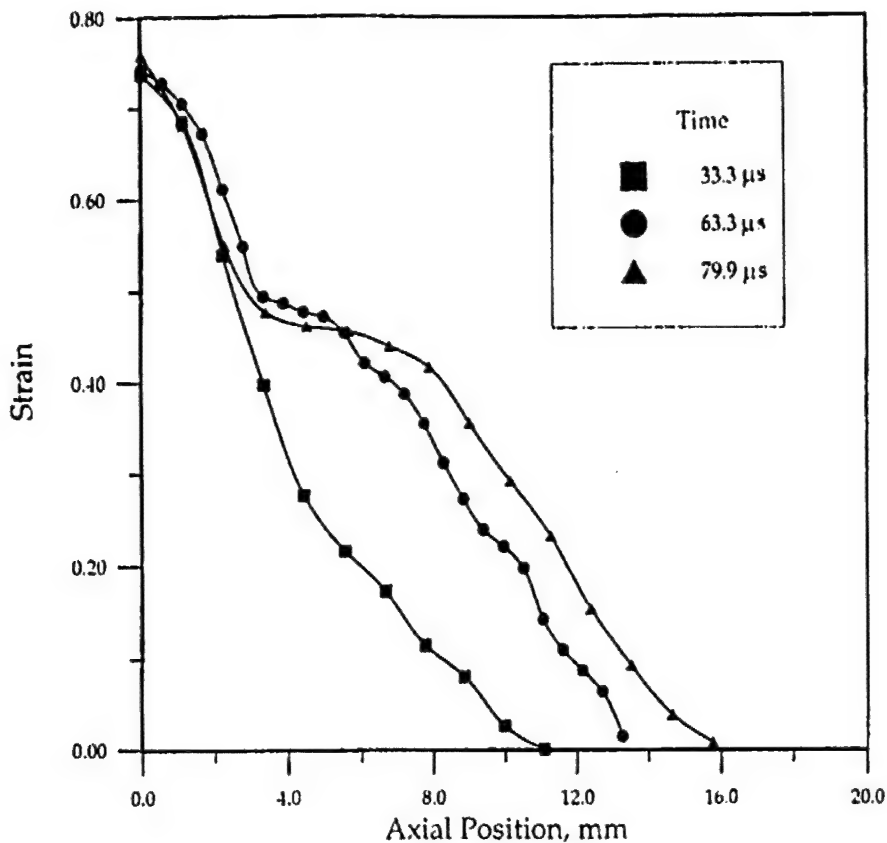


Fig. 3 Strain versus axial position in specimen UK-145 at the three different times of Fig. 2

reported in Fig. 3, can be made. Rewriting equation (1) in terms of the initial diameter  $D_0$  and the current diameter  $D$  gives

$$e = 1 - \frac{D_0^2}{D^2} \quad (8)$$

Differentiation of equation (8) gives

$$de = -2 \frac{D_0^2}{D^2} \frac{dD_0}{D} + 2 \frac{D_0^2}{D^2} \frac{dD}{D} \quad (9)$$

Substituting from equation (8) and rearranging, equation (9) can be written as

$$de = 2(1 - e) \left( \frac{dD}{D} - \frac{dD_0}{D_0} \right) \quad (10)$$

Knowing the measurement uncertainties for the initial diameter,  $dD_0 = \pm 0.025 \text{ mm} (\pm 0.001 \text{ in})$ , and the uncertainty in the measured diameter from the data in Fig. 6,  $dD = \pm 0.17 \text{ mm} (\pm 0.007 \text{ in})$ , the maximum magnitude of the error in the strain can be estimated using equation (10) (Fig. 7).

At low strains, the uncertainties in the measurements of  $D$  and  $D_0$  are large compared with the magnitude of the

strain. The maximum error at low strain is  $\pm 0.05$ . As  $D$  increases, the uncertainties in  $D$  and  $D_0$  remain constant, and therefore the magnitude of the error at large strain decreases. Equation (10) also indicates that, if the magnitudes of  $dD$  and  $dD_0$  are constant, then the uncertainty in the strain,  $de$ , will be reduced if larger diameter specimens are tested. By increasing the specimen size to 12.7 mm (0.500 in) the maximum error is reduced to  $\pm 0.03$ .

## 5 DISCUSSION

The strain rates shown in Fig. 4 peak at about  $10^4 \text{ s}^{-1}$ . These peak rates are comparable in order of magnitude with average rates calculated by Whiffen [2]. Very much higher rates would be expected at the beginning of the event, near the impact end of the rod. However, the frames (shown in Fig. 2) selected for analysis were chosen for computational convenience to be relatively widely separated in time. Additional computations based on a very high framing rate (about  $10^6$  frames/s) and focused on initial impact would be expected to show a substantially higher peak strain rate.

Taylor has a plastic deformation front that propagates along the rod as a discontinuity in cross-sectional area and,

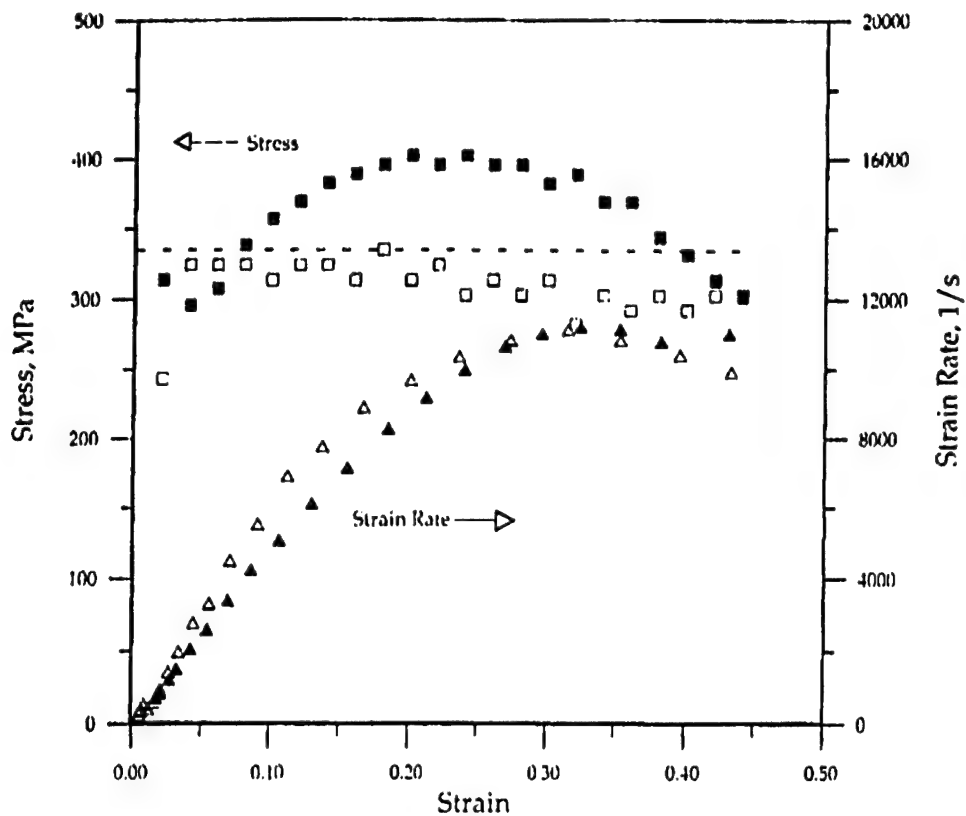


Fig. 4 Stress and strain rate versus strain for the OFE copper of specimen UK-145: ■, data obtained using strain profiles at times 33.3 and 63.3  $\mu$ s; □, data obtained using strain profiles at time 63.3 and 79.9  $\mu$ s; - - -, stress calculated using Taylor's [1] original analysis

Table 1 Plastic wave speeds

Areal strain	Velocity (m/s) for the following time intervals	
	63.3-33.3 $\mu$ s	79.9-63.3 $\mu$ s
0.02	128.3	114.5
0.04	123.3	138.6
0.06	126.7	138.6
0.08	135.0	138.6
0.1	140.0	135.5
0.12	143.3	138.6
0.14	146.7	138.6
0.16	148.3	135.5
0.18	150.0	141.6
0.2	151.7	135.5
0.22	150.0	138.6
0.24	151.7	132.5
0.26	150.0	135.5
0.28	150.0	132.5
0.3	146.7	135.5
0.32	148.3	126.5
0.34	143.3	132.5
0.36	143.3	129.5
0.38	136.7	132.5
0.4	133.3	129.5
0.42	128.3	132.5
0.44	125.0	132.5
0.46	116.7	138.6

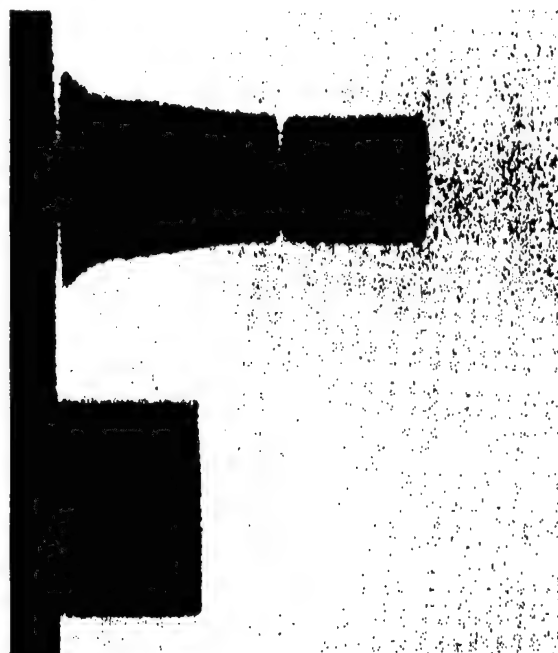


Fig. 5 One frame from the photographic record of the Taylor impact test of specimen SC-06. In the photograph the anvil face is to the left and the deformed specimen has just begun to rebound to the right. Also shown is the obturator (upper right) separating from the specimen and the fiducial (lower left)

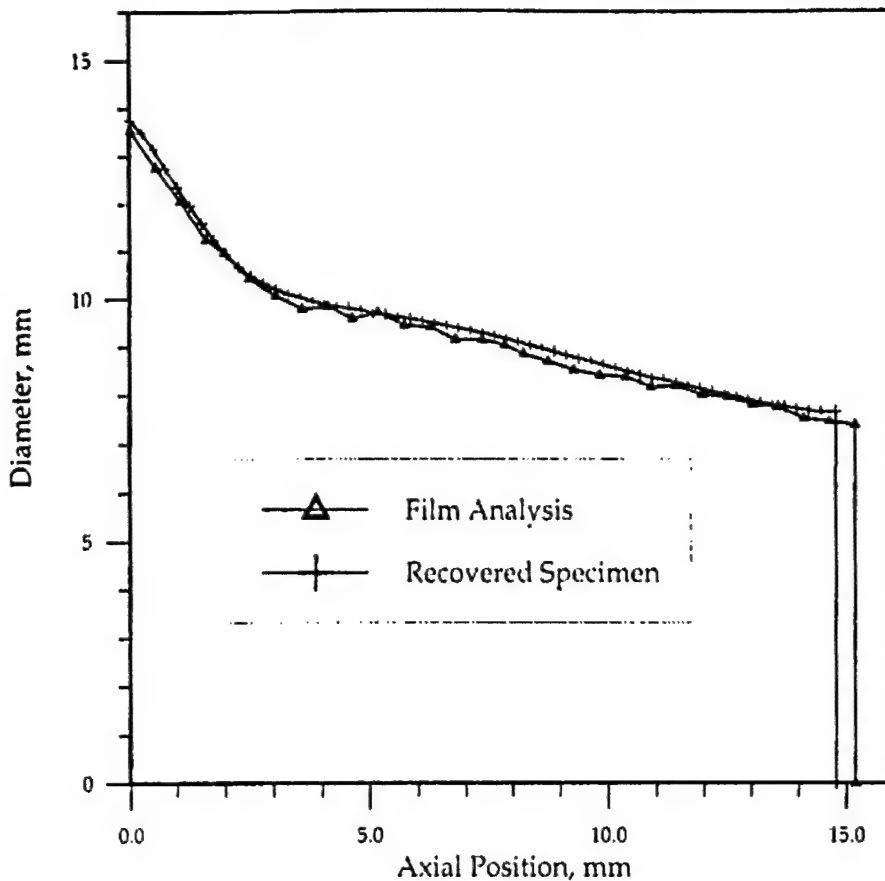


Fig. 6 Comparison of the deformed profile of specimen SC-06 as determined by film analysis and by direct measurements

consequently, in areal strain. In such a case the strain rate would be infinite. In actuality, the strain rate must build up from zero ahead of the front to some finite maximum value and then drop back to zero. Evidence of this behaviour can be seen in Fig. 4. From equation (4) and the information gathered on the first time interval (full triangles) the strain rate increases by two orders of magnitude as the strain varies from 1 to 30 per cent. Above 30 per cent the strain rate is relatively constant.

Decreases in rate at large strain are not observed until the second time interval is analysed (open triangles). The decrease occurs in material close to the impact face. Curves of strain rate versus strain for the two time intervals are, otherwise, remarkably alike.

Also shown in Fig. 4 are stress versus strain results. For the first time interval (full squares) the stress given by equation (7) initially increases as strain increases. At low strains, the stress is nearly equal to the quasi-static yield strength (300 MPa). As the strain reaches 0.20, the stress has increased to 400 MPa. Between the strains of 0.20 and 0.28, the stress is nearly constant. For strains above 0.28, the stress decreases, reducing to 300 MPa at a strain of 0.44. With the back end speed  $u$  equal to a constant, the variation in stress must be attributed to the change in the plastic wave speed  $v$  (see Table 1, second column). Most of

the stress values exceed that calculated from Taylor's original analysis (335 MPa).

The stress for the second time interval (open squares) is nearly constant for strains between 0 and 0.20. Above a strain of 0.20, the stress decreases from 315 to 300 MPa. These stress values fall below those calculated using data from the first time interval, and below that calculated using Taylor's original analysis.

The variations in stress calculated using equation (7) result from the assumptions contained in the analysis. Taylor assumes that a plastic-rigid interface exists in the deforming specimen, this interface being a discontinuity in cross-sectional area. Material that crosses from the rigid rod segment into the plastic region is assumed to flow instantaneously to its final position. The data in Fig. 2 or Fig. 3 show that this discontinuity does not exist. Furthermore, the material particle velocity is not zero as it enters the plastic region. The particle velocity would have some axial and radial components that would vary with time in accordance with the local stress state and constitutive behaviour. When the strain rate reaches a maximum in Fig. 4, at a strain of 0.30, the radial velocity component is for that plane (at that time) reaching its peak value.

The second assumption is that the rigid-plastic interface

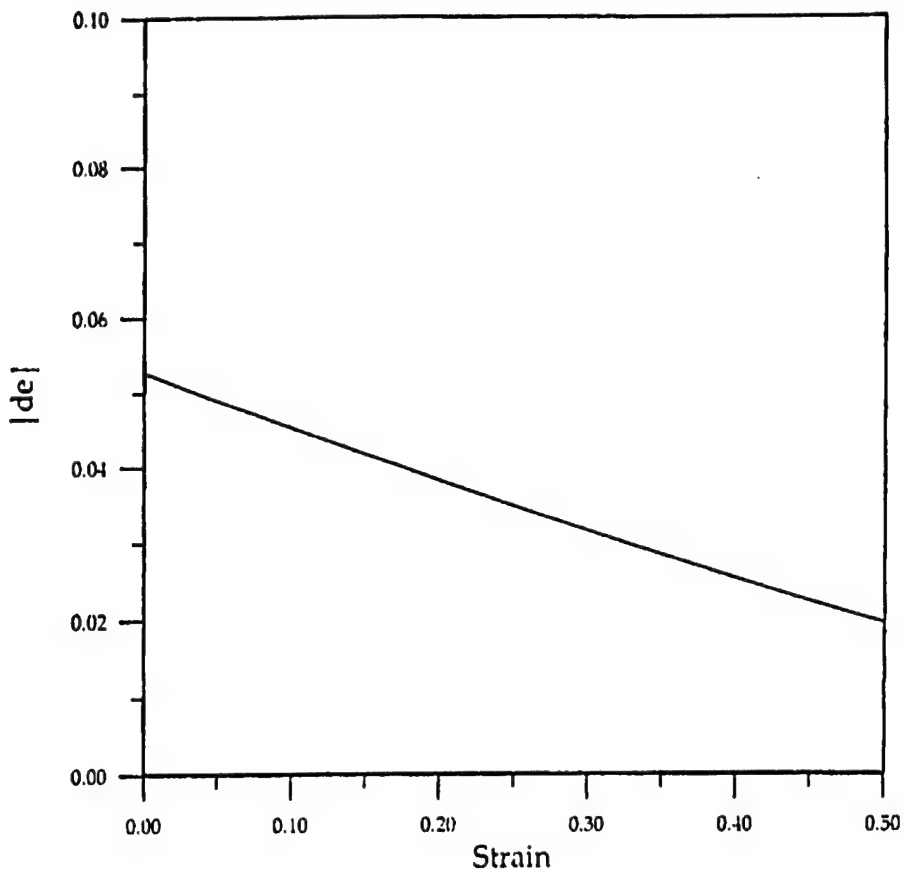


Fig. 7 Maximum magnitude of the uncertainty in the strain deduced from the film analysis

moves at a constant speed. Taylor makes this assumption in order to define the history of the interface motion relative to the final dimensions of the recovered specimen. The velocity of the interface,  $v$ , is eliminated from equation (7) in favour of specimen geometry parameters [see Taylor's equation (22)]. Ignoring the fact that the interface, as defined by Taylor, does not exist, the data in Table 1 show that the wave speeds are not constant. The drop in stress calculated for the second time interval results from a lower value of back-end speed  $u$  and overall lower values of plastic wave speeds  $v$ .

Taylor's analysis that leads to the dashed line in Fig. 4 assumes a rigid-plastic material, i.e. a material having a single value of flow stress. This value must naturally be an average of the varying values exhibited by a real material as strain and strain rates vary. As shown in the figure, the (constant) Taylor value approximately averages the high stress for early deformation and the lower stress that occurs later.

Improving the constitutive analysis of the type developed by Taylor requires more detailed understanding of the motion of material inside the plastic zone. Adding high-speed photography to the experimental diagnostics has provided strain information with an estimate of the strain rate. These data alone provide insight into the constitutive behaviour by way of the motion of material in the plastic zone. Additional sources for data are experimental tech-

iques that track particle position in the specimen and analysis of the impact experiment using finite-element-based representation.

## 6 CONCLUSIONS

High-speed film data of the Taylor impact experiment when properly analysed can provide additional information on the constitutive properties of material under high-strain-rate conditions. Analysis of images from test UK-145 have provided estimates of the stress, strain and strain rate. In this report an interpretative analysis similar to Taylor's was used to find the stress. For the drawn OFE copper the calculated stresses ranged from 300 to 400 MPa. Approximate strain rates for the experiment were determined by differencing strain profiles at different times. The peak strain rate was  $11\,000\text{ s}^{-1}$ . The strain rate data indicate that a wide range of rates occur in the plastically deforming region of the specimen material.

## ACKNOWLEDGEMENTS

The authors acknowledge the support of the US Air Force Research Laboratory, Munitions Directorate, Eglin Air

Force Base, Florida, the technical assistance of Leonard L. Wilson and Harold Gilliland and many helpful discussions with Dr Paul Maudlin of Los Alamos National Laboratory.

## REFERENCES

- 1 **Taylor, G. I.** The use of flat-ended projectiles for determining dynamic yield stress. I: theoretical considerations. *Proc. R. Soc. Lond. A*, 1948, **194**, 289-299.
- 2 **Whiffen, A. C.** The use of flat-ended projectiles for determining dynamic yield stress. II: test on various metallic materials. *Proc. R. Soc. Lond. A*, 1948, **194**, 300-322.
- 3 **Carrington, W. E. and Gayler, M. L. V.** The use of flat-ended projectiles for determining dynamic yield stress. III: changes in microstructure caused by deformation under impact at high-striking velocities. *Proc. R. Soc. Lond. A*, 1948, **194**, 323-331.
- 4 **Hawkyard, J. B.** A theory for the mushrooming of flat-ended projectiles impinging on a flat rigid anvil, using energy considerations. *Int. J. Mech. Sci.*, 1969, **11**, 313-333.
- 5 **Jones, S. E., Gillis, P. P. and Foster Jr, J. C.** On the equation of motion of the undeformed section of a Taylor impact specimen. *J. Appl. Physics*, 1987, **61**, 499-502.
- 6 **Hamstad, M. A. and Gillis, P. P.** Effective strain rates in low-speed uniaxial tension tests. *Mater. Res. Stand.*, 1966, **6**, 569-573.
- 7 **House, J. W., Wilson, L. L. and Nixon, M. E.** High strain-rate material behavior using Taylor anvil experiments. In *Proceedings of the Sixth International Conference on The Mechanical Behavior of Materials*, Kyoto, Japan, 1991, Vol. 1, pp. 343-349.

## **APPENDIX F**

**VALIDATING THE HIGH STRAIN-RATE STRENGTH ESTIMATES  
GENERATED FROM HIGH-SPEED FILM DATA AND A REVISED  
ELEMENTARY THEORY FOR THE TAYLOR IMPACT TEST**

**John D. Cinnamon, Captain, US Air Force**  
Department of Astronautics  
US Air Force Academy, Colorado

**J. W. House, Materials Scientist**  
USAF Research Laboratory, Armament  
Directorate, Eglin Air Force Base, Florida

**S. E. Jones, University Research Professor**  
Dept of Aerospace Engineering and Mechanics  
University of Alabama, Tuscaloosa, Alabama

**W. K. Rule, Senior Engineer**  
SCP Global Technologies, Boise, Idaho

**ABSTRACT**

An elementary theory describing the Taylor Impact Test is revised in this paper to utilize high-speed film data. This approach generates high strain-rate strength estimates for materials undergoing high-speed deformation. First, film data from the Taylor Impact Test, at a rate of  $\frac{1}{2}$  million frames per second, is reduced using computer image analysis. This film data is utilized to validate assumptions made about transient and steady state impact behavior in the deformation event. The film data is then used in the theoretical model to create strength estimates.

**LIST OF SYMBOLS AND ABBREVIATIONS**

$\beta$	dimensionless ratio
$\rho$	specimen density
$\sigma$	dynamic stress
$\sigma_0$	constant reference stress
$\sigma_s$	quasi-static stress
$A$	current cross-sectional area
$A_0$	initial cross-sectional area
$e$	compressive engineering strain
$h$	deformed section length

The resulting strength estimates are validated utilizing post-test specimen measurements in conjunction with the EPIC code. A revised form of the Johnson-Cook Strength model is then utilized in the EPIC calculations to force a match between the calculated post-test specimen geometry and the actual post-test measurements. The dynamic stress versus strain-rate diagrams (at constant strain) developed from the elementary theory and the EPIC code agree extremely well.

$\ell$	undeformed section length
$L$	current specimen length
$L_0$	undeformed specimen length
$m$	slope of a linear fit
$s$	displacement of back end of specimen
$u$	velocity of the plastic wave front
$v$	current velocity of specimen back end
$v_0$	initial (impact) velocity of specimen

## INTRODUCTION

The Taylor test (Taylor, 1948; Whiffen, 1948) is a high strain rate impact test, which can produce strain-rates of  $10^4$  to  $10^5$  per second and higher. In 1998, Jones, *et al.*, introduced an elementary theory to describe the Taylor impact test. This approach described the event as being comprised of an initial transient phase followed by a quasi-steady state phase. This process can be modeled one-dimensionally, especially for low caliber specimens.

In this paper, film of the impact event is reduced to validate several aspects of the theory presented by Jones, *et al.* (1998). In addition, the elementary theory is slightly modified to utilize available high-speed film frames of the event. The film data can be used in the one-dimensional model to produce dynamic strength estimates for the specimen material.

An independent method of validating the stress and strain rates generated by the one-dimensional model is presented using the EPIC code and post-test specimen measurements. Rule and Jones (1998), outlines this approach in detail. The material properties can be independently determined by forcing the EPIC code to match the post-test measurements. These results agree with those provided by the one-dimensional model and the film record very well.

## AN ELEMENTARY THEORY

The elementary theory for the Taylor impact test from Jones, *et al.* (1998) is reviewed here. The theory is a one-dimensional analytical approach to the impact event. Specific details of this theory is available in Jones, *et al.* (1998). The equations are modified to present time to utilize the available high-speed film data analyzed in this paper. This iteration is based on a continual effort to refine our understanding of the impact event (House, 1989; Jones, *et al.*, 1987; Jones, *et al.*, 1991; Wilson, *et al.*, 1989; Cinnamon, *et al.*, 1991). The goal of this effort is to estimate the state of stress of the specimen material at high strain rates.

The impact event is divided into two basic phases. The first is an initial transient phase, and the second is a quasi-steady phase that includes the terminal transient.

As detailed in Jones, *et al.* (1998), analysis of the plastic wave front leads to an equation of motion, which takes the form

$$\epsilon \dot{\ell} = v - u = (1 - \beta)v \quad (1)$$

where  $\epsilon$  is the compressive engineering strain on the plastic wave front,  $\ell$  is the current undeformed section length,  $v$  is the velocity of the undeformed section,  $u$  is the velocity of the plastic wave front, and  $\beta = u/v$  (see Figure 1.). Dots over the variables denote differentiation with respect to time. The engineering strain behind the deformation front,  $\epsilon$ , can be expressed in terms of the change in area across the front,  $\epsilon = (A_0/A) - 1$ , where  $A_0$  and  $A$  are the initial and current cross-sectional areas of the specimen, respectively.

The primary focus of Jones, *et al.* (1998) was to estimate the state of stress for the material from post-test measurements. In this paper, a reduction of the high-speed film record taken during the impact event can provide this data directly. We will return to a post-test approach later in this presentation to validate our results.

The dynamic stress behind the deformation front is given by

$$\sigma = (1 + \epsilon) \left[ \sigma_0 + \frac{(1 - \beta)^2}{\epsilon} \rho v^2 \right] \quad (2)$$

where  $\sigma_0$  is a constant reference stress and  $\rho$  is the specimen density (Jones, *et al.*, 1998). The reference stress can be calculated from

$$\sigma_0 = \frac{\sigma_s(\epsilon)}{(1 + \epsilon)} \quad (3)$$

where  $\sigma_s(\epsilon)$  is the quasi-static stress at the indicated strain.

An estimate for the strain-rate of the deforming specimen at the wave front based on Taylor's original estimate (1948), takes the form

$$\dot{\epsilon} = \frac{-v}{L_0 - \ell}. \quad (4)$$

This estimate is especially good immediately after the initial transient (Jones, *et al.*, 1995). Equations (1-4) form the foundation for a theory that allow us to examine the Taylor test from a different perspective

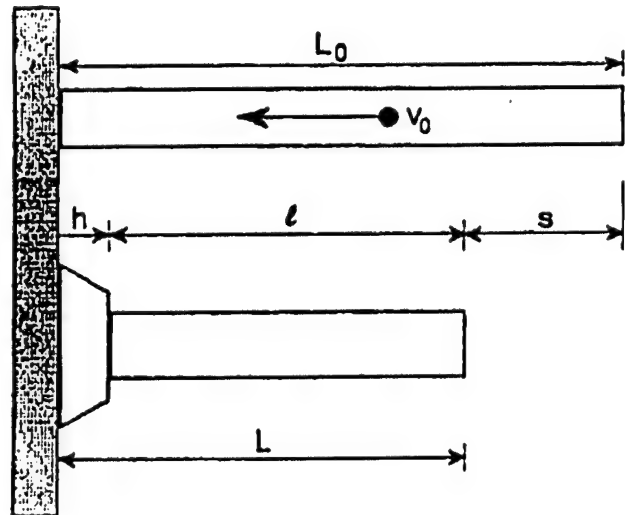


Figure 1. A uniform cylinder of length  $L_0$  impacts an uncompliant target with velocity  $v_0$ . Subsequent deformation is modeled using undeformed section length,  $\ell$ ; deformed section length,  $h$ ; and current rod length,  $L$ . The displacement of the back end of the specimen is  $s$ .

THIS  
PAGE  
IS  
MISSING  
IN  
ORIGINAL  
DOCUMENT

## FILM REDUCTION OVERVIEW

In many of the approaches to date, the models rely on post-test measurements to generate strength estimates. A unique opportunity exists if film data can be used to analyze the event as it progresses.

In some Taylor tests, high-speed film data is available to examine the impact event. Details of this can be found in House (1989) and Wilson, *et al.*, (1989). Obtaining usable data can be a challenge, due to the significant number of variables in the test. In this paper, we take our best film record (SC-102, OFE as received Copper) to perform the measurements.

The film data is available at various speeds. This particular shot was taken at 500,000 frames per second. A typical frame appears in Figure 2.

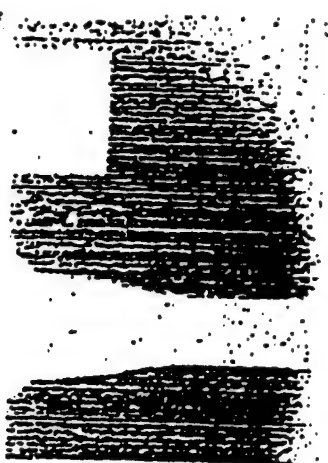


Figure 2. A typical frame from the film record of the Taylor impact test. The specimen is the lower object deforming against the anvil face to the left. A magnet of known dimension (fiducial) appears above the specimen for calibration.

From the film, it is possible to calculate a significant number of the parameters of interest. Figure 3 highlights two of measurements that are available from a specimen. These parameters can be measured from the film at any time interval at a fixed level of strain.

## FILM REDUCTION

Making measurements from the film data is a time consuming process. The steps we followed to produce our results were as follows.

First, the film was taken of the impact event. The Cordon camera (House, 1989; Wilson, *et al.*, 1989) setup allows for 82 unique frames of data (although some additional frames are available as some of the initial frames are overwritten at the end of the process). The film is then developed into slide strips using traditional wet film developing.

At this point, the frames were scanned into a computer using the highest resolution available (1200 pixels per inch). A typical frame (after being cropped) turned out to be about 890 pixels by 1350 pixels. Obviously this conversion reduces the accuracy of the film data. However, our ability to measure this data is significantly enhanced when the film data is in a digital form.

Once the film is in a computer graphics file, measurements are possible. The measurements were made using Scion Image for Windows (1998). The process begins when the pre-impact frames are measured. The calibration of the measurements is the critical initial step. On each frame, the vertical length of the magnet is measured and checked against the known vertical length of the undeformed specimen. By verifying these two measurements match is a validation of the edge choice. That is, an incorrect edge choice would lead to setting an incorrect pixels/inch value in the vertical direction, and thereby leading to an erroneous measurement for the known vertical length of the specimen. After this measurement was taken, the horizontal length of the magnet is taken, setting another pixels/inch conversion in that direction. This is necessary due to fact that the film plane has some distortion between the vertical and horizontal directions. With these calibration measurements, the software now knows how many pixels are in each inch in each direction - Scion Image refers to this difference as an aspect ratio.

At this point, the images can be examined and data concerning the impact can be gathered. By choosing a particular number of pixels in the vertical direction, we can look at the plastic wave at a particular strain value. Once we have decided what strains to look at, the measurements are fairly straightforward.

Measuring film in this manner has some significant limitations. One of the primary limitations is the time required to analyze a single event. The authors were unable to devise any form of automation that might accelerate the process.

Secondly, as in any image analysis, the topic of edge definition and the threshold values for choosing an edge is problematic. The fiducial increases our confidence in a reliable and reproducible technique. This data reduction does, however, lead to scatter in the data. But, the results are reasonable given the limitations inherent in this optical approach.

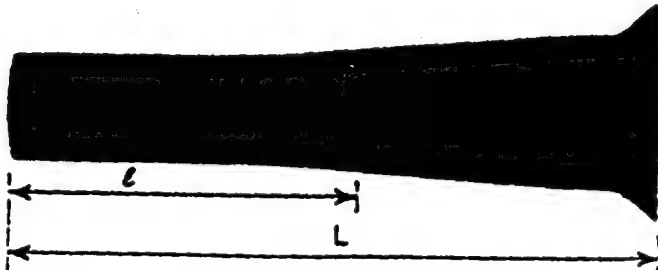


Figure 3. A typical deformed specimen with the undeformed section length,  $l$ , at a chosen strain level, and the current overall specimen length  $L$ .

## RESULTS

The first frames of data provide us with a verification of the impact velocity and allow another validation of our film reduction techniques. As the deformation occurs, we can measure mushroom diameter, the cross-sectional area of the mushroom, and plastic wave position,  $h$ .

With the cross-sectional area of the mushroom, we can calculate the total volume of the mushroom behind the plastic wave. Knowing this information, we can calculate the position of the back end, despite it being off of the film frame. The velocity of  $h$  is  $u$ , and the velocity of the back end,  $\dot{h}$ , is  $v$ .

One of the primary assumptions about the transient phase of this one-dimensional analysis is that  $v$  does not begin decreasing during this phase. Our film analysis showed that this was, in fact, observable until about 60 microseconds into the event.

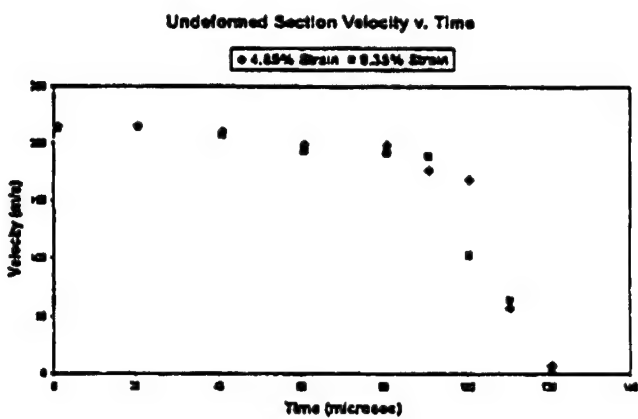


Figure 4. Undeformed section velocity versus time.

Figures 4 and 5 illustrate the information available from film reduction. Figure 4 demonstrates that the assumption that  $v$  remains fairly constant for the transient phase of the event is valid. Figure 5 shows the progression of the various measurements during the event.

Also available from the film measurements is a verification of the linearity between  $\ell/L_0$  and  $L/L_0$  during the impact. This relationship was extensively used in Jones, *et al.* (1998). Figures 6 and 7 clearly show this linearity for both of the strain levels we investigated in this paper.

Based on these measurements from the film data, we can produce estimates of the stress and strain-rate during the event. From Jones, *et al.* (1998), we can use the linearity between  $\ell/L_0$  and  $L/L_0$  to compute the constant  $\beta$ , where

$$\beta = 1 + me \quad (5)$$

and  $m$  is the slope of the linear fit between  $\ell/L_0$  and  $L/L_0$ .

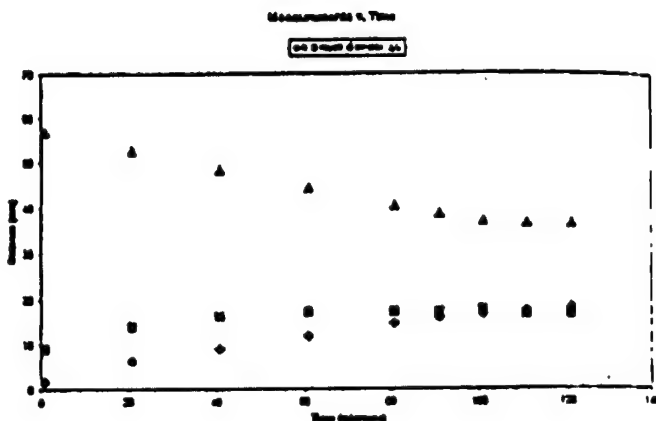


Figure 5. Various measurements from the film during the Taylor Impact Test

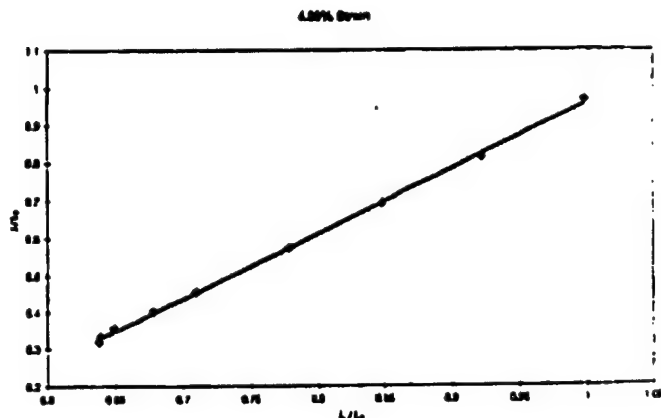


Figure 6. Linearity of  $\ell/L_0$  versus  $L/L_0$  for 4.85% Strain

At this point, we can reduce equations (2) and (3) to

$$\sigma = \sigma_s + \frac{(1+e)(1-\beta)^2}{e} \rho v^2 \quad (6)$$

where  $\sigma_s$  is taken to be 290 MPa for 4.85% strain and 295 MPa for 9.35% strain, and  $\rho$  is the material density.

The strain-rate can be estimated from equation (4). With equations (4) and (6), we can construct the stress versus strain-rate diagrams for the event.

To provide a comparison to the data generated from the film record and the one-dimensional theory presented in Jones,

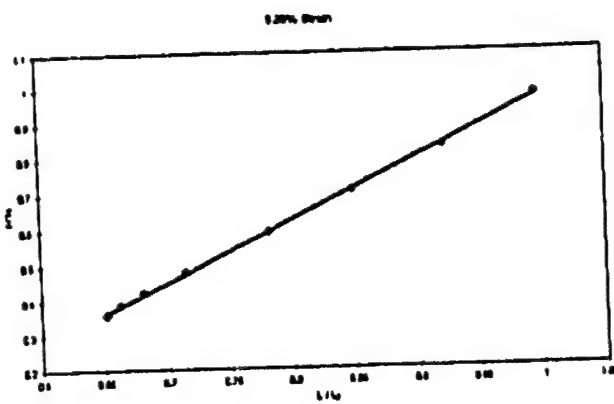


Figure 7. Linearity of  $\ell/L_0$  versus  $L/L_0$  for 9.35% Strain

et al., (1998), we consider the post-test analysis given in Rule and Jones (1998). This approach can be summarized as a modification of the Johnson-Cook strength model (Johnson and Cook, 1983) to accommodate high strain-rate behavior of the material. Rule and Jones (1998), use post-test measurements of Taylor specimens and an optimizer to force the EPIC code to reproduce these post-test measurements after modeling a known impact. With this technique, a set of empirical coefficients can be derived that allow this matching to post-test geometry. These coefficients form the basis of the revised form of the Johnson-Cook strength model, which takes the form

$$\sigma = (C_1 + C_2 \epsilon'') \left[ 1 + C_3 \ln \epsilon' + C_4 \left( \frac{1}{C_5 - \ln \epsilon'} - \frac{1}{C_5} \right) (1 - T^M) \right] \quad (7)$$

A complete explanation of the empirically derived constants  $C_1, \dots, C_5, N$ , and  $M$  can be found in Rule and Jones (1998). This equation allows us to generate an independent stress versus strain-rate diagram that can be used for comparison with the one-dimensional model.

Figures 8 and 9 are the result of this comparison. The discrete data points are those taken from film frames and analyzed using the one-dimensional model. The continuous curve is the revised Johnson-Cook model described in Rule and Jones (1998) for the same material. The revised Johnson-Cook model does prescribe a maximum stress value that does not appear in these figures.

The figures demonstrate remarkable agreement between the film reduction and the revised Johnson-Cook model. In addition, the curves have the form that we would expect, with the stress increasing dramatically as strain-rates exceed  $10^4/s$ .

#### CONCLUSIONS AND RECOMMENDATIONS

In this paper, we examined a technique to use film of the Taylor Impact event to create stress versus strain-rate diagrams.

This approach was very time consuming. Developing a way to expedite this data reduction will be one of our next efforts to continue analyzing available film data.

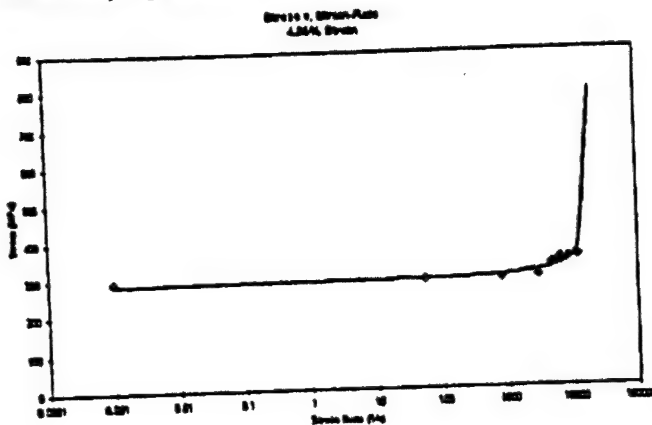


Figure 8. Stress versus Strain-Rate at 4.85% Strain for Copper

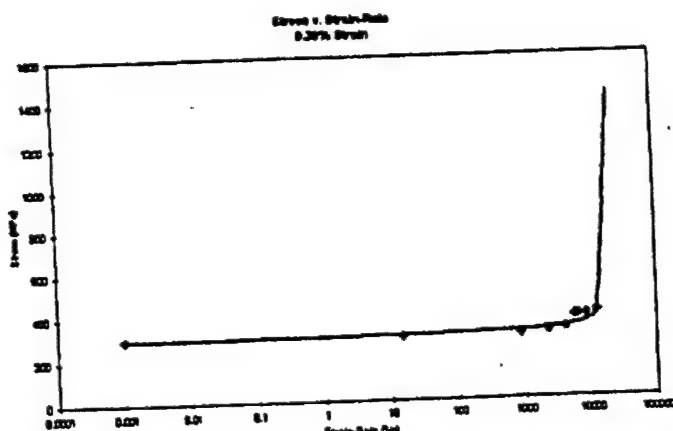


Figure 9. Stress versus Strain-Rate at 9.35% Strain for Copper

Generating good film data is another challenge. We need to increase our resolution of the impact event. One way is to change the lens on the camera to effectively zoom in on the plastic wave front – perhaps by assuming symmetrical deformation and only looking at one side of the centerline of the specimen. Another way is to find a better optical scanning technique to gain all we can from the film frames. A final way is to focus on increasing the contrast created on the film so that edge detection is an easier process.

Additional efforts in this technique will also involve examination of additional shots of Copper and other materials.

Despite our current limitations, we were able to produce remarkable results. This approach further emphasizes the validity and usefulness of the Taylor Impact Test in generating strength estimates at high strain-rates.

## REFERENCES

Cinnamon, J. D., Jones, S. E., Foster, J. C., Jr., and Gillis, P. P., 1991, "An Analysis of Early Time Deformation Rate and Stress in the Taylor Impact Test," *Mech Beh of Mat - VI, Proc of Sixth Inter Conf*, Vol 1.

House, J. W., 1989, "Taylor Impact Testing," *Technical Report, AFATL-TR-89-41*, AD-A215 018.

Johnson, G. R. and Cook, W. H., 1983, "A Constitutive Model and Data for Metals Subjected to Large Strains, High Strain Rates, and High Temperatures," *Proc. 7th International Symposium on Ballistics*, The Hague, The Netherlands.

Jones, S. E., Gillis, P. P., and Foster, J. C., Jr., 1987, "On the Equation of Motion of the Undeformed Section of a Taylor Specimen," *J. Appl. Phys.* 61(2), 15.

Jones, S. E., Gillis, P. P., Foster, J. C., Jr., and Wilson, L. L., 1991, "A One-Dimensional, Two-Phase Flow Model for Taylor Impact Specimens," *J. Eng. Mater. Technol. (Trans. ASME)* 113, 228.

Jones, S. E., Maudlin, Paul J., and Foster, J. C., Jr., 1995, "Constitutive Modeling Using the Taylor Impact Test," in *High Strain Rate Effects on Polymer, Metal and Ceramic Matrix Composites and Other Advanced Materials*, Y. D. S. Rajapakse and J. R. Vinson, eds., ASME, AD-Vol. 48, 161-166.

Jones, S. E., Drinkard, J. A., Rule, W. K., and Wilson, L. L., 1998, "An Elementary Theory for the Taylor Impact Test," *Int. J. Impact Engng*, Vol. 21., Nos. 1-2, pp. 1-13.

Rule, W. K. and Jones, S. E., 1998, "A Revised Form for the Johnson-Cook Strength Model," *Int. J. Impact Engng*, 21 (8), 609.

*Scion Image for Windows.* 1998. Release Beta 3b. Scion Corporation, 82 Worman's Mill Ct., Suite H, Frederick, MD 21701. Phone: (301) 695-7870. FAX: (301) 695-0035. eMail: [info@scioncorp.com](mailto:info@scioncorp.com). Web Site: <http://www.scioncorp.com>

Taylor, G. I., 1948, "The use of flat-ended projectile for determining dynamic yield stress I. Theoretical considerations," *Proc. Roy. Soc. London A*, 194, 289.

Whiffen, A. C., 1948, "The use of flat-ended projectile for determining dynamic yield stress II. Tests on various metallic materials," *Proc. Roy. Soc. London A*, 194, 300.

Wilson, L. L., House, J. W., and Nixon, M. E., 1989, "Time Resolvable Deformation from the Cylinder Impact Test," *Technical Report, AFATL-TR-89-76*.

---

## **APPENDIX G**

## AN ESTIMATE FOR STRAIN-RATE IN THE TAYLOR IMPACT TEST

S. E. Jones<sup>1</sup>, L. L. Wilson<sup>2</sup>, and William K. Rule<sup>3</sup>

1. Senior Scientist, U.S. Air Force, Eglin AFB, FL, (on leave from the University of Alabama), 2. Senior Engineer, SAIC, Eglin AFB, FL,  
3. Software Analyst/Engineer, Trus Joist MacMillan, Boise, Idaho.

**ABSTRACT-** Many ductile metals exhibit a large increase in yield strength as a critical high strain-rate is approached. Modeling the performance of rapidly loaded structures constructed from such materials requires a prediction of stress versus strain-rate behavior that includes this strengthening phenomenon. This paper describes an approach to obtain a function to predict high strain rate behavior from a single Taylor impact test specimen. Results are provided for OFHC copper.

**INTRODUCTION:** In order to simulate many high-speed events, mechanical properties of the materials involved at elevated strain-rates must be found. For example, impact and penetration problems frequently require the state of stress at strain-rates exceeding  $10^4$ /sec. Acquiring this information is a challenging problem. The most reliable method for determining the state of stress at high strain-rates is the Split-Hopkinson Pressure Bar experiment. But, it is generally acknowledged that  $10^4$ /sec is the limiting strain-rate for this experiment. At the same time, most metals are very sensitive to rate in the neighborhood of  $10^4$ /sec, which makes testing difficult.

The Taylor impact test (Taylor [1948]) presents an opportunity to easily achieve strain-rates in excess of  $10^4$ /sec. The challenge, in this case, is reducing the data to acquire mechanical properties. Over the past few years, this problem has been extensively studied. The solutions fall into two basic categories: one-dimensional models (e.g., Taylor [1948]; Hawkyard [1969]; or Jones, et al [1997]) and computer-aided solutions (e.g., Johnson and Holmquist [1988]; or Rule and Jones [1998]). Both categories have their advantages. One-dimensional analyses can predict the state of stress with no implicit assumption about the mathematical structure of the constitutive behavior of the material involved. However, there are simplifying assumptions to bring the problem to one-dimension and limits on its applicability. The computer-aided solution has fewer limits on its applicability, but assumptions must be made regarding the mathematical structure of the constitutive equation before any computation can be made. In this paper, we focus on one-dimensional modeling and present a new estimate for strain-rate.

### STRAIN-RATE ESTIMATE AND RESULTS FOR OFHC COPPER:

Consider a Taylor cylinder after the initial transient has been completed (see Jones, et al [1991]). The velocity-dependent undeformed section length  $\ell$  is given by

$$\ell = \bar{\ell} \exp \left\{ -\frac{\rho(1-\beta)}{2e\sigma_0} (v_0^2 - v^2) \right\} \quad (1)$$

where  $\rho$  is the specimen density,  $e$  is the engineering strain at the deformation front,  $\beta$  is a parameter related to the velocity change across the deformation front,  $v_0$  is the specimen impact speed,  $v$  is the current speed of the undeformed section, and  $\bar{\ell}$  is the undeformed section length at the end of the initial transient. A discussion of this result is contained in Jones, et al [1997]. The velocity-dependent normal stress at the deformation front is

$$\sigma = (1+e) \left( \sigma_0 + \frac{(1-\beta)^2}{e} \rho v^2 \right) \quad (2)$$

where  $\sigma_0$  is a reference stress related to the yield stress of the specimen material at strain  $e$ . We will use these estimates for stress and undeformed section length to produce an estimate for velocity-dependent strain-rate.

Consider an increment  $\Delta\ell$  of the undeformed section that is undeformed at time  $t$ , but is deformed at time  $t + \Delta t$ . The velocity of the increment at time  $t$  is  $v$ , but at time  $t + \Delta t$  the velocity is  $u$ . This means that the change in kinetic energy during this period of time is

$$\Delta KE = \frac{1}{2} \rho A_0 \Delta \ell v^2 - \frac{1}{2} \rho A_0 \Delta \ell u^2 = \frac{1}{2} \rho A_0 \Delta \ell (v^2 - u^2). \quad (3)$$

We assume that all of the available energy goes into deforming the specimen material and that this work  $W$  is given by

$$W = \int_V \left( \int \sigma d\varepsilon \right) dV \cong A_0 \Delta \ell \int \sigma d\varepsilon \quad (4)$$

where  $V$  is the volume of deformed material and  $\varepsilon$  is the longitudinal engineering strain. The integral in Eqn. (4) can be transformed and approximated using the mean value theorem and the equation of motion for the undeformed section. The equation of motion is

$$\rho \dot{v} = \sigma_0 \quad (5)$$

which means that

$$dt = \frac{\rho \ell}{\sigma_0} dv. \quad (6)$$

Now,

$$\int \sigma d\varepsilon = \int_{v}^{v+\Delta v} \sigma \frac{d\varepsilon}{dt} dt = \int_{v}^{u} \sigma \frac{d\varepsilon}{dt} \frac{\rho \ell}{\sigma_0} dv = (u - v) \sigma(v^*) \frac{\rho \ell(v^*)}{\sigma_0} \frac{d\varepsilon}{dt}(v^*) \quad (7)$$

where  $v^*$  is a velocity between  $u$  and  $v$ . Using this equation in Eqn. (4), equating the result to Eqn. (3), and solving for  $d\varepsilon/dt(v^*)$  leads to

$$\frac{d\epsilon}{dt}(v^*) = -\frac{\sigma_0}{2} \frac{u+v}{\sigma(v^*)\ell(v^*)} \quad (8)$$

as an estimate for the strain-rate at the deformation front. If we approximate  $v^*$  by  $(u+v)/2$ , the average velocity between  $u$  and  $v$ , then we can see that

$$\frac{d\epsilon}{dt}(v^*) = -\frac{\sigma_0 v^*}{\sigma(v^*)\ell(v^*)} \quad (9)$$

or

$$\frac{d\epsilon}{dt}(v) = -\frac{1}{(1+e)\ell} \frac{v \exp\left\{\frac{\rho(1-\beta)}{2e\sigma_0}(v_0^2 - v^2)\right\}}{1 + \frac{(1-\beta)^2}{e\sigma_0} \rho v^2} \quad (10)$$

where dependence on  $v^*$  was replaced by dependence on  $v$ , with no loss. Equation (10) is the velocity-dependent strain-rate estimate.

A Taylor test was conducted using an OFHC copper specimen with the properties shown in Table 1. As described previously (Jones et al. [1997]), the dynamic properties determined for this specimen are given in Table 2.

Table 1: OFHC Copper Taylor Specimen Properties

Impact Velocity = 212 m/s	Initial Length = 0.0314 m
Initial Diameter = 0.00417 m	Density = 8910 kg/m <sup>3</sup>
$\sigma_0 (e = -0.036) = -292.5$ MPa	$\sigma_0 (e = -0.058) = -305.7$ MPa
$\sigma_0 (e = -0.112) = -332.2$ MPa	

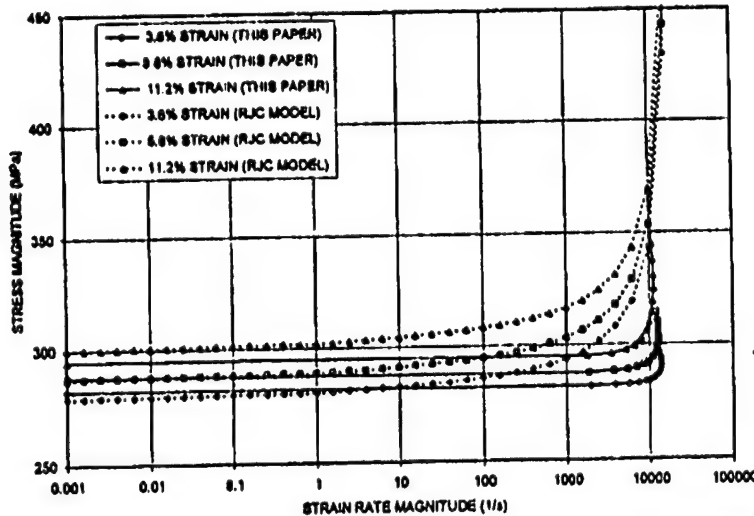
Table 2: Dynamic Properties of the Taylor Impact Specimen

$e$	$\bar{\ell}$	$\beta$
-0.036	0.0158	0.9434
-0.058	0.0170	0.9125
-0.112	0.0195	0.8480

Equations (2) and (10) were then employed (with the data of Tables 1 and 2) to calculate stresses and strain-rates, respectively, as a function of undeformed section velocity  $v$ . The stress versus strain-rate results are shown in the Fig. below for the three strain levels. The undeformed section velocity was allowed to vary between 0 and 212 m/s (initial impact velocity) to create these plots.

For comparison, the Fig. below also shows stress versus strain-rate plots for the Revised Johnson Cook (RJC) model obtained by Rule and Jones (1998). The RJC model results were obtained using a hybrid numerical-experimental technique where the EPIC finite element code was employed to reduce the data

from 14 Taylor specimens (including the one considered above) using an assumed form for the stress versus strain-rate function. Thus, the RJC results provide an independent check of the accuracy of Eqn. (10). It is evident from the Fig. below that there is a very good agreement between the two models with respect to predicting the strain-rate at which the yield strength suddenly increases.



**CONCLUSIONS:** An efficient technique has been developed to predict the strain rate behavior of ductile metals subjected to high loading rates. Complete stress versus strain-rate behavior can now be obtained from the post-test measurement of a single Taylor impact specimen. The results obtained from the present formulation for OFHC copper were found to agree well with those obtained previously from the EPIC finite element code using the RJC model.

#### REFERENCES:

- Hawkyard, J. B. (1969), *Int. J. Mech. Sci.* **11**, 313.
- Johnson, G. R. and Holmquist, T. J. (1988), *J. Appl. Phys.* **64**, 3901.
- Jones, S. E., et al. (1991), *J. Eng. Mater. Technol. (Trans. ASME)* **113**, 228.
- Jones, S. E., et al. (1997), *Int. J. Impact Engng.* **21**, 1.
- Rule, W. K. and Jones, S. E. (1998), *Int. J. Impact Engng.* **21**, 609.
- Taylor, G. I. (1948), *Proc. Roy. Soc. London A* **194**, 289.

## **APPENDIX H**

# Optimizing Material Strength Constants Numerically Extracted from Taylor Impact Data

by D. J. Allen, W. K. Rule and S. E. Jones

**ABSTRACT**—Advanced design requirements have dictated a need for the mechanical properties of materials at high strain rates. Mechanical testing for these data poses a significant problem for experimentalists. High-speed testing machines have a limited capability at rates approaching  $10^2/\text{s}$ . The split Hopkinson pressure bar is the most reliable alternative for rates approaching  $10^4/\text{s}$ . Plate impact experiments are capable of generating strain rates of  $10^8/\text{s}$  and higher. The Taylor impact test occupies a place of particular importance by providing data at strain rates on the order of  $10^4/\text{s}$ – $10^5/\text{s}$ . The issue at present is extracting the data. This paper provides a method for obtaining dynamic strength model material constants from a single Taylor impact test. A polynomial response surface is used to describe the volume difference (error) between the deformed specimen from the Taylor test and the results of a computer simulation. The volume difference can be minimized using an optimizer, with the result being an optimum set of material constants. This method was applied to the modified Johnson-Cook model for OFHC copper. Starting from a nominal set of material constants, the iterative process improved the relative volume difference from 23.1 percent to 4.5 percent. Other starting points were used that yielded similar results. The material constants were validated by comparing numerical results with Taylor tests of cylinders having varying aspect ratios, calibers and impact velocities.

## Introduction

The goal of this study was to develop a methodology to allow a single Taylor impact test to be used as a simple and cost-efficient means for obtaining and refining constants for dynamic material strength models. The majority of these models contain several material dependent constants. Normally, these constants are obtained by performing several complicated and sometimes costly experiments. The methodology presented here obtains the constants by minimizing the difference between the displacement results of a Taylor impact test and a hydrocode simulation of the event. The EPIC hydrocode was used for this study.<sup>1,2</sup>

EPIC treats plastic behavior by first assuming that stress increments are elastic and then correcting for cases where the equivalent (von Mises) stress  $\sigma$  exceeds the local yield strength of the material  $\sigma_{\max}$  as given by the strength model. The correction simply involves scaling the local stress components by the factor  $\sigma_{\max}/\sigma$ , thus forcing the stress state to

stay on the yield surface. Subsequent iterations ensure that equilibrium is maintained despite the stress corrections.

## Johnson-Cook Strength Model

The strength model used in this study was a modified form of the Johnson-Cook equation<sup>3–4</sup>

$$\sigma_{\max} = [A + B\dot{\epsilon}^n] [\dot{\epsilon}^n C] [1 - T^m]. \quad (1)$$

where  $\dot{\epsilon}$  is the equivalent plastic strain and  $\dot{\epsilon}^n = \dot{\epsilon}/\dot{\epsilon}_0$  is the dimensionless plastic strain rate ( $\dot{\epsilon}_0 = 1.0 \text{ s}^{-1}$ ).  $T^m$  is the homologous temperature.  $A$ ,  $B$ ,  $n$ ,  $C$  and  $m$  are five empirical material constants.

This model was selected because it is widely used and accepted. It is one of several models available in EPIC. The form of the model was developed by observing how the strength of metals vary under different loading conditions, including a wide range of strains, strain rates and temperatures. Previously, test data for calibrating the strength model coefficients of different materials were produced using torsion tests over a range of strain rates, split Hopkinson pressure bar tests over a range of temperatures and quasi-static and dynamic uniaxial tension tests.

Many physically based alternatives to the modified Johnson-Cook strength model are available.<sup>5,6</sup> Strength models are continuously evolving in form and complexity.

## Taylor Impact Test

With material strength models becoming more complex, there is a need for simpler and more cost-efficient ways of obtaining material constants. One such way is by using the Taylor impact test. The Taylor impact test was performed in the 1940s by Sir Geoffrey Taylor<sup>7</sup> for the purpose of predicting the dynamic yield stress of materials subjected to high strain rates. The test consists of firing a cylinder at a flat, rigid target at speeds high enough to develop the strain rates of interest. His theory used the final deformed shape of the cylinder to determine a dynamic yield or flow stress of the material. Since then, Taylor's analytical theory has been modified by Lee and Tupper,<sup>8</sup> Hawkyard<sup>9</sup> and Jones, Gillis and Foster.<sup>10</sup>

Recently, the Taylor test has also been used to evaluate material strength models.<sup>3,5,11–13</sup> The computational results of hydrocodes using these models can be compared to the results of a Taylor test to evaluate the effectiveness of the model's form and the accuracy of its coefficients. This test

D. J. Allen is a Graduate Student, W. K. Rule is Associate Professor and S. E. Jones is Professor, Department of Aerospace Engineering and Mechanics, University of Alabama, Box 870280, Tuscaloosa, AL 35487-0280.

Original manuscript submitted: September 23, 1996.  
Final manuscript received: March 21, 1997.

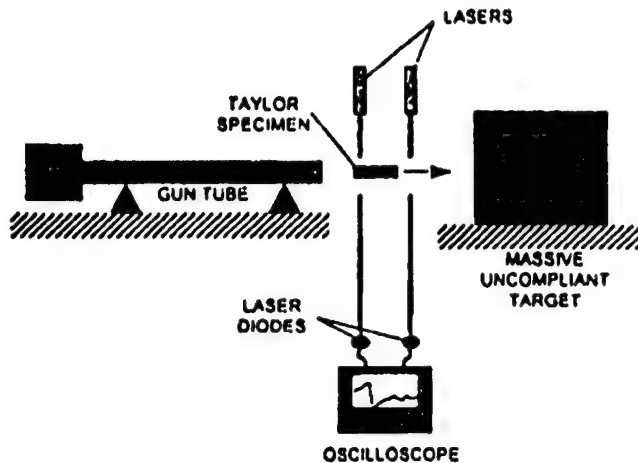


Fig. 1—Schematic drawing of Taylor test equipment

provides the high strains and strain rates necessary to evaluate the model independently of the tests used to obtain the material constants.

Until now, the Taylor test has rarely been used for obtaining constants for material strength models. Johnson and Holmquist<sup>14</sup> used the Taylor test to determine constants for both the Johnson-Cook and Zerilli-Armstrong models. Their method used only three dimensions from the deformed specimen (length, maximum diameter and an intermediate diameter) and was therefore only able to predict as many as three constants. The method to be presented here uses the entire profile and the length of the deformed specimen to determine the constants. For this reason, this method will theoretically be able to determine all constants in any given strength model.

The Taylor test setup used for this study is shown in Fig. 1 and is discussed in some detail by Allen.<sup>15</sup> OFHC (oxygen-free, high-conducting) copper was selected as the material for the impact specimen. OFHC copper is readily available, commonly used in high strain rate applications and can be easily machined into cylinders of the desired length and diameter. The primary specimen for use in the study was 7.87 mm in diameter, with an aspect ratio (length:diameter) of 5:1. This aspect ratio was chosen because specimens shorter than this do not usually display the complex curvature in the deformation profile that may be needed to uniquely determine model constants. With longer specimens, the greater mass can cause difficulties in achieving high velocities without fracturing the specimens.

The deformed lengths of the Taylor specimens were measured using calipers. The deformed profiles were measured using an optical comparator, which uses a light source to cast a magnified specimen shadow onto a viewing screen. The screen is divided into the desired units of measurement and scaled to the magnification used. Using the optical comparator, deformed profiles were measured to within  $\pm 0.03$  mm.

#### Numerical Model for the Taylor Impact Specimen

A numerical model of a Taylor specimen requires specification of the following material properties: density; specific heat; initial, ambient, melting and absolute zero temperatures; and constants describing the strength model and the equation of state. The material properties used were ob-

TABLE 1—NOMINAL MATERIAL PROPERTIES OF OFHC<sup>a</sup> COPPER

Density (kg/m <sup>3</sup> )	8952
Specific heat (J/kg°C)	383.4
Specimen temperature (°C)	21.1
Melting temperature (°C)	1083
Modified Johnson-cook model constants	
Shear modulus (GPa)	46.3
$A$ (MPa)	89.6
$B$ (MPa)	291.6
$n$ (dimensionless)	0.310
$C$ (dimensionless)	0.025
$m$ (dimensionless)	1.090
Mie-Gruneisen equation of state constants	
$K_1$ (GPa)	137.1
$K_2$ (GPa)	175.1
$K_3$ (GPa)	564.2
$\Gamma$ (dimensionless)	1.960

a. OFHC = oxygen-free, high-conducting

tained from the material library included in EPIC. For this study, only the constants for the strength model were modified. The values of the OFHC copper properties used are given in Table 1.

The Taylor cylinder was modeled using three-node, triangular, axisymmetric, solid elements. For simplicity, the target was modeled as a rigid, frictionless surface. This has been the approach for numerically modeling the Taylor anvil in the past. It is assumed that the physical target is sufficiently rigid and free of friction to allow this approximation to be made.

#### Mesh Refinement

A mesh refinement study was performed to determine the minimum number of nodes required to converge to a solution. The preprocessor in EPIC automatically generates the element mesh for an axisymmetric model by having the user input the number of element rings in the radial direction and the number of element layers in the longitudinal direction. The primary Taylor cylinder was modeled six different times with the number of element rings varying from 1 to 6. This gave a broad range of mesh densities, with the number of nodes varying from 32 to 787. The calculated deformed shapes produced by each of the six meshes were compared to measured results for a Taylor cylinder fired at 197 m/s. The comparison was based on the volume difference that will later be used to optimize the strength model constants. Because volume difference was the key index used for assessing the accuracy of the finite element results, it also provided a good index for mesh convergence and for determining the end of the impact event.

The volume difference is the sum of the longitudinal volume difference and the radial volume difference (which are based on profile and length discrepancies, respectively) between the physical test and the finite element model. Before determining the radial volume difference, the longitudinal dimensions of the finite element model were scaled such that its total length equaled that of the physical specimen. This was done to ensure that length discrepancies did not affect the calculation of the radial volume difference. For the physical specimen, the radius was measured every 0.51 mm along the entire length using the optical comparator. The finite el-

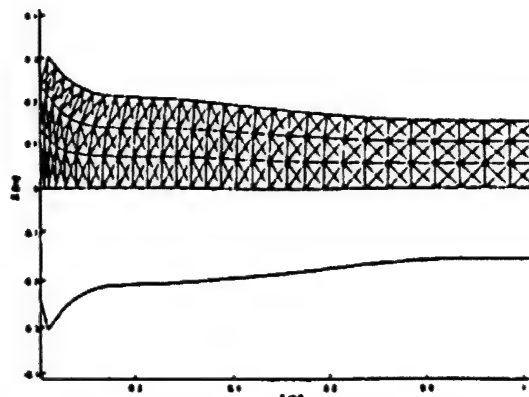


Fig. 2—Typical finite element mesh after impact

lement model's radius at each corresponding position was interpolated from a third-order polynomial fit through the four nearest profile node positions. For each 0.51-mm slice of the cylinder, the radial difference between the physical specimen profile and the finite element model profile forms a quadrilateral. The area of the quadrilateral was determined, and the volume of a ring generated by revolving this area around the longitudinal axis was calculated. The volume of this ring represents the volume difference associated with the 0.51-mm slice. The sum of the volume differences (always considered positive) for each of the slices represented the radial volume difference for the finite element model. When determining the longitudinal volume difference, it was assumed that there was essentially no plastic deformation toward the unimpacted end of the Taylor specimen. Accordingly, the longitudinal volume difference was given by the length difference between the measured and numerically modeled Taylor specimens times the undeformed cross-sectional area.

The results of the mesh refinement study are shown in Table 2. It can be seen that the mesh density did not seem to significantly affect the longitudinal volume difference for the models studied here. However, the radial volume difference, and hence the total volume difference, were greatly influenced by the mesh density. As the mesh density increased, the volume difference decreased until three element rings were reached, at which point the volume difference became essentially constant, indicating that the finite element solution reached convergence. Three element rings were used on all subsequent meshes. The effect of mesh density on computer runtime is also shown in Table 2. Figure 2 shows a typical deformed three-ring mesh.

#### End of Event Test

A Taylor test simulation was run where the geometry data were output every 10  $\mu$ s, starting at 30  $\mu$ s and ending at 130  $\mu$ s. It was found that both the radial and longitudinal volume differences become essentially constant at approximately 100  $\mu$ s. Although this shows that the event ends at 100  $\mu$ s, for the remainder of the study, the simulation was allowed to run to 130  $\mu$ s to capture any end of event time variances due to altering the strength model constants.

#### Determination of Strength Model Constants

The method presented here uses a complete second-order polynomial to describe how the volume difference varies with

changes in the strength model constants. The dimensionless polynomial used was of the following form:

$$\begin{aligned} V/V_0 = & 1 + \alpha_1 x_1 + \alpha_2 x_2 + \alpha_3 x_3 + \alpha_4 x_4 + \alpha_5 x_5 \\ & + \alpha_6 x_1 x_2 + \alpha_7 x_1 x_3 + \alpha_8 x_1 x_4 + \alpha_9 x_1 x_5 \\ & + \alpha_{10} x_2 x_3 + \alpha_{11} x_2 x_4 + \alpha_{12} x_2 x_5 + \alpha_{13} x_3 x_4 \\ & + \alpha_{14} x_3 x_5 + \alpha_{15} x_4 x_5 + \alpha_{16} x_1^2 + \alpha_{17} x_2^2 \\ & + \alpha_{18} x_3^2 + \alpha_{19} x_4^2 + \alpha_{20} x_5^2. \end{aligned} \quad (2)$$

where  $V$  is the volume difference and  $V_0$  is the baseline volume difference. The baseline volume difference is the volume difference that is obtained if the constants are not changed from their baseline values. The design variables  $x_i$  indicate percentage changes (from baseline) in the strength model constants, with  $x_1, x_2, x_3, x_4$  and  $x_5$  corresponding, respectively, to  $A, B, n, C$  and  $m$  of eq (1).

Equation (2) describes a  $p$ -dimensional response surface where  $p$  is equal to the number of strength model constants to be determined. Response surfaces are commonly used in optimization calculations to predict function behavior in the vicinity of known functional values. A complete second-order polynomial in  $p$ -dimensions requires  $q$  coefficients, where

$$q = 2p + \sum_{i=1}^p (i-1). \quad (3)$$

For this study using eq (1),  $p = 5$  and thus  $q = 20$ , but these vary for models with differing numbers of strength model constants. A second-order polynomial was chosen because it can represent local minimums within the response surface. Higher order polynomials would more accurately describe the response surface but would require a great deal more data to determine the many additional polynomial coefficients.

To determine  $\alpha$  of eq. (2),  $q$  linearly independent values of  $V/V_0$  are needed. This required  $q$  EPIC runs using different strength model constants obtained by applying various combinations of  $x_i$  to span the  $p$ -dimensional space. Equation (2) is only valid in the vicinity of the baseline point and loses accuracy at points farther away. In this study, the variations on  $x_i$  used to determine  $\alpha$  were initially limited to  $\pm 10$  percent.

Knowing the baseline volume difference  $V_0$  and the coefficients of eq (2), the  $V/V_0$  ratio (and thus  $V$  the volume difference) can be minimized by varying  $x_i$ . This was conveniently accomplished using a spreadsheet function (the Solver tool of Microsoft<sup>®</sup> Excel<sup>®</sup>). Of course, other optimization routines could also be used for this purpose. The set of  $x_i$  determined by the optimizer serves as the initial point on the response surface for the next iteration of the solution process.

To start each iteration, the newest volume difference data point (as selected by the optimizer at the end of the previous iteration) was incorporated into eq (2) to define a new set of  $\alpha$ . One old volume difference data point was discarded so that only the number of data points defined by eq (3) was used to determine  $\alpha$ . The data point discarded was that farthest from the current baseline point as determined by the maximum distance  $d_j$  determined by the following formula:

$$d_j = \sqrt{\sum_{i=1}^p (x_{i,j} - x_{i,new})^2}. \quad (4)$$

TABLE 2—MESH REFINEMENT STUDY RESULTS

Number of Element Rings	Number of Nodes	Radial Volume Difference (mm <sup>3</sup> )	Longitudinal Volume Difference (mm <sup>3</sup> )	Total Volume Difference (mm <sup>3</sup> )	Approximate (66 MHz 486) Run time (min)
1	32	357	92	449	2
2	103	290	82	372	4
3	214	205	84	289	11
4	365	203	85	288	25
5	556	197	85	282	53
6	787	192	85	277	92

where  $x_{i,new}$  are the design variable coordinates of the new baseline point (as determined by the optimizer in the previous iteration) and  $x_{i,j}$  represent the percentage changes of the  $j$ th data point used to define the previous response surface. Retaining the volume difference data points nearest to the new baseline point provides the best possible description of the response surface in the direction that the iterative process is moving. Note that only one new EPIC run is required for each response surface update.

An algorithm was devised to determine design variable move constraints for the optimizer. Move constraints prevented the optimizer from extrapolating a solution too far from the defined response surface. Large extrapolations can be inaccurate, which can cause the optimization process to diverge. This algorithm determined the move constraints based on how the response surface was initially defined and how the actual  $V/V_0$  (from an EPIC analysis) compared with the  $V/V_0$  predicted by eq (2).

As stated above, the response surface was initially defined limiting the design variables to changes of  $\pm 10$  percent. Then, for the first iteration, the design variable changes were constrained to remain in the range of  $\pm 20$  percent. This represented a 10-percent extrapolation beyond the data points used to define the response surface. In subsequent iterations, the percentage change limits were halved when the percentage error in the predicted volume difference [given by eq (2)], as compared with the results of an actual EPIC calculation, exceeded the move constraints of that iteration. This scheme ensured that the response surface was kept valid and allowed for zooming in on the optimum in a numerically stable and efficient fashion.

The material constants finally used to produce the smallest possible volume difference are assumed to be the best material constants obtainable from the Taylor test.

#### Test Case 1—Coefficient Optimization Starting from Nominal Initial Values

Initially, the nominal Johnson-Cook material strength constants provided by the material library within EPIC for OFHC copper were used to start the optimization process. These constants were given earlier in Table 1. Although this set of constants was obtained specifically for this material, the manufacturing history can cause the material characteristics of OFHC copper to vary somewhat. These nominal constants were expected to provide reasonably accurate results when compared to the Taylor test results. Figure 3 compares the profile of the EPIC solution obtained using these nominal constants with the experimental profile of the primary specimen (described previously) launched at 214 m/s. Here, the EPIC solution can be seen to match the curvature changes

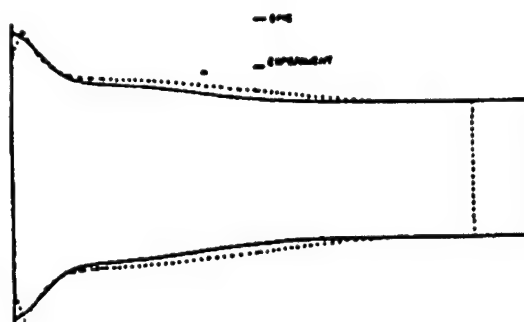


Fig. 3—Comparison of measured and calculated Taylor specimen profiles using nominal strength model constants

in the profile of the measured specimen. However, there is a considerable difference in the overall length. The volume differences corresponding to these nominal constants were calculated to be 408 mm<sup>3</sup>, 259 mm<sup>3</sup> and 149 mm<sup>3</sup> for the total, radial and longitudinal differences, respectively. To get a sense of the magnitude of this error, the relative volume difference can be calculated by dividing the total volume difference by the final deformed specimen volume of 1765 mm<sup>3</sup>. The relative volume difference was 23.1 percent for this initial model based on nominal values for the material constants.

Following the methodology described above, 20 EPIC runs were made to initially define the response surface. The initial array of  $\alpha$  was then calculated, and the iterative process was performed to minimize  $V/V_0$  using the above design variable move constraint algorithm. It was necessary to perform six iterations to approach a local minimum as indicated in Table 3. The third iteration produced a volume difference greater than the preceding iteration. This indicates that the response surface was inaccurate in the region of interest for this iteration. The deformed physical specimen and the EPIC model output using the constants obtained from the sixth iteration are shown in Fig. 4. The final relative volume difference was 4.5 percent.

#### Test Case 2—Coefficient Optimization Starting from Calibrated Initial Values

To define a starting point independent of the nominal values described in the previous section, a new set of constants was calculated to accurately match the results of a quasi-static tension test of OFHC copper. Known values for the variables  $\epsilon$  (0.2-percent offset),  $\dot{\epsilon}^*$  ( $= 1.667 \times 10^{-4}$ ) and  $T^*$  ( $= 0$ ) were inserted into the strength model, and then material constants  $A$  and  $B$  were adjusted proportionally such that the

TABLE 3—ITERATION HISTORY FOR MATERIAL CONSTANTS OPTIMIZATION STARTING FROM NOMINAL VALUES

Iteration	A (MPa)	B (MPa)	n	C	m	Volume Difference (mm <sup>3</sup> )
0	89.6	291.6	0.3100	0.02500	1.0900	408
1	107.6	350.0	0.2480	0.02875	0.8720	152
2	102.4	385.0	0.2232	0.02587	0.7848	100
3	107.5	404.2	0.2120	0.02716	0.8240	103
4	104.9	394.7	0.2176	0.02652	0.8044	85
5	106.2	389.7	0.2149	0.02685	0.7943	80
6	105.6	392.1	0.2136	0.02702	0.7893	80

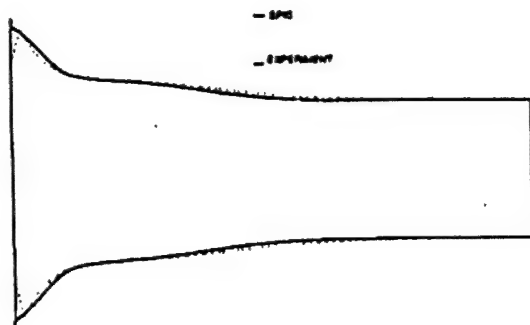


Fig. 4—Comparison of measured and calculated Taylor specimen profiles using calibrated strength model constants

yield strength obtained from the tension test (306 MPa) was matched by eq (1). These values were  $A = 258$  MPa and  $B = 840$  MPa. It was observed that  $n$ ,  $C$  and  $m$  do not change significantly for various alloys of the same metal. Accordingly, these constants were left unchanged from their nominal values (Table 1). Using these calibrated material constants in an EPIC run produced an initial relative volume difference of 29.3 percent.

From this baseline point,  $V/V_0$  was minimized using eight iterations of the response surface approach. The optimum had a relative volume difference of 2.8 percent, somewhat less than that of the first analysis. The optimal coefficients obtained for this analysis were  $A = 132$  MPa,  $B = 430$  MPa,  $n = 0.1786$ ,  $C = 0.01280$  and  $m = 0.5581$ .

#### Averaged Material Constants

It was initially thought that the two apparently different sets of optimized constants obtained here might indicate a uniqueness problem. Ideally, a valid strength model should produce a single local minimum point in the volume difference response surface. A test was devised to determine if the two sets of constants were independent of each other or if they actually described essentially the same local minimum on the response surface. It was assumed that if the two sets of constants represented different local minimum points, then their mean values would produce a set of constants that would be meaningless and would yield inaccurate results when used to simulate the Taylor test. The mean values of the two previously obtained sets of constants were  $A = 118.9$  MPa,  $B = 411.2$  MPa,  $n = 0.1961$ ,  $C = 0.01991$  and  $m = 0.6737$ . These constants were used for an EPIC run that yielded a relative volume difference of only 2.3 percent. These averaged constants actually produced more accurate results than the previously determined sets of constants. Because the mean set

of material constants produced accurate results, it was assumed that the first two sets of constants actually described the same local minimum on the volume difference response surface. Apparently, the response surface is relatively flat in the vicinity of the local minimum.

#### Test Case 3—Constrained Coefficient Optimization

Ideally, one set of material constants should allow for accurate strength predictions over all possible plastic strains, strain rates and temperatures. However, comprehensiveness appears to be too much to ask of simple strength models. This may not necessarily be a problem, since the material constants can be fit for various regimes of interest for the material.

In the second test case, the initial strength model constants were adjusted to match the quasi-static yield strength obtained from a tension test. As the optimization proceeded, the constants were altered to the point where the strength calculated from the model could no longer reproduce the quasi-static yield strength. To determine if the constants for the Johnson-Cook model could be forced to provide for the correct quasi-static yield strength and still give accurate Taylor test results, a third optimization run was conducted with  $A$ ,  $B$ ,  $n$  and  $C$  constrained to change such that the quasi-static yield stress was always correctly predicted. This was easy to impose with the spreadsheet function. This third material constant optimization test case was started from the same set of constants as that of the second optimization test case.

The final, optimal, relative volume difference for this third test case was 9.7 percent. The measured and calculated profiles are compared in Fig. 5. Although the fit of Fig. 5 was not as good as those obtained from the first two test cases, the fit was quite remarkable considering that the constants used to generate the numerical results are forced to span strain rates ranging over eight orders of magnitude.

#### Material Constants Validation

Previously, three sets of material constants were obtained to simulate a Taylor impact test using the primary OFHC copper cylinder (7.87 mm in diameter with a 5:1 aspect ratio) and an impact velocity of 214 m/s. These constants were found to produce reasonably accurate results for this geometry and impact velocity. The accuracy of these material constants was evaluated by simulating six different Taylor tests for which experimental data were available. The first two tests used cylinders having the same diameter and aspect ratio as before, but with higher and lower impact velocities. The next two tests used cylinders of the same diameter and approximately the same impact velocity as before, but having aspect ratios of 3:1 and 10:1. The final two tests used 12.7 mm and

TABLE 4—RESULTS OF THE VALIDATION TESTS

Test	Diameter (mm)	Aspect Ratio	Impact Velocity (m/s)	Relative Volume Difference (%)	
				Mean Constants	Physical Constants
1	7.87	5:1	234	2.9	11.8
2	7.87	5:1	182	3.2	8.8
3	7.87	3:1	210	5.8	14.3
4	7.87	10:1	197	3.0	8.7
5	12.7	7.5:1	195	3.9	13.1
6	4.32	7.5:1	211	3.5	10.6

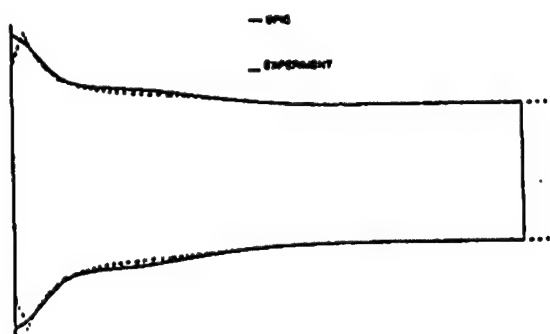


Fig. 5—Comparison of measured and calculated Taylor specimen profiles using constrained strength model constants

4.32 mm diameter cylinders with 7.5:1 aspect ratios. Table 4 lists the characteristics of the six validation tests.

The six validation tests were run using two sets of material constants for each. The first set of constants was the mean of the first two optimization test cases (mean constants). These were used because they represent the most accurate set of constants obtained. The second set of constants (physical constants) was the set found from the third test case. This set was used to determine if material constants with physical meaning (valid for the quasi-static tension test) could be used to accurately simulate other impact conditions. The results of the validation tests are also listed in Table 4.

Although none of the results from the validation tests using the mean constants proved to be as accurate as the relative volume error obtained for the primary cylinder, they were still acceptable. No pattern based on impact velocity, aspect ratio or caliber was found to imply that the mean constants yield more accurate results under one set of conditions as opposed to another. The relative volume differences obtained from the second and fourth validation tests using the physical constants were more accurate than the results of the primary test. However, none of the results obtained with physical constants were comparable to the accuracy obtained using the mean constants.

## Summary

A new methodology was developed for using the Taylor impact test to obtain constants for material strength models. This methodology uses the Taylor specimen's entire deformed geometry and can theoretically be employed to determine all of the constants of any material strength model. This is accomplished by using a second-order polynomial to describe the volume difference between a deformed Taylor test cylinder and a finite element simulation of the test. This polynomial represents a response surface having design variables

that are percentage changes in the constants of the strength model being used. Using a spreadsheet function (such as the Solver tool of Microsoft® Excel®) or some other optimization package, the volume difference can be minimized by changing the design variables to yield a more accurate set of material constants. This is repeated in an iterative scheme, using the newest set of constants as the starting point of each minimization until the volume difference cannot be further reduced. Use of the methodology is illustrated by obtaining material constants for a modified Johnson-Cook model of OFHC copper.

## References

1. Johnson, G.R., "EPIC-3, a Computer Program for Elastic-plastic Impact Calculations in 3 Dimensions," Contract Report BRL-CR-343, Honeywell Inc., Hopkins, MN (1997).
2. Johnson, G.R., "Material Characterization for Warhead Computations," *Tactical Missile Warheads*, ed. J. Carleone, American Institute of Aeronautics and Astronautics, Washington, DC, 165-197 (1993).
3. Johnson, G.R. and Cook, W.H., "A Constitutive Model and Data for Metals Subjected to Large Strains, High Strain Rates and High Temperatures," *Proc. 7th Int. Symp. Ballistics, The Hague, Netherlands* (April 1983).
4. Holmquist, T.J. and Johnson, G.R., "Determination of Constants and Comparison of Results for Various Constitutive Models," *J. De Physique IV*, 1, C3-853-C3-860 (1991).
5. Zerilli, F.J. and Armstrong, R.W., "Dislocation-mechanics-based Constitutive Relations for Material Dynamics Calculations," *J. Appl. Phys.*, 61 (5), 1816-1825 (1987).
6. Follansbee, P.S. and Kocks, U.F., "A Constitutive Description of the Deformation of Copper Based on the Use of Mechanical Threshold Stress as an Internal State Variable," *Acta Metall.*, 36 (1), 81-93 (1988).
7. Taylor, G.I., "The Use of Flat-ended Projectiles for Determining Dynamic Yield Stress," *Proc. Roy. Soc. London, Series A*, 194, 289-299 (1948).
8. Lee, E.H. and Tupper, S.J., "Analysis of Plastic Deformation in a Steel Cylinder Striking a Rigid Target," *J. Appl. Mech.*, 21, 63-70 (1954).
9. Hawkyard, J.B., "A Theory for the Mushrinking of Flat-ended Projectiles Impinging on a Flat Rigid Anvil, Using Energy Considerations," *Int. J. Mech. Sci.*, 11, 313-333 (1969).
10. Jones, S.E., Gillis, P.P. and Foster, J.C., Jr., "On the Equation of Motion of the Undeformed Section of a Taylor Impact Specimen," *J. Appl. Phys.*, 61, 499-502 (1987).
11. Mauldin, P.J., Davidson, R.F. and Henniger, R.J., "Implementation and Assessment of the Mechanical-threshold-stress Model Using the EPIC2 and PINON Computer Codes," Contract Report LA-11895-MS, Los Alamos National Laboratory, Los Alamos, NM (1990).
12. Hummerberg, J.E., Preston, D.L. and Wallace, D.C., "A New Model of Rate Dependent Elastic-plastic Flow," *APS 1991 Topical Conf. Shock Compression of Condensed Matter*, Williamsburg, VA (1991).
13. Pazienda, G., Pezzica, G. and Vignolo, G.M., "Determination of the Armstrong-Zerilli Constitutive Model for AISI 316 H Stainless Steel and Application to Cylinder Impact Tests," *7th Dymat Technical Conf.*, St. Louis, MO (1992).
14. Johnson, G.R. and Holmquist, T.J., "Evaluation of Cylinder-impact Test Data for Constitutive Model Constants," *J. Appl. Phys.*, 64, 3901-3910 (1988).
15. Allen, D.J., "Use of the Taylor Impact Test to Determine Constants for Material Strength Models," *MS thesis, University of Alabama, Tuscaloosa* (1995).

## **APPENDIX I**

## TAYLOR IMPACT TESTING OF HIGH STRENGTH STEELS

**S. E. Jones, David L. Ahern III, Marcus A. Taylor**

College of Engineering, University of Alabama

Tuscaloosa, AL 35487-0280

and

**William K. Rule**

Adjunct Professor of Mechanical Engineering, Boise State University  
Boise, ID 83725

### ABSTRACT

Data from high strength steel Taylor tests is reduced using a one-dimensional model developed by the authors and a Revised Johnson-Cook strength model introduced earlier by two of the authors. When applying these methods to recovered specimens, a significant difficulty was encountered. The very limited deformation zone in the specimens provided such a narrow region for measurement that there was considerable uncertainty in some of the calculations. A further difficulty is the very low strain to failure for most of the materials limited the impact velocities, thus contributing to the narrow deformation zone. A discussion of some of the measurement techniques that were utilized is included. The results indicate that rate sensitivity in all of the materials increases considerably as strain rates of  $10^4$  / sec are approached.

### INTRODUCTION

There are generally two approaches to reducing Taylor impact test data. These are one-dimensional analyses of post-test specimens (Taylor (1948)) and computational analyses of specimen geometry (Johnson and Holmquist (1988); Rule and Jones (1998)). The latter approach generally employs some constitutive model with undetermined constants. The specimen geometry, either current from high-speed film records or from the recovered specimen, is used to evaluate the unknown constants in the constitutive relation.

Traditionally, measurements of recovered specimens have been used to estimate the "dynamic yield strength" of the specimen material. This is useful in some penetration models, but has limited value to material scientists because it is not associated with a particular strain or strain-rate. Recently, a one-dimensional theory was presented (Jones et al. (1998)) that estimates the state of stress with Taylor test data. The principal assumption behind this theory is the observation that the particle velocity behind the deformation front,  $u$ , is proportional to the undeformed section speed,  $v$ . The results of this analysis produced an estimate of the state of stress at strain-rates in excess of  $10^4$  / sec. These estimates agreed fairly well with a modification of the traditional Johnson-Cook Strength Model given by Rule and Jones (1998) for four different metals. With the exception of quasi-static compression data, only length and diameter measurements from 17 caliber Taylor impact specimens were used.

In this paper, the one-dimensional analysis and the Revised Johnson-Cook Strength Model are applied to several high strength steels. The complication presented by these materials is very low strain to failure due to limited ductility and high strength. Another complication is dynamic buckling of some of the lower caliber specimens. This necessitated an increase in the diameter in some cases. The ultimate purpose of the tests of these materials is to acquire

constitutive data in the high strain rate regime in order to assist in the simulation of hard target penetration events.

## ONE-DIMENSIONAL ANALYSIS

The one-dimensional theory for estimating the state of stress at high strain rates was presented by Jones, et al (1998). A short summary will be presented here for convenience.

Conservation of mass across the plastic wave front is given by

$$e\dot{\ell} = v - u. \quad (1)$$

The impulse-momentum equations applied at the wave front leads to

$$\rho\ell\dot{v} = \sigma_0 \quad (2)$$

and

$$\sigma = (1+e) \left[ \sigma_0 + \frac{\rho}{e} (v - u)^2 \right]. \quad (3)$$

Addition of the current lengths in Figure 1 produces the kinematical equation

$$h + \ell + s = L_0 \quad (4)$$

which applies to all deformed configurations of the cylindrical specimen. Equations (1-4) are the basis for the one-dimensional data reduction in this paper. A complete discussion of development of these equations is contained in Jones, et al (1998). The nomenclature for these equations is:  $e < 0$  is the compressive engineering strain behind the plastic wave front,  $\ell$  is the undeformed section length,  $\rho$  is the specimen density (assumed constant after the initial transient),  $\sigma_0 < 0$  is a reference compressive stress related to the quasi-static yield stress of the specimen material, and  $h$ ,  $\ell$ , and  $s$  are lengths shown in Figure 1.

The fundamental assumption that allows us to integrate the differential equations is  $u = \beta v$ , where  $\beta$  is a strain dependent constant. We can now integrate Equation (1) directly and to use the results in Equation (3). The stress at the plastic wave front then takes the form

$$\sigma = (1+e) \left[ \sigma_0 + \frac{(1+\beta)^2}{e} \rho v^2 \right]. \quad (5)$$

The state of stress at a particular compressive strain  $e$  can now be estimated with (5) and the following estimate for strain rate

$$\dot{e} = \frac{-v}{L_0 - \ell} \quad (6)$$

where one of the integrals of motion can be used to find  $\ell$  and express it in the form

$$\ell = \bar{\ell} \exp \left\{ \frac{1-\beta}{2e\sigma_0} \rho(v^2 - v_0^2) \right\} = \ell_f \exp \left\{ \frac{1-\beta}{2e\sigma_0} \rho v^2 \right\}. \quad (7)$$

In these equations,  $\bar{\ell}$  is the undeformed section length at the end of the initial transient period (see Jones, et al, 1991) and  $\ell_f$  is the undeformed section length at the end of the event when  $v=0$ . Together, (5) and (6), with (7), comprise a parametric constitutive relation for the material in the parameter  $v$ . The reference stress  $\sigma_0(e)$  can be related to the quasi-static yield stress  $\sigma_s(e)$  by  $\sigma_0 = (1+e)\sigma_s$ , which is the limit as  $v \rightarrow 0$  in Equation (5). All that remains is to estimate the state of stress with Equations (5) and (6) is to determine the parameter  $\beta$ .

### ESTIMATING $\beta$

The technique devised by Jones, et al (1998) for estimating  $\beta$  from post-test measurements, utilized the integral of motion

$$\frac{\ell_f}{L_0} = -\frac{1-\beta}{e} \frac{L_f}{L_0} + \frac{\bar{\ell}}{L_0} + \frac{1-\beta}{e} - \frac{1-\beta}{e} \frac{\bar{s}}{L_0} \quad (8)$$

which is a consequence of  $u = \beta v$ .  $L_f$  is the specimen length at the end of event and  $\bar{s}$  is the displacement of the undeformed section at the end of the initial transient. This is the equation of a straight line in the  $\ell_f/L_0$ ,  $L_f/L_0$  plane.

For impacts with sufficiently high velocity, the data from recovered specimens can be used to find the slope and the intercept of this line. The slope  $m = -(1-\beta)/e$  can be used to find  $\beta$ . Herein lies the difficulty with high strength steels. For a ductile material, such as copper, the slope of the line described by Equation (8) is fairly easy to find. Copper Taylor test data from 17 caliber specimens is shown in Figure 2. Notice that  $L_f/L_0$  ranges from 0.68 to 0.83. This means that the slope of the lines corresponding to the indicated fixed strains can be found without much uncertainty and minor measurement errors do not significantly affect the result. However, this is not the case for high strength steels. The range of  $L_f/L_0$  is very narrow. The data presented in Figure 3 is from six impact tests with Astralloy V®, a high strength steel from which the impact face of the target is fabricated. Notice that  $L_f/L_0$  ranges from about 0.91 to about 0.94. Now, there is a premium placed on the accuracy of each data point in the set, because any uncertainty can influence the slope of the line and ultimately the value of  $\beta$ . These measurements were done with an optical comparator. Despite the narrow range of the data, there is a very consistent linear trend.

For each particular strain, the slope of the line can be determined and the corresponding value of  $\beta$  can be found. Now, Equation (7) can be used to find  $\bar{\ell}$  and the state of stress in the specimen material can be estimated from the end of the initial transient to the conclusion of the event with Equations (5) and (6).

## THE REVISED JOHNSON-COOK STRENGTH MODEL

The Johnson-Cook (JC) strength model was first proposed in 1983 and has the following form:

$$\sigma = (C_1 + C_2 \epsilon^N) (1 + C_3 \ln \dot{\epsilon}^*) (1 - T^{*M}) \quad (9)$$

where:  $\sigma$  is the equivalent yield strength,  $\epsilon$  is the equivalent plastic strain,  $\dot{\epsilon}^*$  is the dimensionless equivalent plastic strain rate (made dimensionless by dividing the equivalent plastic strain rate by a unit plastic strain rate),  $T^*$  is the homologous temperature, and  $C_1$ ,  $N$ , and  $M$  are empirical coefficients and exponents.

Many ductile metals display an enormous increase in yield stress for strain rates in excess of  $10^3/s$  (see Fig. 1 of Follansbee and Kocks, 1988, for instance). This observed behavior provided the motivation for the development of the revised Johnson-Cook (RJC) strength model (1998) which takes the form:

$$\sigma = (C_1 + C_2 \epsilon^N) \left[ 1 + C_3 \ln \dot{\epsilon}^* + C_4 \left( \frac{1}{C_5 - \ln \dot{\epsilon}^*} - \frac{1}{C_5} \right) \right] (1 - T^{*M}) \quad (10)$$

where  $C_4$  and  $C_5$  are additional empirical coefficients.

The strain rate sensitivity has been enhanced by the term  $1/(C_5 - \ln \dot{\epsilon}^*)$  where  $C_5$  is the natural logarithm of a critical strain rate level. This term tends to infinity as the strain rate approaches the critical strain rate. Note that this strain rate sensitivity enhancement term contribution tends toward zero for low strain rates due to the  $-1/C_5$  correction term in Equation (10).

The original JC strength model provides for specifying a maximum value for the yield strength. However, a limiting value is usually not required for high strain rate simulations since the sensitivity to strain rate is relatively low (linear logarithmic dependence). However, the RJC strength model as discussed to this point predicts a physically untenable infinite yield strength as  $\ln \dot{\epsilon}^*$  approaches  $C_5$ . To prevent this unrealistic occurrence the RJC model simply assumes that there exists a maximum value that the strain rate sensitivity factor in Equation (10) can attain for each material which can not be exceeded regardless of the prevailing strain and temperature state.

## RESULTS

With a premium placed on the accuracy of measurements, a laser micrometer was used to determine the specimen profiles and the undeformed section lengths. This device was adopted because measurements to an accuracy of 5 microns can be achieved. A reference dimension was established at the undeformed end of the cylinder and used to calibrate the instrument. Each projectile was then mounted in a custom fabricated holder and placed into the bench micrometer. The projectile was moved through the laser beam producing an accurate profile of the cylinder. The profile geometries were used to evaluate the RJC constants (see Rule and Jones, 1998, for the details) and to determine the undeformed section lengths at the fixed compressive strains of 5%, 8%, 10%, and 15%. These strain levels were arbitrarily selected.

Three steels were tested: AF 1410, 4340, and ES-1, an experimental steel of interest to the Air Force. The very high strength of these steels dictated that the data would occupy a narrow range on the abscissa of the graph. Notice that the data, although very linear, ranges from a least value of somewhat less than 0.93 to slightly greater than 0.97. What complicates these measurements further is the fact that we have not determined a minimum velocity to assure that initial transient behavior is complete. For the one-dimensional analysis, this leaves us with only a few data points because most of the specimens fracture or buckle at the higher impact velocities around 200m/s and show very little deformation at the lowest impact velocities around 130m/s. Figures 4-6 display the data from the Taylor cylinder tests. The slopes from these lines are used to find the values of  $\beta$  from which the calculations for the estimates for the one-dimensional state of stress are made.

Before making the high strain-rate estimates, we can use the test data to estimate the quasi-static properties of the materials. This method was proposed by Jones, et al, 1998, and utilizes a very simple deformed specimen geometry to provide an additional relationship for  $\bar{\ell}$

$$\frac{\bar{\ell}}{L_0} = \frac{b}{\beta} - \frac{1-\beta}{\beta} \frac{1+e}{e} \quad (11)$$

with which the quasi-static flow stress

$$\sigma_s(e) = \frac{(1+e)(1-\beta)}{2e\ln(\bar{\ell}/\ell_f)} \rho v_0^2 \quad (12)$$

can be calculated. When high quality specimens are used, this formula generally produces excellent results. This has been confirmed by published results on OFHC Copper and Wrought Iron by Jones, et al (1998). The slopes of the lines in Figure 3 are used to find the values of  $\beta$  for the indicated strains and the intercepts  $b$  are used in Equation (11) to find the estimate for  $\bar{\ell}/L_0$ . This is then used in Equation (12) to find the quasi-static stresses for the material. To demonstrate this process, we are including the reduction of Astralloy-V® steel data originally published by Jones, et al (1996) with Equations (11) and (12). In this case, the 0.164 caliber specimens were provided by Astralloy Wear Technology in Birmingham, AL, and were accurately machined to a tolerance of  $5 \times 10^{-4}$  in. Six specimens of ten survived the impact without failing and the results are shown in Figure 3 and summarized in Table 1. The agreement with independent compression tests performed with a testing machine and a load cell is remarkable.

The data from a series of Taylor impact tests on AF 1410, 4340, and ES-1 was reduced with Equations (11) and (12). The recovered specimens were evaluated at three compressive strains, 5%, 8%, and 10%. These strains were arbitrarily selected and other strains could easily be substituted, provided that they are not too large. The quasi-static stress estimates for the three materials are given in Table 2. Using these estimates, the high strain-rate behavior of the specimen materials can be estimated with Equations (5) and (6). The results of the calculations are shown in Figures 7-9. In each case, the stress shows the characteristic increase in rate hardening in the neighborhood of a strain-rate of  $10^4$  /sec.

Figures 7-9 also display the results of RJC calculations on the same materials. In two cases, data from Split-Hopkinson Pressure Bar tests was used. In one case, 4340 steel, the quasi-static estimates from Equation (12) were used. The only other data used to evaluate the RJC constants are the profiles of the recovered Taylor cylinders. Hence, there are some discrepancies in the limits as the strain-rate approaches zero. We believe that these discrepancies are the result of uncertainties in the initial specimen geometry. The quasi-static estimates are the averages for all the specimens in a particular material group. When measurements of post-test specimens are made, it is presumed that the initial diameter of the specimens is uniform. The machining of some of these specimens was not to the strict tolerance that was specified, which was  $\pm 5 \times 10^{-4}$  in. These specimens were hard steel and difficult to machine with conventional equipment. However, an uncertainty of 0.001 in. in a nominal diameter of 0.164 in. is the equivalent of more than 1% apparent strain in the specimen. Still, the results are good and the agreement between the RJC constitutive model and the one-dimensional model is very satisfactory.

## CONCLUSIONS

Data from Taylor tests of some high strength steel penetrator casing materials is reported in this paper. A typical, deformed specimen is shown in Figure 10. As the reader can see, the deformation zone is very slight and not very distinct. For a lower strength material, like OFHC copper, the deformation profile in the specimen is very pronounced, making measurement fairly direct by several procedures.

For the hard steel cylinders in this paper, only the most accurate measuring techniques could be successfully applied. Even a modest uncertainty in the measuring process can produce large uncertainties in the results. This is the reason why the initial state of the specimen is so critical for the lower caliber specimens. Higher caliber specimens, in the range of 30-50 calibers, do not reflect the uncertainty in such a profound way. But, the effects of radial inertia are uncertain. When high quality lower caliber specimens do not fail on impact or dynamically buckle, the results are generally excellent, as reflected by the Astralloy-V® specimens described earlier. A good "rule of thumb" is the correlation that is achieved by the quasi-static estimates with Equations (11) and (12). When this is good, as it was in the Astralloy-V® case, the results across the full range of strain-rates are very consistent. There was scatter in the quasi-static estimates for the materials in this paper, but their averages are very much in range. When all things are taken into consideration, the results presented in this paper for high strength steels are very credible.

## REFERENCES:

Follansbee, P. S. and Kocks, U. F., 1988, "A Constitutive Description of the Deformation of Copper Based on the use of Mechanical Threshold Stress as an Internal State Variable," *Acta Metall.*, 36(1), 81.

Johnson, G. R. and Cook, W. H., 1983, "A Constitutive Model and Data for Metals Subjected to Large Strains, High Strain Rates, and High Temperatures," Proceedings of the 7<sup>th</sup> International Symposium on Ballistics, The Hague, The Netherlands.

Johnson, G. R. and Holmquist, T. J., 1988, "Evaluation of cylinder-impact test data for constitutive model constants," *J. Appl. Phys.*, 64(8), 3901.

Jones, S. E., Gillis, P. P., Foster, J. C., Jr., and Wilson, L. L., 1991, "A One-Dimensional, Two-Phase Flow Model for Taylor Impact Specimens," *Journal of Engineering Materials and Technology*, Trans. ASME, **113**, 228.

Jones, S. E., Barkey, M., Rule, W. K., and Huber, E., 1996, "Mechanical Characterization of Hardened Astralloy-V® Using the Taylor Impact Test," AIAA-96-4294, 1996 AIAA Space Programs and Technologies Conference, Huntsville, AL.

Jones, S. E., Drinkard, J. A., Rule, W. K., and Wilson, L. L., 1998, "An elementary theory for the Taylor impact test," *Int. J. Impact Engng.*, **21**, 1.

Rule, W. K. and Jones, S. E., 1998, "A revised form of the Johnson-Cook strength model", *Int. J. Impact Engng.*, **21**, 609.

Taylor, G. I., 1948, "The use of flat-ended projectiles for determining dynamic yield stress I. Theoretical considerations," *Proc. Roy. Soc. London*, **A-194**, 289.

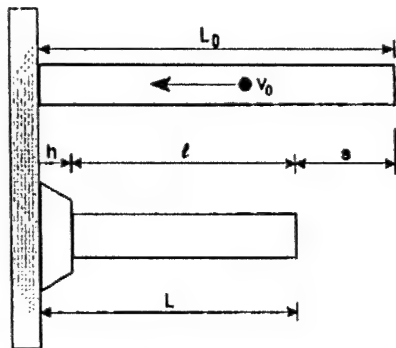


**Figure 1. Undeformed and Idealized deformed specimen geometries.**

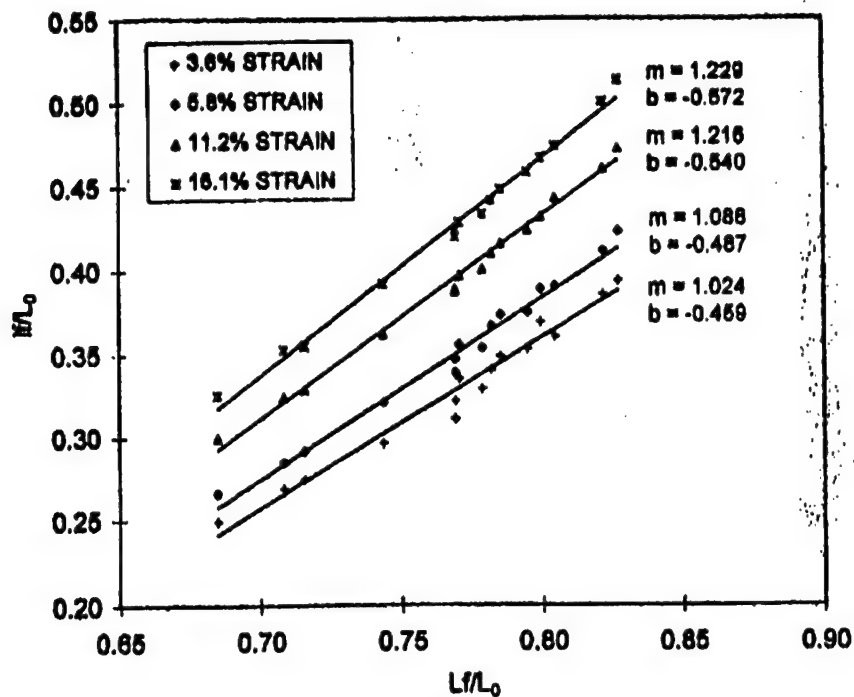


Figure 2. The results of 17-caliber OFHC copper impact tests.

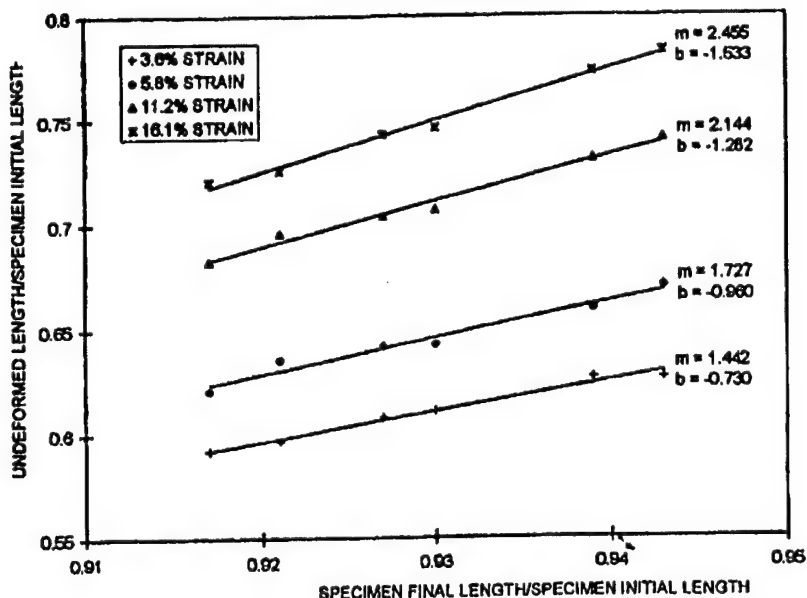


Figure 3. The results of 17-caliber Astralloy-V® impact tests.

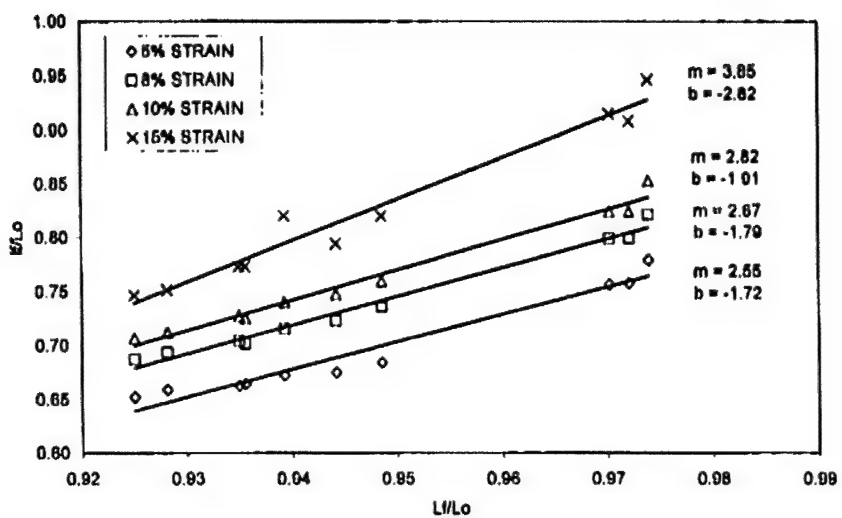


Figure 4. The results of AF1410 steel impact tests.

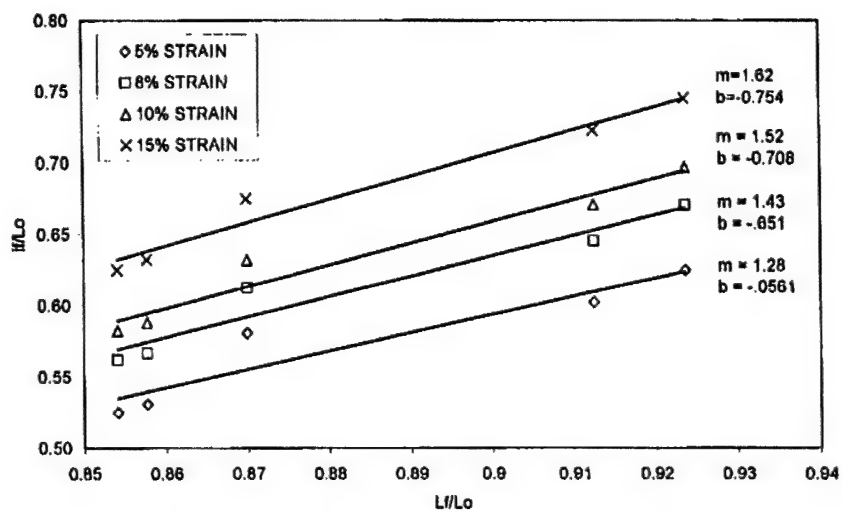


Figure 5. The results of 4340 steel impact tests.

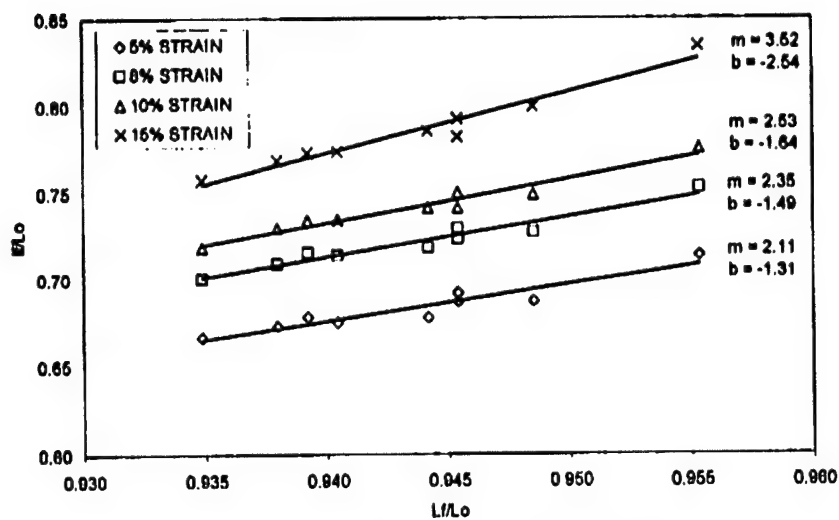


Figure 6. The results of ES 1 Impact tests.

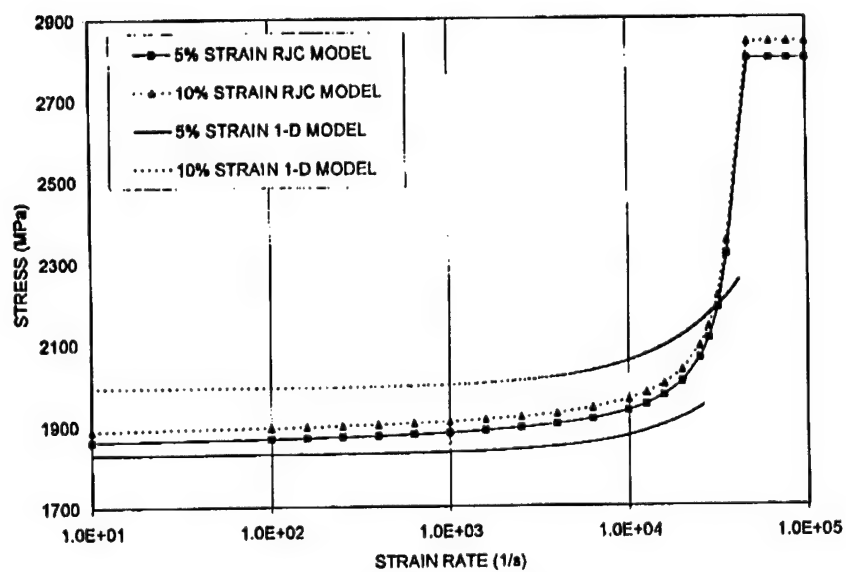


Figure 7. Comparison of 1-D and RJC stress versus strain rate models for AF1410 steel.

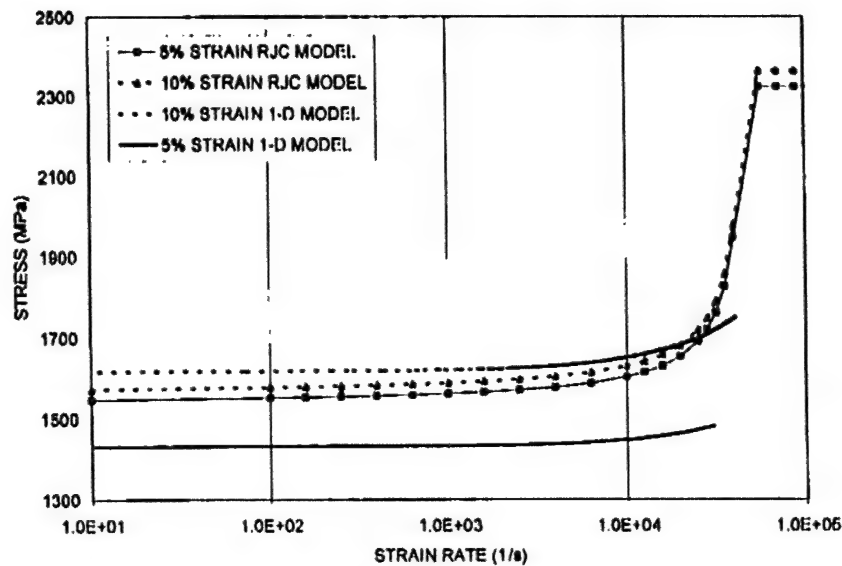


Figure 8. Comparison of 1-D and RJC stress versus strain rate models for 4340 steel.

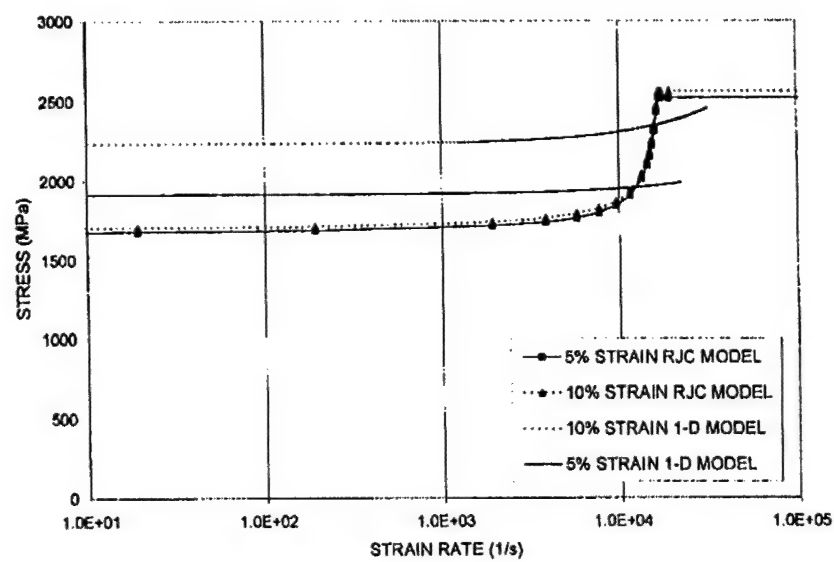


Figure 9. Comparison of 1-D and RJC stress versus strain rate models for ES 1.

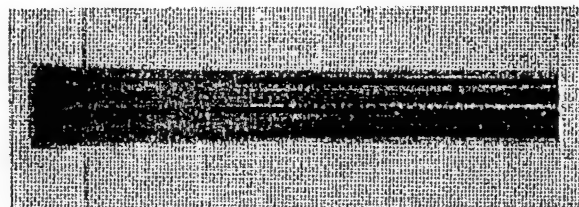


Figure 10. Typical deformed high strength steel Taylor specimen.

**Table 1. Astralloy quasi-static stress comparison (MPa).**

	Q <sub>s</sub> (3.6%)	Q <sub>s</sub> (5.8%)	Q <sub>s</sub> (11.2%)	Q <sub>s</sub> (16.1%)
1-D Model Data	-1750	-1850	-1930	-1970
Machine Test Data	-1750	-1840	-1930	-1970

**Table 2. Quasi-static stress comparison (MPa).**

	STRAIN LEVEL		
	5%	8%	10%
AF1410	-1835	-1960	-1990
4340 HSCM	-1440	-1566	-1630
ES-1	-1920	-2140	-2250

## **APPENDIX J**

# TAYLOR TEST ANALYSIS OF AN UNCONVENTIONAL MATERIAL

L. L. Wilson and J. C. Foster, Jr.,  
Wright Laboratory  
Eglin AFB, Florida

S.E. Jones  
Aerospace Engineering and Mechanics  
University of Alabama  
Tuscaloosa, Alabama

P. P. Gillis  
Chemical and Materials Engineering  
University of Kentucky  
Lexington, Kentucky

Taylor cylinder testing is a useful method for obtaining the state of stress at high strain-rates. The conventional test involves normally impacting a ductile metal against an uncompliant target. The recovered specimen is measured and the constitutive properties of the material are deduced from the specimen geometry.

The test has undergone numerous modifications and interpretations since it was proposed by G.I. Taylor [1]. In this short paper, we cannot do justice to the many investigators who have contributed to the advancement of our present understanding of the test. A more complete list may be found in other papers, e.g. [2]. Recently [3], a new method for interpreting Taylor test data was proposed. This method was applied to ductile metals for which there are recovered Taylor specimens. The purpose of this paper is to demonstrate that the method can also be applied to "unconventional materials". By "unconventional," we mean those materials for which a suitable Taylor specimen cannot be recovered. Such materials are polymers. For example, the mechanical properties of a dense urethane, adiprene-100, are deduced in this paper. In this case, the recovered specimen is replaced by a high speed film record of the impact event. The images of specific frames are digitized and all of the information, generally available only from a recovered specimen, can be obtained. In fact, a single quality film record is capable of delivering the results of numerous

tests. Thus, as demonstrated in [3], estimates for constitutive behavior can be achieved using only measurements of specimen length, diameter, and velocity. The impact test was performed at Eglin AFB, FL., and the digitized data was reduced by Dr. Paul J. Maudlin and Mr. Eric Harstad, Los Alamos National Laboratory, and shared with the authors.

## THEORY

The fundamental relationship for application of the theory [3] is the linearity between the dimensionless ratios  $\xi = \ell / L$  and  $\eta = (L - s) / L$ . Refer to Figure 1 for the definitions of these variables.

$$\xi = m\eta + b \quad (1)$$

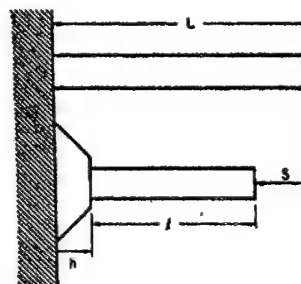


FIGURE 1

Deformed and undeformed Taylor specimens. L is the original length.  $\ell$  is the length undeformed section, s is the displacement of the undeformed section.

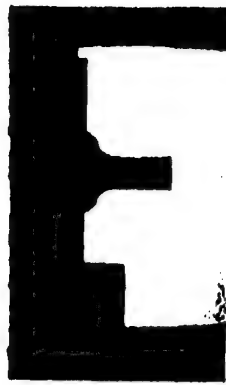
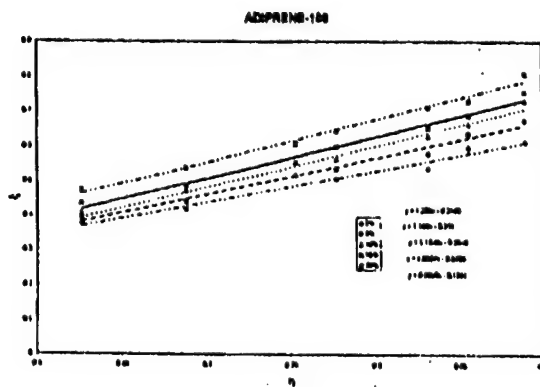


FIGURE 2

A typical digitized image of the deformed impact specimen. The lower body is the fiducial, a structure with known dimensions which gives longitudinal and lateral dimensions.

The dimensionless ratios  $\xi$  and  $\eta$  plotted in Figure 3 for a succession of different times ranging from  $13 \mu$  sec to  $29 \mu$  sec.



---

## **APPENDIX K**

# Relationship Between Strain Rate, Temperature, and Impact Failure Mechanism for Poly(Vinyl Chloride) and Poly(Ethylene Terephthalate)

JANET L. GREEN and CHARLES A. PETTY

Chemical Engineering Department  
Michigan State University  
East Lansing, Michigan 49924

PETER P. GILLIS and ERIC A. GRULKE

Chemical and Materials Engineering  
University of Kentucky  
Lexington, Kentucky 40506

One approach to the purification of recycled thermoplastic mixtures is selective grinding to induce differences in sizes and shapes between polymers with different compositions. These mixtures can then be separated using one of several technologies including conventional sieving or hydrocyclones. Recycled poly(vinyl chloride) and poly(ethylene terephthalate) often are cross-contaminated with each other since they have overlapping density ranges and are very difficult to separate using methods such as flotation. Selective grinding followed by physical separation might be a preferred method for separating such a polymer pair if processing "windows" for inducing differences in failure mechanisms can be found. There is a temperature range over which PET fails in a ductile mode while PVC fails in a brittle mode for impact grinding experiments. This range is not accurately predicted by failure mechanism and  $\beta$ -transition temperature diagrams.

## INTRODUCTION

Plastic recycling has been gaining momentum because of decreasing landfill space, concerns about environmental contamination, and increasing costs of raw materials. Methods for producing high purity recycled materials are important objectives for the commodity plastics industry. Simple and economical approaches to plastics purification are separations based on differences in physical properties, such as density. Some polymer pairs have similar density ranges and cannot be separated by sink-float technologies. One such pair is poly(vinyl chloride) (PVC) and poly(ethylene terephthalate) (PET), which often appear together in mixed chipped plastic streams from recycled polymer bottles. Several groups have recently reported selective grinding processes for this pair. The selective grinding product can be separated using conventional screening, or methods based on differences between the acceleration of particles such as air cyclones or hydrocyclones (1).

Famechon (2) has reported a process for crushing a

blend of PVC and PET particles, resulting in mixtures with larger PET particles after each operating stage. An Australian firm (3) has reported an impact grinding process that also accomplishes a size difference. Streams rich in PVC particles are ground under liquid nitrogen at a temperature below  $-100^{\circ}\text{C}$ , producing PVC particles less than 500 microns in characteristic size. A 99% pure PVC product is recovered by screening separation. These differences in shape and size are thought to be based on differences in the failure mechanisms between the two thermoplastics at the grinding conditions. Plastics failing in the brittle mode tend to fragment to many particles of smaller size than plastics failing in the ductile mode. However, predictions of the failure mechanisms for polymers are few, and are rarely applied to grinding technologies. Engineering a selective grinding process, in which one thermoplastic would be comminuted at a rate higher than another or to a different particle size distribution than another, will depend on identifying appropriate grinding conditions, and on modeling the grinding process.

## Research Approach

In general, the relationships between the grinding conditions, specifically, temperature and strain rate, and failure mechanism are not well-correlated. The following sequence of work was used to determine information needed to develop selective grinding processes. Failure mechanism diagrams based on tensile and compressive tests were compared to impact test results over a range of conditions to identify processing "windows" in which selective grinding was possible. Once differences in failure mechanisms between two polymers were identified, grinding experiments were used to determine a size distribution model for each thermoplastic. The effects of processing conditions, temperature and impact rate, on the model coefficients were determined, and then were used to engineer a selective grinding process. This paper reports the first part of this sequence: the development of failure mechanism diagrams and their comparison to impact failure tests for the two thermoplastics, PVC and PET.

Post-consumer recycled bottle chips, a likely feed material for a selective grinding process, have variability in their homopolymer properties, bottle production conditions, thickness, and thermal history. This material was used to test the general concept of predicting selective grinding conditions since it is typical of that expected in an actual process. This approach assumes that impact grinding fracture mechanisms are primarily dependent on homopolymer type.

## FAILURE MECHANISM DIAGRAMS FOR PVC AND PET

The failure mechanism, brittle or ductile, determines the size and shape of the comminuted particle. Brittle failure tends to be catastrophic without any indication of plastic deformation and usually leads to many particles of small size. Ductile failure is characterized by yielding of the material, sometimes resulting in the appearance of a neck. It leads to long fibrils at the failure surface and a few large particles. Although the glass transition temperature ( $T_g$ ) is often used as a reference point for brittle-ductile failure transitions, it is not always an accurate predictor. Brittle fracture usually occurs at temperatures below about 0.8 times the glass transition temperature ( $T_g$ ). This rule of thumb does not apply to the PVC-PET pair since both have  $T_g$ 's near 80°C; however, PVC has a brittle tempera-

ture of about -20°C for low extension rates, while PET does not have a definite brittle-ductile transition. In fact, PET is known to exhibit ductile behavior at cryogenic temperatures under some deformation conditions (4). Other mechanisms for failure include cold drawing and adiabatic heating (viscous flow); neither of these will be considered for developing a selective grinding process.

Table I compares some physical properties for several commodity polymers as well as their tendency for brittle fracture. Factors that promote brittle fracture are low temperature, high loading (impact) rate, low molecular weight, high crosslinking, low crystallinity, high glass transition temperature, and low polarity (4-7). The last five factors depend on the polymer composition. Those factors available to manipulate during grinding are the polymer temperature and the impact rate.

The brittle-ductile transition temperature of polystyrene homo- and copolymers has been studied in tension (8), compression (9) and fatigue (10). This transition was found to be temperature and rate dependent. Weaver and Beatty (10) related the  $\beta$ -relaxation temperature to the brittle-ductile transition temperature under fatigue failure.

Shape differences between two materials might be induced by grinding if conditions were found to fracture one in a ductile mode and the other in a brittle mode. Size differences should also occur since the size of progeny particles should depend on the mode of fracture.

Ahmad and Ashby (11) developed tensile and compressive failure mechanism diagrams for several homopolymers. Their method was used here to develop similar diagrams for PVC and PET. Impact tests and impact grinding may subject the specimen to both tensile and compressive forces. The specimen will fail if either of these failure strengths are exceeded. The relationships between impact failure, and failure under tension or compression are not clear from the previous literature. Kausch (12) found that the deformation mechanism for solid polymers under grinding is compressive yielding, while the mechanism during impact loading is elastic compressive and/or tensile deformation. Prasher (13) proposed that impact failure should be similar to compressive failure since the chief difference between impact and compression stress is the strain rate. The strain rates for conventional tensile and compressive tests are on the order of  $1 \text{ s}^{-1}$  or less.

Table 1. Properties of Typical Consumer Waste Thermoplastics (5, 6).

Resin	Density (g/cm <sup>3</sup> )	Glass Transition Temp. (C)	Fracture at Cryogenic Temp.	Brittle Temp. (C)	Crystallinity	Polarity
PP	~0.90-0.91	-20	Fractures	< 20	High	Low
HDPE	~0.94-0.97	-122	Difficult to Fracture	~ -150	High	Low
PVC	~1.32-1.40	75	Easy to Fracture	~ -20	Low	Polar
PET	~1.33-1.42	79	Difficult to Fracture	—	Intermediate	Polar
PS	~1.04-1.07	100	Fractures	~ 90	Low	Nonpolar

rates for the Izod impact test are about  $100 \text{ s}^{-1}$ , and rates for impact grinding can be  $10,000 \text{ s}^{-1}$ . Impact rates are known to affect the brittle-ductile transition temperature.

Dynamic stress fracture is thought to include four steps (14). After impact, there is rapid nucleation of microfractures followed by growth of the fracture nuclei. Adjacent microfractures coalesce, and fragments or spalls then form.

### Tensile Failure Diagrams

In ductile fracture, the stress-strain response of the material is characterized by a drop in the stress prior to fracture and some necking. The theory of Eyring provides a reasonable basis for the description of yielding. The equation for the yield strength in ductile failure is

$$\sigma_y = \frac{kT}{v_1} \cdot \left( \frac{H_1 + \ln\left(\frac{2\dot{\epsilon}}{\dot{\epsilon}_{01}}\right)}{RT} \right) + \frac{kT}{v_2} \cdot \sinh^{-1}\left(\frac{\dot{\epsilon}}{\dot{\epsilon}_{02}}\right) \cdot \exp\left(\frac{H_2}{RT}\right) \quad (1)$$

Here  $k$  is Boltzmann's constant,  $T$  is temperature,  $v_1$  is the stress activation volume,  $H_1$  is the activation energy,  $R$  is the ideal gas constant,  $\dot{\epsilon}$  is the strain rate, and  $\dot{\epsilon}_{01}$  is the pre-exponential for the strain rate.

In brittle fracture, the stress-strain response of the material is nearly linear up to the breaking point. The Griffith criterion then provides a reasonable basis for the description of brittle fracture. According to Williams (7), the stress to cause brittle fracture is given by

$$\sigma_f = \sigma_{f,0} \cdot \left( \frac{\sigma_y}{\sigma_{y,0}} \cdot \left( 1 - \alpha_m \cdot \frac{T}{T_g} \right) \right)^{1/2} \quad (2)$$

where the subscripts  $f$  and  $y$  refer to the fracture and yield stress, the subscript 0 refers to values at  $0^\circ\text{K}$ ,  $T$  is the temperature,  $T_g$  is the glass transition temperature, and  $\alpha_m$  is the temperature coefficient of the elas-

tic modulus [estimated from literature values (15)]. Equation 2 has an obvious temperature dependence but is also strain-rate dependent through the occurrence of the yield stress,  $\sigma_y$ .

A tensile failure diagram can now be constructed in the following way. At various strain rates and temperatures, Eqs 1 and 2, respectively, predict ductile and brittle failure stresses. For each set of conditions, the failure mode having the lower stress will prevail. In Fig. 1, tensile failure strength is plotted vs. temperature for three different strain rates. Values of all constants correspond to PVC (Tables 2 and 3). At each strain rate, there is a transition temperature below which failure is brittle and above which failure is ductile. This temperature appears as the break in slope in the strain-temperature curve. Table 4 compares predicted brittle-ductile transition temperatures for tensile failure to literature measurements.

The three pairs of transitions temperatures are noted from Fig. 1 and listed in Table 4. They are then plotted in Fig. 2, showing log strain versus temperature. In this strain rate versus temperature space, they partially map the brittle-to-ductile failure boundary. At low temperatures or high strain rates, brittle failure occurs; at high temperatures or low rates, ductile. For simplicity the three transition points are connected by line segments to approximate the entire boundary. The region to the right of this boundary consists of temperature-strain rate combinations expected to produce ductile failure; to the left, brittle failure.

This procedure is repeated for PET. Tensile failure strength is plotted versus temperature in Fig. 3 for the same three strain rates as above. The transition temperatures are tabulated in Table 4 and plotted in Fig. 4 to define the brittle-ductile transition in temperature-strain rate space. However, from Fig. 2, the tran-

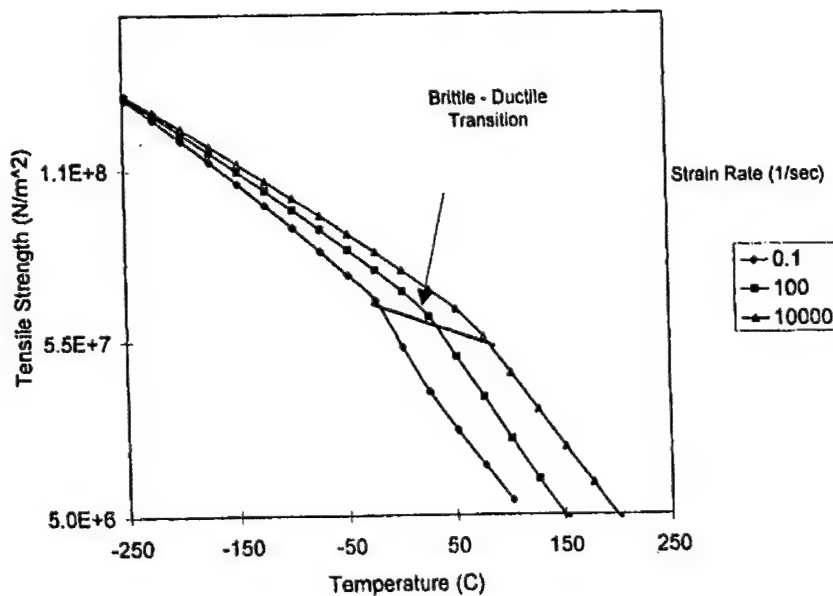


Fig. 1. Tensile failure mechanism diagram for PVC.

## Relationship Between Strain Rate, Temperature, and Impact Failure

Table 2. Constants for Tensile Yield Behavior Model.

Polymer	$v_1$ (m <sup>3</sup> )	$v_2$ (m <sup>3</sup> )	$H_1$ (J/mol)	$H_2$ (J/mol)	$\epsilon_{c1}$ (s <sup>-1</sup> )	$\epsilon_{c2}$ (s <sup>-1</sup> )
PVC	$3.1 \times 10^{-27}$	$2.15 \times 10^{-27}$	$2.95 \times 10^8$	$5.86 \times 10^4$	$1.0 \times 10^{34}$	$2.35 \times 10^9$
PET	$1.21 \times 10^{-27}$	$0.86 \times 10^{-27}$	$1.88 \times 10^8$	$7.15 \times 10^4$	$1.28 \times 10^{22}$	$1.94 \times 10^{14}$

PVC data from Brauwers-Crown et al. (16).

PET data from Foot et al. (17).

Table 3. Constants for Tensile Brittle Behavior Model.

Polymer	$T_g$ (°K)	$\alpha_m$	$\sigma_{f,0}$ (MPa)	$\sigma_{y,0}$ (MPa)	$E_0$ (GPa)
PVC	352	0.295 <sup>a</sup>	127 <sup>b</sup>	190 <sup>c</sup>	9.94 <sup>d</sup>
PET	337	0.295 <sup>a</sup>	282 <sup>b</sup>	368 <sup>c</sup>	10.0 <sup>d</sup>

<sup>a</sup>Assumed.

<sup>b</sup>Estimated.

<sup>c</sup>Calculated from  $E = E_0 \cdot (1 - \alpha_m \cdot \frac{T}{T_g})$

<sup>d</sup>Extrapolated, using data from Polymer Handbook (18).

<sup>e</sup>Obtained from EDD Database (19).

sition boundary for PVC is added to the plot for PET. Now there is a region between the two boundaries in which PET is expected to fail in a ductile mode and PVC in a brittle mode. That implies a range of temperature-strain rate conditions over which these two polymers should fail in different modes and might be separated as described above.

The shape of the potential processing window shown in Fig. 4 is interesting. It suggests that the required process be at a carefully controlled temperature ( $\pm 25^\circ\text{C}$ ), but that wide latitude is allowed in the deformation rate. The exact location of the window depends on the accuracy of Eqs 1 and 2, and the accompanying mechanical property constants of Tables 2 and 3. For example, a 20% increase in the value of the brittle failure stress at 0°K would decrease the transition by as much as 75°K for PET or 200°K for PVC (21). While these curves may not be perfectly correct, they do suggest a window exists, and they suggest a regime in which to look for it.

### Compressive Failure Diagrams

In some processing, failure may occur under compression. The same sort of procedure can be used to construct compressive failure diagrams. The compressive failure-mechanism behavior was modeled using Eqs 3 and 4, which are analogous to Eqs 1 and 2 for tensile failure.

### Plasticity

$$\sigma_y = \sigma_{y,0} \left( \frac{2+\alpha}{2} \right) \left[ 1 + \left( \frac{RT_g}{H} \right) \left( \frac{T}{T_g} \right) \ln \left( \frac{\dot{\epsilon}}{\dot{\epsilon}_0} \right) \right]^{1/2} \quad (3)$$

### Brittle Fracture

$$\sigma_f = \sigma_{f,0} \left[ \frac{\sigma_y}{\sigma_{y,0}} \left( 1 - \alpha_m \frac{T}{T_g} \right) \right]^{1/2} \quad (4)$$

Here,  $\alpha$  is the fractional difference between compressive and tensile strengths given by

$$\alpha = \frac{2 \cdot (\sigma_c - \sigma_t)}{(\sigma_c + \sigma_t)} \quad (5)$$

and  $\sigma_c$  and  $\sigma_t$  are the compressive and tensile strengths. The values of the parameters used in these equations are given in Tables 5 and 6. Compressive failure diagrams for PVC and PET were constructed in the same manner as the tensile failure diagrams.

Figure 5 shows the brittle-ductile transitions for both polymers in compressive failure. In contrast with Fig. 4 for tensile failure, PET will still exhibit brittle behavior at temperatures where PVC will begin to act in a

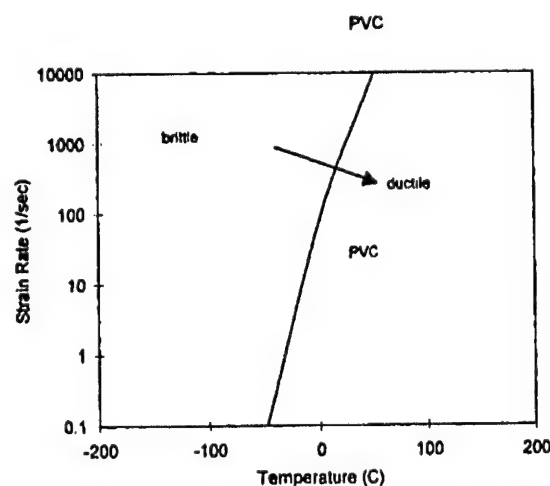


Fig. 2. Brittle-ductile transition for tensile failure: PVC.

Table 4. Brittle-Ductile Transition Temperatures for Tensile Failure.

Strain Rates (sec <sup>-1</sup> )	PVC		PET	
	Predicted	Literature [Vincent (20)]	Predicted	Literature [Foot (17)]
0.1	-48/-23°C	-25°C	-98/-73°C	-80°C
100	2/27°C	0°C	-48/-23°C	-20°C
10,000	52/77°C	—	2/27°C	—

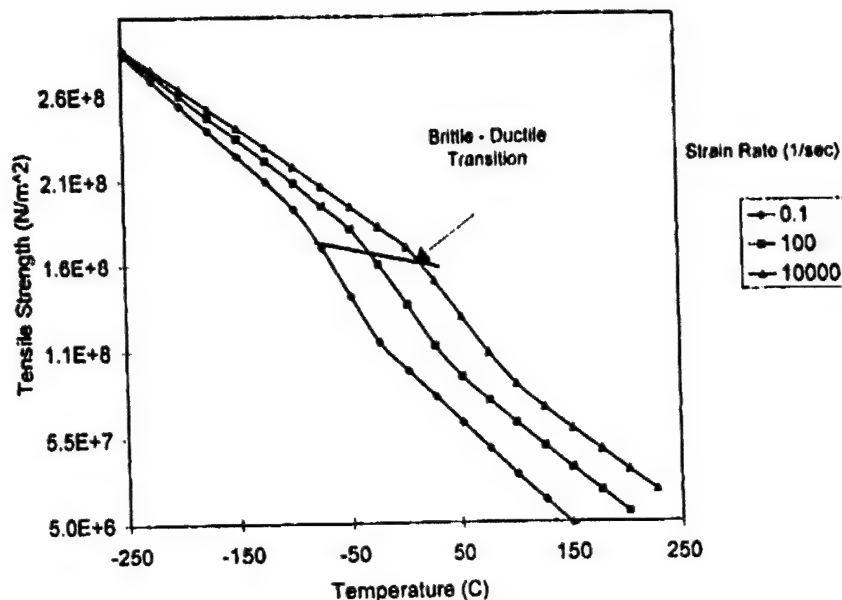


Fig. 3. Tensile failure mechanism diagram for PET.

ductile fashion. However, at any given temperature and strain rate, the compressive strength of PET is about twice that of PVC so that more energy needs to be applied to PET to obtain failure. Also, the brittle-ductile transitions for compression occur at much higher temperatures for those for tension. Therefore, at a given set of impact grinding conditions, the material is expected to fail under tension.

#### IMPACT TRANSITION TEMPERATURE ESTIMATIONS FROM $\beta$ -RELAXATION PROCESS

As the temperature of a polymer is lowered, various molecular motions (or relaxations) occur. The secondary relaxation, known as the  $\beta$ -relaxation process, and its corresponding temperature,  $T_\beta$ , have been related to transitions that are observed in impact behavior with changes in loading rate and temperature [Foot et al. (17); Yano and Yamaoka (4)]. The  $\beta$ -relaxation temperature occurs at the secondary peak below that of the glass transition temperature, and is associated with the motion of polymer side-groups. This process is evaluated by determining the dynamic mechanical responses at various temperatures using a free oscillating torsion pendulum. A method for estimating the brittle-ductile transition using the  $\beta$ -relaxation temperature as a function of the time to failure and temperature has been presented by Menges and Boden (22). The time to failure is given as

$$t_f = 1/(2\pi f) \quad (6)$$

where  $f$  is the frequency of the test. The time to failure,  $t_0$ , which is the inverse of the strain rate, is related to the temperature by

$$t = t_0 \cdot \exp\left(\frac{\Delta U}{RT}\right) \quad (7)$$

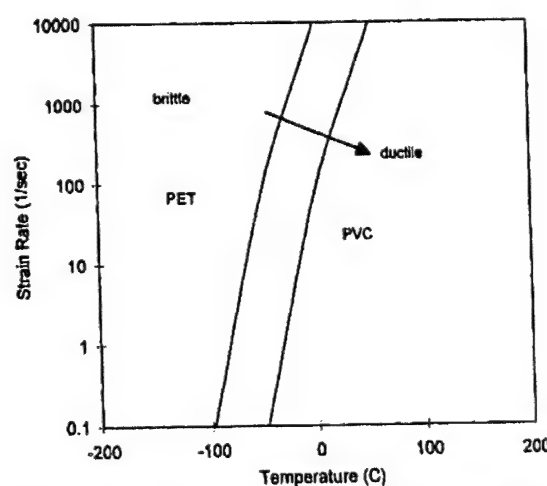


Fig. 4. Brittle-ductile transition for tensile failure: PVC and PET.

Table 5. Constants for Compressive Yield Behavior Model.

Polymer	$\sigma_c$ (MPa) <sup>a</sup>	$\sigma_t$ (MPa) <sup>a</sup>	H (J/mol)	$\varepsilon_0$ (s <sup>-1</sup> )
PVC	55.2	40.7	$2.95 \times 10^5$	$1.0 \times 10^{38}$
PET	75.8	48.3	$1.88 \times 10^5$	$1.28 \times 10^{22}$

<sup>a</sup>Modern Plastics Encyclopedia (6).

PVC data from Bauwens-Crowell et al. (18).

PET data from Foot et al. (17).

Table 6. Constants for Compressive Brittle Behavior Model.

Polymer	$T_g$ (K)	$\alpha_m$	$\sigma_{f,0}$ (MPa)	$\sigma_{y,0}$ (MPa)	$E_0$ (GPa)
PVC	352	0.295 <sup>a</sup>	127 <sup>b</sup>	190 <sup>c</sup>	9.94 <sup>d</sup>
PET	337	0.295 <sup>a</sup>	282 <sup>b</sup>	369 <sup>c</sup>	10.0 <sup>e</sup>

<sup>a</sup>Assumed.

<sup>b</sup>Estimated.

<sup>c</sup>Calculated from Eq 3.

<sup>d</sup>Extrapolated, using data from Polymer Handbook (18).

<sup>e</sup>Obtained from EDD Database (19).

## Relationship Between Strain Rate, Temperature, and Impact Failure

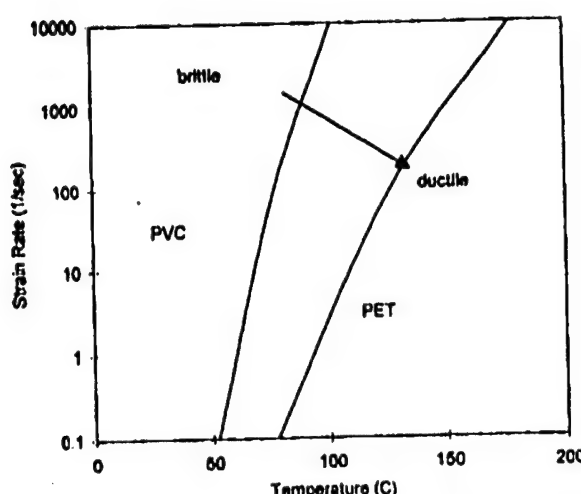


Fig. 5. Brittle-ductile transition for compressive failure: PVC and PET.

where  $t_0$  is the pre-exponential factor,  $\Delta U$  is the activation energy,  $R$  is the ideal gas constant, and  $T$  is the reference temperature. Values for  $T_\beta$  and  $\Delta U$  are listed in Table 7. The time constant,  $t_0$ , was calculated for  $T_\beta$  and a strain rate of  $0.160 \text{ sec}^{-1}$  (1 Hz). Equation 10 was rearranged to calculate the  $\beta$ -relaxation temperatures for a range of times to failure.

Figure 6 illustrates the brittle-ductile transitions for PVC and PET as functions of the temperature and strain rates. This Figure shows a processing window in which PET will fail in a ductile manner while PVC will fail in a brittle manner (similar to that predicted for tensile failures, Fig. 3). The region of brittle fracture is to the left of the transition line. The estimates for the brittle-ductile transitions for PVC are  $-80$  and  $-35^\circ\text{C}$  for strain rates typical of tension and Izod testing, respectively, while those for PET were  $-85$  and  $-60^\circ\text{C}$ . According to these values, PET will begin to exhibit ductile behavior at lower temperature than PVC. At a time to failure of  $100 \mu\text{s}$ , which is comparable to the time scale for deformation during impact grinding, the brittle-ductile transition for PVC is estimated to be about  $12^\circ\text{C}$  for PVC and  $-35^\circ\text{C}$  for PET. These predictions of the brittle-ductile transition were compared to data from Izod ( $\dot{\epsilon} \sim 10^2 \text{ s}^{-1}$ ), impact grinding ( $\dot{\epsilon} \sim 10^4 \text{ s}^{-1}$ ) and ballistics ( $\dot{\epsilon} \sim 10^5 \text{ s}^{-1}$ ) tests. These strain rates bracket the range expected in typical impact grinding equipment. The experimental methods are described in the following section.

Table 7.  $\beta$ -Relaxation Temperature and Activation Energy.

Material	$T_\beta$ at 1 Hz (K)	$\Delta U$ (kJ/mol)	$t_0$ (s)
PVC	218 <sup>a</sup>	54.4 <sup>a</sup>	$1.46 \times 10^{-14}$
PET	200 <sup>b</sup>	71.5 <sup>c</sup>	$3.39 \times 10^{-20}$

<sup>a</sup>Menges (22).

<sup>b</sup>Armeniades (23).

<sup>c</sup>Foot (17).

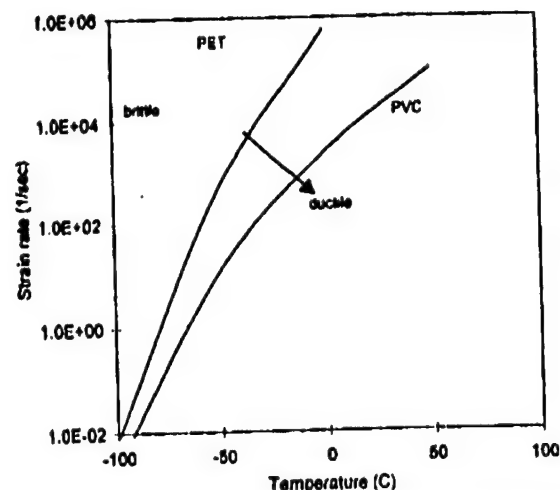


Fig. 6. Brittle-ductile transition predicted by  $\beta$ -relaxation temperature.

## IMPACT TESTING METHODS

### Izod Impact

#### Materials

Post-consumer bottle flakes of PVC and PET were utilized for these experiments. PET flakes were dried and then injection molded at about  $260^\circ\text{C}$  into impact specimens for the Izod impact tests. PVC impact specimens were injection molded at about  $185^\circ\text{C}$  from general-purpose Geon PVC containing 25% recycled content. The specimens had a width of 12.7 mm (0.5 in.), a length of 63.5 mm (2.5 in.), and a thickness of 3.17 mm (0.125 in.).

#### Equipment

A notch cutter (Testing Machine Inc., Model TMI 22-05) was used to produce the stress-concentrator indentation on the samples. The samples were impacted on an Izod impactor (Testing Machines Inc., Model 43-02). A 10 lb pendulum was used for the PVC samples, while a 1 lb pendulum was used for the PET samples. The morphology of fracture surfaces were evaluated using a JEOL T-330 scanning electron microscope (SEM) to determine the failure mechanisms of each specimen.

The impact testing was conducted according to the ASTM-D256 standard. Each desired test temperature was obtained by placing a sample in a Nalgene Dewar containing a heat-transfer medium for 3 min. The Dewar temperature was adjusted by placing dry ice in a methanol bath below room temperature, or an immersion heater in a water bath above room temperature.

### Impact Grinding

Impact grinding experiments were done on chips from post-consumer bottles of PVC and PET. The grinder was a Bantam Mikro-Pulverizer (Micron Powder Systems) impact grinder with carbide-tipped hammers

on a 12.5 mm radius. The rotation speed could be varied from 8000 to 14,000 rpm (53 to 93 m/s). Chips were fed to the mill using an auger system. The temperature of the bottle flakes was varied from -196 to 80°C by using liquid nitrogen, refrigeration or heating in an oven. The precise temperature of the chips at the point of impact could not be controlled. However, a thermocouple in the exit stream from the mill provided the mill outlet temperature, which was representative of the chip temperature. Three mill outlet temperatures, 0, 22, and 80°C, were achieved with the equipment.

### High Speed Video

A high speed motion analyzer system (Kodak Ektapro 1012 Motion Analyzer: video imager, macrofocussing zoom lens, video monitor, VCR and printer) was used to observe particles in the grinding chamber. A 12-mm-thick transparent acrylic window was fitted to the grinder. The comminution was recorded at 1000 - 6000 frames per second (fps) using a 67 mm diameter lens with a macrofocussing zoom.

### Taylor Testing

#### Materials

PET and PVC rods 9.53 mm (0.375 in.) in diameter were cut to lengths of 38.1 mm (1.5 in.), 57.15 mm (2.25 in.), and 76.2 mm (3 in.) and used as projectiles. Samples were tested at room temperature.

#### Ballistics Testing

The PVC and PET projectiles were accelerated using a powder charge from a gun at velocities of 300 to 600 m/s toward a massive steel anvil. Velocities were measured by a light beam method, and could be changed by altering the amount of powder charge used. The final lengths and appearances of the samples were noted. SEM was used to observe the failure mechanisms of the materials.

#### Scanning Electron Microscopy

Failure surfaces were examined using a JEOL scanning electron microscope. Specimens were covered with gold by sputtering to reduce surface charging.

#### CHARACTERISTIC STRAIN RATES OF IMPACT TESTS

Strain rates can be scaled using characteristic velocities and sample dimensions (13). The Izod test has a well-defined geometry in which the center of the sample is loaded. Owing to the low strain rate, some flexing of the beam may occur prior to fracture. In this case, the strain rate should be related to the sample dimensions by

$$\dot{\epsilon} = \frac{6 \cdot D \cdot v}{L^2} \quad (8)$$

where  $\dot{\epsilon}$  is the strain rate,  $D$  is the depth of the beam,  $L$  is the span of the support points, and  $v$  is the velocity of impact (based on an impact on the middle of a simply supported beam).

Equation 8 might be applied to the case of a thin plastic chip being impacted by a hammer in a grinding operation if the particle deforms significantly prior to failure. High speed video of single particle breakage in the hammer mill showed that PVC particles broke into fragments with little or no apparent flexing. Usually, these particles fractured within two or three impacts. PET chips also broke into fragments with little or no apparent flexing. However, more than five hits were required for most PET particles to fragment. When the residence time in the grinding chamber was short, many chips left the grinder without being broken. PET chips often showed internal crazing, which was consistent with the previously described mechanism for dynamic stress fracture. The primary breakage mechanism was particle-hammer. Particle-wall impacts did not seem to result in fracture, and projected particles back into the hammer path.

The high speed video information and the particle morphologies after grinding were used to model the fracture process for an estimate of the strain rate. The PVC chip dimensions of 7.6 mm diameter and 0.7 mm thickness meant that most of the area available for hammer impact was the flat surface (about 85%) rather than the edge. Chip fracture was probably due to the movement of the shock wave through the thickness of the particle. The PET chip dimensions of 4.6 mm diameter and 0.7 mm thickness gave about two-thirds of the surface area as flat surface. For these chip geometries, the characteristic strain rate was estimated as the velocity of the hammer divided by the chip thickness.

$$\dot{\epsilon} = \frac{v}{t} \quad (9)$$

The characteristic strain rates varied from 70,000 to 140,000 s<sup>-1</sup> for the chips and rotation speeds used in the impact grinding experiments. These estimates represented maximum values because they assume that all samples were struck perpendicular to the flat surface.

The calculation of characteristic strain rates for Taylor tests is a matter of much debate (24-27). There is a wide range of strain rates throughout the sample during the deformation process. For cases in which the test produces consistent shapes, strains can be estimated by the specimen's final geometry. In our experiments, however, the PVC projectiles often recovered entirely from their deformed shape back to their initial geometry. The PET projectiles, on the other hand, often shattered into fragments. However, it was possible to determine the lengths of the deformed and undeformed PET specimen, and estimate its total deformation. For the case of mushrooming projectiles, Hawkyard (24) has estimated the total strain in the

## Relationship Between Strain Rate, Temperature, and Impact Failure

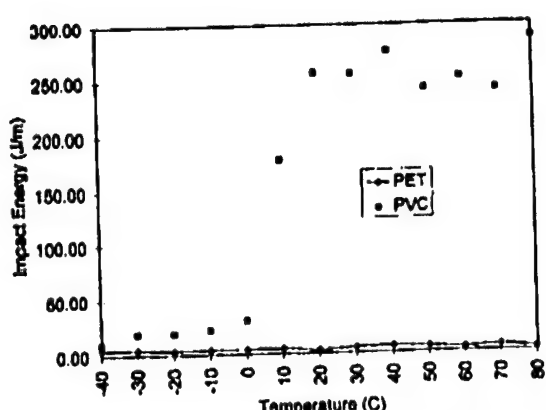


Fig. 7. Izod impact strength for PVC and PET at various temperatures.

sample by relating the kinetic energy balance to the sample's undeformed length. A characteristic strain rate can be calculated by dividing the projectile velocity by the original length of the deformed material.

$$\dot{\varepsilon} = \frac{v}{l_{\text{deformed}}} \quad (10)$$

Strain rates calculated by Eq. 10 for PVC samples ranged from 6000 to 15,000  $\text{s}^{-1}$  and for PET samples ranged from 5000 to 15,000  $\text{s}^{-1}$  under the conditions of our tests. These estimates were lower bounds since they did not describe the large strain rates that occurred as the sample began to deform.

## COMPARISON OF EXPERIMENTS TO THEORY

### Izod Impact Failure

**Poly(Vinyl Chloride).** Strength versus testing temperature is shown in Fig. 7. The amount of energy required to break a PVC test specimen varies widely with temperature. At temperatures less than  $-10^{\circ}\text{C}$ , the impact strengths were low and were all less than 27 J/m. Scanning electron photomicrographs of the fracture surface showed characteristics typical of brittle

fracture. Figure 8 shows the surface for samples tested at  $-40^{\circ}\text{C}$ . There is a sharp fracture edge, and no obvious necking—which is consistent with brittle fracture.

There was a step change in PVC Izod Impact strength over the temperature range,  $0^{\circ}\text{C} < T < 20^{\circ}\text{C}$ . The impact energy increased by an order of magnitude. Inspection of the samples of PVC specimens tested above  $0^{\circ}\text{C}$  showed that only partial breaks occurred. Fracture surfaces were whitish in color from deformation during impact, which is consistent with a ductile failure mechanism. Scanning electron photomicrographs taken for samples tested at 0, 20, and  $80^{\circ}\text{C}$  all showed ductile fracture. Figure 9 ( $20^{\circ}\text{C}$ ) shows obvious necking. The circular depressions are similar in size to PVC suspension macroparticles. At temperature above  $20^{\circ}\text{C}$ , the Izod impact strength is independent of temperature and ductile failure occurs. The PVC brittle-ductile transition temperature predicted by the tensile failure mechanism and the  $\beta$ -relaxation diagrams for strain rates typical of the Izod test is confirmed by these experiments.

**Poly(Ethylene Terephthalate).** The PET impact test specimens all break via a brittle fracture mechanism over the temperature range,  $-40$  to  $80^{\circ}\text{C}$ . Scanning electron photomicrographs of all fracture surfaces were quite similar (Fig. 10), showing no obvious necking even at high magnification. The tensile failure mechanism and  $\beta$ -relaxation diagrams predict a brittle-ductile transition in the range of  $-48$  to  $-23^{\circ}\text{C}$ . This transition was not observed by our Izod tests.

### Impact Grinding

Scanning electron microscopy was used to determine the type of fracture for each grinding condition. At room temperature and higher, PVC particles failed in a ductile manner with obvious signs of plastic yielding. At a mill outlet temperature of  $0^{\circ}\text{C}$ , the PVC particles had more distinct crack patterns identifiable with brittle fracture. The brittle-ductile transition occurred between 0 and  $25^{\circ}\text{C}$ . This was similar to the transition temperature observed in the Izod test, and

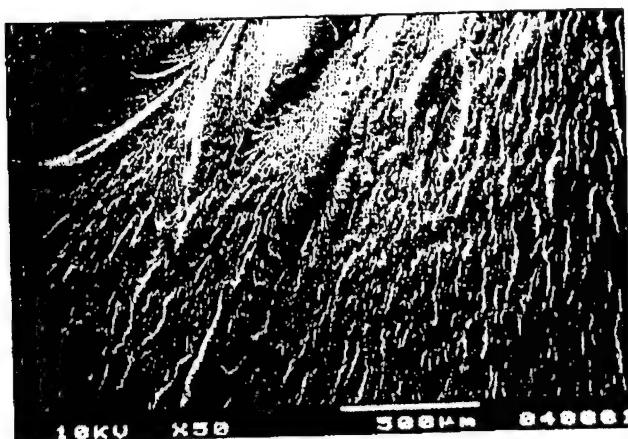


Fig. 8. SEM ( $\times 50$ ) of PVC Izod test specimen impacted at  $-40^{\circ}\text{C}$ .

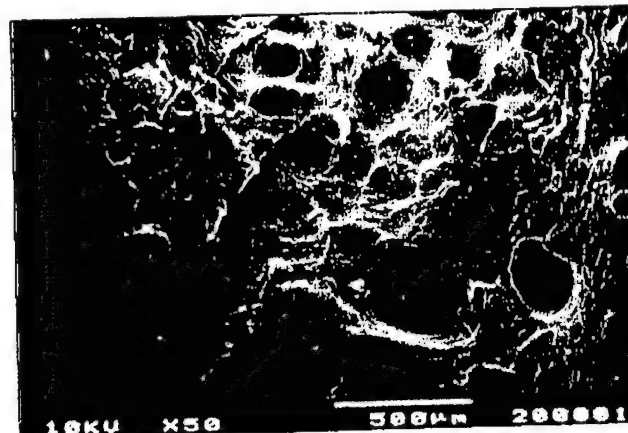


Fig. 9. SEM ( $\times 50$ ) of PVC Izod test specimen impacted at  $20^{\circ}\text{C}$ .

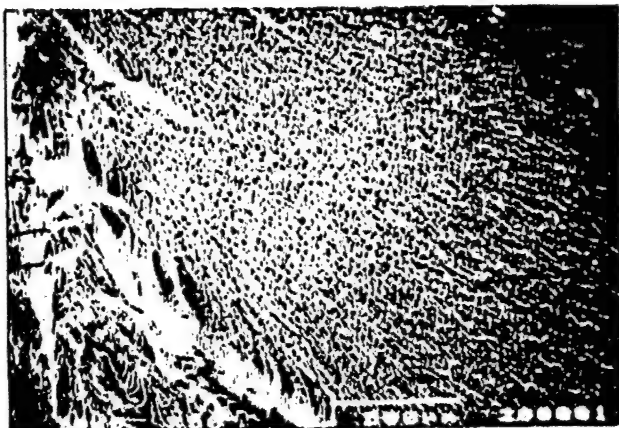


Fig. 10. SEM ( $\times 50$ ) of PET Izod test specimen impacted at 20°C.

it was lower than that predicted by the tensile failure mechanism diagram. When PVC failed in a brittle manner, its progeny particles had a lower aspect ratio compared with the parent particles than for ductile failure samples.

PET particles showed ductile yielding at room temperature and higher. At a mill outlet temperature of 0°C, its fracture surfaces showed characteristics of both brittle and ductile fracture. Yano and Yamaoka (4) reported that PET's nodular structure and small isometric crystallites might increase its ductility by providing an energy-absorbing structure. Chips which had been impacted but which had not fragmented showed a number of internal crazes when examined optically. These crazes were consistent with the dynamic stress fracture mentioned previously.

#### Taylor Impact Tests

The failure mechanisms of PVC and PET were the same as observed for Izod impacting at room temperature. The PVC samples deformed and decreased in length, while the PET samples shattered. The SEM

photographs in Figs. 11 and 12 depict the yielding of the PVC material, and the brittle fractured surface of the PET material. The PVC material flowed, as if stretched. Higher projectile velocities led to adiabatic heating and decomposition in the PVC samples. The PET fracture surfaces had blunt edges from stable crack propagation. No adiabatic heating was observed in these samples.

The adiabatic heating failure of PVC was not anticipated from the failure mechanism diagrams or the impact grinding studies at apparently higher strain rates. PET was expected to fail ductilely rather than brittlely. These results suggest that there are effects of sample shape on the mechanism for failure which are not accounted for.

#### CONCLUSIONS

Brittle-ductile transition temperatures estimated by tensile failure mechanism diagrams predict a processing window of temperatures and strain rates in which PVC should fail in the brittle mode and PET should fail in the ductile mode. A similar processing window is predicted by  $\beta$ -relaxation temperatures. Impact grinding tests confirm the presence of such a processing window. The brittle-ductile transition temperature predicted for strain rates typical of the Izod test was confirmed for PVC but not for PET. The PVC transition for impact grinding conditions occurs at lower temperatures than predicted by the failure mechanism diagrams. The brittle-ductile transition of PET was not clearly observed under impact grinding conditions. Compression failure mechanism diagrams predict a reversal of the transition lines of the polymer pair, and do not agree with the impact test results. Taylor tests at room temperature show adiabatic heating for PVC and brittle fracture for PET. This paper has demonstrated that selective impact grinding of two homopolymers can be predicted from tensile testing and  $\beta$ -relaxation properties. Particle size distribution differences are reported and analyzed in a related paper (28).



Fig. 11. SEM of PVC Taylor test sample impacted at 398 m/s.

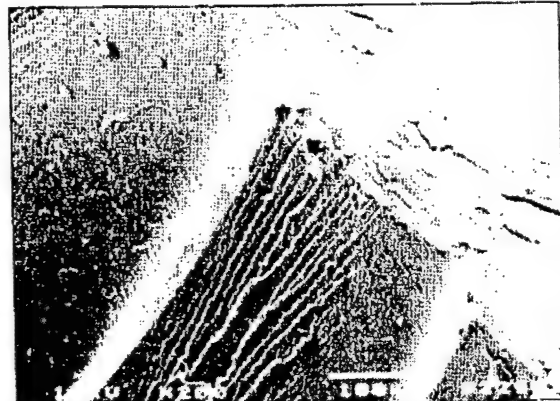


Fig. 12. SEM of PET Taylor test sample impacted at 369 m/s.

## ACKNOWLEDGMENTS

We would like to thank Mr. Alan Olson of the Geon Corporation for supplying samples of resin and chipped recycled bottles and Professor Stanley Jones of The University of Alabama for performing the Taylor impact tests. We acknowledge the following research sponsors: the Office of Naval Research, American Plastics Council, Michigan Materials Processing Institute, and the Research Excellence Fund and Summer Acceleration Fellowship Fund of Michigan State University.

## REFERENCES

1. D. Carlton, M S Thesis, Michigan State University (1995).
2. R. Famechon, "Separation of Waste PET and PVC for Recycling," Patent FR2643011, 1990.
3. P. Mapleton, "Cryogenics Improve PVC Separation," *Modern Plastics*, Nov. 1991, p. 32.
4. O. Yano and H. Yamaoka, *Progress in Polymer Science*, **20**, 585 (1995).
5. N. Bratton, *Cryogenic Recycling and Processing*, CRC Press, Boca Raton, Fla. (1980).
6. *Modern Plastics Encyclopedia '93*, McGraw-Hill, New York.
7. J. G. Williams, *Fracture Mechanics of Polymers*, Ellis Horwood, Chichester, United Kingdom (1984).
8. C. W. Macosko and G. J. Brand, *Polym. Eng. Sci.*, **12**, 444 (1972).
9. C. L. Beatty and J. L. Weaver, *Polym. Eng. Sci.*, **18**, 1109 (1978).
10. J. L. Weaver and C. L. Beatty, *Polym. Eng. Sci.*, **18**, 1117 (1978).
11. Z. Ahmad and M. Ashby, *J. Mater. Sci.*, **23**, 2037 (1988).
12. H. Kausch, *Polymer Fracture*, Springer-Verlag, Berlin (1987).
13. C. L. Prasher, *Crushing and Grinding Process Handbook*, Wiley, New York (1987).
14. D. A. Schockley, L. Seaman and D. R. Curran, in *Metallurgical Effects at High Strain Rates*, R. W. Rohde et al., eds., Plenum Press, New York (1973).
15. S. N. Kukureka, and I. M. Hutchings, *Int. J. Mech. Sci.*, **26**, 617 (1984).
16. C. Bauwens-Crowet, J. C. Bauwens, and G. Holmes, *J. Polym. Sci.: Part A-2*, **7**, 735 (1969).
17. J. S. Foot, R. W. Truss, I. M. Ward, and R. A. Duckett, *J. Mater. Sci.*, **22**, 1437 (1987).
18. J. Brandrup and E. H. Immergut, *Polymer Handbook*, Wiley Interscience (1986).
19. GE Plastics, *Engineering Design Database* (1992).
20. P. Vincent, *Polymer*, **1**, 425 (1960).
21. J. L. Green, PhD thesis, Michigan State University (1996).
22. G. Menges and H. Boden, "Deformation and Failure of Thermoplastics on Impact," in *Failure of Plastics*, W. Brostow and R. Corneliusen, eds., New York (1986).
23. C. Armeniades and I. Kurtyama, "Mechanical Behavior of Poly(ethylene terephthalate) at Cryogenic Temperatures," in *Cryogenic Properties of Polymers*, T. Serafini and J. Koenig, eds., Marcel Dekker, Inc., New York (1968).
24. J. B. Hawkyard, *Int. J. Mech. Sci.*, **11**, 313 (1969).
25. W. Johnson, A. K. Sengupta, S. K. Chosh, and S. R. Reid, "Mechanics of the High Speed Impact of Rods and Plates," in *Stress Transients in Solids*, J. S. Rinchart, ed., Hyperdynamics, Santa Fe, N.M. (1973).
26. R. A. Duckett, S. Rabinowitz and I. M. Ward, *J. Mater. Sci.*, **5**, 909 (1970).
27. J. Newton, "The High-Speed Impact Strength of Polymers," *Applied Polymer Symposium No. 17*, 95 (1971).
28. J. L. Green, C. A. Petty, and E. A. Grulke, "Impact Grinding of Thermoplastics. A Size Distribution Function Model," *Polym. Eng. Sci.*, in press (1997).

Received October 16, 1996  
Revised April 1997

## **APPENDIX L**

# Testing Machines and Strain Sensors

Joel W. House, Air Force Research Laboratory  
Peter P. Gillis, University of Kentucky

MECHANICAL TESTING MACHINES have been commercially available since 1886 (Ref 1) and have evolved from purely mechanical machines (like the popular "Little Giant" hand-cranked tensile tester of Tinius Olsen, circa 1900, shown in Fig. 1) to more sophisticated electromechanical and servohydraulic machines with advanced electronics and microcomputers. Electronic circuitry and microprocessors have increased the reliability of experimental data, while reducing the time to analyze information. This transition has made it possible to determine rapidly and with great precision ultimate tensile strength and elongation, yield strength, modulus of elasticity, and other mechanical properties. Current equipment manufacturers also offer workstation configurations that automate mechanical testing.

Conventional test machines for measuring mechanical properties include tension testers, compression testers, or the more versatile universal testing machine (UTM) (Ref 2). UTM's have the capability to test material in tension, compression, or bending. The word *universal* refers to the variety of stress states that can be studied. UTM's can load material with a single, continuous (monotonic) pulse or in a cyclic manner. Other conventional test machines may be limited to either tensile loading or compressive loading, but not both. These machines have less versatility than UTM equipment, but are less expensive to purchase and maintain. The basic aspects of UTM equipment and test-

ing generally apply to tension or compression testing machines as well.

This article reviews the current technology and examines force application systems, force measurement, strain measurement, important instrument considerations, gripping of test specimens, test diagnostics, and the use of computers for gathering and reducing data. Emphasis is placed on UTM's with some separate discussions of equipment factors for tensile testing and compression testing. The influence of the machine stiffness on the test results is also described, along with a general assessment of test accuracy, precision, and repeatability of modern equipment.

## Testing Machines

Although there are many types of test systems in current use, the most common are universal testing machines, which are designed to test specimens in tension, compression, or bending. The testing machines are designed to apply a force to a material to determine its strength and resistance to deformation. Regardless of the method of force application, testing machines are designed to drive a crosshead or platen at a controlled rate, thus applying a tensile or compressive load to a specimen. Such testing machines measure and indicate the applied force in pound-force (lbf), kilogram-force (kgf), or newtons (N). These customary force units are related by the following: 1 lbf = 4.44822 N; 1 kgf = 9.80665 N. All current testing machines are capable of indicating the applied force in either lbf or N (the use of kgf is not recommended).

The load-applying mechanism may be a hydraulic piston and cylinder with an associated hydraulic power supply, or the load may be administered via precision-cut machine screws driven by the necessary gears, reducers, and motor to provide a suitable travel speed. In some light-capacity machines (only a few hundred pounds maximum), the force is applied by an air piston and cylinder. Gear-driven systems obtain load capacities up to approxi-

mately 600 kN ( $1.35 \times 10^5$  lbf), while hydraulic systems can obtain forces up to approximately 4500 kN ( $1 \times 10^6$  lbf).

Whether the machine is a gear-driven system or hydraulic system, at some point the test machine reaches a maximum speed for loading the specimen. Gear driven test machines have a maximum crosshead speed limited by the speed of the electric motor in combination with the design of the gear box transmission. Crosshead speed of hydraulic machines is limited to the capacity of the hydraulic pump to deliver a steady pressure on the piston of the actuator or crosshead. Servohydraulic test machines offer a wider range of crosshead speeds; however, there are continuing advances in the speed control of screw-driven machines, which can be just as versatile as, or perhaps more versatile than, servohydraulic machines.

Conventional gear-driven systems are generally designed for speeds of about 0.001 to 500 mm/min ( $4 \times 10^{-6}$  to 20 in./min), which is suitable for quasi-static testing. Servohydraulic systems are generally designed over a wider range of test speeds, such as:

- 1  $\mu$ m/h test speeds for creep-fatigue, stress-corrosion, and stress-rupture testing
- 1  $\mu$ m/min test speeds for fracture testing of brittle materials
- 10 m/s (400 in./s) test speeds for dynamic testing of components like bumpers or seat belts

Servohydraulic UTM systems may also be designed for cycle rates from 1 cycle/day to over 200 cycles/s. Gear-driven systems typically allow cycle rates between 1 cycle/h and 1 cycle/s.

**Gear-driven (or screw-driven) machines** are electromechanical devices that use a large actuator screw threaded through a moving crosshead (Fig. 2). The screw is turned in either direction by an electric motor through a gear reduction system. The screws are rotated by a variable-control motor and drive the moveable crosshead up or down. This motion can load the specimen in either tension or compression, depending on how the specimen is to be held and tested.

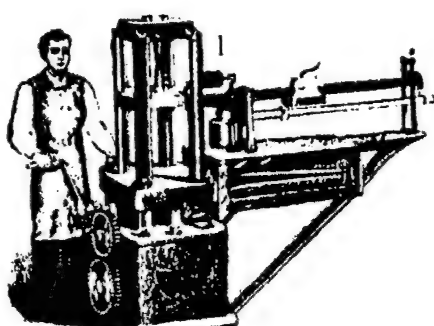


Fig. 1 "Little-Giant" hand-cranked tensile tester of Tinius Olsen, circa 1900

Screw-driven testing machines currently used are of either a one-, two-, or four-screw design. To eliminate twist in the specimen from the rotation of the screws in multiple-screw systems, one screw has a right-hand thread, and

the other has a left-hand thread. For alignment and lateral stability, the screws are supported in bearings on each end. In some machines, loading crossheads are guided by columns or guideways to achieve alignment.

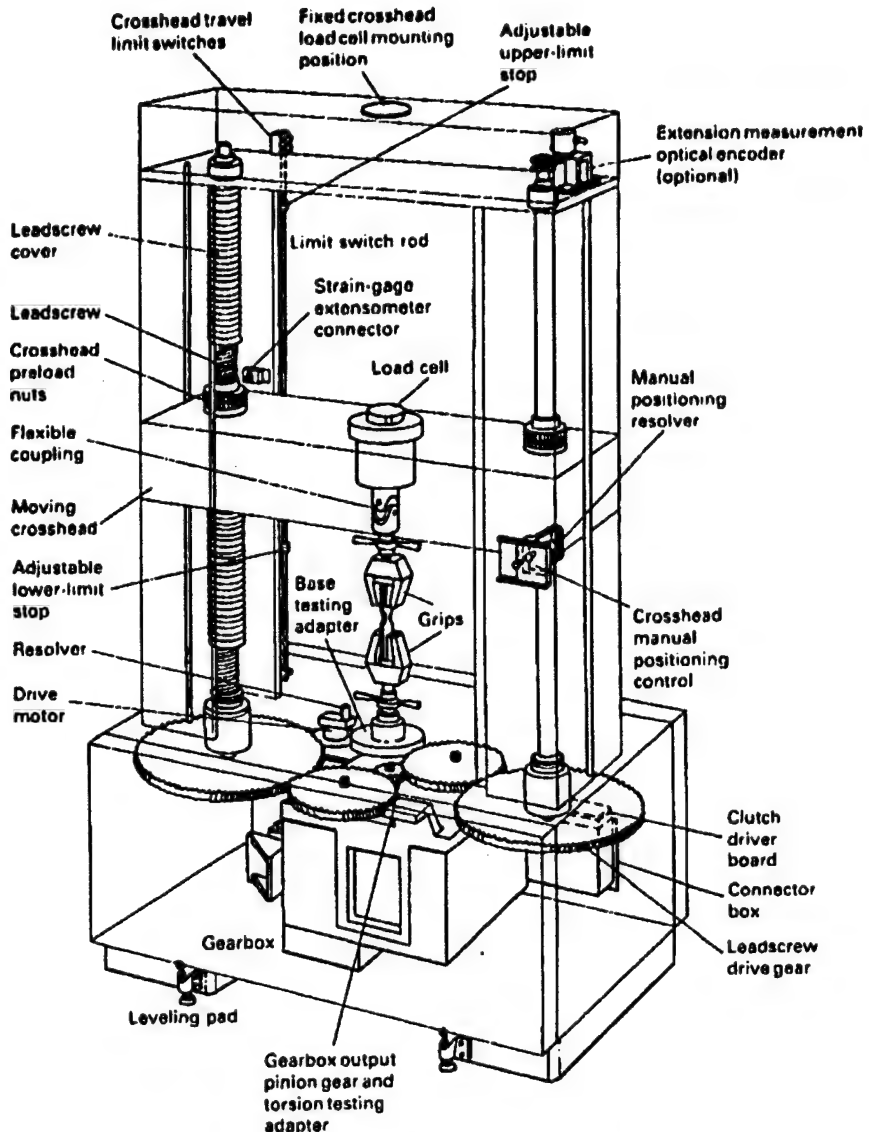


Fig. 2 Components of an electromechanical (screw-driven) testing machine. For the configuration shown, moving the lower (intermediate) head upward produces tension in the lower space between the crosshead and the base.

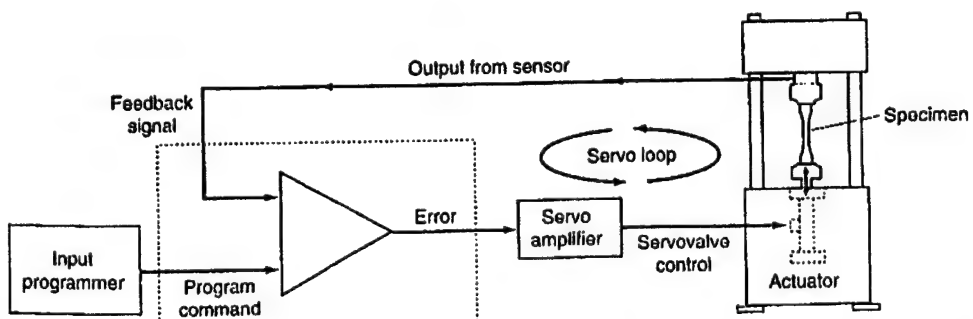


Fig. 3 Schematic of a basic servohydraulic, closed-loop testing machine

A range of crosshead speeds can be achieved by varying the speed of the electric motor and by changing the gear ratio. A closed-loop servodrive system ensures that the crosshead moves at a constant speed. The desired or user-selected speed and direction information is compared with a known reference signal, and the servomechanism provides positional control of the moving crosshead to reduce any error or difference. State-of-the-art systems use precision optical encoders mounted directly on preloaded twin ball screws. These types of systems are capable of measuring crosshead displacement to an accuracy of 0.125% or better with a resolution of 0.6  $\mu\text{m}$ .

As noted above, typical screw-driven machines are designed for speeds of 1 to 20  $\text{mm/min}$  (0.0394–0.788  $\text{in./min}$ ) for quasi-static test applications; however, machines can be designed to obtain higher speeds, although the useful force available for application to the specimen decreases as the speed of the crosshead motion increases. Modern high-speed systems generally are useful in ranges up to 500  $\text{mm/min}$  (20  $\text{in./min}$ ) (Ref 3). Nonetheless, top crosshead speeds of 1250  $\text{mm/min}$  (50  $\text{in./min}$ ) can be attained in screw-driven machines, and servohydraulic machines can be driven up to  $2.5 \times 10^5 \text{ mm/min}$  ( $10^4 \text{ in./min}$ ) or higher.

Due to the high forces involved, bearings and gears require particular attention to reduce friction and wear. Backlash, which is the free movement between the mechanical drive components, is particularly undesirable. Many instruments incorporate antibacklash preloading so that forces are translated evenly through the lead screw and crosshead. However, when the crosshead direction is constantly in one direction, antibacklash devices may be unnecessary.

Servohydraulic machines use a hydraulic pump and servohydraulic valves that move an actuator piston (Fig. 3). The actuator piston is attached to one end of the specimen. The motion of the actuator piston can be controlled in both directions to conduct tension, compression, or cyclic loading tests.

Servohydraulic test systems have the capability of testing at rates from as low as  $45 \times 10^{-11} \text{ m/s}$  ( $1.8 \times 10^{-9} \text{ in./s}$ ) to 30  $\text{m/s}$  (1200  $\text{in./s}$ ) or more. The actual useful rate for any particular system depends on the size of the actuator, the flow rating of the servovalve, and the noise level present in the system electronics. A typical servohydraulic UTM system is shown in Fig. 4.

Hydraulic actuators are available in a wide variety of force ranges. They are unique in their ability to economically provide forces of 4450  $\text{kN}$  (1,000,000 lbf) or more. Screw-driven machines are limited in their ability to provide high forces due to problems associated with low machine stiffness and large and expensive loading screws, which are increasingly more difficult to produce as the force rating goes up.

**Microprocessors for Testing and Data Reduction.** Contemporary UTMs are controlled by microprocessor-based electronics. One class of controller is based on dedicated micropro-

cessors for test machines (Fig. 4). Dedicated microprocessors are designed to perform specific tasks and have displays and input functions that are limited to those tasks. The dedicated microprocessor sends signals to the experimental apparatus and receives information from various sensors. The data received from sensors can be passed to oscilloscopes or computers for display and storage. The experimental results consist of time and voltage information that must be further reduced to analyze material behavior. Analysis of the data requires the conversion of test results, such as voltage, to specific quantities, such as displacement and load, based on known conversion factors.

The second class of controller is the personal computer (PC) designed with an electronic interface to the experimental apparatus, and the appropriate application software. The software takes the description of the test to be performed, including specimen geometry data, and establishes the requisite electronic signals. Once the test is underway, the computer controls the tests and collects, reduces, displays, and stores the data. The obvious advantage of the PC-based controller is reduced time to generate graphic results, or reports. The other advantage is the elimination of some procedural errors, or the reduction of the interfacing details between the operator and the experimental apparatus. Some systems are designed with both types of controllers. Having both types of controllers provides maximum flexibility in data gathering with a minimal amount of time required for reducing data when conducting standard experiments.

## Principles of Operation

The operation of a universal testing machine can be understood in terms of the main elements for any stress analysis, which include material response, specimen geometry, and load or boundary condition.

Material response, or material characterization, is studied by adopting standards for the other two elements. Specimen geometries, which are specific for tension, compression, or

bending tests, are described in separate sections at the end of this article. This section briefly describes load condition factors, such as strain rate, machine rigidity, and various testing modes by load control, speed control, strain control, and strain-rate control.

Strain rate, or the rate at which a specimen is deformed, is a key test variable that is controlled within prescribed limits, depending on the type of test being performed. Table 1 summarizes the general strain-rate ranges that are required for various types of property tests. Creep tests require low strain rates, while conventional (quasi-static) tension and compression tests require strain rates between  $10^{-5}$  and  $10^{-1} \text{ s}^{-1}$ .

A typical mechanical test on metallic materials is performed at a strain rate of approximately  $10^{-3} \text{ s}^{-1}$ , which yields a strain of 0.5 in 500 s. Conventional equipment and techniques generally can be extended to strain rates as high as  $0.1 \text{ s}^{-1}$  without difficulty. Tests at higher strain rates necessitate additional considerations of machine stiffness and strain measurement techniques. In terms of machine capability, servohydraulic load frames equipped with high-capacity valves can be used to generate strain rates as high as  $200 \text{ s}^{-1}$ . These tests are complicated by load and strain measurement and data acquisition.

If the crosshead speed is too high, inertia effects can become important in the analysis of the specimen stress state. Under conditions of high crosshead speed, errors in the load cell output and crosshead position data may become unacceptably large. A potential exists to damage load cells and extensometers under rapid loading. The damage occurs when the specimen fractures and the load is instantaneously removed from the specimen and the load frame.

At strain rates greater than  $200 \text{ s}^{-1}$ , the required crosshead speeds exceed the speeds easily obtained with screw-driven or hydraulic machines. Specialized high strain rate methods are discussed in more detail in the Section "High Strain Rate Testing" in this Volume.

**Determination of Strain Rates for Quasi-Static Tension Tests.** Strength properties for most materials tend to increase at higher rates of deformation. In order to quantify the effect of deformation rate on strength and other properties, a specific definition of strain rate is required. During a conventional (quasi-static) tension test, for example, ASTM E 8 "Tension Testing of Metallic Materials" prescribes an

upper limit of deformation rate as determined quantitatively during the test by one of the following methods (listed in decreasing order of precision):

- Rate of straining
- Rate of stressing (when loading is below the proportional limit)
- Rate of crosshead separation during the tests
- Elapsed time
- Free-running crosshead speed

For some materials, the free-running crosshead speed, which is the least accurate, may be adequate, while for other materials, one of the remaining methods with higher precision may be necessary in order to obtain test values within acceptable limits. When loading is below the proportional limit, the deformation rate can be specified by the "loading rate" units of stress per unit of time such that:

$$\dot{\sigma} = E\dot{\epsilon}$$

where, according to Hooke's law,  $\sigma$  is stress,  $E$  is the modulus of elasticity,  $\dot{\epsilon}$  is strain, and the superposed dots denote time derivatives.

ASTM E 8 specifies that the test speed must be low enough to permit accurate determination of loads and strains. When the rate of stressing is stipulated, ASTM E 8 requires that it not exceed 690 MPa/min (100 ksi/min). This corresponds to an elastic strain rate of about  $5 \times 10^{-5} \text{ s}^{-1}$  for steel or  $15 \times 10^{-5} \text{ s}^{-1}$  for aluminum. When the rate of straining is stipulated, ASTM E 8 prescribes that after the yield point has been passed, the rate can be increased to about  $1000 \times 10^{-5} \text{ s}^{-1}$ ; presumably, the stress rate limitation must be applied until the yield point is passed. Lower limits are also given in ASTM E 8.

In ASTM standard E 345, "Tension Testing of Metallic Foil," the same upper limit on the rate of stressing is recommended. In addition, a lower limit of 7 MPa/min (1 ksi/min) is given. ASTM E 345 further specifies that when the yield strength is to be determined, the strain rate must be in the range from approximately  $3 \times 10^{-5}$  to  $15 \times 10^{-5} \text{ s}^{-1}$ .

**Inertia Effects.** A fundamental difference between a high strain rate tension test and a quasi-static tension test is that inertia and wave propagation effects are present at high rates. An analysis of results from a high strain rate test thus requires consideration of the effect of stress wave propagation along the length of the test specimen in order to determine how fast a uniaxial test can be run to obtain valid stress-strain data.

For high loading rates, the strain in the specimen may not be uniform. Figure 5 illustrates an elemental length  $dx_0$  of a tension test specimen whose initial cross-sectional area is  $A_0$  and whose initial location is prescribed by the coordinate  $x$ . Neglecting gravity, no forces act on this element in its initial configuration. After the test has begun, the element is shown displaced by a distance  $u$ , deformed to new dimensions

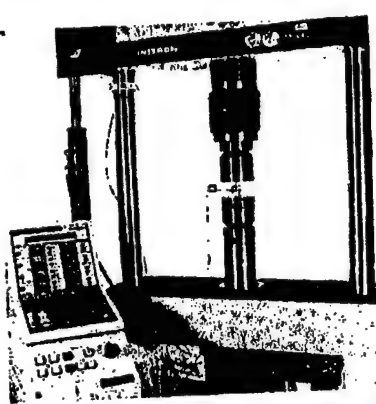


Fig. 4 Servohydraulic testing machine and load frame with a dedicated microprocessor-based controller

Table 1 Strain rate ranges for different tests

Type of test	Strain rate range, $\text{s}^{-1}$
Creep tests	$10^{-8}$ to $10^{-5}$
Pseudostatic tension or compression tests	$10^{-5}$ to $10^{-1}$
Dynamic tension or compression tests	$10^{-1}$ to $10^2$
Impact bar tests involving wave propagation effects	$10^2$ to $10^4$

Source: Ref 4

$dx$  and  $A$ , and subjected to forces  $F$  and  $F + dF$ . The difference,  $dF$ , between these end-surface forces causes the motion of the element that is manifested by the displacement,  $u$ . This motion is governed by Newton's second law, force equals mass times acceleration:

$$dF = \rho_0 A_0 dx_0 \left( \frac{d^2 u}{dt^2} \right) \quad (\text{Eq 1})$$

where  $\rho_0 A_0 dx_0$  is the mass of the element,  $A_0 dx_0$  is the volume,  $\rho$  is the density of the material, and  $(d^2 u / dt^2)$  is its acceleration. Tests that are conducted very slowly involve extremely small accelerations. Thus, Eq 1 shows that the variation of force  $dF$  along the specimen length is negligible.

However, for tests of increasingly shorter durations, the acceleration term on the right side of Eq 1 becomes increasingly significant. This produces an increasing variation of axial force along the length of the specimen. As the force becomes more nonuniform, so must the stress. Consequently, the strain and strain rate will also vary with axial position in the specimen. When these effects become pronounced, the concept of average values of stress, strain, and strain rate become meaningless, and the test results must be analyzed in terms of the propagation of waves through the specimen. This is shown in Table 1 as beginning near strain rates of  $10^2 \text{ s}^{-1}$ .

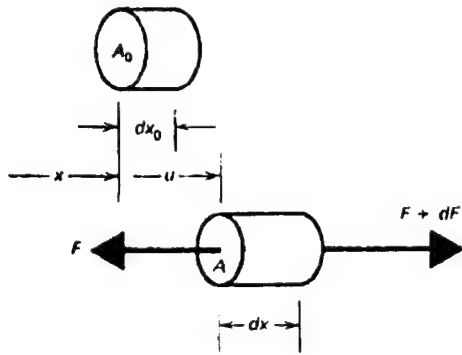


Fig. 5 The deformation of an elemental length,  $dx_0$ , of a tension test specimen of initial cross-sectional area,  $A_0$ , by a stress wave. The displacement of the element is  $u$ ; the differential length of the element as a function of time is  $dx$ ; the forces acting on the faces of the element are given by  $F$  and  $F + dF$ .

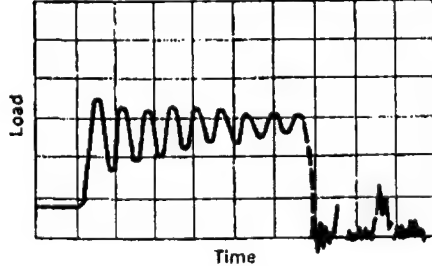


Fig. 6 Oscilloscope record of load cell force versus time during a dynamic tension test depicting the phenomenon of ringing. The uncontrolled oscillations result when the loading rate is near the resonant frequency of the load cell. The scales are arbitrary. Source: Ref 5

In an intermediate range of strain rates (denoted as dynamic tests in Table 1), an effect known as "ringing" of the load-measuring device obscures the interpretation of test data. An example of this condition is shown in Fig. 6, which is a tracing of load cell force versus time during a dynamic tensile test of a 2024-T4 aluminum specimen. Calculation showed that the oscillations apparent in the figure are consistent with vibrations at the approximate natural frequency of the load cell used for this test (Ref 5, 6).

In many machines currently available for dynamic testing, electronic signal processing is used to filter out such vibrations, thus making the instrumentation records appear much smoother than the actual load cell signal. However, there is still a great deal of uncertainty in the interpretation of dynamic test data. Consequently, the average value of the high-frequency vibrations associated with the load cell can be expected to differ from the force in the specimen. This difference is caused by vibrations near the natural frequency of the testing machine, which are so low that the entire test can occur in less than  $1/10$  of a cycle. Hence, these low-frequency vibrations usually are impossible to detect in a test record, but can produce significant errors in the analysis of test results. The ringing frequency for typical load cells ranges from 2400 to 3600 Hz.

**Machine Stiffness.** The most common misconception relating to strain rate effects is that the testing machine is much stiffer than the specimen. Such an assumption leads to the concept of deformation of the specimen by an essentially rigid machine. However, for most tests the opposite is true: the conventional tensile specimen is much stiffer than most testing machines. As shown in Fig. 7, for example, if crosshead displacement is defined as the relative displacement,  $\Delta$ , that would occur under conditions of zero load, then with a specimen gripped in a testing machine and the driving mechanism engaged, the crosshead displacement equals the deformation in the gage length of the specimen plus elastic deflections in components such as the machine frame, load cell, grips, and specimen ends. Before yielding, the gage length deformation is a small fraction of the crosshead displacement.

After the onset of gross plastic yielding of the specimen, conditions change. During this phase of deformation, the load varies slowly as the material strain hardens. Thus, the elastic deflections in the machine change slowly, and most of the relative crosshead displacement produces plastic deformation in the specimen. Qualitatively, in a test at approximately constant crosshead speed, the initial elastic strain rate in the specimen will be small, but the specimen strain rate will increase when plastic flow occurs.

Quantitatively, this effect can be estimated as follows. Consider a specimen having an initial cross-sectional area  $A_0$  and modulus of elasticity  $E$  gripped in a testing machine so that its axially stressed gage length initially is  $L_0$ . (This discussion is limited to the range of testing speeds where wave propagation effects are negligible. This restriction implies that the load is uniform throughout the gage length of the specimen.) Denote the stiffness of the machine, grips, and so on, by  $K$  and the crosshead displacement rate (nominal crosshead speed) by  $S$ . The ratio  $S/L_0$  is sometimes called the nominal rate of strain, but because it is often substantially different from the rate of strain in the specimen, the term specific crosshead rate is preferred (Ref 8).

Let loading begin at time  $t$  equal to zero. At any moment thereafter, the displacement of the crosshead must equal the elastic deflection of the machine plus the elastic and plastic deflections of the specimen. Letting  $s$  denote the engineering stress in the specimen, the machine deflection is then  $sA_0/K$ . It is reasonable to assume that Hooke's law adequately describes the elastic deformation of the specimen at ordinary stress levels. Thus, the elastic strain  $e_e$  is  $s/E$ .

Denoting the average plastic strain in the specimen by  $e_p$ , the above displacement balance can be expressed as:

$$\int_0^t S dt = s \left( \frac{A_0}{K} + \frac{L_0}{E} \right) + e_p L_0 \quad (\text{Eq 2})$$

Differentiating Eq 2 with respect to time and dividing by  $L_0$  gives:

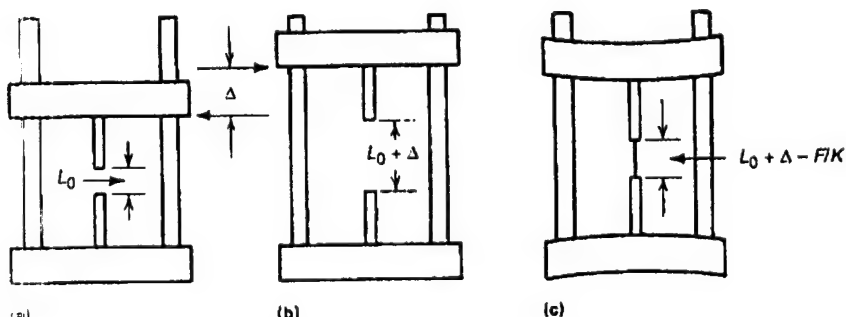


Fig. 7 Schematic illustrating crosshead displacement and elastic deflection in a tension testing machine.  $\Delta$  is the displacement of the crosshead relative to the zero load displacement;  $L_0$  is the initial gage length of the specimen;  $K$  is the composite stiffness of the grips, loading frame, load cell, specimen ends, etc.;  $F$  is the force acting on the specimen. The development of Eq 2 through 12 describes the effects of testing machine stiffness on tensile properties. Source: Ref 7

$$\frac{S}{L_0} = \left( \frac{S}{E} \right) \left( \frac{A_0 E}{K L_0} + 1 \right) + \dot{\epsilon}_p \quad (\text{Eq 3})$$

The strain rate in the specimen is the sum of the elastic and plastic strain rates:

$$\dot{\epsilon} = \dot{\epsilon}_e + \dot{\epsilon}_p = \left( \frac{S}{E} \right) + \dot{\epsilon}_p \quad (\text{Eq 4})$$

Using Eq 3 to eliminate the stress rate from Eq 4 yields:

$$\dot{\epsilon} = \frac{\left( \frac{S K}{A_0 E} + \dot{\epsilon}_p \right)}{\left( \frac{K L_0}{A_0 E} + 1 \right)} \quad (\text{Eq 5})$$

Thus, it is seen that the specimen strain rate usually will differ from the specific crosshead rate by an amount dependent on the rate of plastic deformation and the relative stiffnesses of the specimen ( $A_0 E / L_0$ ) and the machine,  $K$ .

**Accounting for Testing Machine Stiffness.** Machine stiffness is the amount of deflection in the load frame and the grips for each unit of load applied to the specimen. This deflection not only encompasses elastic deflection of the load frame, but includes any motion in the grip mechanism, or at any interface (threads, etc.) in the system. These deflections are substantial during the initial loading of the specimen, that is, through the elastic regime. This means that the initial crosshead speed (specified by the operator) is not an accurate measure of specimen displacement (strain). If the strain in the elastic regime is not accurately known, then extremely large errors may result in the calculation of Young's modulus ( $E$ , the ratio of stress versus strain in the elastic regime). In the analysis by Hockett and Gillis (Ref 9), the machine stiffness  $K$  is accounted for in the following equation:

$$K = \left( \frac{S}{P_0} - \frac{L_0}{A_0 E} \right)^{-1} \quad (\text{Eq 6})$$

where  $L_0$  is initial specimen gage length,  $S$  is crosshead speed of the testing machine,  $A_0$  is initial cross-sectional area of the specimen,  $P_0$  is specimen load rate ( $dF/dt = A_0 \dot{\sigma}$ ), and  $E$  is Young's modulus of the specimen material.

Research in this area showed that a significant amount of scatter was found in the measurement of machine stiffness. This variability can be attributed to relatively small differences in test conditions. For characterization of the elastic response of a material and for a precise measure of yield point, the influence of machine stiffness requires that an extensometer, or a bonded strain gage, be used. After yielding of the specimen material, the change of machine deflection is very small because the load changes slowly. If the purpose of the experiment is to study large strain behavior, then the error associated with the use of the crosshead displacement is small relative to other forms of experimental uncertainties.

**Control Modes.** During a test, control circuits and servomechanisms monitor and control

the key experimental conditions, such as force, specimen deformation, and the position of the movable crosshead. These are the key boundary conditions, which are analyzed to provide mechanical property data. These boundary conditions on the specimen can also be controlled in different ways, such as constant load control, constant strain control, and constant crosshead speed control. Constant crosshead speed is the most common method for tension tests.

**Constant Load Rate Testing.** With appropriate modules on a UTM system, a constant load rate test can be accomplished easily. In this configuration, a load-control module allows the machine with the constant rate of extension to function as a constant load rate device. This is accomplished by a feedback signal from a load cell, which generates a signal that automatically adjusts to the motion controller of the crosshead. Usually, the servomechanism system response is particularly critical when materials are loaded through the yield point.

**Constant Strain Rate Testing.** Commercial systems have been developed to control the experiment based on a constant rate of straining in the specimen. These systems rely on extensometers measuring the change in gage length to provide data on strain as a function of time. The resulting signal is processed to determine the current strain rate and is used to adjust the crosshead displacement rate throughout the test. Again, servomechanism response time is particularly critical when materials are taken through yield.

To maintain a constant average strain rate during a test, the crosshead speed must be adjusted as plastic flow occurs so that the sum ( $SK/A_0 E + \dot{\epsilon}_p$ ) remains constant. For most metallic materials at the beginning of a test, the plastic strain rate is ostensibly zero, and from Eq 5 the initial strain rate is:

$$\dot{\epsilon}_0 = \frac{\left( \frac{S_0}{L_0} \right)}{1 + \left( \frac{A_0 E}{K L_0} \right)} \quad (\text{Eq 7})$$

where  $S_0$  is the crosshead speed at the beginning of the test. For materials that have a definite yield,  $\dot{\epsilon} = 0$  at the yield point. Therefore, from Eq 3 and 4, the yield point strain rate is:

$$\dot{\epsilon}_1 = \left( \frac{S_1}{L_0} \right) \quad (\text{Eq 8})$$

where  $S_1$  is the crosshead speed at the yield point. Equating these two values of strain rate shows that the crosshead speed must be reduced from its initial value to its yield-point value by a factor of:

$$\frac{S_0}{S_1} = \left( 1 + \frac{A_0 E}{K L_0} \right) \quad (\text{Eq 9})$$

For particular measured values of machine stiffness given in Table 2, this factor for a standard 12.8 mm (0.505 in.) diameter steel specimen is typically greater than 20 and can be as high as 100. Only for specially designed machines will the relative stiffness of the machine

exceed that of the specimen. Even for wire-like specimens, the correspondingly delicate gripping arrangement will ensure that the machine stiffness is less than that of the specimen. Thus, large changes in crosshead speed usually are required to maintain a constant strain rate from the beginning of the test through the yield point.

Furthermore, for many materials, the onset of yielding is quite rapid, so that this large change in speed must be accomplished quickly. Making the necessary changes in speed generally requires not only special strain-sensing equipment, but also a driving unit that is capable of extremely fast response. The need for fast response in the driving system eliminates the use of screw-driven machines for constant strain-rate testing. Servohydraulic machines may be capable of conducting tests at constant strain rate through the yield point of a material.

Equation 9 indicates the magnitude of speed changes required only for tests in which there is no yield drop. For materials having upper and lower yield points, the direction of crosshead motion may have to be reversed after initial yielding to maintain a constant strain rate. This reversal may be necessary, because plastic strains beyond the upper yield point can be imposed at a strain rate greater than the desired rate by recovery of elastic deflections of the machine as the load decreases. For a description of yield point phenomena, see the article "Mechanical Behavior under Tensile and Compressive Loads" in this Volume.

Another important test feature related to the speed change capability of the testing machine is the rate at which the crosshead can accelerate from zero to the prescribed test speed at the beginning of the test. For a slow test this may not be critical, but for a high-speed test, the yield point could be passed before the crosshead achieves full testing speed. Thus, the crosshead may still be accelerating when it should be decelerating, and accurate information concerning the strain rate will not be obtained. With the advent of closed-loop servohydraulic machines and electromagnetic shakers, the speed at which the ram (crosshead) responds is two orders of magnitude greater than for screw-driven machines.

**Tests at Constant Crosshead Speeds.** Machines with a constant rate of extension are the most common type of screw-driven testers and are characterized by a constant rate of crosshead travel regardless of applied loads. They permit testing without speed variations that might alter test results; this is particularly important when testing rate-sensitive materials such as polymers, which exhibit different ultimate strengths and elongations when tested at different speeds.

Table 2 Experimental values of testing machine stiffness

Machine stiffness	Source	
kg/mm	lb/in.	
740	41,500	Ref 10
460	26,000	Ref 11
1800	100,000	Ref 12
1390-2970	77,900-166,500	Ref 13

For a gear-driven system, applying the boundary condition is as simple as engaging the electric motor with a gear box transmission. At this point, the crosshead displacement will be whatever speed and direction was selected. More sophisticated systems use a command signal that is compared with a feedback signal from a transducer monitoring the position of the crosshead. Using this feedback circuit, the desired boundary condition can be achieved.

Tension tests usually can be carried out at a constant crosshead speed on a conventional testing machine, provided the machine has an adequate speed controller and the driving mechanism is sufficiently powerful to be insensitive to changes in the loading rate. Because special accessory equipment is not required, such tests are relatively simple to perform. Also, constant crosshead speed tests typically provide as good a comparison among materials and as adequate a measure of strain-rate sensitivity as constant strain-rate tests.

Two of the most significant test quantities—yield strength and ultimate tensile strength—frequently can be correlated with initial strain rate and specific crosshead rate, respectively. The strain rate up to the proportional limit equals the initial strain rate. Thus, for materials that yield sharply, the time-average strain rate from the beginning of the test to yield is only slightly greater than the initial strain rate:

$$\dot{\epsilon}_0 = \left( \frac{S}{I_0} \right) \frac{1 + \frac{A_0 E}{K L_0}}{1 + \frac{A_0 E}{K L_0}} \quad (\text{Eq 10})$$

even though the instantaneous strain rate at yield is the specific crosshead rate:

$$\dot{\epsilon}_1 = \left( \frac{S}{L_0} \right) \quad (\text{Eq 11})$$

However, beyond the yield point, the stress rate is small so that the strain rate remains close to the specific crosshead rate (Eq 11). Thus, ductile materials, for which a rather long time will elapse before reaching ultimate strength, have a time-average strain rate from the beginning of the test to ultimate that is only slightly less than the specific crosshead rate. Also, because the load rate is zero at ultimate as well as at yield, the instantaneous strain rate at ultimate equals the specific crosshead rate.

During a test at constant crosshead speed, the variation of strain rate from initial to yield-point values is precisely the inverse of the crosshead speed change required to maintain a constant strain rate (Eq 9):

$$\frac{\dot{\epsilon}_1}{\dot{\epsilon}_0} = \left( 1 + \frac{A_0 E}{K L_0} \right) \quad (\text{Eq 12})$$

Consequently, in an ordinary tension test, the yield strength and ultimate tensile strength may be determined at two different strain rates, which can vary by a factor of 20 to 100, depending on machine stiffness. If a yield drop occurs, elastic recovery of machine deflections

will impose a strain rate even greater than the specific crosshead rate given by Eq 12.

A point of interest from the analysis involves testing of different sized specimens at about the same initial strain rate. Assuming that these tests are to be made on one machine under conditions for which  $K$  remains substantially constant, the crosshead speed must be adjusted to ensure that specimens of different lengths, diameters, or materials will experience the same initial strain rate. In the typical case where the specimen is much stiffer than the machine,  $(1 + A_0 E / K L_0)$  in Eq 10 can be approximated simply by  $(A_0 E / K L_0)$ , so that the initial strain rate is approximately  $\dot{\epsilon}_0 = S / A_0 E$ . Thus, specimens of various lengths, tested at the same crosshead speed, will generally experience nearly the same initial strain rate. However, changing either the specimen cross section or material necessitates a corresponding change in crosshead speed to obtain the same initial rate.

A change in specimen length has substantially the same effect on both the specific crosshead rate ( $S / L_0$ ) and the stiffness ratio of specimen to machine ( $A_0 E / K L_0$ ) and, therefore, has no net effect. For example, an increase in specimen length tends to decrease the strain rate by distributing the crosshead displacement over the longer length; however, at the same time, the increase in length reduces the stiffness of the specimen so that more of the crosshead displacement goes into deformation of the specimen and less into deflection of the machine. These two effects are almost exactly equal in magnitude. Thus, no change in initial strain rate is expected for specimens of different lengths tested at the same crosshead speed.

## Measuring Load

Prior to the development of load cells, testing machine manufacturers used several types of devices for the measurement of force. Early systems, some of which are still in use, employ a graduated balanced beam similar to platform-scale weighing systems. Subsequent systems have used Bourdon tube hydraulic test gages, Bourdon tubes with various support and assist devices, and load cells of several types. One of the most common load-measuring systems, prior to the development of load cells, was the displacement pendulum, which measured load by the movement of the balance displacement pendulum. The pendulum measuring system was used widely, because it is applicable to both hydraulic and screw-driven machines and has a high degree of reliability and stability. Many machines of this design are still in use, and they are still manufactured in Europe, India, South America, and Asia. Another widely used testing system was the Emery-Tate oil-pneumatic system, which accurately senses the hydraulic pressure in a closed, flat capsule.

**Load Cells.** Current testing machines use strain-gage load cells and pressure transducers. In a load cell, strain gages are mounted on precision-

machined alloy-steel elements, hermetically sealed in a case with the necessary electrical outlets, and arranged for tensile and/or compressive loading. The load cell can be mounted so that the specimen is in direct contact, or the cell can be indirectly loaded through the machine crosshead, table, or columns of the load frame. The load cell and the load cell circuit are calibrated to provide a specific voltage as an output signal when a certain force is detected. In pressure transducers, which are variations of strain-gage load cells, the strain-gaged member is activated by the hydraulic pressure of the system.

Strain gages, strain-gage load cells, and pressure transducers are manufactured to several degrees of accuracy; however, when used as the load-measuring mechanism of a testing machine, the mechanisms must conform to ASTM E 4, as well as to the manufacturer's quality standards. Load cells are rated by the maximum force in their operating range, and the deflection of the load cell must be maintained within the elastic regime of the material from which the load cell was constructed. Because the load cell operates within its elastic range, both tensile and compressive forces can be monitored.

Electronics provide a wide range of signal processing capability to optimize the resolution of the output signal from the load cell. Temperature-compensating gages reduce measurement errors from changes in ambient temperature. A prior knowledge of the mechanical properties of the material being studied is also useful to obtain full optimization of these signals.

Within individual load cells, mechanical stops can be incorporated to minimize possible damage that could be caused by accidental overloads. Also, guidance and supports can be included to prevent the deleterious effects of side loading and to give desired rigidity and ruggedness. This is important in tension testing of metals because of the elastic recoil that can occur when a stiff specimen fails.

**Calibration of Load-Measuring Devices.** Calibration of load-measuring devices refers to the procedure of determining the magnitude of error in the indicated loads. Only load-indicating mechanisms that comply with standard calibration methods (e.g., ASTM E 74) should be used for the load calibration and verification of universal testing machines (see the section "Force Verification of Universal Testing Machines" in this article).

Calibration of load-measuring devices for mechanical test machines is covered in specifications of several standards organizations such as:

Specification number	Specification title
ASTM E 74	Standard Practice for Calibration of Force-Measuring Instruments for Verifying the Force Indication of Testing Machines
EN 10002-3	Part 3: Calibration of Force-Proving Instruments Used for the Verification of Testing Machines
ISO 376	Metallic Materials—Calibration of Force-Proving Instruments Used for the Verification of Testing Machines
BS EN 10002-3	Calibration of Force-Proving Instruments Used for the Verification of Uniaxial Testing Machines

To ensure valid load verification, calibration procedures should be performed by skilled personnel who are knowledgeable about testing machines and related instruments and the proper use of calibration standards.

Load verification of load-weighing systems can be accomplished using methods based on the use of standard weights, standard weights and lever balances, and elastic calibration devices. Of these calibration methods, elastic calibration devices have the fewest inherent problems and are widely used. The two main types of elastic load-calibration devices are elastic proving rings and strain-gage load cells, as briefly described below.

The elastic proving ring (Fig. 8a, b) is a flawless forged steel ring that is precisely machined to a fine finish and closely maintained tolerances. This device has a uniform and repeatable deflection throughout its loaded range. Elastic proving rings usually are designed to be used only in compression, but special rings are designed to be used in tension or compression.

As the term "elastic device" implies, the ring is used well within its elastic range, and the deflection is read by a precise micrometer. Proving rings are available with capacities ranging from 4.5 to over 5000 kN (1000 to  $1.2 \times 10^6$  lbf). Their usable range is from 10 to 100% of load capacity, based on compliance with the ASTM E 74 verification procedure.

Proving rings vary in weight from about 2 kg (5 lb) to hundreds of kilograms (or several hundred pounds). They are portable and easy to use. After initial certification, they should be recalibrated and recertified at intervals not exceeding 2 years.

Proving rings are not load rings. Although the two devices are of similar design and construction, only proving rings that use a precise

micrometer for measuring deflection can be used for calibration. Load rings employ a dial indicator to measure deflection and usually do not comply with the requirements of ASTM E 74.

Calibration strain-gage load cells are precisely machined high-alloy steel elements designed to have a positive and predetermined uniform deflection under load. The steel load cell element contains one or more reduced sections, onto which wire or foil strain gages are attached to form a balanced circuit containing a temperature-compensating element.

Strain-gage load cells used for calibration purposes are either compression or tension-compression types and have built-in capacities ranging from about 0.4 to 4000 kN (100 to 1,000,000 lbf). Their usable range is typically from 5 to 100% of capacity load, and their accuracy is  $\pm 0.05\%$ , based on compliance with applicable calibration procedures, such as ASTM E 74. Figure 9 illustrates a load cell system used to calibrate a UTM. This particular system incorporates a digital load indicator unit.

**Comparison of Elastic Calibration Devices.** The deflection of a proving ring is measured in divisions that are assigned a value in lbf, kgf, or N. The force is then calculated in the desired units. Although the deflection of a load cell is given numerically and a force value can be assigned with a load cell reading, electric circuits can provide direct readout in lbf, kgf, or N. Thus, certified load cells are more practical and convenient to use and minimize errors in calculation.

In small capacities (5 to 20 kN, or 1000 to 5000 lbf), proving rings and load cells are of similar size and weight (2 to 5 kg, or 4 to 10 lb). In large capacities (2000 to 2700 kN, or 400,000 to 600,000 lbf), load cells are about one half the size and weight of proving rings. Proving rings are a single-piece, self-contained

unit. A load cell calibration kit consists of two parts: the load cell and the display indicator (Fig. 9). Although the display indicator is designed to be used with a load cell of any capacity, it can only be used with load cells that have been verified with it as a system.

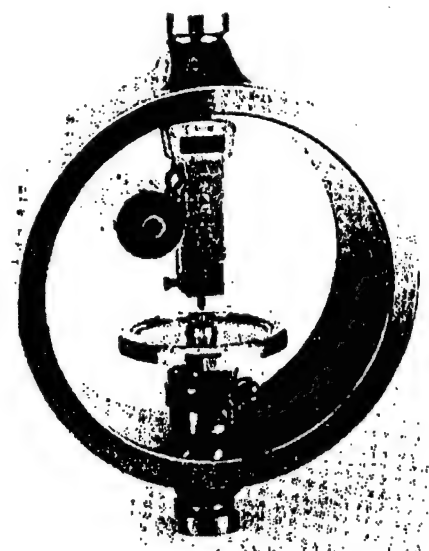
Although both proving rings and load cells are portable, the lighter weight and smaller size of high-capacity load cells enhance their suitability for general use. Load cells and their display indicators require a longer setup time; however, their direct readout feature reduces the overall calibration and reporting time. After initial certification, the load cell should be recalibrated after one year and thereafter at intervals not exceeding two years.

Both types of calibration devices are certified in accordance with the provisions of calibration standards. In the United States, devices are certified in accordance with ASTM E 74 and the verification values determined by the National Institute of Standards and Technology (NIST). NIST maintains a 1,000,000 lbf deadweight calibrator that is kept in a temperature- and humidity-controlled environment. This force-calibrating machine incorporates twenty 50,000 lb stainless steel weights, each accurate to within  $\pm 0.25$  lb. This machine, and six others of smaller capacities, are used to calibrate elastic calibrating devices, which in turn are employed to accurately calibrate other testing equipment.

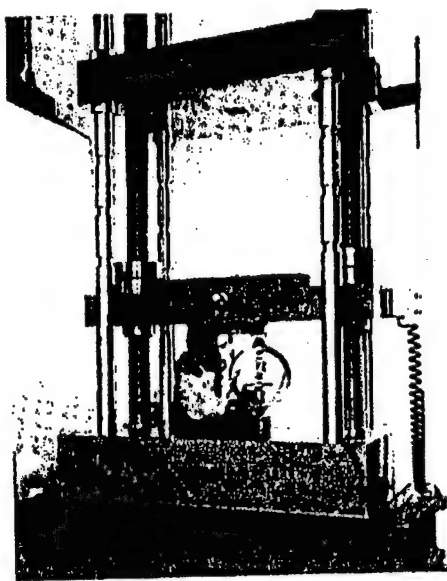
Elastic calibrating devices for verification of testing machines are calibrated to primary standards, which are weights. The masses of the weights used are determined to 0.005% of their values.

## Strain Measurement

Deformation of the specimen can be measured in several ways, depending on the size of



(a)



(b)

Fig. 8 Proving rings. (a) Elastic proving ring with precision micrometer for deflection/load readout. (b) Load calibration of 120,000 lbf screw-driven testing machine with a proving ring

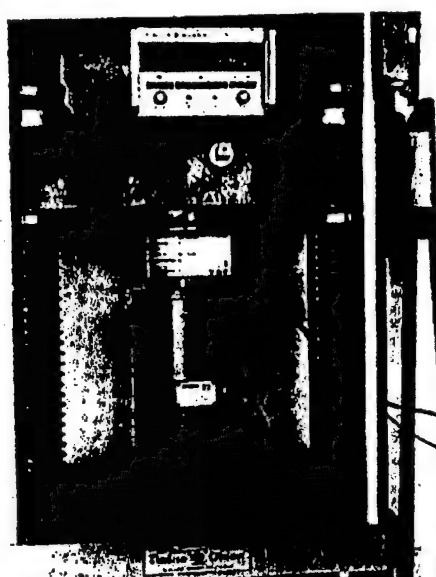


Fig. 9 Load cell and digital load indicator used to calibrate a 200,000 lbf hydraulic testing machine

specimen, environmental conditions, and measurement requirements for accuracy and precision of anticipated strain levels. A simple method is to use the velocity of the crosshead while tracking the load as a function of time. For the load and time data pair, the stress in the specimen and the amount of deformation, or strain, can be calculated. When the displacement of the platen is assumed to be equal to the specimen displacement, an error is introduced by the fact that the entire load frame has been deflected under the stress state. This effect is related to the concept of machine stiffness, as previously discussed.

**Extensometry.** The elongation of a specimen during load application can be measured directly with various types of devices, such as clip-on extensometers (Fig. 10), directly-mounted strain gages (Fig. 11), and various optical devices. These devices are used extensively and can provide a high degree of deformation- (strain-) measurement accuracy. Other more advanced instrumentations, such as laser interferometry and video extensometers, are also available.

Various types of extensometers and strain gages are described below. Selection of a device for strain measurement depends on various factors:

- The useable range and accuracy of the gage
- Techniques for mounting the gage
- Specimen size
- Environmental test conditions
- Electronic circuit configuration and analysis for signal processing

The last item should include the calibration of the extensometer device over its full operating range. In addition, one challenge of working

with clip-on extensometers is to ensure proper attachment to the specimen. If the extensometer slips as the specimen deforms, the resulting signal will give a false reading.

**Clip-on extensometers** can be attached to a test specimen to measure elongation or strain as the load is applied. This is particularly important for metals and similar materials that exhibit high stiffness. Typical extensometers have fixed gage lengths such as 25 or 50 mm (1 or 2 in.). They are also classified by maximum percent elongation so that a typical 25 mm (1 in.) gage length unit would have different models for 10, 50, or 100% maximum strain. Extensometers are used to measure axial strain in specimens. There also are transverse strain-measuring devices that indicate the reduction in width or diameter as the specimen is tested.

The two basic types of clip-on extensometers are linear variable differential transformer (LVDT) devices and strain-gage devices. These two types are described along with a description of earlier dial-type extensometers.

**Early extensometers** were held to the specimen with center points matching the specimen gage-length punch marks, and elongation was indicated between the points by a dial indicator. Because of mechanical problems associated with these early devices, most dial extensometers use knife edges and leaf-spring pressure for specimen attachment. An extensometer using a dial indicator to measure elongation is shown in Fig. 12. The dial indicator usually is marked off in 0.0025 mm (0.0001 in.) increments and measures the total extension between the gage points. This value divided by the gage length gives strain in mm/mm, or in./in.

**LVDT extensometers** employ an LVDT with a core, which moves from specimen deformation and produces an electrical signal propor-

tional to amount of core movement (Fig. 13). LVDT extensometers are small, light weight, and easy to use. Knife edges provide an exact point of contact and are mechanically set to the exact gage length. Unless the test report specifies total elongation, center punch marks or scribed lines are not required to define the gage length. They are available with gage lengths ranging from 10 to 2500 mm (0.4 to 100 in.) and can be fitted with breakaway features (Fig. 14), sheet metal clamps, low-pressure clamping arrangements (film clamps, as shown in Fig. 15), and other devices. Thus, they can be used on small specimens—such as thread, yarn, and foil—and on large test specimens—such as reinforcing bars, heavy steel plate, and tubing up to 75 mm (3 in.) in diameter.

Modifications of the LVDT extensometer also permit linear measurements at temperatures ranging from -75 to 1205 °C (-75 to 2200 °F). Accurate measurements can also be made in a vacuum. For standard instruments, the working temperature range is approximately -75 to 120 °C (-100 to 250 °F). However, by substituting an elevated-temperature transformer coil, the usable range of the instrument can be extended to -130 to 260 °C (-200 to 500 °F).

**Strain-gage extensometers**, which use strain gages rather than LVDTs, are also common and are lighter in weight and smaller in size, but strain gages are somewhat more fragile than LVDTs. The strain gage usually is mounted on a pivoting beam, which is an integral part of the extensometer. The beam is deflected by the movement of the extensometer knife edge when the specimen is stressed. The strain gage

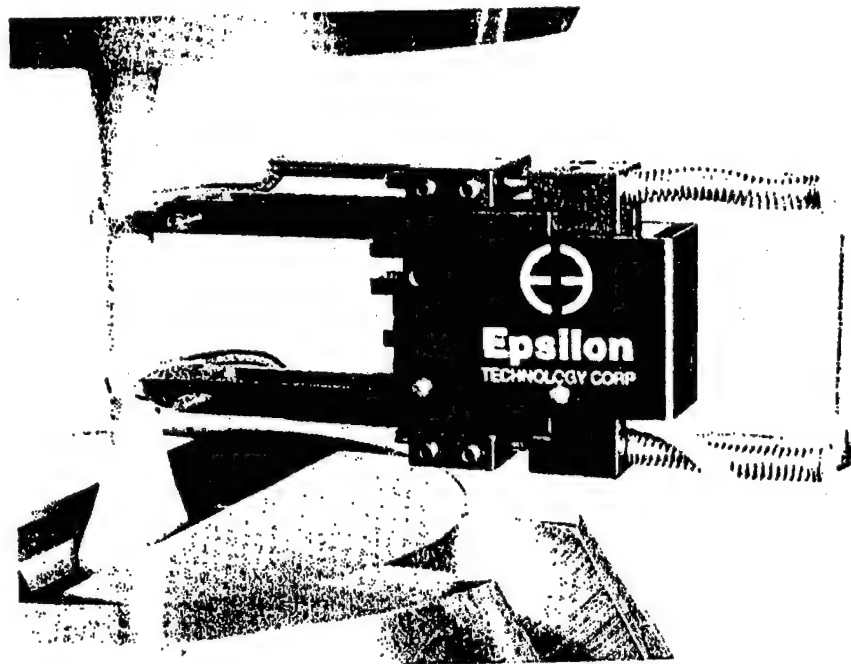


Fig. 10 Test specimen with an extensometer attached to measure specimen deformation. Courtesy of Epsilon Technology Corporation

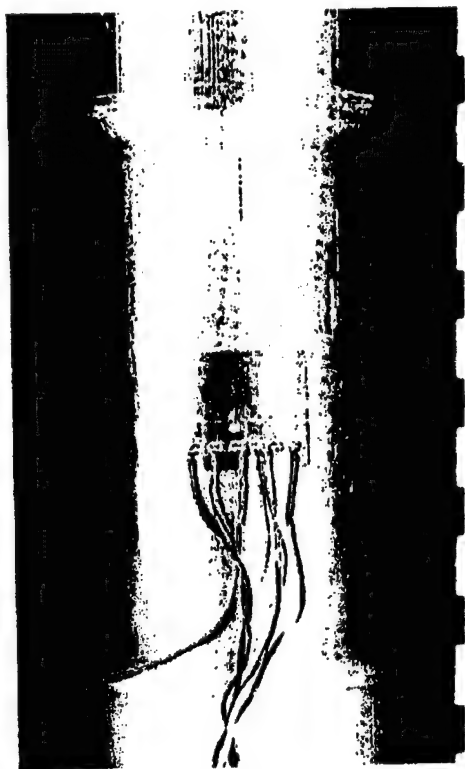


Fig. 11 Strain gages mounted directly to a specimen

attached to the beam is an electrically conductive small-sized grid that changes its resistance when deformed in tension, compression, bending, or torsion. Thus, strain gages can be used to supply the information necessary to calculate strain, stress, angular torsion, and pressure.

Strain gages have been improved and refined, and their use has become widespread. Basic types include wire gages, foil gages, and capacitive gages. Wire and foil bonded resistance strain gages are used for measuring stress and strain and for calibration of load cells, pressure transducers, and extensometers. These gages typically measure 9.5 to 13 mm ( $\frac{1}{2}$  to  $\frac{1}{2}$  in.) in width and 13 to 19 mm ( $\frac{1}{2}$  to  $\frac{3}{4}$  in.) in length and are adhesively bonded to a metal element (Fig. 16).

Operation of strain-gage extensometers is based on gages that are bonded to a metallic element and connected to a bridge circuit. Deflection of the element, due to specimen strain, changes the gage's resistance that produces an output signal from a bridge circuit. This signal is amplified and processed by signal conditioners before being displayed on a digital readout, chart recorder, or computer. The circuitry in the strain-measuring system allows multiple ranges of sensitivity, so one transducer can be used over broad ranges. The magnification ratio, which is the ratio of output to extensometer deflection, can be as high as 10,000 to 1.



Fig. 12 Dial-type extensometer, 50 mm (2 in.) gage length

**Strain Gages Mounted Directly to the Test Specimen.** For some strain measurements, strain gages are mounted on the part being tested (Fig. 11). When used in this manner, they differ from extensometers in that they measure average unit elongation over nominal gage length rather than total elongation between definite gage points. For some testing applications, strain gages are used in conjunction with extensometers (Fig. 16).

In conventional use, wire or foil strain gages, when mounted on structures and parts for stress analysis, are discarded with the tested item. Thus, strain gages are seldom used in production testing of standard tension specimens. Foil strain gages currently are the most widely used, due to the ease of their attachment.

**Averaging Extensometers.** Typically extensometers are either nonaveraging or averaging types. A nonaveraging extensometer has one fixed nonremovable knife edge or center point and one movable knife edge or center point on the same side of the specimen. This arrangement results in extension measurements that are taken on one side of the specimen only; such measurements do not take into account that elongation may be slightly different on the other side.

For most specimens, notably those with machined rounds or reduced gage length flats, there is no significant difference in elongation between the two sides. However, for as-cast specimens, high-modulus materials, some forged parts, and specimens made from tubing, a difference in elongation sometimes exists on opposite sides of the specimen when subjected to a tensile load. This is due to part configuration and/or internal stress. Misalignment of grips also contributes to elongation measurement

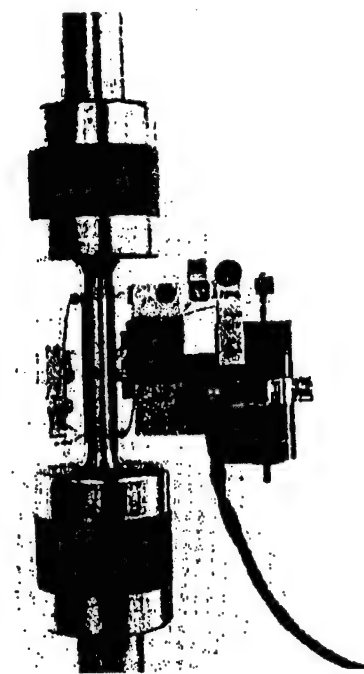


Fig. 13 Averaging LVDT extensometer (50 mm, or 2 in. gage length) mounted on a threaded tension specimen

variations in the specimen. For these situations, averaging extensometers are used. Averaging extensometers use dual-measuring elements that measure elongation on both sides of a sample; the measurements are then averaged to obtain a mean strain.

**Optical Systems.** Lasers and other systems can also be used to obtain linear strain measurements. Optical extensometers are particularly useful with materials such as rubber, thin films, plastics, and other materials where the weight of a conventional extensometer would distort the workpiece and affect the readings obtained. In the past, such strain-measuring systems were expensive, and their principal use has been primarily in research and development work. However, these optical techniques are becoming more accessible for commercial testing machines. For example, benchtop UTM systems with a laser extensometer are available (Fig. 17). This laser extensometer allows accurate measurement of strain in thin films, which would not otherwise be practical by mechanical attachment of extensometer devices. Optical systems also allow non-contact measurement from environmental test chambers.

**Calibration, Classification, and Verification of Extensometers.** All types of exten-

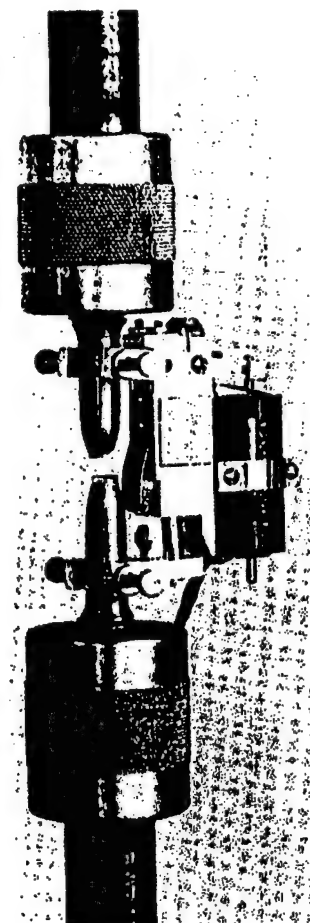


Fig. 14 Breakaway-type LVDT extensometer (50 mm, or 2 in. gage length) that can remain on the specimen through rupture

someters for materials testing must be verified, classified, and calibrated in accordance with applicable standards. Calibration of extensometers refers to the procedure of determining the magnitude of error in strain mea-

surements. Verification is a calibration to ascertain whether the errors are within a predetermined range. Verification also implies certification that an extensometer meets stated accuracy requirements, which are defined by classifications such as those in ASTM E 83 (Table 3).

Several calibration devices can be used, including an interferometer, calibrated standard gage blocks and an indicator, and a micrometer screw. Applicable standards for extensometer calibration or verification include:

Specification number	Specification title
DIN EN 10002-4	Part 4: Verification of Extensometers Used in Uniaxial Testing, Tensile Metallic Materials - Verification of Extensometers Used in Uniaxial Testing
ISO 9513	Verification of Extensometers Used in Uniaxial Testing
BS EN 10002-4	Verification of Extensometers Used in Uniaxial Testing
ASTM E 83	Standard Practice for Verification and Classification of Extensometers
BS 3846	Methods for Calibration and Grading of Extensometers for Testing of Materials

Verification and classification of extensometers are applicable to instruments of both the averaging and nonaveraging type.

Procedures for the verification and classification of extensometers can be found in ASTM E 83. It establishes six classes of extensometers (Table 3), which are based on allowable error deviations, as discussed later in this article. This standard also establishes a verification procedure to ascertain compliance of an instrument to a particular classification. In addition, it stipulates that a certified calibration apparatus must be used for all applied displacements and that the accuracy of the apparatus must be five times more precise than allowable classification errors. Ten displacement readings are required for verification of a classification.

*Class A extensometers*, if available, would be used for determining precise values of the modulus of elasticity and for precise measurements of permanent set or very slight deviations from Hooke's law. Currently, however, there are no commercially available extensom-

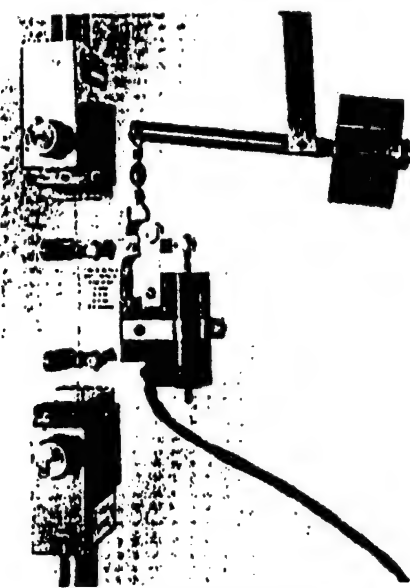


Fig. 15 Averaging LVDT extensometer (50 mm, or 2 in. gage length) mounted on a 0.127 mm (0.005 in.) wire specimen. The extensometer is fitted with a low-pressure clamping arrangement (film clamps) and is supported by a counterbalance device.

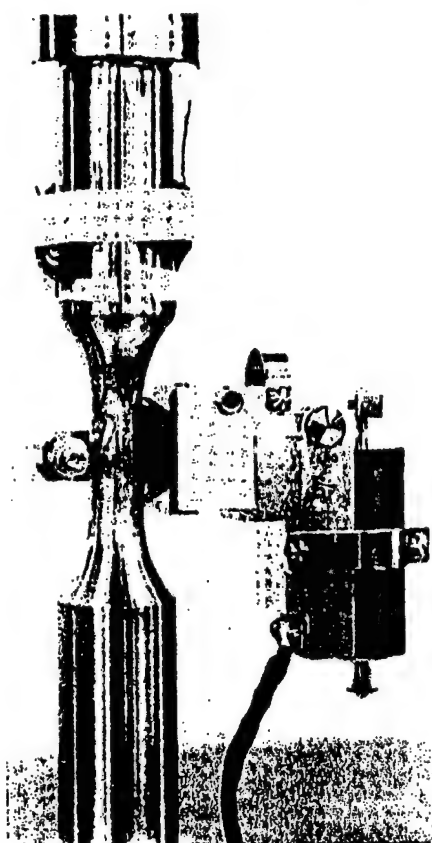


Fig. 16 Fatigue test specimen with bonded resistance strain gages and a 25 mm (1 in.) gage length extensometer mounted on the reduced section

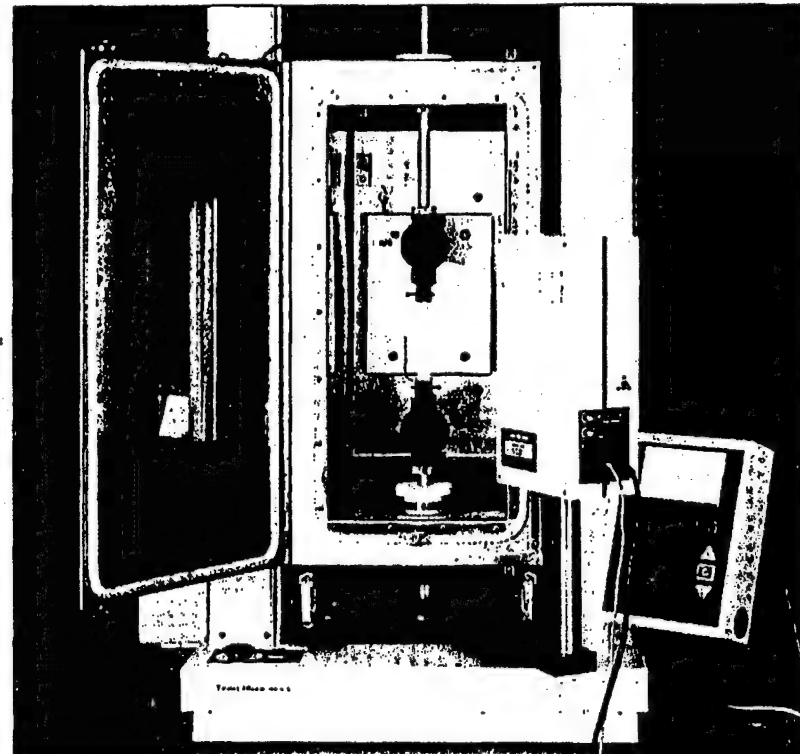


Fig. 17 Bench-top UTM with laser extensometer. Courtesy of Tinius Olsen Testing Machine Company, Inc.

eters manufactured that are certified to comply with class A requirements.

**Class B-1 extensometers** are frequently used to determine values of the modulus of elasticity and to measure permanent set or deviations from Hooke's law. They are also used for determining values such as the yield strength of metallic materials.

**Class B-2 extensometers** are used for determining the yield strength of metallic materials.

All LVDT and strain-gage extensometers can comply with class B-1 or class B-2 requirements if their measuring ranges do not exceed 0.5 mm (0.02 in.). Instruments with measuring ranges of over 0.5 mm (0.02 in.) can be class C instruments.

Most electrical differential transformer extensometers of 500-strain magnification and higher can conform to class B-1 requirements throughout their measuring range. Extensometers of less than 500-strain magnification can comply only with class B-1 requirements in their lower (40%) measuring range and are basically class B-2 instruments.

**Dial Extensometers.** Although all dial instruments usually are considered class C instruments, the majority (up to a gage length of 200 mm, or 8 in.) are class B-1 and class B-2 in their initial 40% measuring range, and class C throughout the remainder of the range. Dial instruments are used universally for determining yield strength by the extension-under-load method and yield strength of 0.1% offset and greater.

**Class C and D Extensometers.** Extensometers with a gage length of 610 mm (24 in.) begin in class C, although their overall measuring range must be considered as class D.

## Gripping Techniques

The use of proper grips and faces for testing materials in tension is critical in obtaining meaningful results. Trial and error often will

solve a particular gripping problem. Tension testing of most flat or round specimens can be accommodated with wedge-type grips (Fig. 18). Wire and other forms may require different grips, such as capsular or snubber types. The load capacities of grips range from under 4.5 kgf (10 lbf) to 45,000 kgf (100,000 lbf) or more. ASTM E 8 describes the various types of gripping devices used to transmit the measured load applied by the test machine to the tension test specimen.

**Screw-action grips**, or mechanical grips, are low in cost and are available with load capacities of up to 450 kgf (1000 lbf). This type of grip, which is normally used for testing flat specimens, can be equipped with interchangeable grip faces that have a variety of surfaces. Faces are adjustable to compensate for different specimen thicknesses.

**Wedge-type grips** (Fig. 18) are self-tightening and are built with capacities of up to 45,000 kgf (100,000 lbf) or more. Some units can be tightened without altering the vertical position of the faces, making it possible to preselect the exact point at which the specimen will be held. The wedge-action design works well on hard-to-hold specimens and prevents the introduction of large compressive forces that cause specimen buckling.

**Pneumatic-action grips** are available in various designs with capacities of up to 90 kgf (200 lbf). This type of grip clamps the specimen by lever arms that are actuated by compressed air cylinders built into the grip bodies. A constant force maintained on the specimen compensates for decrease of force due to creep of the specimen in the grip. Another advantage of this design is the ability to optimize gripping force by adjusting the air pressure, which makes it possible to minimize specimen breaks at the grip faces.

**Buttonhead grips** enable the rapid insertion of threaded-end or mechanical-end specimens. They can be manually or pneumatically operated, as required by the type of material or test conditions.

**Alignment.** Whether the specimen is threaded into the crossheads, held by grips, or is in direct contact with platens, the specimen must be well aligned with the load cell. Any misalignment will cause a deviation from uniaxial stress in the material studied.

## Force Verification of Universal Testing Machines

The calibration and verification of UTM systems refer to two different methods that are not synonymous. Calibration of testing machines refers to the procedure of determining the magnitude of error in the indicated loads. Verification is a calibration to ascertain whether the errors are within a predetermined range. Verification also implies certification that a machine meets stated accuracy requirements. Valid verification requires device calibration by skilled personnel who are knowledgeable about testing machines, related instruments, and the proper use of device calibration standards (such as ASTM E 74 for load indicators and ASTM E 83 for extensometer devices). After verification is performed, the calibrator or agency must issue reports and certificates attesting to compliance of the equipment with the verification requirements, including the loading range(s) for which the system may be used.

**Force Verification.** For the load verification to be valid, the weighing system(s) and associated instrumentation and data systems must be verified annually. In no case should the time interval between verifications exceed 18 months. Testing systems and their loading ranges should be verified immediately after relocation of equipment, after repairs or parts replacement (mechanical or electric/electronic) that could affect the accuracy of the load-measuring system(s), or whenever the accuracy of indicated loads is suspect, regardless of when the last verification was made.

Force verification standards for mechanical testing machines include specifications from various standards organizations such as:

Specification number	Specification title
EN 10002-2	Metallic Materials—Tensile Testing—Part 2: Verification of the Force Measurements
DIN EN 10002-2	Part 2: Verification of the Force-Measuring System of Tensile Testing Machines
BS 1610	Materials Testing Machines and Force Verification Equipment
BS EN 10002-2	Verification of the Force Measuring System of the Tensile Testing Machine
ASTM E 4	Standard Practices for Force Verification of Testing Machines

To comply with ASTM E 4, one or a combination of the three allowable verification methods must be used in the determination of the loading range or multiple loading ranges of the testing system. These methods are based on the use of:

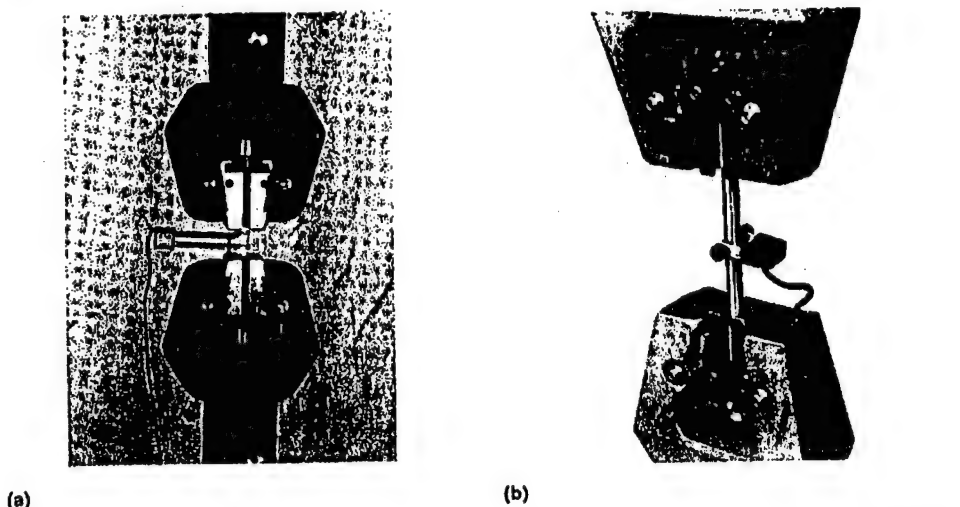


Fig. 18 Test setup using wedge grips on (a) a flat specimen with axial extensometer and (b) a round specimen with diametral extensometer

- Standard weights
- Standard weights and lever balances
- Elastic calibration devices

For each loading range, at least five (preferably more) verification load levels must be selected. The difference between any two successive test loads must not be larger than one third of the difference between the maximum and minimum test loads. The maximum can be the full capacity of an individual range. For example, acceptable test load levels could be 10, 25, 50, 75, and 100%, or 10, 20, 40, 70, and 100%, of the stated machine range.

Regardless of the load verification method used at each of the test levels, the values indicated by the load-measuring system(s) of the testing machine must be accurate to within  $\pm 1\%$  of the loads indicated by the calibration standard. If all five or more of the successive test load deviations are within the  $\pm 1\%$  required in ASTM E 4, the loading ranges may be established and reported to include all of the values. If any deviations are larger than  $\pm 1\%$ , the system should be corrected or repaired immediately. For determining accuracy of values at various test loads (or the deviation from the indicated load of the standard), ASTM E 74 specifies the required calibration accuracy tolerances of the three allowable types of verification methods.

For determining material properties, the testing machine loads should be as accurate as possible. In addition, deformations resulting from load applications should be measured as precisely as possible. This is particularly important because the relationship of load to deformation, which may be, for example, extension or compression, is the main factor in determining material properties.

As described previously, load accuracy may be ensured by following the ASTM E 4 procedure. In a similar manner, the methods contained in ASTM E 83, if followed precisely, will ensure that the devices or instruments used for deformation (strain) measurements will operate satisfactorily.

Manufacturers of testing machines calibrate before shipping and certify conformance to the manufacturer's guarantee of accuracy and any applicable standards, such as ASTM E 4. Subsequent calibrations can be made by the manufacturer or another organization with recognized equipment that is properly maintained and recertified periodically.

**Example: Calibrating a 60,000 lbf Capacity Testing Machine.** A 60,000 lbf capacity dial-type UTM of either hydraulic or screw-driven design will have the following typical scale ranges:

- 0 to 60,000 lbf reading by 50 lbf divisions
- 0 to 30,000 lbf reading by 25 lbf divisions
- 0 to 12,000 lbf reading by 10 lbf divisions
- 0 to 1200 lbf reading by 1 lbf divisions

As discussed previously, the ASTM required accuracy is  $\pm 1\%$  of the indicated load above

10% of each scale range. Most manufacturers produce equipment to an accuracy of  $\pm 0.5\%$  of the indicated load or  $\pm 1$  division, whichever is greater.

According to ASTM specifications, the 60,000 lbf scale range must be within 1% at 60,000 lbf ( $\pm 600$  lbf) and at 6000 lbf ( $\pm 60$  lbf). In both cases, the increment division is 50 lbf. Although the initial calibration by the manufacturer is to closer tolerance than ASTM E 4, subsequent recalibrations are usually to the  $\pm 1\%$  requirement. In the low range, the machine must be accurate ( $\pm 1\%$ ) from 120 to 1200 lbf. Thus, the machine must be verified from 120 to 60,000 lbf.

If proving rings are used in calibration, a 60,000 lbf capacity proving ring is usable down to a 6000 lbf load level. A 6000 lbf capacity proving ring is usable down to a 600 lbf load level, and a 1000 lbf capacity proving ring is usable down to a 100 lbf load level.

If calibrating load cells are used, a 60,000 lbf capacity load cell is usable down to a 3000 lbf load level, a 6000 lbf capacity load cell is usable to a 300 lbf load level, and a 600 lbf capacity load cell is usable down to a 120 lbf load level.

Before use, proving rings and load cells must be removed from their cases and allowed to stabilize to ambient (surrounding) temperature. Upon stabilization, either type of unit is placed on the table of the testing machine. At this stage, proving rings are ready to operate, but load cells must be connected to an appropriate power source and again be allowed to stabilize, generally for 5 to 15 min.

Each system is set to zero, loaded to the full capacity of the machine or elastic device, then unloaded to zero for checking. Loading to full capacity and unloading must be repeated until a stable zero is obtained, after which the load verification readings are made at the selected test load levels.

For the highest load range of 60,000 lbf, loads are applied to the calibrating device from its minimum lower limit (6000 lbf for proving rings and 3000 lbf for load cells) to its maximum 60,000 lbf in a minimum of five steps, or test load levels, as discussed in the section "Force Verification" in this article. In the verification loading procedure for proving rings, a "set-the-load" method usually is used. The test load is determined, and the nominal load is preset on the proving ring. The machine load readout is read when the nominal load on the proving ring is achieved. For load cells, a "follow-the-load" method can be used, wherein the load on the display indicator is followed until the load reaches the nominal load, which is the preselected load level on the readout of the testing machine.

In both methods, the load of the testing machine and the load of the calibration device are recorded. The error,  $E$ , and the percent error,  $E_p$ , can be calculated as:

$$E = A - B$$

$$E_p = \frac{(A - B)}{B} \times 100 \quad (\text{Eq 13})$$

where  $A$  is the load indicated by the machine being verified in lbf, kgf, or N, and  $B$  is the correct value of the applied load (lbf, kgf, or N), as determined by the calibration device.

This procedure is repeated until each scale range of the testing machine has been calibrated from minimum to maximum capacity. The necessary reports and certificates are then prepared, with the loading range(s) indicated clearly as required by ASTM E 4. Figures 8(b) and 9 illustrate UTMs being calibrated with elastic proving rings and calibration load cells.

## Tensile Testing

Tensile testing requirements are specified in various standards for a wide variety of different materials and products. Table 4 lists various tensile testing specifications from several standards organizations. These specifications define requirements for the test apparatus, test specimens, and test procedures.

Standard tensile tests are conducted using a threaded tensile specimen geometry, like the standard ASTM geometry (Fig. 19) of ASTM E 8. To load the specimen in tension, the threaded specimen is screwed into grips attached to each crosshead. The boundary condition, or load, is applied by moving the crossheads away from one another.

For a variety of reasons, it is not always possible to fabricate a specimen as shown in Fig. 19. For thin plate or sheet materials, a flat, or dog-bone, specimen geometry is used. The dog-bone specimen is held in place by wedge-shaped grips. The holding capacity of the grip provides a practical limit to the strength of material that a machine can test. Other specimen geometries can be tested, with certain cautionary formulas for critical dimensions are given in ASTM E 8.

**Accuracy, Repeatability, and Precision of Tension Tests.** Accuracy and precision of test results can only be quantified when known quantities are measured. One difficulty of assessing data is that no agreed-upon "standard" exists as reference material with known properties for strength and elongation. Tests of the "standard material" would reveal the system accuracy, and repeated experiments would quantify its precision and repeatability.

A variety of factors influence accuracy, precision, and repeatability of test results. Sources for errors in tension testing are mentioned in the appendix of ASTM E 8. Errors can be grouped into three broad categories:

- **Instrumental errors:** These can involve machine stiffness, accuracy and resolution of the load cell output, alignment of the specimen, gripping of the specimen, and accuracy of the extensometer.
- **Testing errors:** These can involve initial measurement of specimen geometry, electronic zeroing, and establishing a pre-stress level in the specimen.

- Material factors:** These describe the relationship between the material intended to be studied and that being tested. For example, does the material in the specimen represent the parent material, and is it homogenous? Other material factors would include specimen preparation, specimen geometry, and material strain-rate sensitivity.

The ASTM committee for tensile testing reported on a round robin set of experiments to assess repeatability and to judge precision of standard quantities. In this series (see appendix of ASTM E 8) six specimens of six materials were tested at six different laboratories. The comparison of measurements within a laboratory and between laboratories is given in Table 5. The data show the highest level of reproducibility in the strength measurements; the lowest reproducibility is found in elongation and reduction of area. Within-laboratory results were always more reproducible than those between laboratories.

## Compression Testing

Compression tests are conducted to provide engineering data on compressive strength and

compressive failure. These data can differ substantially from tensile properties. Data on the response of materials to compression are needed for engineering design, such as loading concrete structures, or in metal fabrication, such as forging and rolling. One advantage of compression testing is the elimination of necking instability found in tensile testing of ductile metals. However, the geometry of compression specimens can cause buckling instabilities and failure, and frictional effects between the specimen and the platens can cause burring. From a practical point of view, compression testing can reach the capacity of some machines because the force requirement increases with material hardening and with the increase in cross-sectional area of the specimen. This increase in area contributes to the frictional effects as well.

When testing high-strength brittle materials to failure, there exists a potential hazard from fragments of the specimen being ejected at high velocity. Personnel and equipment should be appropriately shielded.

**General Procedures.** Various standards for compression testing are listed in Table 6 along with ASTM E 9. The most common specimen geometry for compression testing is a right circular cylinder with flat planar ends. ASTM E 9 identifies three sizes of specimens grouped as small, medium, and long. These samples differ

in the ratio of length to diameter. Other shapes can be tested, but to avoid geometric buckling, special fixtures are required.

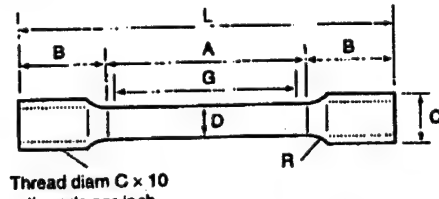
To load the standard specimen (right circular cylinder) a pair of platens attached to the crossheads make contact with the specimen. These platens must be flat, smooth, and parallel to one another. To avoid frictional effects, the specimen and platen interface is lubricated with silicon grease. In the case of compression testing, the crossheads move toward one another.

Compression tests can be performed using UTM equipment with or without a subpress, or with a unit specifically designed for compression testing. The unit specifically designed for compression testing may be portable for such purposes as in-the-field measurement of concrete compressive-failure strength. Figure 20 shows a diagram of a subpress. This unit is inserted between the crosshead platens of a conventional UTM machine. The subpress eliminates any lateral loads when aligned in the UTM.

The boundary condition for compression testing can be established by load rate or with crosshead speed, such that the specimen deforms at a strain rate of 0.005/min as given in ASTM E 9. The analysis of deformation should be limited to the region of the test where deformation occurs homogeneously. The test should also be halted if the load reaches the capacity of the load cell as a result of increased cross-sectional area of the specimen.

Table 4 Tension testing standards for various materials and product forms

Specification number	Specification title
ASTM A 770	Standard Specification for Through-Thickness Tension Testing of Steel Plates for Special Applications
ASTM A 931	Standard Test Method for Tension Testing of Wire Ropes and Strand
ASTM B 557	Standard Test Methods of Tension Testing Wrought and Cast Aluminum- and Magnesium-Alloy Products
ASTM B 557M	Standard Test Methods of Tension Testing Wrought and Cast Aluminum- and Magnesium-Alloy Products [Metric]
ASTM C 565	Standard Test Methods for Tension Testing of Carbon and Graphite Mechanical Materials
ASTM C 1275	Standard Test Method for Monotonic Tensile Strength Testing of Continuous Fiber-Reinforced Advanced Ceramics with Solid Rectangular Cross-Section Specimens at Ambient Temperature
ASTM C 1359	Standard Test Method for Monotonic Tensile Strength Testing of Continuous Fiber-Reinforced Advanced Ceramics with Solid Rectangular Cross-Section Specimens at Elevated Temperatures
ASTM D 76	Standard Specification for Tensile Testing Machines for Textiles
ASTM E 8	Standard Test Methods for Tension Testing of Metallic Materials
ASTM E 8M	Standard Test Methods for Tension Testing of Metallic Materials [Metric]
ASTM E 338	Standard Test Method of Sharp-Notch Tension Testing of High-Strength Sheet Materials
ASTM E 345	Standard Test Methods of Tension Testing of Metallic Foil
ASTM E 602	Standard Method for Sharp-Notch Tension Testing with Cylindrical Specimens
ASTM E 740	Standard Practice for Fracture Testing with Surface-Crack Tension Specimens
ASTM E 1450	Standard Test Method for Tension Testing of Structural Alloys in Liquid Helium
ASTM F 1501	Standard Test Method for Tension Testing of Calcium Phosphate Coatings
ASTM F 152	Standard Test Methods for Tension Testing of Nonmetallic Gasket Materials
ASTM F 19	Standard Test Method for Tension and Vacuum Testing Metallized Ceramic Seals
ASTM F 1147	Standard Test Method for Tension Testing of Porous Metal Coatings
BS EN 10002	Tensile Testing of Metallic Materials
BS 18	Method for Tensile Testing of Metals (Including Aerospace Materials)
BS 4759	Method for Determination of K-Values of a Tensile Testing System
BS 3688-1	Tensile Testing
BS 3500-6	Tensile Stress Relaxation Testing
BS 3500-3	Tensile Creep Testing
BS 3500-1	Tensile Rupture Testing
BS 1687	Medium-Sensitivity Tensile Creep Testing
BS 1686	Long-Period, High-Sensitivity, Tensile Creep Testing
DIN 53455	Tensile Testing: Testing of Plastics
DIN 53328	Testing of Leather, Tensile Test
DIN 50149	Tensile Test, Testing of Malleable Cast Iron
EN 1002-1	Metallic Materials—Tensile Testing—Part 1: Method of Test at Ambient Temperature
ISO 204	Metallic Materials—Uninterrupted Uniaxial Creep Testing Intension—Method of Test
ISO 783	Metallic Materials—Tensile Testing at Elevated Temperature
ISO 6892	Metallic Materials—Tensile Testing at Ambient Temperature
JIS B 7721	Tensile Testing Machines
JIS K 7113	Testing Methods for Tensile Properties of Plastics (English Version)



Thread diam C x 10 threads per inch

Abbreviation	Dimension	Measurement	
		in.	mm
G	Gage length	2.4606	62.5 ± 0.1
D	Diameter	0.4920	12.5 ± 0.2
R	Radius of fillet	0.3937	10.0
A	Length of reduced section	2.953	75
L	Approximate overall length	5.7086	145.0
B	Length of end section	1.378	35.0
C	Diameter of end section	0.787	20

Fig. 19 Standard ASTM geometry for threaded tensile specimens. Dimensions for the specimen are taken from ASTM B8M (metric units), or ASTM E8 (English units).

Table 5 Results of round-robin testing

Property	Coefficient of variation, %	
	Within laboratory	Between laboratory
Tensile strength	0.91	1.30
0.02% yield strength	2.67	4.46
0.2% yield strength	1.35	2.32
Elongation in 5D	2.97	6.36
Reduction in area	2.80	4.59

Source: ASTM E8

**Table 6 Compression testing standards for various materials and products forms**

Specification number	Specification title
ASTM A 236	Standard Method of Compression Testing of Cast Iron (discontinued)
ASTM B 485	Standard Method for Diametral Compression Testing of Cemented Carbides (discontinued)
ASTM C 1358	Standard Test Method for Monotonic Compressive Strength Testing of Continuous Fiber-Reinforced Advanced Ceramics with Solid Rectangular Cross-Section Specimens at Ambient Temperature
ASTM E 9	Standard Test Methods of Compression Testing of Metallic Materials at Room Temperature
BS 1881-115	Specification for Compression Testing Machines for Concrete
DIN 18554-1	Testing of Masonry, Determination of Compressive Strength and of Elastic Modulus
DIN 52185	Testing of Wood; Compression Test Parallel to Grain
DIN 52192	Testing of Wood; Compression Test Perpendicular to Grain
DIN 53517	Testing of Rubber and Elastomers
ISO 3132	Wood—Testing in Compression Perpendicular to Grain
ISO 4385	Plain Bearings—Compression Testing of Metallic Bearing Materials
JIS Z 0234	Testing Methods of Static Compression for Package Cushioning Materials
JIS Z 0235	Testing Methods of Dynamic Compression for Package Cushioning Materials

**Specimen Geometry.** As previously noted, a right circular cylinder is the standard specimen defined in ASTM E 9. Most common in compression testing is a right circular cylinder with a length-to-diameter ratio in the range of 1 to 3. Longer specimens can be tested but failure from buckling instability will occur.

Measuring loads that cause a column of material to buckle can be the purpose of the experiment. Sheet or thin plate material can be tested to some extent. Specimens must be held in fixtures that constrain the material motion to the load plane, preventing buckling. This type of test configuration can provide useful engineering data for in-service conditions; it cannot measure material properties beyond a few percent strain.

Specimens of cylindrical shape will barrel as the deformation becomes large. Barreling is the influence of frictional effects, between the platens and the specimen, that changes the stress state in the material. When barreling occurs, the assumption of homogenous stress state throughout the sample is no longer valid. Lubricants and Teflon sheet material placed at the interfaces have been found to reduce this effect. At large strains, the stress at the interface will squeeze the lubrication from between the platens and the specimen.

Short specimen length makes it difficult to use an extensometer on the sample. The short specimen length means the gap between the platen

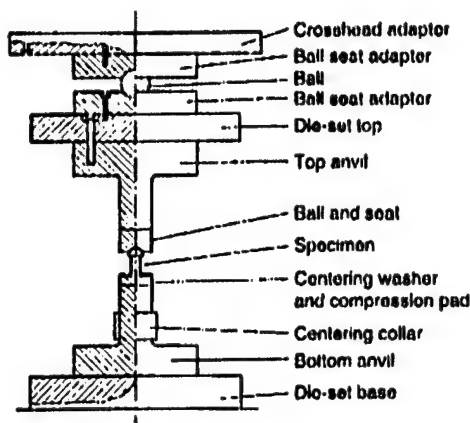


**Fig. 20** Subpress used during compression testing. Source: ASTM E 9

faces (through which the arms of an extensometer must extend) is narrow at the beginning of the test and will decrease throughout the experiment. Unless the specimen has a length-to-diameter ratio of 3 to 1 or higher, most of the deformation data is taken indirectly from the actuator position. As mentioned above, machine stiffness effects can produce errors in such data.

## Bending Tests

Bending tests require a different specimen geometry and a different configuration for applying the load. The typical specimen geometry is a beam with uniform cross section. In three-point bending, the load is applied at the mid-span of a simply supported beam. In four-point bending, equal loads are applied at equal distances from the simple supports to create a shear-free central region. Various specifications are listed in Table 7.

## REFERENCES

**Table 7 Bend testing standards for various materials and product forms**

Specification number	Specification title
ASTM B 593	Standard Test Method for Bending Fatigue Testing for Copper-Alloy Spring Material
ASTM E 290	Standard Test Method for Semi-Guided Bend Test for Ductility of Metallic Materials
ASTM E 855	Standard Test Methods for Bend Testing of Metallic Flat Materials for Spring Applications Involving Static Loading
ASTM F 1659	Bending and Shear Fatigue Testing of Calcium Phosphate Coatings on Solid Metallic Substrates
ASTM F 383	Standard Test Method for Static Bend and Torsion Testing of Intramedullary Rods, Standard Recommended Practice
ASTM F 384	Standard Practice for Static Bend Testing of Nail Plates
BS 1639	Methods for Bend Testing of Metals
DD 87	Method for Testing Bending Strength and Stiffness of Bone Plates for Use in Orthopedic
DIN 50153	Reverse Bending Test of Sheets or Strips Less Than 3 mm Thick, Testing of Metallic
DIN 51211	Testing of Metallic Materials, Reverse Bend Test of Wires
DIN 53457	Determination of the Elastic Modulus by Tensile, Compression and Bend Testing
DIN EN 910	Bend Testing of Welds in Metallic Materials English Version
ISO 1143	Metals—Rotating Bar Bending Fatigue Testing
ISO 144	Steel—Reverse Bend Testing of Wire

1. R.C. Anderson, *Inspection of Metals: Destructive Testing*, ASM International, 1988, p 83–119
2. H.E. Davis, G.E. Troxell, and G.F.W. Hauck, *The Testing of Engineering Materials*, 4th ed., McGraw-Hill, 1982, p 80–124
3. P. Han, Ed., *Tensile Testing*, ASM International, 1992, p 28
4. G.E. Dieter, *Mechanical Metallurgy*, McGraw-Hill, 2nd ed., 1976, p 349
5. D.J. Shippy, P.P. Gillis, and K.G. Hoge, Computer Simulation of a High Speed Tension Test, *J. Appl. Polym. Sci., Applied Polymer Symposia* (No. 5), 1967, p 311–325
6. P.P. Gillis and D.J. Shippy, Vibration Analysis of a High Speed Tension Test, *J. Appl. Polym. Sci.*, Applied Polymer Symposia (No. 12), 1969, p 165–179
7. M.A. Hamstad and P.P. Gillis, Effective Strain Rates in Low-Speed Uniaxial Tension Tests, *Mater. Res. Stand.*, Vol 6 (No. 11), 1966, p 569–573
8. P. Gillis and J.J. Gilman, Dynamical Dislocation Theories of Crystal Plasticity, *J. Appl. Phys.*, Vol 36, 1965, p 3375–3386
9. J.E. Hockett and P.P. Gillis, Mechanics Testing Machine Stiffness, Parts I and II *Int. J. Mech. Sci.*, Vol 13, 1971, p 251–275
10. W.G. Johnston, Yield Points and Delamination in Single Crystals, *J. Appl. Phys.*, Vol 33, 1962, p 2716
11. H.G. Baron, Stress-Strain Curves of Some Metals and Alloys at Low Temperature and High Rates of Strain, *J. Iron Steel Inst. (Brit.)*, Vol 182, 1956, p 354
12. J. Miklowitz, The Initiation and Propagation of the Plastic Zone in a Tension Bar of Mild Steel as Influenced by the Speed of Stretching and Rigidity of the Testing Machine, *J. Appl. Mech. (Trans. ASME)*, Vol 14, 1947, p A-31
13. M.A. Hamstead, "The Effect of Strain Rate and Specimen Dimensions on the Yield Point of Mild Steel," Lawrence Radiation Laboratory Report UCRL-14619, Apr 1966

## **APPENDIX M**

## AN ENGINEERING ANALYSIS OF NORMAL RIGID BODY PENETRATION INTO CONCRETE

**Stanley E. Jones**  
 University of Alabama  
 Dept. of Aerospace Engineering and Mechanics  
 Tuscaloosa, Alabama 35487

**David M. Jerome**  
 Air Force Research Laboratory  
 Munitions Directorate  
 Eglin Air Force Base, Florida 32542

**Leonard L. Wilson**  
 Science Applications International, Corp.  
 1247 North Eglin Parkway  
 Shallmar, Florida 32579

**Frank R. Christopher**  
 Air Force Research Laboratory  
 Munitions Directorate  
 Eglin Air Force Base, Florida 32542

### ABSTRACT

A one-dimensional analysis of normal penetration into semi-infinite concrete targets is presented. This analysis is based on a proposed relationship between the work done by the penetrator during penetration and the resulting crater volume produced in the target. The basis for the assumption that such a relationship must exist is the observation that such relationships have been shown to exist in metal on metal impacts. The resulting formula for penetration depth is extremely simple and is shown to agree with independently reported experimental results up to impact velocities of 1200m/s. Additionally, estimates for penetration time and velocity are given.

### INTRODUCTION

In spite of the incredible advances in computer modeling in the past decade, one-dimensional, engineering models still play a significant role in complex design environments. The advantage that these engineering models offer is simplicity. What they sacrifice is the detail associated with computer solutions. Together, these two approaches can advance a technical effort at a pace that neither can pursue independently.

It must be understood that engineering models are very often based on reasoning that focuses on the primary mechanisms that drive an event. In order to properly evaluate the assumptions behind the development of an engineering model, it is necessary to accept the fact that simplicity is one of the objectives. Instances in which this kind of reasoning has led to useful conclusions are too numerous to mention and everyone has been exposed to engineering models that correlate well with reality. This thinking is the motivation behind the analysis presented in this paper.

For more than two centuries (e.g. Johnson, 1992) the subject of penetration of various targets by non-deforming penetrators has been of interest to military designers and engineers. Some very well known mathematicians and engineers have worked on this problem. For

example, Robins, Euler, and Poncelet made early contributions to the theory of rigid body penetration (see Johnson, 1992, Poncelet, 1829, Rinehart and Pearson, 1965, and Backman, 1976). Nevertheless, many technical problems remain and there is considerable activity in this area today. See for example, Heuze (1990), which is a survey of the general area of penetration mechanics with particular emphasis on analytical, numerical, and experimental approaches. However, the list of contributors is too long to mention in this paper without offending someone. So, we will not attempt to include a comprehensive list of references and instead we will concentrate on those that are especially relevant to our applications.

### THEORY

Penetration of concrete and other geological targets has been modeled in a number of ways to include a variety of effects. However, the relationship between crater volume and available penetrator energy does not seem to have been utilized to any extent. Yet for metal on metal impacts, there has been some success with such relationships (e.g., see Murphey, 1987 or Cinnamon, et al. 1992). The advantage that this has for a non-deforming penetrator is that the cross-sectional area is constant and approximately equal to the cross-sectional area of the penetrator. The crater volume  $V_c$  is equal to the cross-sectional area  $A_0$  times the current penetration depth  $Z$ , i.e.

$$V_c = A_0 Z \quad (1)$$

This situation is described in Figure 1. This relationship ignores the obvious difference between the geometry of recovered targets (see Figure 2) and the narrow "tunnel" indicated by Equation (1). The explanation for this is that the crater geometry at the surface of the target is the result of other mechanical behavior. These processes are mentioned by Forrestal, et al. (1994) within the context of "surface cratering" and the remainder of the penetration path is referred to as the

"tunnel region". Most likely, the "surface crater" is a region of ejecta that forms at the surface from the shock at impact and the combined dynamic stress state that ensues and later separates from the main target.

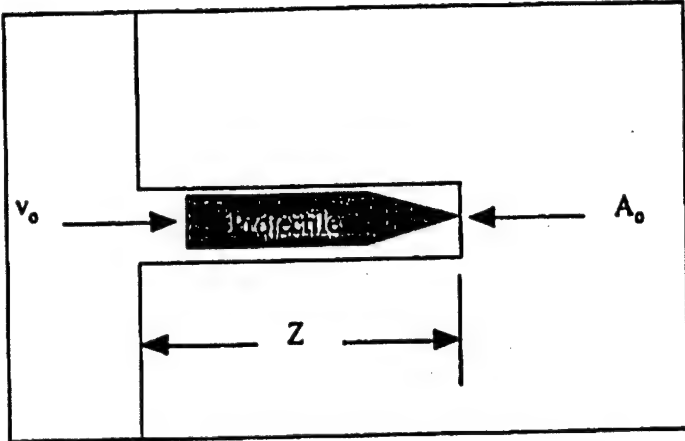


Figure 1. Assumed Crater Geometry for Model

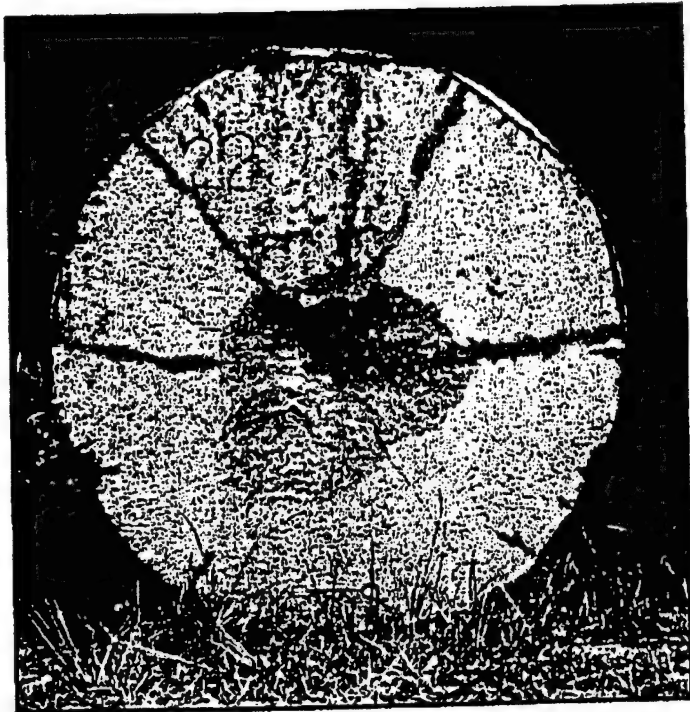


Figure 2. Cylindrical Concrete Target Showing Actual Surface Crater and Tunnel

We will assume that the work done by the penetrator on the target exclusively goes into formation of the tunnel-like crater described by Equation (1). We assume further that the change in energy of the penetrator is approximately proportional to the volume of the crater formed. This means that

$$\frac{1}{2}mv_0^2 - \frac{1}{2}mv^2 = \lambda V_c = \lambda A_0 Z \quad (2)$$

where  $m$  is the mass of the penetrator,  $v_0$  is the impact velocity,  $v$  is the current velocity of the penetrator, and  $\lambda$  is the constant of proportionality. Accepting this relationship, it follows that

$$\lambda = \frac{\frac{1}{2}mv_0^2}{A_0 p} \quad (3)$$

where  $p$  is the total depth of penetration.

By differentiating Equation (2), we find

$$m\dot{v} = -\lambda A_0 = -\frac{\frac{1}{2}mv_0^2}{p} \quad (4)$$

which stipulates that the force acting on the penetrator is constant and equal to the available energy divided by the penetration depth. The negative sign indicates that the force retards the motion. It is evident that the force that acts on the penetrator is not constant, but depends largely on penetrator velocity  $v$ . Thus, the interpretation placed on the right hand side of Equation (4) is that it represents the average force on the penetrator.

Poncelet (1829) originally proposed that the force on the penetrator stemmed from a velocity-dependent pressure  $P$  of the form

$$P = Av^2 + B \quad (5)$$

where  $A$  and  $B$  are constants (see Rinehart and Pearson, 1965). With this pressure estimate, the force acting on the penetrator is

$$PA_0 = (Av^2 + B)A_0 \quad (6)$$

and the average force on the penetrator over the velocity range is

$$\frac{1}{v_0} \int_0^{v_0} PA_0 dv = \left( \frac{1}{3}Av_0^2 + B \right) A_0 \quad (7)$$

The average force estimate given in Equation (7) is an average over the velocity range. One question that might be raised is does this estimate differ from a time average taken over the event time? Using the results of this paper and the impulse-momentum equation, where the time-averaged force appears, one can show that these quantities are identical. By using other estimates for the terminal time, Equation (7) will be very close to the time-averaged force.

By equating Equation (7) to the magnitude of the right hand side of Equation (4) and solving for the penetration depth, it follows that

$$p = \frac{\frac{1}{2}mv_0^2}{\left( \frac{1}{3}Av_0^2 + B \right) A_0} \quad (8)$$

gives the penetration depth. Notice that Equation (8) is simply a work-energy equation with the work done by the resisting force taken equal to the average force times the distance over which it acts, i.e. the penetration depth  $p$ .

#### PENETRATION INTO CONCRETE

Luk and Forrestal (1987) have carefully characterized the constants  $A$  and  $B$  for penetration into concrete. For ogival-nosed penetrators,  $A$  is given by

$$A = N\rho_1 \quad (9)$$

where  $\rho_1$  is the density of the target and  $N$  is given by

$$N = \frac{8\psi - 1}{24\psi^2} \quad (10)$$

The dimensionless constant  $\psi$  is the caliber-radius-head (CRH) for the penetrator nose. The caliber-radius-head is defined by

$$CRH = \frac{s}{2a} = \psi \quad (11)$$

where  $s$  is the ogive or circle radius and  $2a$  is the projectile shank diameter. The constant  $B$  is related to dynamic compressive strength of the target. Specifically,

$$B = Sf'_c \quad (12)$$

where  $f'_c$  is the quasi-static unconfined compressive strength of the target, and  $S$  is a dimensionless constant which is empirically related to the target unconfined compressive strength,  $f'_c$ .

### EXPERIMENTAL VALIDATION

A series of experiments were reported by Forrestal, et al. (1996) involving penetration of grout and concrete targets by 4340 steel projectiles with ogival tips. The targets had unconfined compressive strengths of 13.5 MPa and 21.6 MPa, and a density of 2000 kg/m<sup>3</sup>. The projectiles had caliber-radius-heads of 3.0 and 4.25, which translates to shape factors  $N$  of 0.106 and 0.076, respectively. All projectiles had a mass of 0.064 kg and a diameter of 12.9 mm. With these prescribed inputs into Equation (8), the comparison with experimental data is shown in Figures 3-6. Evidently, Equation (8) captures the essence of the trends in the data and the comparison is very favorable.

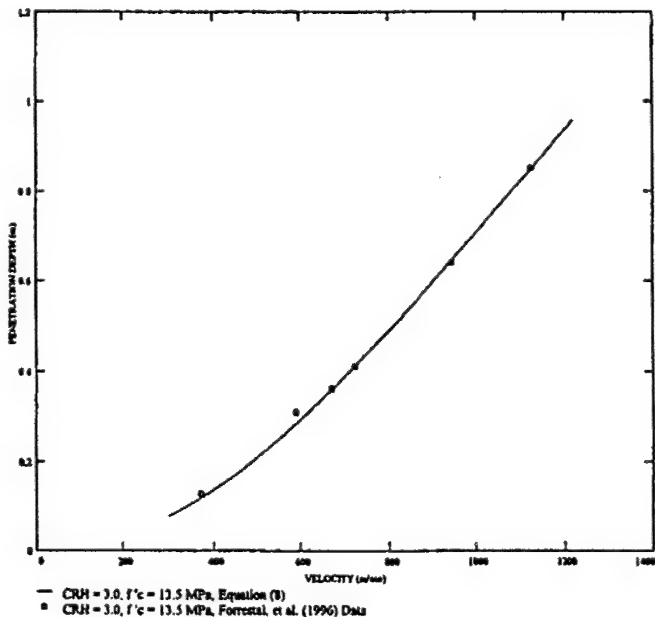


Figure 3. Data and Model Prediction for 0.064 kg, 12.9 mm Dia., CRH = 3.0 Projectile with  $f'_c = 13.5$  MPa

### OBSERVATIONS

Equation (8) is interesting in that it differs markedly from the

result that is obtained by integrating the equation of motion for the penetrator using the retarding force from Equation (6). The result of the integration is

$$p = \frac{m}{2AA_0} \ln(1 + \frac{A}{B} v_0^2) \quad (13)$$

This is Poncelet's penetration formula (see e.g., Rinehart and Pearson,

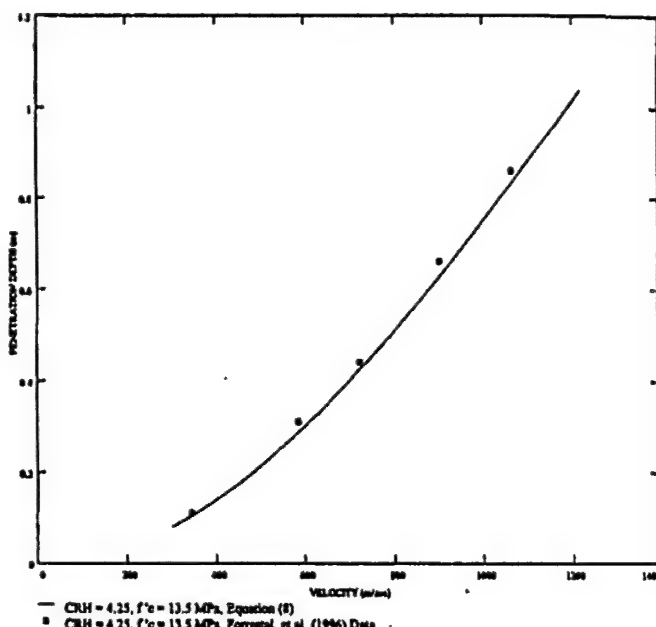


Figure 4. Data and Model Prediction for 0.064 kg, 12.9 mm Dia., CRH = 4.25 Projectile with  $f'_c = 13.5$  MPa

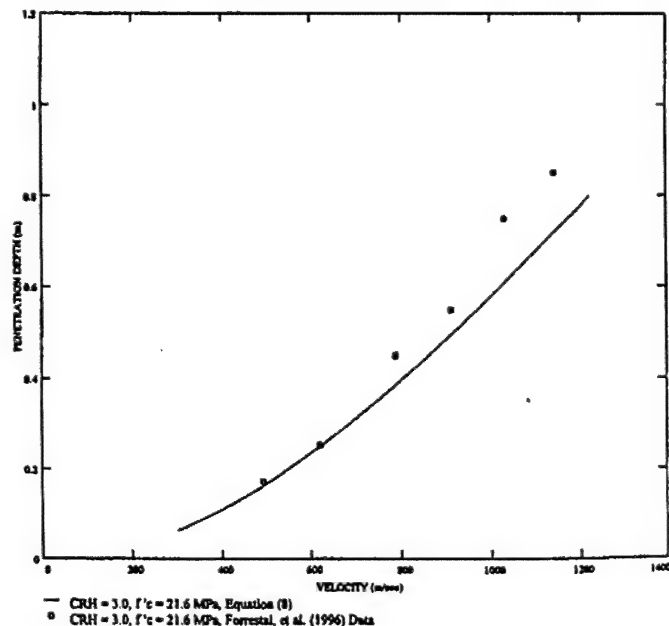


Figure 5. Data and Model Prediction for 0.064 kg, 12.9 mm Dia., CRH = 3.0 Projectile with  $f'_c = 21.6$  MPa

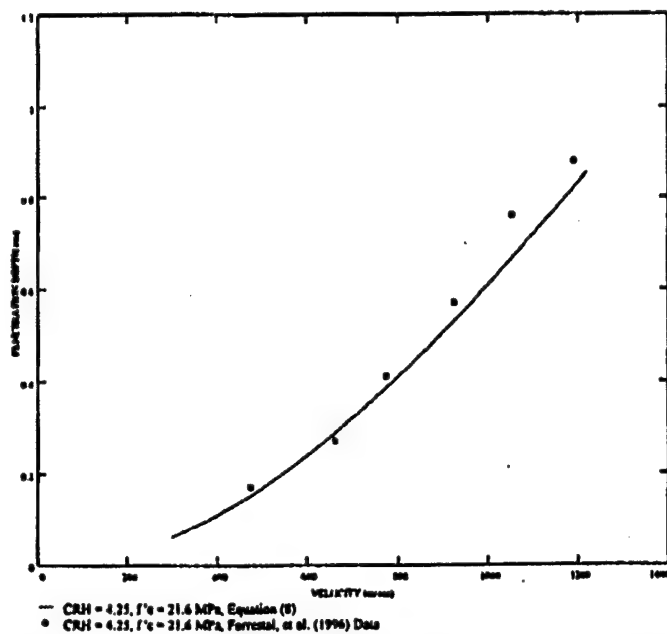


Figure 6. Data and Model Prediction for 0.064 kg, 12.9 mm Dia., CRH = 4.25 Projectile with  $f'_c = 21.6$  MPa

1965). It is similar to penetration formulae published by Forrestal, et al. (1987). However, their contributions toward justifying its use and characterizing A and B for concrete and other geological materials cannot be overstated. The correlation between Equation (13) and the experimental data is virtually the same as Equation (8) for the same input information.

One decided difference between Equations (8) and (13) regards the curvature. Equation (13) is always concave upward with positive slope, which means that  $p$  is always increasing with increasing  $v_0$ . However, Equation (8) changes curvature when  $v_0$  reaches

$$v_0 = \sqrt{\frac{B}{A}} \quad (14)$$

Additionally, penetration depth is limited by an asymptotic limit as  $v_0 \rightarrow \infty$  (in principle) by

$$p_{\max} = \frac{3m}{2A} \quad (15)$$

Unless, the target medium is extremely dense and the mass of the penetrator very low, the performance limit predicted by Equation (8) will play no role in actual penetration problems. In principle, Equation (8) has an asymptotic limit. In practice however, such a limit may never be attained because at the velocities necessary to achieve the limit, the projectile may fail on impact or erode so significantly that the penetration depth is limited by changes in the nose shape factor  $N$ .

Notice that the penetration depth  $p$ , as predicted by Equation (8), depends on three groupings of physical constants:  $mv_0^{2/3}$ ,  $AA_0v_0^{2/3}$ , and  $BA_0$ . It is easy to interpret the role of each of these and to assign significance according to impact velocity. At low velocities, the grouping  $AA_0v_0^{2/3}$  is dominated by the term  $BA_0$ . Thus, we conclude that the effect of tip geometry for the penetrator is

much less significant at low velocities. This fact is borne out by the data in Figures 3-6, where there are insignificant differences between the depths for CRH 3.0 and 4.25 at the lower velocities.

#### OTHER RESULTS

Equation (8) is not the only product of this theory. Having found the penetration depth  $p$  from Equation (8), we have determined the right hand side of Equation (4). This means that by additional integration, we can find  $Z$ ,  $v$ , and the time  $t$ . If we begin with the energy equation, Equation (2), then it is easy to see that

$$v = v_0 \sqrt{1 - \frac{Z}{p}} \quad (16)$$

which expresses the velocity as a function of position. Observing that  $v = dZ/dt$ , we can separate the variables in Equation (16) and integrate again to find

$$t = \frac{2p}{v_0} \left( 1 - \sqrt{1 - \frac{Z}{p}} \right) \quad (17)$$

This also means that  $Z$  can be expressed in terms of  $t$

$$Z = p \left( 1 - \left( 1 - \frac{t}{2p} \right)^2 \right) \quad (18)$$

Now this result can be used to find the velocity as a function of time by eliminating  $Z$  between Equations (16) and (18). This gives us a complete description of the motion of the projectile.

An example will illustrate the value of the above equations. Consider a steel penetrator with an ogival tip (CRH = 4.25) and a mass of 0.064 kg. For this projectile,  $N=0.076$ . Suppose that the projectile impacts (normally) a 20.32 cm thick target at a velocity 1000 m/s. The concrete has a density of 2300 kg/m<sup>3</sup> (approximately 143 lbs/ft<sup>3</sup>) and an unconfined compressive strength of  $f'_c = 51$  MPa (1.95 ksi). We require estimates for the residual velocity of the projectile and the time for penetration of the target.

It is easy to show, using Equation (8), that  $p = 0.78$  m for the data prescribed in this problem. This is the penetration depth for the projectile described into a semi-infinite target having the density and strength indicated. Now,  $p$  can be used in Equation (16) to find the velocity of the projectile exiting the target (residual velocity) is 860 m/s. It is also easy to show that the time for the projectile to complete penetration is 218  $\mu$ sec, using Equation (16). If we wanted to estimate the position of the projectile at any given time during penetration, then Equation (18) could be used to get that information.

#### CONCLUSIONS

In this paper, we have presented a very simple theory for estimating the penetration depth of rigid, ogive-nosed projectiles into concrete. Correlation with independently reported experimental data with two different projectile nose shapes and two different strength targets shows remarkable agreement. In addition, the analysis raises several questions regarding the trends that we may expect in high velocity penetration data. For certain combinations of target strength and density, the theory predicts a point of inflection and an asymptotic limit in the impact velocity/penetration curve. The theory also gives estimates for residual velocity and time of passage through finite thickness concrete targets. It remains to be seen whether the data

trends predicted by the theory will be borne out for higher velocities or other target media.

#### ACKNOWLEDGMENT

The first author gratefully acknowledges the support of the Air Force Office of Scientific Research, Bolling Air Force Base, Washington, DC, through an Intergovernmental Personnel Agreement with the University of Alabama. The remaining authors acknowledge the help and support of the Air Force Research Laboratory.

#### REFERENCES

Backman, M.E., 1976, "Terminal Ballistics", Technical Report NWC TP 5780, Naval Weapons Center, China Lake, CA.

Cinnamon, J.D., Jones, S.E., House, J.W., and Wilson, L.L., 1992, "A One Dimensional Analysis of Rod Penetration," *Int. J. Impact Engng.*, Vol. 12, No. 2, pp. 145-166.

Forrestal, M.J., Altman, B.S., Cargile, J.D., and Hanchak, S.J., 1994 "An Empirical Equation for Penetration Depth of Ogive-Nose Projectiles into Concrete Targets," *Int. J. Impact Engng.*, Vol. 15, No. 4, pp. 395-405.

Forrestal, M.J., Frew, D.J. Hanchak, S.J., and Brar, N.S., 1996, "Penetration of Grout and Concrete Targets with Ogive-Nose Steel Projectiles," *Int. J. Impact Engng.*, Vol. 18, No. 5, pp. 465-476.

Heuze, F.E., 1990, "An Overview of Projectile Penetration Into Geological Materials, with Emphasis on Rocks," *Int. J. Rock Mech. Min. Sci & Geomech. Abstr.*, Vol. 27, No. 1, pp. 1-14.

Johnson, W., 1992, "Benjamin Robins (18th Century Founder of Scientific Ballistics): Some European Dimensions and Past and Future Perceptions," *Int. J. Impact Engng.*, Vol. 12, No. 2, pp. 293-299.

Luk V.K., and Forrestal, M.J., 1987, "Penetration into Semi-Infinite Reinforced Concrete Targets with Spherical and Ogival Nose Projectiles," *Int. J. Impact Engng.*, Vol. 6, No. 4, pp. 291-301.

Murphrey, M.J., 1987, "Survey of the Influence of Velocity and Material on the Projectile Energy/Target Hole Volume Relationship," Proceedings of the Tenth International Symposium on Ballistics, San Diego, CA.

Poncelet, J.V., 1829, *Cours de Mecanique Industrielle*, Paris.

Rinehart, J., and Pearson, J., 1965, Behavior of Materials Under Impulsive Loads, Dover Publications, New York.

---

## **APPENDIX N**

# On the optimal nose geometry for a rigid penetrator

S. E. Jones, W. K. Rule, D. M. Jerome, R. T. Klug

**Abstract** A variational formulation for the net force on the nose of a rigid projectile normally penetrating a compliant target is given. Frictional effects are negligible in this formulation. The variational problem is solved and the result compared to several popular nose geometries. For blunt tipped projectiles, the optimal geometry can significantly enhance penetration by reducing the net force of resistance. For long penetrator noses, the effect has much less value. The most interesting conclusion is that all the optimal geometries have blunt tips.

## Introduction

Penetration mechanics has a long and rich history. Analytical modeling of rigid body penetration dates back to Robins (1742) and Euler (see Euler's *Opera Omnia* (1922)) prior to 1750 (see W. Johnson (1992)). J. Poncelet (1829) introduced a velocity dependent pressure estimate and produced an estimate for penetration depth that is still used today. More recently, Luk and Forrestal (1987) and others (e.g., Forrestal (1991), Forrestal and Luk (1992), Forrestal, et al. (1994), Forrestal, et al. (1995), Batra (1987), or Batra (1988)) have advanced and refined the thinking on this problem for a number of penetration applications. Even the effect of friction was introduced (e.g., Forrestal (1986) or Batra and Chen (1994)).

One of the factors emphasized in the recent contributions is the role played by penetrator nose geometry on the performance of the penetrator. At higher velocities, the depth of penetration is considerably influenced by the geometry of the penetrator nose. It naturally leads to the question as to which nose geometry is optimal from the perspective of depth of penetration?

The analysis presented in this paper answers this question strictly from the perspective of Poncelet's velocity-dependent pressure. It ignores certain failure mechanisms that may be present in the target and may promote

penetration. The analysis further assumes that the target is ideal and that there are no discontinuities in the pressure. The effects of friction are also ignored. This question will be taken up later in another paper. Also ignored are the conditions at entry of the projectile into the target and any spall that may be associated with that event.

## Theory

Consider an axisymmetric penetrator with shank radius  $a$  and tip length  $b$ , as shown in Fig. 1. Consider a pressure  $p$  acting on the nose by interaction with the target with negligible frictional effects. The motion of the penetrator is in the negative  $x$ -direction. The component of force due to the pressure on the surface of the penetrator nose resisting the motion of the penetrator is

$$dF = 2\pi p y \sin \theta \, ds \quad (1)$$

where  $\theta$  is the tangent angle to the surface at point  $(x, y)$  and  $ds$  is the increment of arc length on that surface. The curve joining the tip  $(0, 0)$  on the shank  $(b, a)$  is  $y = y(x)$ . The arc length increment is

$$ds = \sqrt{1 + y'^2} \, dx \quad (2)$$

where  $y' = dy/dx$  from the geometry in Fig. 1. We note that

$$\sin \theta = \frac{y'}{\sqrt{1 + y'^2}} \quad (3)$$

and combining Eqs. (1)–(3) and integrating over the net resisting face provided by the target, we find

$$F = \int_0^b 2\pi p y y' \, dx. \quad (4)$$

For example, if the pressure on the nose of the penetrator is uniform  $p = p_0$ , then

$$F = 2\pi p_0 \int_0^b y y' \, dx = \pi a^2 p_0 \quad (5)$$

If the pressure is not uniform, then the resulting integration is not so simple. For example, if the pressure is a function of the component of axial velocity acting normal to the nose (as proposed by Luk and Forrestal (1987)), then  $p$  is given by

$$p = A v^2 \sin^2 \theta + B \quad (6)$$

where  $A$  and  $B$  are target dependent physical constants that will be discussed further and  $v$  is the current axial

---

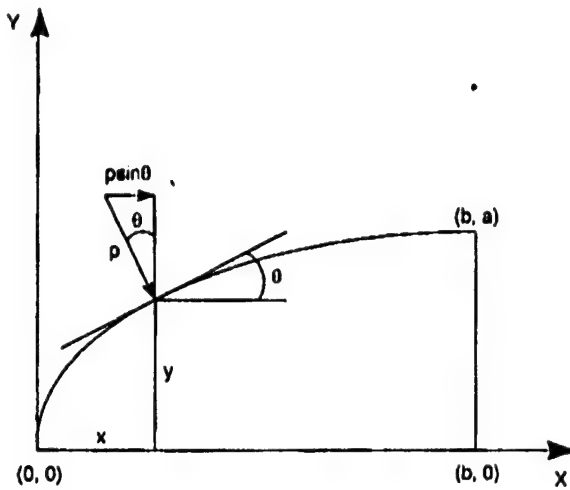
Communicated by R. Batra, 16 June 1998

S. E. Jones<sup>1</sup>, D. M. Jerome, R. T. Klug  
Senior Scientist, U.S. Air Force, Eglin AFB, FL

W. K. Rule  
Department of Aerospace Engineering and Mechanics,  
The University of Alabama

<sup>1</sup>on leave from the University of Alabama

Correspondence to: S. E. Jones



414

Fig. 1. Planar cross-section of the nose of an axisymmetric rod penetrator. The tip passes through zero at  $x = 0$  and  $a$  at  $x = b$ . The remainder of the penetrator is a cylinder of length  $L$ .

velocity of the penetrator. The pressure can be related to  $y = y(x)$  by Eq. (3) and Eq. (6) becomes

$$p = A\nu^2 \frac{y'^2}{1+y'^2} + B \quad (7)$$

Using this pressure relation in Eq. (4), we find that the net force  $F$  resisting the motion of the penetrator is

$$\begin{aligned} F &= 2\pi \int_0^b yy' \left( A\nu^2 \frac{y'^2}{1+y'^2} + B \right) dx \\ &= 2\pi A\nu^2 \int_0^b \frac{yy'^3}{1+y'^2} dx + \pi a^2 B \\ &= \pi a^2 \left( \frac{2A\nu^2}{a^2} \int_0^b \frac{yy'^3}{1+y'^2} dx + B \right) \\ &= \pi a^2 (AN\nu^2 + B) \end{aligned} \quad (8)$$

where

$$N = \frac{2}{a^2} \int_0^b \frac{yy'^3}{1+y'^2} dx \quad (9)$$

The constant  $N$  contains the only effect due to penetrator nose geometry.

For example, if the nose of the penetrator is hemispherical, then  $b = a$  and

$$y = \sqrt{a^2 - (a - x)^2} \quad (10)$$

For this nose geometry, Eq. (9) becomes

$$N = \frac{2}{a^4} \int_0^a (a - x)^3 dx = \frac{1}{2} \quad (11)$$

Another simple geometry is that of a conical nose. In this case,

$$y = \frac{a}{b} x \quad (12)$$

and

$$N = \frac{a^2}{a^2 + b^2} \quad (13)$$

A more complex, but highly useful nose geometry, is the ogive. The ogive is a circular arc of radius  $s$  tangent to the shank at  $x = b$  and passing through zero at  $x = 0$  (see Figure 2). This means that

$$y = \sqrt{s^2 - (b - x)^2} - (s - a) \quad (14)$$

where

$$s = \frac{a^2 + b^2}{2a} \quad (15)$$

Substituting Eq. (14) into Eq. (9) and performing the tedious integration, we can show that

$$N = \frac{4a^3s - a^4}{6a^2s^2} = \frac{2(a^4 + 2a^2b^2)}{3(a^2 + b^2)^2} \quad (16)$$

However, Luk and Forrestal (1987) introduced the notation,  $s = 2a\psi$ , where  $\psi$  is a dimensionless constant, and Eq. (16) becomes

$$N = \frac{8\psi - 1}{24\psi^2} \quad (17)$$

which is their result.

#### Some elementary comparisons

It is interesting to compare the values of  $N$  obtained from several simple geometries where integration is exact. First, let us change to the dimensionless variables  $z = y/a$ ,  $\xi = x/b$ , and Eq. (9) becomes

$$N = 2a^2 \int_0^1 \frac{zz'^3}{1+z'^2} d\xi \quad (18)$$

where  $z' = dz/d\xi$  and  $a = b/a$ .

Consider conical, ogival, and fractional power geometries. The resulting values of  $N$  are given below.

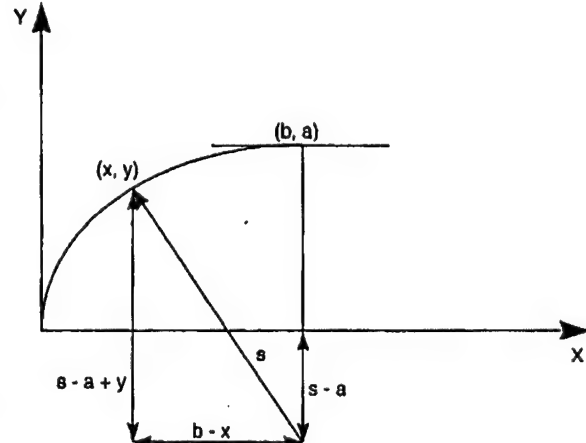


Fig. 2. The ogival nose geometry. The tip passes through zero at  $x = 0$  and the tangent is zero at  $x = b$ . The remainder of the projectile is a cylinder of length  $L$ .

$$N = \frac{\alpha^2}{1 + \alpha^2} \quad (\text{cone. } z = \xi) \quad (19)$$

$$N = \frac{2\alpha^2(\alpha^2 + 2)}{3(1 + \alpha^2)^2}$$

(ogive, z.

$$= \frac{1}{\alpha} \sqrt{\left(\frac{1 + \alpha^2}{2\alpha}\right)^2 - (1 - \xi)^2 - \left(\frac{\alpha^2 + 1}{2\alpha^2} - 1\right)} \quad (20)$$

$$N = \frac{\alpha^2}{4} \ln\left(1 + \frac{4}{\alpha^2}\right) \quad (\text{fractional power, } z = \sqrt{\xi}) \quad (21)$$

A comparison of these results is shown in Fig. 3. For smaller values of  $\alpha$  (long penetrator nose) all of the geometries have comparable values of  $N$  and the slight differences will only be reflected at high velocities. For  $\alpha = 1$  (short penetrator nose), the fractional power geometry at  $N = 0.402$  is somewhat better than the other two at  $N = 0.50$ .

#### Optimal tip geometry

For each fixed nose length  $b$  and shank radius  $a$ , the value of  $N$  varies. The net force on the penetrator nose (Eq. (8)) is least when the value of  $N$  is a minimum. Such a penetrator will achieve maximal penetration depth, assuming that no changes in the nose geometry or erosion occur. Thus, we arrive at the variational problem of choosing the optimal path  $y = y(x)$  between the tip and the shank that minimizes the integral

$$I = \int_0^b \frac{yy^3}{1 + y^2} dx, \quad (22)$$

where  $y(0) = 0$ ,  $y(b) = a$ .

As indicated, this is a variational problem (e.g., see Lanczos (1966), Pars (1962), or Vujanovic and Jones (1989)). The path that minimizes  $I$  satisfies the Euler-Lagrange equation

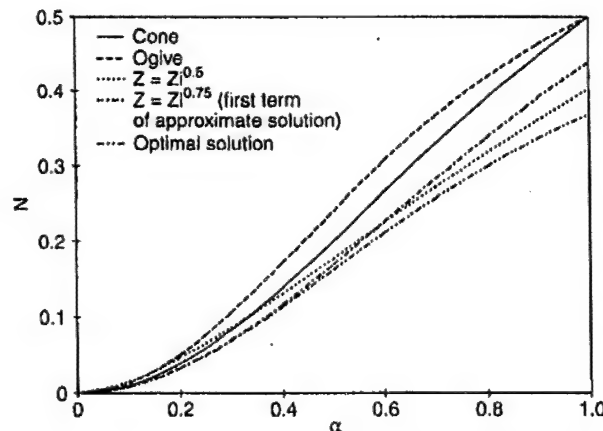


Fig. 3. Comparison of  $N$  values as a function of  $\alpha$  for various nose shapes

$$y(3 - y^2)y'' + y^2(1 + y'^2) = 0 \quad (23)$$

where  $y'' = d^2y/dx^2$  and  $y(0) = 0$ ,  $y(b) = a$ . This two-point boundary value problem is challenging because it is singular in neighborhood of  $x = 0$  and highly nonlinear.

We can achieve some insight into the solution to Eq. (23) by changing to dimensionless variables. Let  $z = z(\xi) = y/a$  and  $\xi = x/b$ . Now, Eq. (23) becomes

$$z(3 - \alpha^2 z^2)z'' + z^2(1 + \alpha^2 z'^2) = 0 \quad (24)$$

where  $z' = dz/d\xi$ ,  $z'' = d^2z/d\xi^2$ , and  $\alpha = a/b$ . The boundary conditions transform to  $z(0) = 0$  and  $z(1) = 1$ .

The dimensionless constant  $\alpha = a/b$  is generally less than 1 for the cases that interest us. Consider a regular perturbation expansion in the parameter  $\alpha^2$ , say

$$z = z_0(\xi) + \alpha^2 z_1(\xi) + \dots \quad (25)$$

where terms of the order of  $\alpha^4$  have been neglected. Substituting Eq. (25) into Eq. (24), collecting terms of the same order of magnitude and equating them to zero leads to

$$3z_0 z_0'' + z_0'^2 = 0 \quad (26)$$

$$(3z_1 - z_0 z_0'^2)z_0'' + 3z_0 z_1'' + 2z_0' z_1' + z_0'^4 = 0 \quad (27)$$

Terms of the order of  $\alpha^4$  and higher have been neglected.

The boundary conditions for  $z$  are independent of  $\alpha$  and this infers

$$z_0(0) = 0, \quad z_0(1) = 1 \quad (28)$$

$$z_1(0) = z_1(1) = 0 \quad (29)$$

as the boundary conditions for Eqs. (26) and (27). Solving Eq. (26) subject to Eq. (28) leads to

$$z_0 = \xi^{\frac{1}{3}} \quad (30)$$

Substituting this result into Eq. (27) and simplifying gives us the linear equation

$$3\xi^2 z_1'' + \frac{3}{2} \xi z_1' - \frac{9}{16} z_1 = -\frac{27}{64} \xi^{\frac{1}{3}} \quad (31)$$

to solve for  $z_1$  subject to the boundary conditions in Eq. (29). The result is

$$z_1 = \frac{9}{16} \left( \xi^{\frac{1}{3}} - \xi^{\frac{4}{3}} \right). \quad (32)$$

This means that to two terms, the approximate optimal solution is

$$z \cong \xi^{\frac{1}{3}} + \frac{9}{16} \alpha^2 \left( \xi^{\frac{1}{3}} - \xi^{\frac{4}{3}} \right). \quad (33)$$

It is interesting to note that the penetrator having this nose geometry does not have a sharp tip.

Equation (18) can be analytically evaluated using only the first term ( $z = \xi^{\frac{1}{3}}$ ) of Eq. (33). The resulting approximate  $N$  value is given by

$$N \cong \frac{27\alpha^2}{32} \left[ 1 - \frac{9\alpha^2}{8} + \frac{81\alpha^4}{128} \ln\left(1 + \frac{16}{9\alpha^2}\right) \right]. \quad (34)$$

Since only the first term of the approximate solution was used the  $N$  values given by Eq. (34) would be expected to be accurate for only relatively small values of alpha. This will be demonstrated in the next section.

#### Numerical solution to Eq. (24)

A numerical solution for Eq. (24) was obtained by assuming a solution of the following form

$$z = a_1 \xi^n + a_2 \xi^{2n} + a_3 \xi^{3n} \quad (35)$$

416

where  $a_1$  and  $n$  are adjustable parameters which are a function of alpha. A least squares approach was used to obtain values for these parameters as will now be described. For a particular alpha value, Eq. (24) was evaluated (using the assumed function, Eq. (35)) at 20 evenly spaced  $\xi$  values from 0.05 to 1. These twenty function values were then squared and summed to produce an aggregate fit error. An optimizer was used to adjust the  $a_i$  and  $n$  values to minimize the fit error. After optimization, the coefficients obtained for Eq. (24) produced errors that were typically on the order of  $\pm 0.001$ . Typical optimal parameter values for various values of alpha are shown in Table 1, and plotted in Fig. 4. From Fig. 4 it can be clearly seen that as alpha approaches zero,  $a_1$  and  $a_2$  approach zero,  $a_3$  tends to unity, while  $n$  approaches 0.25. This means that the optimal solution approaches,  $z = \xi^{\frac{1}{4}}$ , the first term of the approximate optimal solution (Eq. (34)), as expected.

Nose penetration efficiency is indicated by a small value of the parameter  $N$  in Eq. (18).  $N$  versus alpha for five different nose shapes are compared in Fig. 3. Closed form functions for  $N$  versus alpha where previously given for conical, ogival, fractional power ( $z = \xi^{\frac{1}{n}}$ ), and first term of approximate solution ( $z = \xi^{\frac{1}{4}}$ ) nose shapes in Eqs. (19), (20) (21) and (34), respectively. To plot the results for the optimal solution given by Eq. (35) the  $N$  integral of Eq. (18) was evaluated numerically using the trapezoidal rule. Care was taken to allow for the singularity at  $\xi = 0$  by small increments in the numerical algorithm ( $\Delta \xi = 0.00005$ ) in the vicinity of the singularity. Figure 3 indicates that, as expected, the optimal nose shape had the lowest  $N$  for all alpha values. This figure also shows that using only one term of the approximate solution ( $z = \xi^{\frac{1}{4}}$ ) produces accurate optimal  $N$  predictions for values of alpha less than 0.4.

In Fig. 5 the two term approximate solution of Eq. (33) is compared with the optimal solution of Eq. (35) for small and large alpha values. As one would expect, the solutions

Table 1. Typical optimal parameters for the assumed nose shape function  $z = a_1 \xi^n + a_2 \xi^{2n} + a_3 \xi^{3n}$

Alpha	$a_1$	$a_2$	$a_3$	$n$
0.1	0.0063	-0.0024	0.9961	0.2499
0.3	0.0791	-0.0999	1.0208	0.2464
0.5	0.3107	-0.5869	1.2762	0.2300
0.7	0.7007	-1.4191	1.7184	0.2082
0.9	1.1273	-2.2558	2.1285	0.1915
1.1	1.5066	-2.9351	2.4286	0.1802

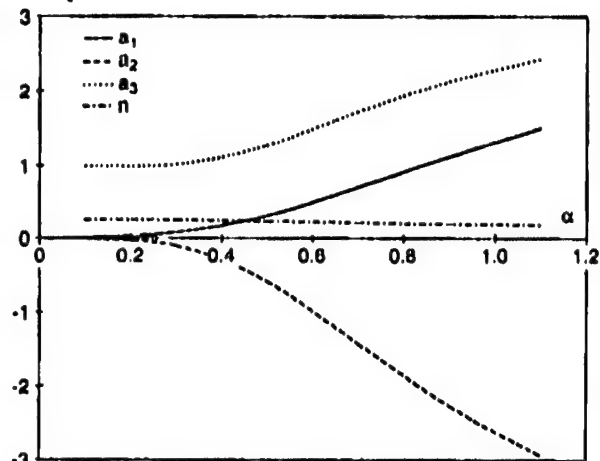


Fig. 4. Variation of optimal shape parameters  $a_1$ ,  $a_2$ ,  $a_3$ , and  $n$  as a function of alpha

are virtually identical for the small alpha case where the approximate solution is valid. There are significant differences between the approximate and the optimal solutions for the large alpha case.

Finally, the shape of a typical 50 caliber bullet and an optimally shaped penetrator are compared in Fig. 6. It can be noted that there are significant differences in the shapes. This is not surprising since the bullet may not have been designed for depth of penetration. Many low caliber projectiles are not designed to maximize depth of penetration. Instead, they are designed to enhance mushrooming of the projectile and damage to the target.

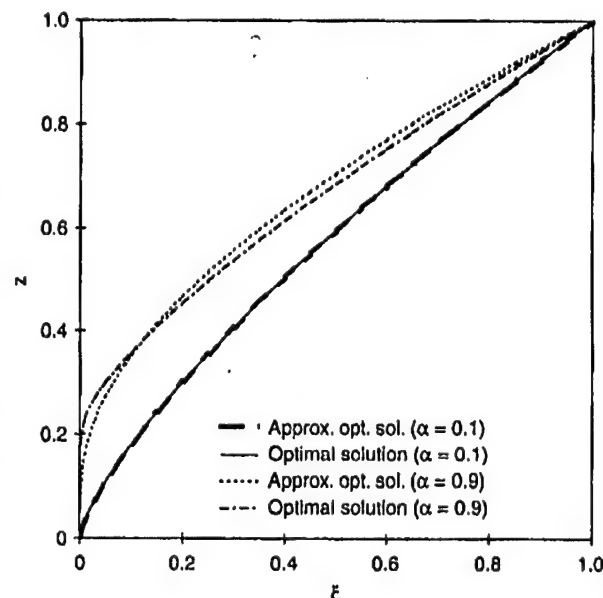


Fig. 5. Comparison of optimal numerical solutions with the approximate solution of Eq. (33) for  $\alpha = 0.1$  and  $0.9$

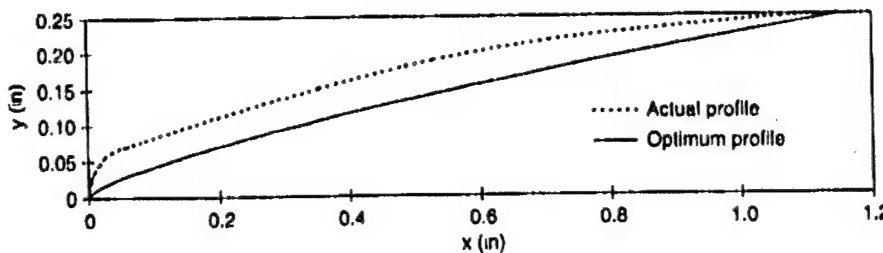


Fig. 6. Comparison of the optimal and actual profile of a 50 caliber bullet

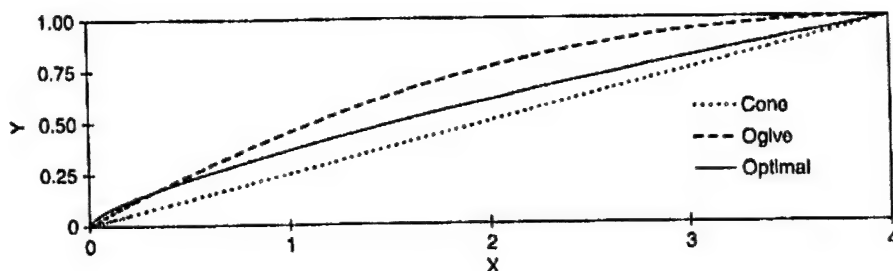


Fig. 7. Comparison of conical, ogival and optimal shapes for a penetrator with  $a = 1$  and  $b = 4$  ( $\alpha = 0.25$ )

### Conclusions

In this paper, we have presented an analysis of penetrator nose geometry that results in some interesting conclusions. Using Poncelet's velocity-squared pressure law, the net resistive force on the penetrator as a function of nose geometry was presented. It was clear from the form taken of the net force that there was an optimal geometry for each radius to nose length ratio  $\alpha$ . This naturally lead to a variational problem from which the optimal nose geometry followed. The solution to this problem is interesting in that it somewhat contradicts our intuition. Instinctively, we think of a sharp penetrator as having the most favorable geometry. Indeed, cones and ogives are very popular noses for cylindrical projectiles. However, from the perspective of reducing the net force on the projectile an all together different geometry is predicted by the analysis. Of course, there may be other mechanisms for target failure or different objectives for projectiles other than achieving maximum penetration depth by minimizing the net force on the penetrator. For example, Fig. 6 shows a comparison between the nose geometry of a standard 50 caliber bullet and the optimal geometry for the same nose length. There is a substantial difference probably due to the defeat objectives of the bullet.

Another comparison between conical, ogival, and the optimal geometry is shown in Fig. 7. The nose length is two diameters. This corresponds to  $\alpha = 0.25$  and a caliber-radius-head (CRH, e.g., see Luk and Forrestal (1987)) of  $\psi = 4.25$  (Eq. (17)). The distinct differences between the geometries are noted. The value of  $N$  for the conical tip is 0.059. For the ogive,  $N = 0.076$  and for the optimal geometry  $N = 0.049$ . These differences will be insignificant for the lower impact velocities and may not matter very much at very high impact velocities because of the erosion that takes place during penetration of certain abrasive targets.

### References

- Batra RC (1987) Effect of nose shape and strain-hardening on steady state penetration of viscoplastic targets. In: Owen, DRJ, Hinton, E, Onate E, (eds): Computational plasticity, models, software and applications, 463-475
- Batra RC (1988) Steady state penetration of thermoviscoplastic targets. Computational Mechanics. 3, 1-12
- Batra RC, Chen X (1994) Effect of frictional force and nose shape on axisymmetric deformations of a thick thermoviscoplastic target. Acta Mechanica. 106, 87
- Euler L Neve Grundsatz der Artillerie. Berlin. (reprinted as: Euler's opera omnia. Druck and Verlag Von B. G. Teubner, 1922)
- Forrestal MJ (1986) Penetration into dry porous rock. Int. J. Solids Struct. 22, 1485
- Forrestal MJ (1991) Penetration of strain hardening targets with rigid spherical-nose rods. J. Appl. Mech. 58, 7
- Forrestal MJ, Luk VK (1992) Penetration into soil targets. Int. J. Impact Engng. 12, 3
- Forrestal MJ, Altman BS, Cargile JD, Hanchak SJ (1994) An empirical equation for penetration depth of ogive-nose projectiles into concrete targets. Int. J. Impact Engng. 15, 395
- Forrestal MJ, Tzou DY, Askari E, Longcope DB (1995) Penetration into ductile metal targets with rigid spherical-nose rods. Int. J. Impact Engng. 16, 5/6, 699
- Johnson W (1992) Benjamin Robins (18th century founder of scientific ballistics): some European dimensions and past and future perceptions. Int. J. Impact Engng. 12, 2, 293
- Lanczos C (1966) The Variational Principles of Mechanics. Toronto, University of Toronto Press
- Luk VK, Forrestal MJ (1987) Penetration into semi-infinite reinforced concrete targets with spherical and ogival nose projectiles. Int. J. Impact Engng. 6, 4, 291
- Pars LA (1962) An Introduction to the Calculus of Variations. London, Heinemann
- Poncelet JV (1829) Cours de Mecanique Industrielle. Paris
- Robins B (1742) New Principles in Gunnery. London
- Vujanovic BD, Jones SE (1989) Variational Methods in Non-conservative Phenomena. Boston, Academic Press

---

## **APPENDIX O**



PERGAMON

International Journal of Impact Engineering 24 (2000) 403-415

INTERNATIONAL  
JOURNAL OF  
**IMPACT  
ENGINEERING**

[www.elsevier.com/locate/ijimpeng](http://www.elsevier.com/locate/ijimpeng)

# On the optimal nose geometry for a rigid penetrator, including the effects of pressure-dependent friction

S.E. Jones<sup>a,\*†,1</sup>, William K. Rule<sup>b</sup>

<sup>a</sup>*U.S. Air Force Research Laboratory, Munitions Directorate, Eglin AFB, FL, USA*

<sup>b</sup>*Trus Joist MacMillan, Boise, ID, USA*

Received 10 March 1998; accepted 22 August 1998

## Abstract

In a related paper (Jones et al., *Comput Mech*, 1998;22:413) the problem of maximizing the depth of penetration by a normally impacting cylindrical projectile by optimizing the nose geometry was considered. These results were accomplished by neglecting any frictional resistance offered by the target and only considering the normal pressure acting against the penetrator nose. The problem of maximizing the penetration depth achieved by the normal impact of a cylindrical projectile including the effects of friction acting on the penetrator nose is a much more challenging problem. In this paper, the normal impact and penetration problem is considered including the effects of pressure-dependent friction. © 2000 Elsevier Science Ltd. All rights reserved.

## 1. Introduction

In an earlier paper, Jones et al. [1] presented the nose geometry for a normal impacting, rigid projectile that maximizes penetration depth. This problem was solved by neglecting all forms of friction that act on the penetrator nose. By assuming that the pressure that acts on the nose of the penetrator is of Poncelet form [2] (see also [3,4, p. 15] or [5, pp. 200, 210]), it was shown that the nose had a fairly simple geometry. In spite of the simplicity of this result, it is surprising that the optimal geometry had a blunt nose regardless of the nose length.

For moderate to low impact velocities there seemed to be little to gain from the optimal geometry over most others. However, at very high impact velocities (say, those in excess of 1000 m/s), substantial differences could be noted in penetration depth when compared to other conventional geometries. As indicated earlier, the projectile impacts normally and it is assumed

\* Corresponding author.

<sup>†</sup> On leave from the University of Alabama.

that the energy level is high enough to neglect any of the effects associated with entry into the target.

There has been much effort directed toward understanding the various forms that friction can take (e.g., [6] or [7]). This is a very complicated problem, especially when high sliding speeds are involved (e.g., [8-10]). Very little appears to be known about the friction that acts on bodies during high velocity penetration. However, evidence points toward some pressure dependence with a reduced coefficient of friction. The simplest form that such friction can take is that which is proportional to the pressure, similar to classical Coulomb friction. Other forms have been proposed (e.g., [9]) and these could be incorporated into the analysis presented in this paper with more difficulty. The present effort utilizes a friction force that is proportional to the pressure and this has a substantial effect on the results. Some unexpected complexities make any form of approximate solution practically impossible. A numerical study of the solutions to the Euler-Lagrange equation is performed. The results are both interesting and useful.

## 2. Force of resistance on the projectile

Consider a rigid axisymmetric projectile normally penetrating a semi-infinite target. The cross-section of the tip is shown in Fig. 1. The length of the nose is  $b$  and the radius of the shank of the projectile is  $a$ . For all acceptable nose geometries  $y = y(x)$ ,  $y(0) = 0$  and  $y(b) = a$ . We assume in this analysis that the effects of friction are negligible beyond the nose at  $x = b$ .

The increment of force resisting the motion of the projectile is

$$dF = 2\pi y(p \sin \theta + f \cos \theta) ds, \quad (1)$$

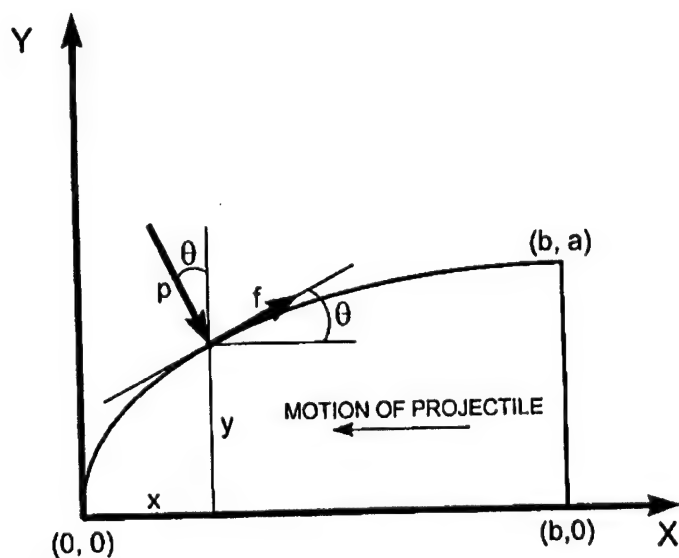


Fig. 1. Cross-section of the nose of an axisymmetric penetrator. The penetrator is acted upon by a continuous pressure  $p$  and friction (per unit area)  $f$ . The length of the nose of the projectile is  $b$  and the radius of the shank is  $a$ .

where

$$ds = \sqrt{1 + y'^2} dx \quad (2)$$

is the increment of arc length on the surface of the nose. From the geometry in Fig. 1, it is easy to see that

$$y' = \tan \theta, \quad (3)$$

$$\sin \theta = \frac{y'}{\sqrt{1 + y'^2}} \quad (4)$$

and

$$\cos \theta = \frac{1}{\sqrt{1 + y'^2}}. \quad (5)$$

Substituting Eqs. (2), (4) and (5) into Eq. (1), we find

$$dF = 2\pi y(y'p + f) dx \quad (6)$$

which can be integrated between  $x = 0$  and  $b$  to give the net force  $F$  resisting the motion of the projectile

$$F = 2\pi \int_0^b (yy'p + yf) dx. \quad (7)$$

### 3. Friction on the projectile

There are a number of forms that friction may take. Among the simplest for this problem is friction proportional to the normal pressure  $p$ . Take the coefficient of friction to be  $\mu$  and

$$f = \mu p. \quad (8)$$

As we assumed in our previous paper [1], the pressure  $p$  is of the Poncelet type

$$p = Av^2 \sin^2 \theta + B, \quad (9)$$

where  $A$  and  $B$  are constants,  $v$  is the current axial velocity of the projectile, and  $v \sin \theta$  is the normal component of axial velocity contributing to the pressure at the surface of the nose (see [3]). Now, substituting Eqs. (8) and (9) into Eq. (7), we find

$$F = 2\pi \int_0^b \left[ Av^2 y \frac{y^3 + \mu y'^2}{1 + y'^2} + B(yy' + \mu y) \right] dx, \quad (10)$$

where  $\sin \theta$  in Eq. (9) has been replaced by the right-hand side of Eq. (4).

When  $\mu = 0$  in Eq. (10), we return to the problem considered in [1] in which the net resistive force has the form

$$F = 2\pi Av^2 \int_0^b \frac{yy'^3}{1 + y'^2} dx + \pi a^2 B \quad (11)$$

and it is easy to see that maximum depth of penetration can be achieved when the integral  $I$

$$I = \int_0^b \frac{yy'^3}{1+y'^2} dx \quad (12)$$

is a minimum, because  $F$  is a minimum. However, when friction is included it is not so easy to see which geometry will optimize the depth of penetration looking at Eq. (10).

#### 4. Maximum penetration depth

The equation of motion of the projectile is

$$\begin{aligned} m\ddot{v} &= -F \\ &= -\pi a^2(ANv^2 + BM), \end{aligned} \quad (13)$$

where  $m$  is the projectile mass and

$$\begin{aligned} N &= \frac{2}{a^2} \int_0^b y \frac{y'^3 + \mu y'^2}{1+y'^2} dx \\ &= 2\alpha \int_0^1 z \frac{\alpha z'^3 + \mu z'^2}{1+\alpha^2 z'^2} d\xi \end{aligned} \quad (14)$$

and

$$\begin{aligned} M &= 1 + \frac{2\mu}{a^2} \int_0^b y dx \\ &= 1 + \frac{2\mu}{\alpha} \int_0^1 z d\xi. \end{aligned} \quad (15)$$

In the last two equations,  $x = b\xi$ ,  $y = az$ ,  $\alpha = a/b$ , where  $z = z(\xi)$  and  $\xi$  are dimensionless variables with  $z(0) = 0$  and  $z(1) = 1$ .

Because  $N$  and  $M$  are time-independent functions, Eq. (13) can be simply integrated, which leads to

$$P = \frac{m}{2\pi a^2 AN} \ln \left( 1 + \frac{AN}{BM} v_0^2 \right), \quad (16)$$

where  $P$  is the penetration depth. In order to find the geometry that maximizes  $P$ , we must vary  $z$  in Eqs. (14) and (15) for each fixed value of  $\alpha$  and  $\mu$ . Suppose that  $z = w(\xi)$  maximizes  $P$  in Eq. (16). Consider variations of this path with

$$z = w + \varepsilon\eta, \quad (17)$$

where  $\varepsilon$  is a parameter and  $\eta = \eta(\xi)$  is any differentiable function with  $\eta(0) = \eta(1) = 0$ . Substituting Eq. (17) into Eqs. (14) and (15), we see that  $N = N(\varepsilon)$  and  $M = M(\varepsilon)$ . Further, it is now clear from Eq. (16) that  $P = P(\varepsilon)$  with  $\max P = P(0)$ . Hence, it follows that  $dP/d\varepsilon = 0$  at  $\varepsilon = 0$ .

By differentiating Eq. (16) with respect to  $\epsilon$ , we find

$$\begin{aligned} \frac{dP}{d\epsilon} = & \frac{-m}{2\pi a^2 AN^2} \left\{ \left[ \ln \left( 1 + \frac{AN}{BM} v_0^2 \right) - \frac{(AN/BM)v_0^2}{1 + (AN/BM)v_0^2} \right] \frac{dN}{d\epsilon} \right. \\ & \left. + \frac{Av_0^2}{B} \frac{N^2}{M^2} \frac{1}{1 + (AN/BM)v_0^2} \frac{dM}{d\epsilon} \right\}. \end{aligned} \quad (18)$$

The derivatives  $dN/d\epsilon$  and  $dM/d\epsilon$  can be found by differentiating Eqs. (14) and (15)

$$\frac{dN}{d\epsilon} = 2\alpha \int_0^1 \eta \left[ \frac{\partial \phi}{\partial z} - \frac{d}{d\xi} \left( \frac{\partial \phi}{\partial z'} \right) \right] d\xi, \quad (19)$$

where

$$\phi(z, z') = z \frac{\alpha z'^3 + \mu z'^2}{1 + \alpha^2 z'^2} \quad (20)$$

and

$$\frac{dM}{d\epsilon} = \frac{2\mu}{\alpha} \int_0^1 \eta d\xi. \quad (21)$$

In Eqs. (19) and (20),  $z' = dz/d\xi$ . Now, substituting Eqs. (19) and (21) into Eq. (18) and computing  $\lim_{\epsilon \rightarrow 0} dP/d\epsilon = 0$ , leads to

$$\begin{aligned} & 2\alpha \left[ \ln \left( 1 + \lambda \frac{\bar{N}}{\bar{M}} \right) - \frac{\lambda \bar{N}/\bar{M}}{1 + \lambda \bar{N}/\bar{M}} \right] \int_0^1 \eta \left[ \frac{\partial \phi}{\partial w} - \frac{d}{d\xi} \left( \frac{\partial \phi}{\partial w'} \right) \right] d\xi + \frac{2\mu}{\alpha} \lambda \frac{\bar{N}^2}{\bar{M}^2} \frac{1}{1 + \lambda \bar{N}/\bar{M}} \int_0^1 \eta d\xi \\ & = \int_0^1 \left\{ 2\alpha \left[ \ln(1 + \lambda \bar{N}/\bar{M}) - \frac{\lambda \bar{N}/\bar{M}}{1 + \lambda \bar{N}/\bar{M}} \right] \left[ \frac{\partial \phi}{\partial w} - \frac{d}{d\xi} \left( \frac{\partial \phi}{\partial w'} \right) \right] + \frac{2\mu}{\alpha} \lambda \frac{\bar{N}^2}{\bar{M}^2} \frac{1}{1 + \lambda \bar{N}/\bar{M}} \right\} d\xi = 0, \end{aligned} \quad (22)$$

where

$$\bar{N} = 2\alpha \int_0^1 w \frac{\alpha w'^3 + \mu w'^2}{1 + \alpha^2 w'^2} d\xi \quad (23)$$

and

$$\bar{M} = 1 + \frac{2\mu}{\alpha} \int_0^1 w d\xi \quad (24)$$

and  $\lambda = Av_0^2/B$ . Because Eq. (22) must hold for all admissible variations  $\eta$  on the interval  $0 \leq \xi \leq 1$  with  $\eta(0) = \eta(1) = 0$ , it follows that  $w$  satisfies

$$\alpha^2 \left[ \ln \left( 1 + \lambda \frac{\bar{N}}{\bar{M}} \right) - \frac{\lambda \bar{N}/\bar{M}}{1 + \lambda \bar{N}/\bar{M}} \right] \left[ \frac{\partial \phi}{\partial w} - \frac{d}{d\xi} \left( \frac{\partial \phi}{\partial w'} \right) \right] + \mu \lambda \frac{\bar{N}^2}{\bar{M}^2} \frac{1}{1 + \lambda \bar{N}/\bar{M}} = 0. \quad (25)$$

This equation is the Euler-Lagrange equation for the variational problem described by Eq. (16). It is far more complicated than the usual Euler-Lagrange equation because  $\bar{N}$  and  $\bar{M}$  involve integrals of the dependent variable  $w$  from Eqs. (23) and (24). Additionally, referring back to the definition of  $\phi$  in Eq. (20), we can expand the derivatives indicated in Eq. (25) to get

$$\frac{\partial \phi}{\partial w} - \frac{d}{d\xi} \left( \frac{\partial \phi}{\partial w'} \right) = \frac{\mu \alpha^2 w'^4 - 2\alpha w'^3 - \mu w'^2}{(1 + \alpha^2 w'^2)^2} + w w'' \frac{2\alpha^3 w'^3 + 6\mu \alpha^2 w'^2 - 6\alpha w' - 2\mu}{(1 + \alpha^2 w'^2)^3}, \quad (26)$$

where  $w' = dw/d\xi$  and  $w'' = d^2w/d\xi^2$ . This means that not only are there integrals of the dependent variable and its derivative in Eq. (25), but there are also derivatives through the second order. Eq. (25) is a nonlinear differential-integral equation of extraordinary complexity to be solved subject to the two-point boundary conditions  $w(0) = 0$  and  $w(1) = 1$ . There may be some useful approximations to this problem, but in the interests of expedience we will pass up this approach and solve the problem numerically.

Before turning to the solution of Eq. (25), we should note that it reduces to the Euler-Lagrange equation for the frictionless case [1] when  $\mu = 0$ . When  $\mu \rightarrow 0$ , the second term in Eq. (25) vanishes, while  $\bar{M} \rightarrow 1$  and

$$\bar{N} \rightarrow 2\alpha^2 \int_0^1 \frac{w w'^3}{1 + \alpha^2 w'^2} d\xi. \quad (27)$$

This leaves us with the product

$$\alpha^2 \left[ \ln(1 + \lambda \bar{N}) - \frac{\lambda \bar{N}}{1 + \lambda \bar{N}} \right] \left[ \frac{\partial \phi}{\partial w} - \frac{d}{d\xi} \left( \frac{\partial \phi}{\partial w'} \right) \right] = 0 \quad (28)$$

with

$$\frac{\partial \phi}{\partial w} - \frac{d}{d\xi} \left( \frac{\partial \phi}{\partial w'} \right) = \frac{-2\alpha w'^3}{(1 + \alpha^2 w'^2)^2} + w w'' \frac{2\alpha^3 w'^3 - 6\alpha w'}{(1 + \alpha^2 w'^2)^3}. \quad (29)$$

For  $\alpha^2 \neq 0$  and  $\bar{N} > 0$ , the first of the two factors in Eq. (28) does not vanish. This leaves only the second factor to satisfy Eq. (28). Hence, the factor shown in Eq. (29) must equal zero and this is the Euler-Lagrange equation presented in [1] for the frictionless case.

## 5. Numerical solution methodology

A numerical solution for Eq. (25) was obtained by assuming a solution of the following form:

$$z = a_1 \xi^n + a_2 \xi^{2n} + a_3 \xi^{3n}, \quad (30)$$

where  $a_i$  and  $n$  are adjustable parameters which are a function of  $\alpha$ ,  $\lambda$ , and  $\mu$ . A least-squares approach was used to obtain values for these parameters. For particular  $\alpha$ ,  $\lambda$ , and  $\mu$  values, Eq. (25) was evaluated [using the assumed function, Eq. (30)] at 20 evenly spaced  $\xi$  values from 0.05 to 1. These 20 function values (which ideally should equal zero) were then squared and summed to produce an aggregate fit error. An optimizer was used to adjust the  $a_i$  and  $n$  values to minimize the

fit error. Values of the  $\bar{N}$  [Eq. (23)] and  $\bar{M}$  [Eq. (24)] integrals for insertion into Eq. (25) were obtained by a numerical integration scheme also using 20 evenly spaced  $\xi$  values from 0.05 to 1. The optimizer was constrained to seek solutions with  $z$  and  $z'$  greater than or equal to zero. Further, the parameter  $n$  of Eq. (30) was forced to be positive. These calculations were conveniently conducted using a spreadsheet computer program.

It must be noted that the development of Eq. (25) is a necessary, but not sufficient, condition for maximum penetration depth. It can equally apply to minimum penetration depth. In fact, both maxima and minima are achieved along the same path for different combinations of the physical parameters  $\alpha$ ,  $\lambda$ , and  $\mu$ . This will be illustrated in the next section.

## 6. Typical results

Numerical test cases were investigated using the same model parameters as reported by Forrestal et al. [11] for test results involving firing small steel projectiles into semi-infinite grout

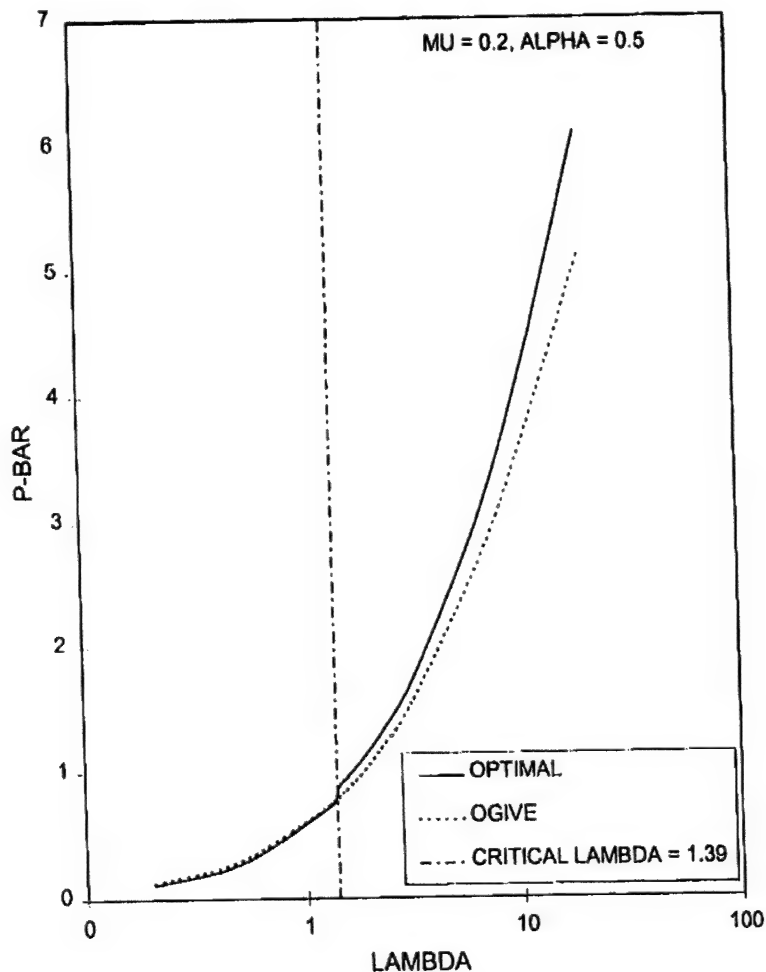


Fig. 2. Plot of  $\bar{P}$  versus  $\lambda$  for optimal and ogival nose shapes. Note that the optimal nose goes blunt (penetration depth minimized) for  $\lambda$  values less than 1.39 for this case ( $\alpha = 0.5$ ,  $\mu = 0.2$ ).

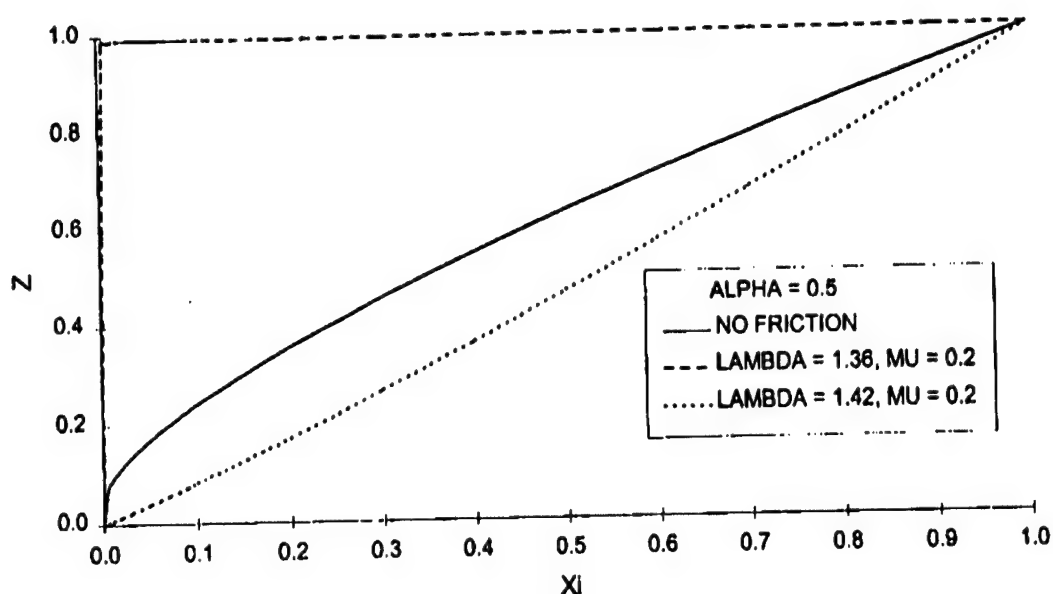


Fig. 3. Comparison of optimal nose shapes with the frictionless optimal nose shape of [1]. For the  $\lambda = 1.42$  case penetration depth is maximized and ogival performance is bettered. Penetration depth is minimized for the  $\lambda = 1.36$  case (nose blunted).

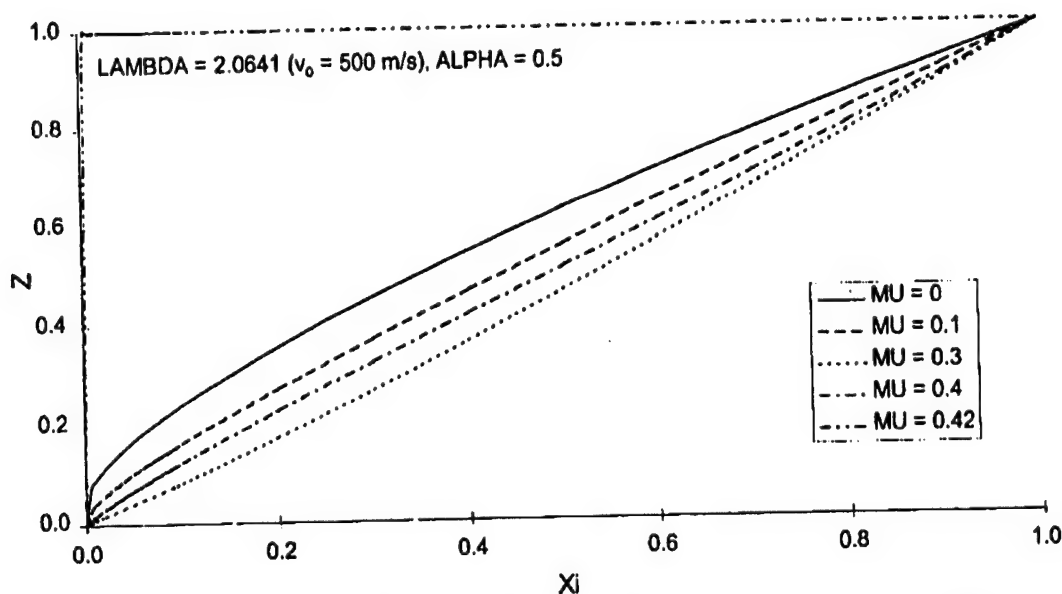


Fig. 4. Plots of optimal nose shape for  $\alpha = 0.5$  and  $\lambda = 2.0641$  ( $v_0 = 500$  m/s) for various values of friction coefficient  $\mu$ .

targets. These tests involved projectiles of mass 65 g and diameter 12.9 mm. The grout target force response coefficients were  $A = 2.32E3$  kg/m<sup>3</sup> (target density) and  $B = 281$  MPa (corresponding to  $f_c' = 13.4$  MPa and a dynamic strength multiplier of 21). The numerical results involved selecting reasonable values of the system parameters  $\alpha$ ,  $\lambda$ , and  $\mu$  for parametric studies.

Initially, a test case was conducted to determine if the formulation described in this paper indeed produced optimal penetration results. One means of accomplishing this is to compare the

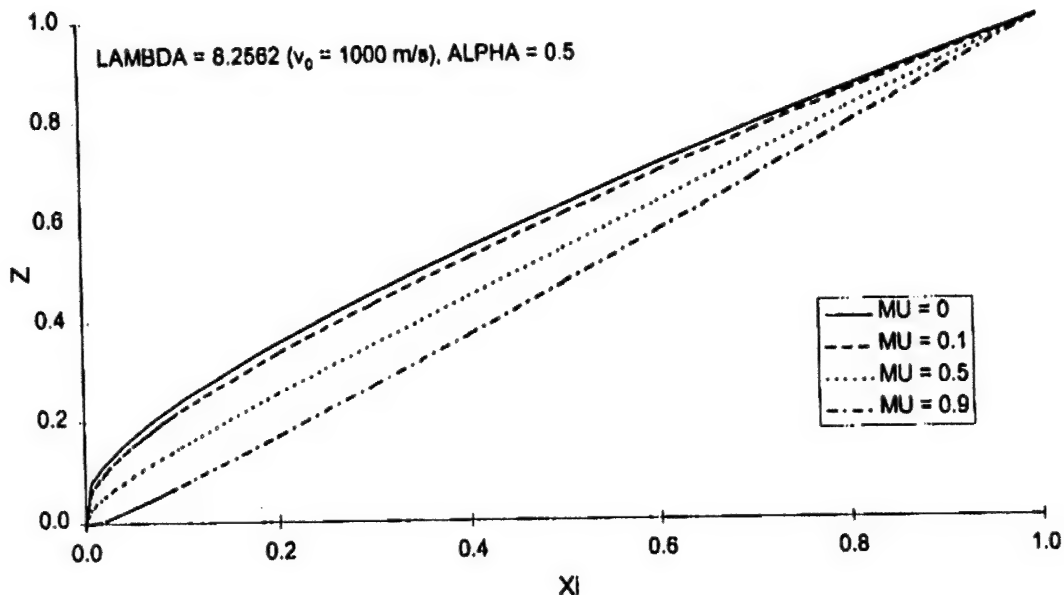


Fig. 5. Plots of optimal nose shape for  $\alpha = 0.5$  and  $\lambda = 8.2562$  ( $v_0 = 1000$  m/s) for various values of friction coefficient  $\mu$ .

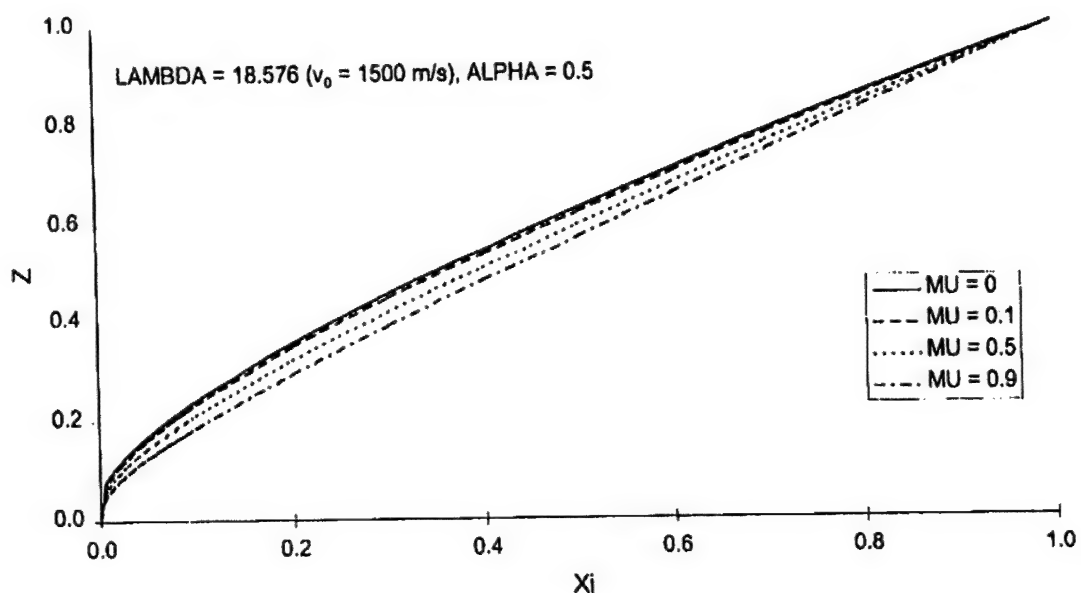


Fig. 6. Plots of optimal nose shape for  $\alpha = 0.5$  and  $\lambda = 18.576$  ( $v_0 = 1500$  m/s) for various values of friction coefficient  $\mu$ .

penetration depths of the optimal nose shape with a well-known effective nose shape — the ogive. Fig. 2 shows a plot of nondimensional penetration depth ( $\bar{P} = 2\pi a^2 AN/m$ ) of optimal and ogival penetrators versus  $\lambda$  for  $\alpha = 0.5$  and  $\mu = 0.2$ . As can be seen from this figure, the optimal penetrator is clearly more effective for the larger  $\lambda$  values. However, for  $\lambda$  values less than approximately 1.39 (lower-velocity impacts) the nature of the optimal solution changes completely. Instead of maximizing penetration depth minimization occurs and the optimizer drives the penetrator to a blunted-ended shape with penetration performance inferior to that of the ogive.

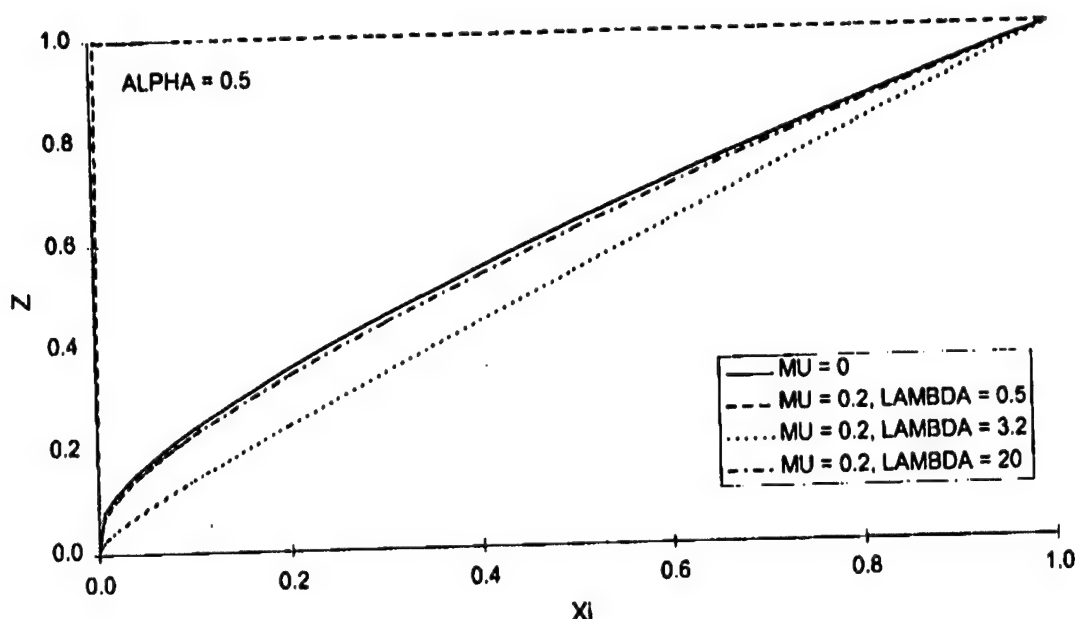


Fig. 7. Plots of optimal nose shape for  $\alpha = 0.5$  and  $\mu = 0.2$  for various values of  $\lambda$ . The frictionless case ( $\mu = 0$ ) is shown for comparison.

Optimized nose shapes are compared with that of the frictionless case in Fig. 3. Further optimized nose shapes are shown in Fig. 4 [ $\alpha = 0.5, \lambda = 2.0641$  ( $v_0 = 500$  m/s)], Fig. 5 [ $\alpha = 0.5, \lambda = 8.2562$  ( $v_0 = 1000$  m/s)], and Fig. 6 [ $\alpha = 0.5, \lambda = 18.576$  ( $v_0 = 1500$  m/s)] for various friction coefficient  $\mu$  levels. Note that at the higher impact velocities (Figs. 5 and 6) blunting did not occur even at very high friction levels.

Fig. 7 shows plots of optimal nose shape ( $\alpha = 0.5, \mu = 0.2$ ) for various values of  $\lambda$ . The frictionless case ( $\mu = 0$ ) is shown in this figure for comparison. Note that at low impact velocities (small  $\lambda$ ) blunting occurs (penetration depth minimized) and that at high impact velocities the optimal shape closely resembles that of the frictionless case.

Critical levels of  $\mu$  at which blunting occurs are plotted as a function of  $\lambda$  for various values of  $\alpha$  in Fig. 8. This figure clearly shows that unrealistically large friction coefficients are necessary to cause a blunt penetrator solution at the higher impact velocities.

Finally, Fig. 9 compares optimal and ogival nose penetration performance as a function of  $\lambda$  for various values of  $\alpha$ . In this figure optimal nose results were not plotted for those values of  $\lambda$  where blunting occurred.

## 7. Conclusions

In this paper, we have presented a variational analysis of normal penetration into semi-infinite targets including the effects of sliding friction on the tip of the penetrator. The choice of friction law for this paper was one of the simplest. However, the choice of friction may be simple, but its effect on the optimization problem is far from simple. Eq. (25) is a nonlinear differential-integral equation of staggering proportions and any form of analytical solution is practically impossible. The most

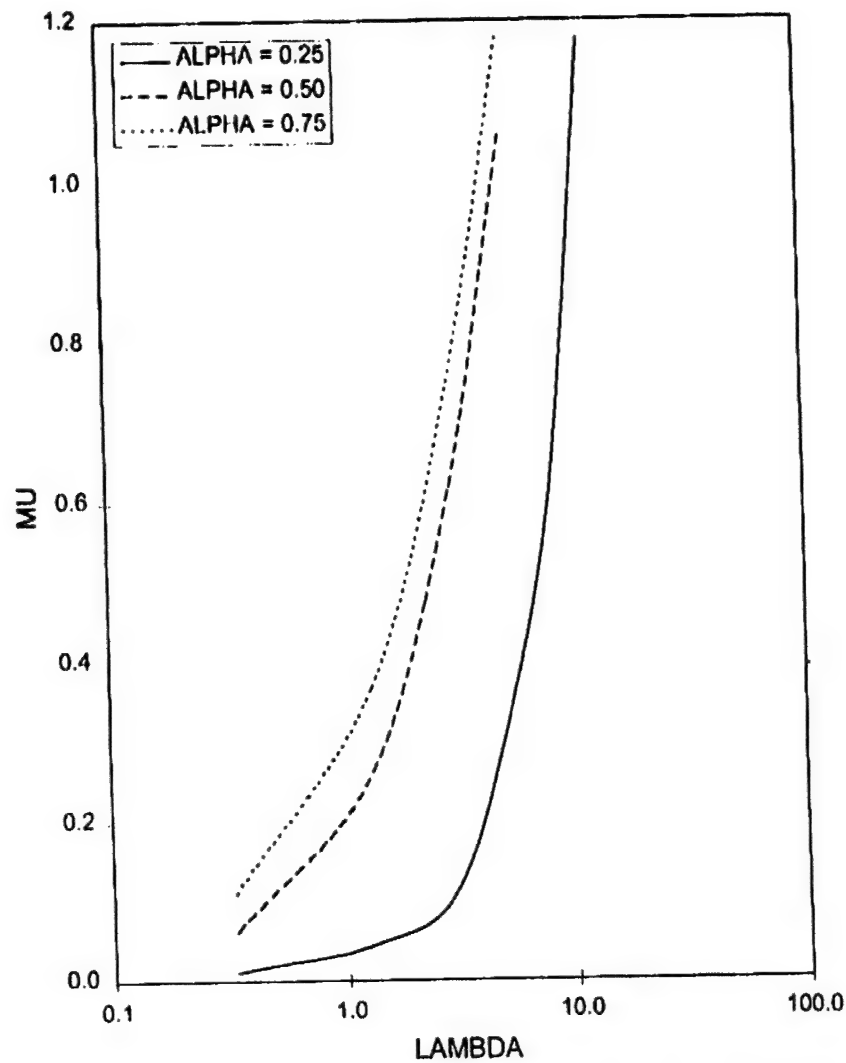


Fig. 8. Plots of the critical  $\mu$  for blunting versus  $\lambda$  for various values of  $\alpha$ .

expedient approach to solving the problem was to employ a weighted residual technique involving a trial solution that contained powers of the independent variable and four free constants chosen by an optimizer to minimize the residual error. This technique produced very satisfactory results when the combination of physical constants  $\alpha$ ,  $\lambda$ , and  $\mu$  dictated a maximum for the variational integral. Except in the neighborhood of the transition to a minimum (conjugate point), the solution was stable and converged rapidly. After the transition to a minimum, the geometry predicted for the penetrator tip was as close to blunt-ended as possible (see Fig. 3). This situation in the variational calculus is not uncommon and is usually detected by examining the sign of the second variation. However, in this instance, that approach is practically impossible due to the severe complexity of the second variation.

The presence of friction alters the geometry for optimal performance at lower impact velocities by sharpening the nose of the projectile. The more friction that is present, the sharper the nose required to achieve maximum depth (of course, this assumes that no erosion is possible and the

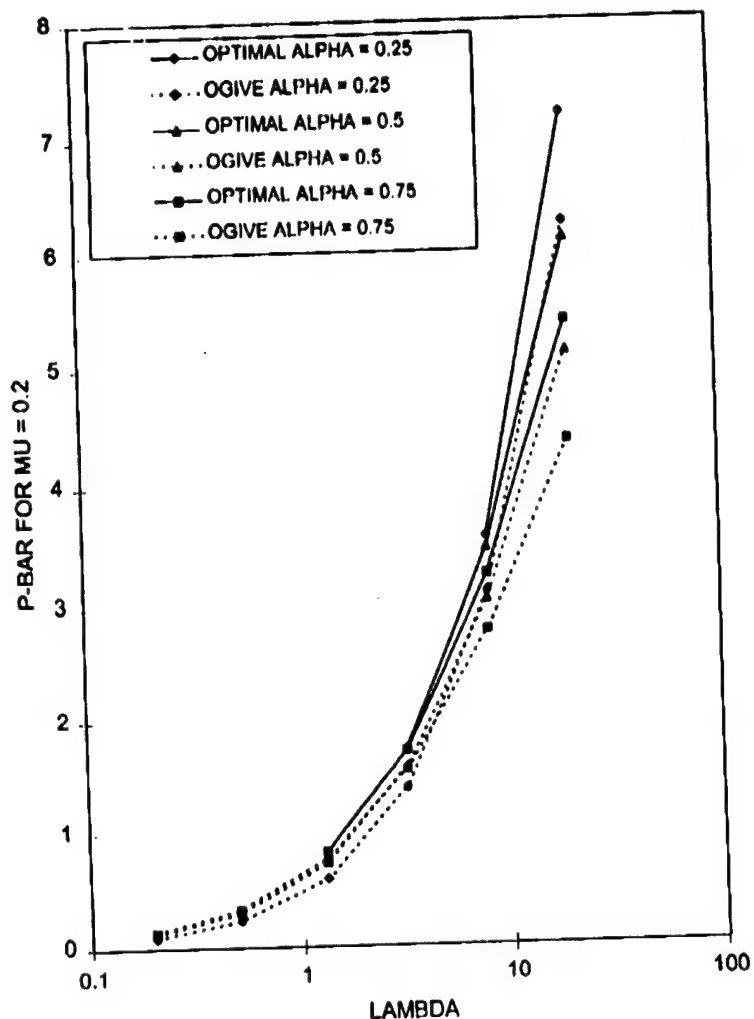


Fig. 9. Plots of  $\bar{P}$  versus  $\lambda$  for optimal and ogival nose shapes for various values of  $\alpha$ . Note that the optimal plots were stopped at the lower levels of  $\lambda$  where blunting occurred.

nose does not fail). However, for higher impact velocities, this sharpening of the nose only occurs for more friction than is reasonable to expect in these problems. For modest friction, the optimal nose geometry is very close to that predicted in the frictionless case. This is very good news indeed. Actual friction levels are extremely difficult to assess, making this analysis awkward to use in the design of a penetrator. This analysis does, however, provide us with qualitative insight into the penetration process and the role that friction plays for high- and low-velocity projectiles.

These conclusions should be verified by using an alternative friction law. This is the direction that future efforts in this area will take.

## References

[1] Jones SE, Rule WK, Jerome DM, Klug RT. On the optimal nose geometry for a rigid penetrator. Proceedings of the International Symposium on Impact and Penetration Problems in Atlanta, GA, October, 1998, Comput Mech 1998;22:413.

- [2] Poncelet JV. *Cours de Mécanique Industrielle*. Paris, 1829.
- [3] Luk K, Forrestal MJ. Penetration into semi-infinite reinforced-concrete targets with spherical and ogival nose projectiles. *Int J Impact Engng* 1987;6(4):291.
- [4] Backman ME, Goldsmith W. The mechanics of penetration of projectiles into targets. *Int J Engng Sci* 1978;16:1.
- [5] Rinehart J, Pearson J. *Behavior of materials under impulsive loads*. New York: Dover, 1965.
- [6] Bowden FP, Tabor D. *The friction and lubrication of solids, Part II*. London: Oxford University Press, 1964.
- [7] Kragelskii IV. *Friction and wear*. Washington: Butterworths, 1965.
- [8] Montgomery RS. Friction and wear at high sliding speeds. *Wear* 1976;36:275.
- [9] Gaffney ES. Measurements of dynamic friction between rock and steel. *DNA Report No. 4161F*, 1976.
- [10] Forrestal MJ, Grady DE. Penetration experiments for normal impact into geological targets. *Int J Solids Struct* 1982;18:229-34.
- [11] Forrestal MJ, Frew DJ, Hanchak SJ, Brar NS. Penetration of grout and concrete targets with ogive-nose steel projectiles. *Int J Impact Engng* 1996;18(5):465.

---

## **APPENDIX P**

## SOME REMARKS ON THE OPTIMAL NOSE GEOMETRY OF A RIGID PENETRATOR IN THE PRESENCE OF FRICTION

William K. Rule

Software Analyst/Engineer, Trus Joist  
MacMillan, 3166 Elder St., Boise, Idaho, 83705,  
Phone: (208)395-2485, Fax: (208)395-2488,  
ruleb@ljm.com

S. E. Jones

Senior Scientist, U. S. Air Force Research  
Laboratory, Munitions Directorate, Eglin AFB,  
FL (on leave from the University of Alabama)

### ABSTRACT

In related papers, the problem of maximizing the depth of penetration by a normally impacting cylindrical projectile by optimizing the nose geometry was considered. In Jones, et al. (1998a), results were accomplished by neglecting any frictional resistance offered by the target and only considering the normal pressure acting against the penetrator nose. The effects of pressure-dependent friction were treated by Jones and Rule (1999). Here, the formulation presented in Jones and Rule (1999) is modified to treat the frictional force as a constant that is intended to represent the shear strength of the target. The results of parametric studies are presented to demonstrate system behavior. Also, experimental data was used with the model to determine the shear strength of a concrete target.

### INTRODUCTION

In two earlier papers Jones, et al. (1998) and Jones and Rule (1999), the authors investigated the geometry of the nose of a rigid penetrator acted upon by a velocity-squared pressure. This was first done in the absence of friction and later in the presence of a pressure-dependent friction. The results were very interesting. Using friction proportional to the pressure, it was noted that the tip of the optimal nose geometry sharpened at lower impact velocities. At higher impact velocities, friction had less influence and the nose geometry returned to the zero friction case, unless the friction coefficient was very large.

One thing is very clear. There is not very much known about friction at high sliding speeds (e.g., see Bowden and Tabor (1964) or Kragelskii (1965)). Much of the work that has been reported is at lower speeds or pressures than those encountered during a penetration event. In view of this, we decided that it was prudent to repeat the analysis presented in Jones and Rule (1999) using an alternative friction law to determine what effect this had on the results.

### THEORY

The problem considered is similar to that recently presented by the authors (1999). A rigid axisymmetric projectile normally impacts a semi-infinite target. The cross-section of the nose is shown in Fig. 1. The length of the nose is  $b$  and the radius of the shank of the projectile is  $a$ . For all acceptable geometries, the surface of the nose is given by  $y=y(x)$  with  $y(0)=0$  and  $y(b)=a$ . We assume that the effects of friction are negligible beyond the nose at  $x=b$ . As shown in Jones and Rule (1999), the net force  $F$  resisting the motion of the projectile is given by

$$F = 2\pi \int_0^b (yy'p + yf) dx \quad (1)$$

where  $p$  is the pressure and  $f$  is the friction acting on the nose of the projectile. In the previous analysis,  $f$  was taken to be proportional to the pressure  $p$ . In this paper, we take  $f=\tau$ , a constant, possibly equal to the shear strength of the target. As we did in the previous paper on this subject, we take the pressure  $p$  to be of the Poncelet form

$$p = Av^2 \sin^2 \theta + B \quad (2)$$

where  $A$  and  $B$  are constants,  $v$  is the current velocity of the projectile,  $v \sin \theta$  is the normal component of the axial velocity contributing to the pressure at the nose, and  $\theta$  is the tangent angle at the surface of the nose (see Fig. 1). Now using Eq. (2) in Eq. (1) and the fact that  $\sin \theta = y' / \sqrt{1+y'^2}$ , we find that the resisting force on the projectile has the form

$$F = 2\pi v^2 \int_0^b \frac{yy'^3}{1+y'^2} dx + 2\pi \int_0^b y dx + m^2 B \quad (3)$$

which can be written as

$$F = mv^2 (ANv^2 + MB) \quad (4)$$

where

$$N = 2\alpha^2 \int_0^1 \frac{xx'^3}{1+\alpha^2 x'^2} d\xi \quad (5)$$

and

$$M = 1 + \frac{2}{\alpha} \gamma \int_0^1 z d\xi. \quad (6)$$

In these equations,  $x = b\xi$ ,  $y = \alpha x$ ,  $\alpha = a/b$ ,  $\gamma = \tau/B$ , and  $z = z(\xi)$  and  $\xi$  are dimensionless variables with  $x(0)=0$  and  $x(1)=1$ . Results similar to Eqs. (4)-(6) were first presented by Luk and Forrestal (1989) for spherical and ogival nose projectiles.

Now, using the force from Eq. (4), the equation of motion for the projectile becomes

$$mv = -mv^2 (ANv^2 + BM). \quad (7)$$

This equation can be integrated to find the depth of penetration  $P$  of the projectile

$$P = \frac{m}{2mv^2 AN} \ln \left( 1 + \frac{AN}{BM} v_0^2 \right) \quad (8)$$

because  $M$  and  $N$  are independent of time. In the last equation,  $m$  is the mass of the projectile and  $v_0$  is the impact speed.

### OPTIMAL NOSE GEOMETRY

Equation (8) is difficult to use to optimize the nose geometry because  $M$  and  $N$  both depend on the nose profile  $y=y(x)$ . However, the conventional approach used in the calculus of variations (e.g., see Lanczos (1996), Pars (1962), or Vujanovic and Jones (1989)) is adequate to find the optimal geometry to maximize the penetration depth,  $P$ . In this context, suppose that  $z = w(\xi)$  is the profile that maximizes the penetration depth. Consider continuous variations of this path  $\eta = \eta(\xi)$  with  $\eta(0) = \eta(1) = 0$  and

$$z = w + \varepsilon \eta \quad (9)$$

where  $\varepsilon$  is a parameter. If we substitute Eq. (9) into Eq. (8) (this means that  $z$  in Eqs. (5) and (6) is modified by the substitution), then it

is clear that  $P = P(\varepsilon)$ . It is further clear that  $P(0)$  is a local extreme for the function  $P$ . Hence, it follows that  $dP/d\varepsilon = 0$  at  $\varepsilon = 0$ . By differentiating Eq. (8) with respect to  $\varepsilon$ , we find

$$\begin{aligned} \frac{dP}{d\varepsilon} = & -\frac{m}{2mv^2 AN^2} \left[ \ln \left( 1 + \frac{AN}{BM} v_0^2 \right) - \frac{\frac{AN}{BM} v_0^2}{1 + \frac{AN}{BM} v_0^2} \right] \frac{dN}{d\varepsilon} \\ & - \frac{m}{2mv^2 AN^2} \left( \frac{AN^2}{B M^2} \frac{1}{1 + \frac{AN}{BM} v_0^2} \frac{dM}{d\varepsilon} \right) \end{aligned} \quad (10)$$

The derivatives of  $N$  and  $M$  with respect to  $\varepsilon$  can be found by differentiating Eqs. (5) and (6). These differentiations lead to

$$\frac{dN}{d\varepsilon} = 2\alpha^2 \int_0^1 \left[ \frac{\partial \phi}{\partial z} - \frac{d}{d\xi} \left( \frac{\partial \phi}{\partial z'} \right) \right] \eta d\xi \quad (11)$$

where

$$\phi = \frac{xx'^3}{1 + \alpha^2 x'^2} \quad (12)$$

and

$$\frac{dM}{d\varepsilon} = \frac{2}{\alpha} \gamma \int_0^1 \eta d\xi. \quad (13)$$

In Eqs. (11) and (12),  $z' = dz/d\xi$ . Now, if we substitute Eqs. (1) and (13) into Eq. (10), take the limit as  $\varepsilon \rightarrow 0$ , and manipulate the integrals, we can show that

$$\begin{aligned} & \int_0^1 \left[ 2\alpha^2 \left[ \ln \left( 1 + \frac{AN}{BM} v_0^2 \right) - \frac{\frac{AN}{BM} v_0^2}{1 + \frac{AN}{BM} v_0^2} \right] \frac{\partial \phi}{\partial w} - \frac{d}{d\xi} \left( \frac{\partial \phi}{\partial w'} \right) \right] \eta d\xi + \\ & \int_0^1 \left[ \frac{AN^2}{B} \left( \frac{N}{M} \right)^2 \frac{1}{1 + \frac{AN}{BM} v_0^2} \frac{2\gamma}{\alpha} \right] \eta d\xi = 0 \end{aligned} \quad (14)$$

for all admissible variations. In this equation,  $\bar{N}$  and  $\bar{M}$  are limits in Eqs. (5) and (6) as  $\varepsilon \rightarrow 0$ , which means that  $z$  is simply replaced by  $w$  in these equations.

Now, if the integral in Eq. (14) equals zero for all admissible variations, then the integrand must be equal to zero. This leads to extremely complicated Euler-Lagrange Equation for the determination of  $w = w(\xi)$  subject to the conditions  $w(0) = 0$  and  $w(1) = 1$ . The equation is

$$\begin{aligned}
& 2\alpha^2 \left[ \ln \left( 1 + \frac{AN}{BM} v_0^2 \right) - \frac{\frac{AN}{BM} v_0^2}{1 + \frac{AN}{BM} v_0^2} \right] \left[ \frac{\partial \phi}{\partial w} - \frac{d}{d\xi} \left( \frac{\partial \phi}{\partial w} \right) \right] \\
& + \frac{Av_0^2}{B} \left( \frac{N}{M} \right)^2 \frac{1}{1 + \frac{AN}{BM} v_0^2} \alpha = \\
& 2\alpha^2 \left[ \ln \left( 1 + \lambda \frac{N}{M} \right) - \frac{\lambda \frac{N}{M}}{1 + \lambda \frac{N}{M}} \right] \left[ \frac{\partial \phi}{\partial w} - \frac{d}{d\xi} \left( \frac{\partial \phi}{\partial w} \right) \right] \\
& + \lambda \left( \frac{N}{M} \right)^2 \frac{1}{1 + \lambda \frac{N}{M}} \alpha = 0 \quad (15)
\end{aligned}$$

where  $\bar{N}$  and  $\bar{M}$  involve integrals of functions of  $w$  and  $w'$  and  $\lambda = Av_0^2/B$  is a dimensionless parameter. This means that Eq. (15) is a nonlinear differential-integral equation with derivatives of the second order and integrals with fixed limits. Finding a solution to this equation is indeed a challenge. We will not attempt to find any form of approximate analytical solution and instead concentrate on a high accuracy numerical approximation.

## NUMERICAL SOLUTION

A numerical solution for Eq. (15) was obtained by assuming a solution of the following form

$$z = a_1 \xi^n + a_2 \xi^{2n} + a_3 \xi^{3n} \quad (16)$$

where  $a_i$  and  $n$  are adjustable parameters which are a function of  $\alpha$ ,  $\lambda$ , and  $\gamma$ . A least squares approach was used to obtain values for these parameters. For particular  $\alpha$ ,  $\lambda$ , and  $\gamma$  values, Eq. (15) was evaluated [using the assumed function, Eq. (16)] at 20 evenly spaced  $\xi$  values from 0.05 to 1. These twenty function values (which ideally should equal zero) were then squared and summed to produce an aggregate fit error. An optimizer was used to adjust the  $a_i$  and  $n$  values to minimize the fit error. Values of the  $\bar{N}$  and  $\bar{M}$  integrals for insertion into Eq. (15) were obtained by a numerical integration scheme also using 20 evenly spaced  $\xi$  values from 0.05 to 1. The optimizer was constrained to seek solutions with  $z$  and  $z'$  greater than or equal to zero. Further, the parameter  $n$  of Eq. (16) was forced to be positive. These calculations were conveniently conducted using a spreadsheet computer program.

It must be noted that the development of Eq. (15) is a necessary, but not sufficient, condition for maximum penetration depth. It can equally apply to minimum penetration depth. In fact, both maxima and minima are achieved along the same path for different combinations of

the physical parameters  $\alpha$ ,  $\lambda$ , and  $\gamma$ . This will be illustrated in the next section.

## TYPICAL RESULTS

Numerical test cases were investigated using the same model parameters as reported by Forrestal, et al (1996) for test results involving firing small steel projectiles into semi-infinite grout targets. These tests involved projectiles of mass 65 g and diameter 12.9 mm. The grout target force response coefficients were  $A = 2.32E3 \text{ kg/m}^3$  (target density) and  $B = 281 \text{ MPa}$  (corresponding to  $f_c' = 13.4 \text{ MPa}$  and an  $S$  multiplier of 21,  $B = Sf_c'$ ). The numerical results involved selecting reasonable values of the system parameters  $\alpha$ ,  $\lambda$ , and  $\gamma$  for parametric studies.

Initially a test case was conducted to determine if the formulation described in this paper indeed produced optimal penetration results. One means of accomplishing this is to compare the penetration depths of the optimal nose shape with a well known effective nose shape - the ogive. Fig. 2 shows a plot of nondimensional penetration depth ( $\bar{P} = 2\pi a^2 AP/m$ ) of optimal and ogival penetrators versus  $\lambda$  for  $\alpha = 0.5$  and  $\gamma = 0.2$ . As can be seen from this figure, the optimal penetrator is clearly more effective for the larger  $\lambda$  values. However, for  $\lambda$  values less than approximately 1.83 (lower velocity impacts) the nature of the optimal solution changes completely. Instead of maximizing penetration depth minimization occurs and the optimizer drives the penetrator to a blunt-ended shape with penetration performance inferior to that of the ogive.

Optimized nose shapes are compared with that of the frictionless case in Fig. 3. Further optimized nose shapes are shown in Fig. 4 [ $\alpha = 0.5$ ,  $\lambda = 8.2562$  ( $v_0 = 1000 \text{ m/s}$ )] for various friction coefficient  $\gamma$  levels. Note that blunting occurred at the highest friction level.

Figure 5 shows plots of optimal nose shape ( $\alpha = 0.5$ ,  $\gamma = 0.2$ ) for various values of  $\lambda$ . The frictionless case ( $\gamma = 0$ ) is shown in this figure for comparison. Note that at the lowest impact velocity shown (small  $\lambda$ ) blunting occurs (penetration depth minimized) and that at the higher impact velocity the optimal shape closely resembles that of the frictionless case.

## EVALUATION OF THE SHEAR STRENGTH OF A CONCRETE TARGET

Recently, Frew et al. (1998) published results for ogive-nose steel rods impacting concrete targets at velocities ranging from 442 to 1165 m/s. The data of Table 1 of Frew et al. (1998) was used with the present model to back-out an effective target shear strength,  $\tau$ . A least squares approach was used to adjust  $\tau$  to minimize the difference between measured and calculated concrete target penetration data. The model parameters used are listed in Table 1.

**Table 1 Model parameters used for comparison with the data of Frew et al. (1998)**

a	1.015E-02 m
b	3.370E-02 m
m	0.478 kg
A	2320 kg/m <sup>3</sup>
B	484.7 MPa (Dynamic Strength Factor = S = 8.3 from Frew, et al. (1998))

The best fit value obtained was  $\tau = 4.93$  MPa ( $\gamma = 1.018E-2$ ) which amounts to 8.4% of the reported  $f_c' = 58.4$  MPa of the concrete. Measured and calculated results are compared in Fig. 6.

## CONCLUSIONS

In this paper, we have presented a variational analysis of normal penetration into semi-infinite targets including the effects of constant friction on the tip of the penetrator. The choice of friction law for this paper was one of the simplest. However, the choice of friction may be simple, but its effect on the optimization problem is far from simple. Eq. (15) is a nonlinear differential-integral equation of staggering proportions and any form of analytical solution is practically impossible. The most expedient approach to solving the problem was to employ a weighted residual technique involving a trial solution that contained powers of the independent variable and four free constants chosen by an optimizer to minimize the residual error. This technique produced very satisfactory results when the combination of physical constants  $\alpha$ ,  $\lambda$ , and  $\gamma$  dictated a maximum for the variational integral. Except in the neighborhood of the transition to a minimum (conjugate point), the solution was stable and converged rapidly. After the transition to a minimum, the geometry predicted for the penetrator nose was as close to blunt-ended as possible (see Fig. 3). This situation in the variational calculus is not uncommon and is usually detected by examining the sign of the second variation. However, in this instance, that approach is practically impossible due to the severe complexity of the second variation.

The presence of friction alters the geometry for optimal performance at lower impact velocities by sharpening the nose of the projectile. The more friction that is present, the sharper the nose required to achieve maximum depth (of course, this assumes that no erosion is possible and the nose does not fail). However, for higher impact velocities, this sharpening of the nose only occurs for more friction than is reasonable to expect in these problems. For modest friction, the optimal nose geometry is very close to that predicted in the frictionless case. This is very useful conclusion indeed. Actual friction levels are extremely difficult to assess, making this analysis awkward to use in the design of a penetrator. This analysis does, however, provide us with qualitative insight into the penetration process and the role that friction plays for high and low velocity projectiles.

## REFERENCES

Bowden, F. B. and Tabor, D., 1964, *The Friction and Lubrication of Solids, Part II*, Oxford University Press, London.

Frew, D. J., Hanchak, S. J., Green, M. L., and Forrestal, M. J., 1998, "Penetration of Concrete Targets with Ogive-Nose Steel Rods," *Int. J. Impact Engng.*, Vol. 21, 6, 489-497.

Forrestal, M. J., Frew, S. J., Hanchak, S. J., and Brar, N. S., 1996, "Penetration of Grout and Concrete Targets with Ogive-Nose Steel Projectiles," *Int. J. Impact Engng.*, Vol. 18, 5, 465-476.

Jones, S. E., Rule, W. K., Jerome, D. M., and Klug, R. T., 1998, "On the Optimal Nose Geometry for a Rigid Penetrator," *Computational Mechanics*, Vol. 22, 413-417. A six page summary paper may be found in *Modeling and Simulation Based Engineering*, Volume II, S. N. Atluri and P. E. O'Donoghue, eds., Tech Science Press, Palmdale, CA, 1120-1123.

Jones, S. E. and Rule, W. K., 1999, "On the Optimal Nose Geometry for a Rigid Penetrator, Including the Effects of Pressure-Dependent Friction," *Int. J. Impact Engng.*, to appear.

Kragelskii, I. V., 1965, *Friction and Wear*, Butterworths, Washington.

Lanczos, C., 1966, *The Variational Principles of Mechanics*, University of Toronto Press, Toronto.

Luk, V. K. and Forrestal, M. J., 1989, "Comment on 'Penetration Into Semi-Infinite Targets with Spherical and Ogival Nose Projectiles,'" *Int. J. Impact Engng.*, Vol. 8, 1, 83-84.

Pars, L. A., 1962, *An Introduction to the Calculus of Variations*, Heinemann, London.

Vujanovic, B. D. and Jones, S. E., *Variational Methods in Nonconservative Phenomena*, Academic Press, Boston.

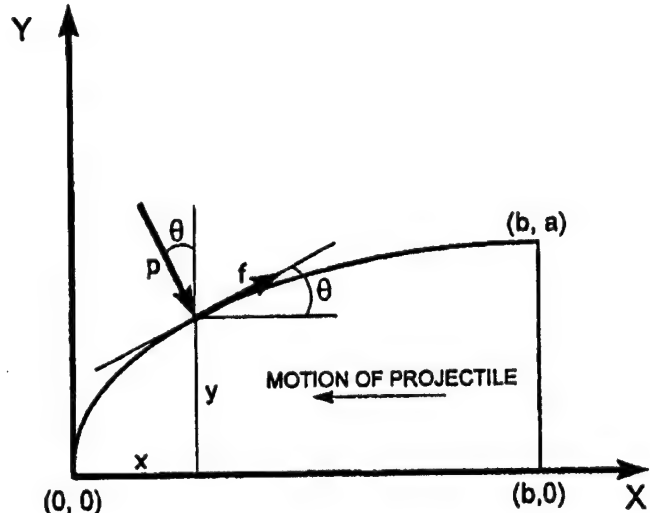


**Figure 1. Cross-section of the nose of an axisymmetric penetrator. The penetrator is acted upon by a continuous pressure  $p$  and friction (per unit area)  $f$ . The length of the nose of the projectile is  $b$  and the radius of the shank is  $a$ .**

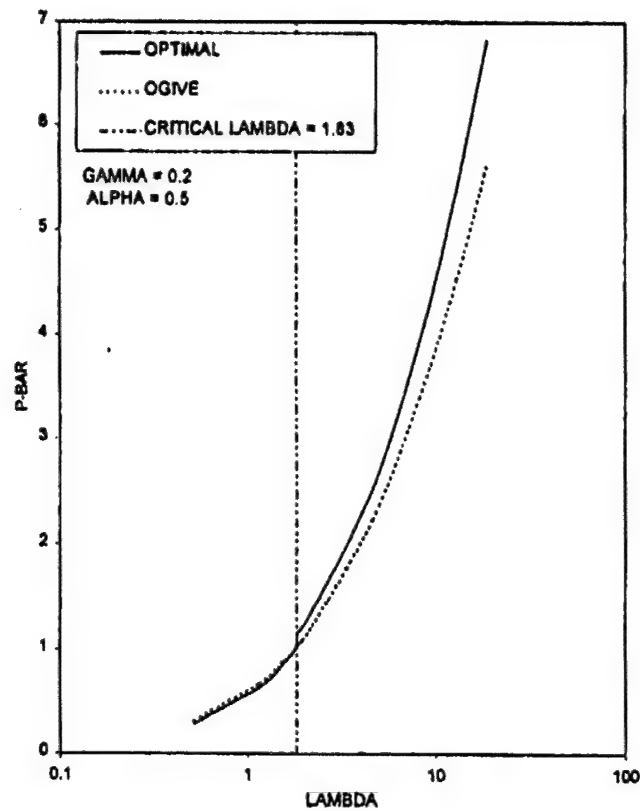


Figure 2. Plot of nondimensional  $\bar{P} = \frac{2\pi a^2 A}{m} P$  versus  $\lambda$  for optimal and ogival nose shapes. Note that the optimal nose goes blunt (penetration depth minimized) for  $\lambda$  values less than 1.83 for this case ( $\gamma = 0.2$ ,  $\alpha = 0.5$ ).

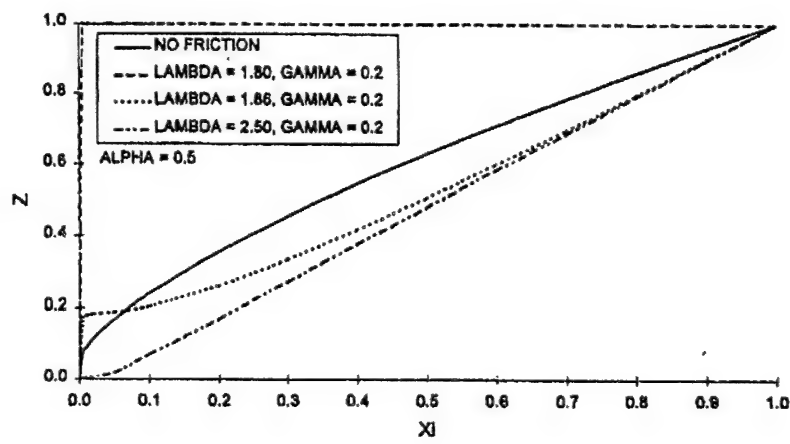


Figure 3. Comparison of optimal nose shapes with the frictionless optimal nose shape of Jones, et al (1998). For the  $\lambda = 1.86$  and 2.50 cases penetration depth is maximized and ogival performance is bettered. Penetration depth is minimized for the  $\lambda = 1.80$  case (nose blunted).

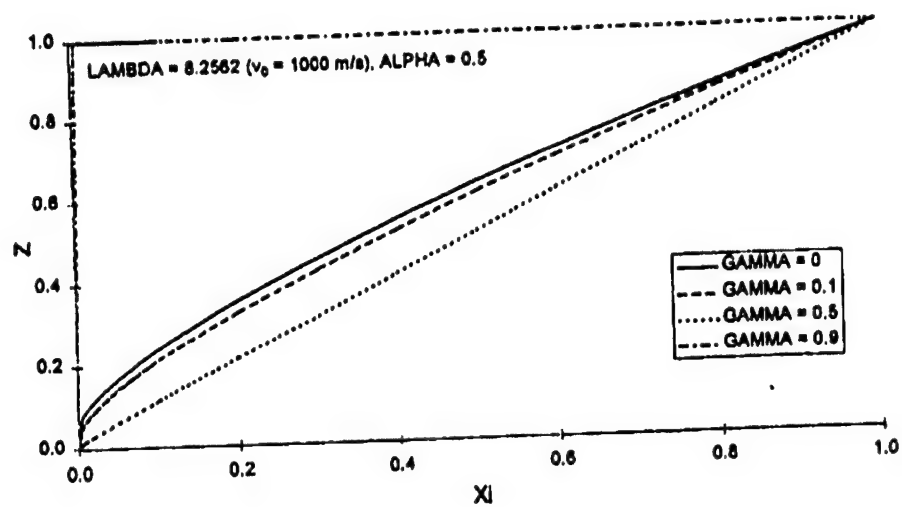


Figure 4. Plots of optimal nose shape for  $\alpha = 0.5$  and  $\lambda = 8.2562$  ( $v_0 = 1000$  m/s) for various values of friction coefficient  $\gamma$ .

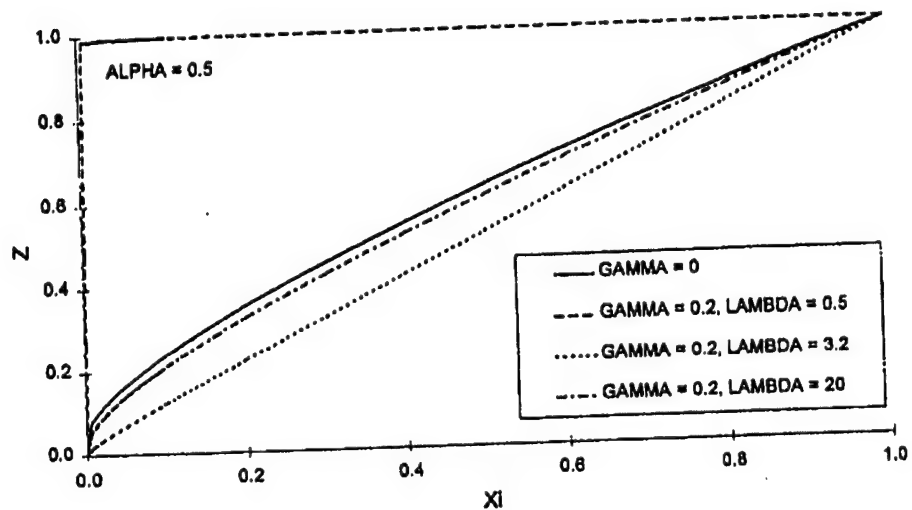


Figure 5. Plots of optimal nose shape for  $\alpha = 0.5$  and  $\gamma = 0.2$  for various values of  $\lambda$ . The frictionless case ( $\gamma = 0$ ) is shown for comparison.

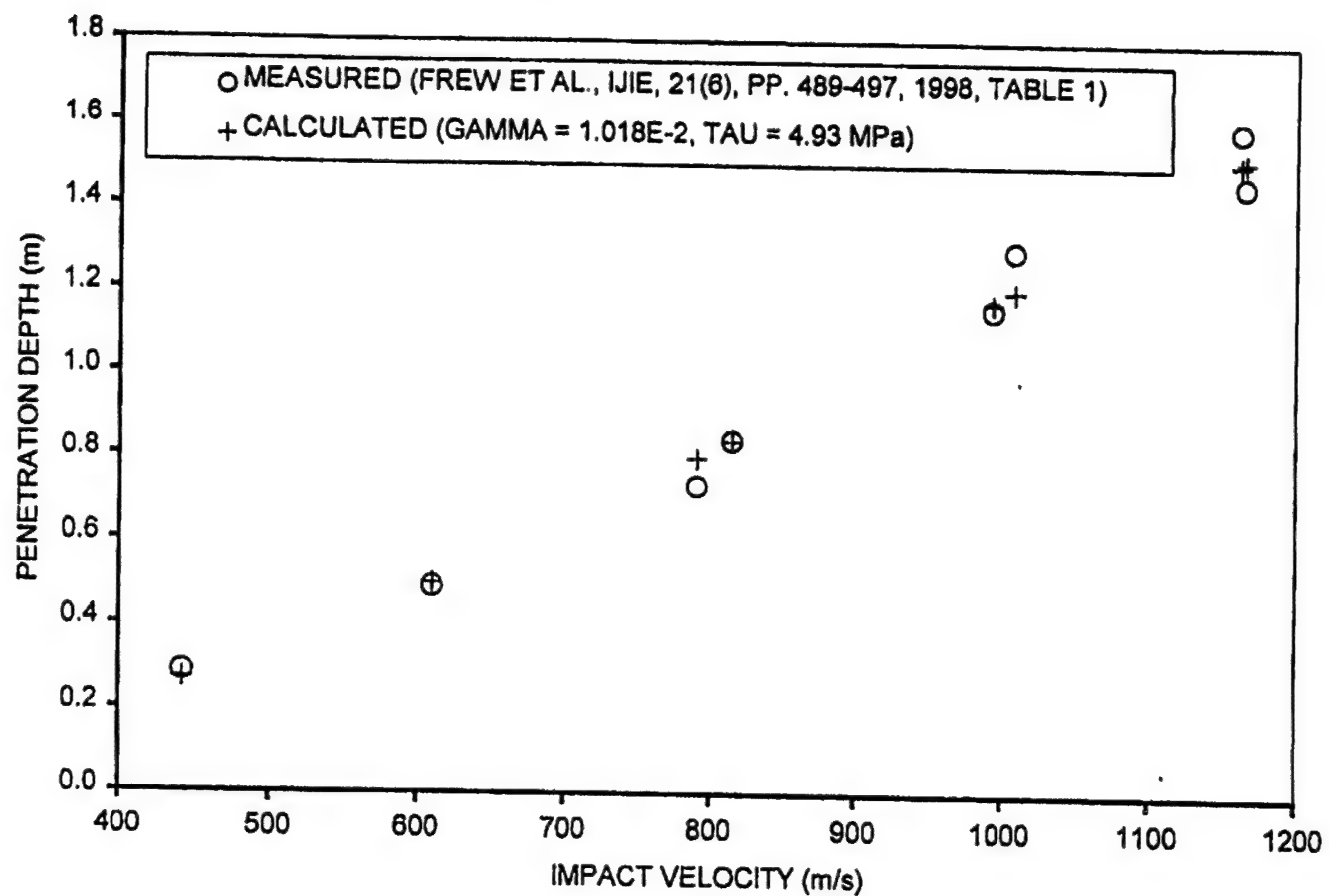


Figure 6. Comparison of measured (Frew, et al (1998)) and calculated concrete penetration data. The measured data was used to obtain a value for the shear strength ( $\tau = 4.93$  MPa) of the concrete target which was then used to generate the calculated results shown.

---

## **APPENDIX Q**

## AN ANALYTICAL ESTIMATE FOR MASS LOSS FROM A HIGH VELOCITY RIGID PENETRATOR

J. C. Foster, Jr.<sup>1</sup>, S. E. Jones<sup>1,2</sup>, O. Toness<sup>1</sup>, R. J. DeAngelis<sup>1,3</sup>, and W. K. Rule<sup>4</sup>

1. Air Force Research Laboratory/Munitions Directorate, Eglin AFB, Florida 32542

2. Dept. of Aerospace Engng. and Mech., University of Alabama, Tuscaloosa, Alabama 35487

3. Dept. of Mech. Engng., University of Nebraska, Lincoln, Nebraska

4. SCP Global Technologies, Boise, Idaho 83704

**Abstract.** Analytical models of the penetration process focus on estimating depth of penetration based on target density, target strength (sometimes associated with the unconfined compressive strength of the target for geological targets), the areal density of the penetrator (W/A), and the impact velocity. In this paper, an expression for work is used in conjunction with thermodynamic considerations to devise a simple estimate for mass lost by a high velocity projectile during the penetration process. The result shows that the mass loss is directly proportional to the tunnel length and the target shear strength. The constant of proportionality is not easy to deduce, however, in that it contains an unusual factor from the work analysis. A method for estimating target shear under high pressure from penetration experiments is introduced.

### INTRODUCTION

Rigid body penetration of geological targets has been explored by many authors [1,2]. Mass loss from these penetrators has been reported [3], but no theory to account for the loss has been proposed. The purpose of this paper is to report a simple one-dimensional estimate for mass loss that successfully correlates the results of a number of experiments.

### AN ESTIMATE FOR THE WORK DONE BY SHEAR

We use the term 'rigid' in the context a penetrator that neither mushrooms nor experiences significant mass loss. In such cases, the contribution to the motion of the body due to inertial change is assumed to be minimal.

Estimates for the work done by all of the forces acting on the nose of the projectile along the tunnel path can be made using a one-dimensional

penetration model. Consider an axisymmetric projectile normally striking and rectilinearly penetrating a semi-infinite target. The nose of the projectile, acted upon by normal and shear stress, is described in Figure 1. Following [1], we take the normal pressure  $p$  acting on the nose of the projectile to have the form

$$p = \rho_1 \sin^2 \theta v^2 + R \quad (1)$$

where  $\rho_1$  is the target density (assumed to be constant),  $\theta$  is the tangent angle to the surface of the nose,  $v$  is the current velocity of the projectile, and  $R$  is the dynamic compressive target strength under high confining pressure. We will take the target shear strength to be of the Mohr-Coulomb type. This has been very successfully employed in applications involving geological targets [2]. In this context,  $\tau$  has the form

$$\tau = \mu p + \tau_0 \quad (2)$$

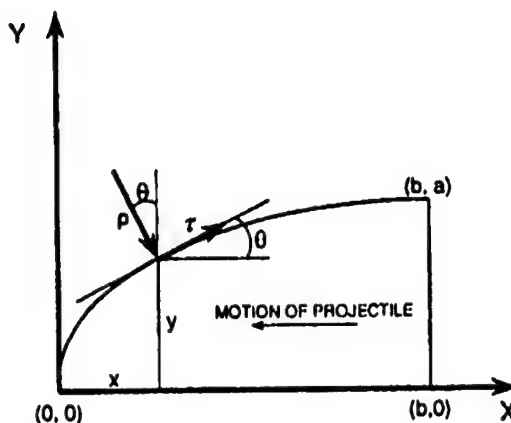


Figure 1. Cross section of projectile nose.

where  $\mu$  and  $\tau_0$  are constants.

Under these conditions, the equation of motion of the projectile is

$$m\dot{v} = -\pi a^2 [\rho_1 N v^2 + R(1 + \mu M) + \tau_0 M] \quad (3)$$

where  $m$  is the mass of the projectile and  $a$  is the radius of the shank. The constants  $N$  and  $M$  are dimensionless nose shape factors defined by

$$N = \frac{2}{a^2} \int_0^b y \frac{y^3 + \mu y^2}{1 + y^2} dx \quad (4)$$

and

$$M = \frac{2}{a^2} \int_0^b y dx \quad (5)$$

where  $y = y(x)$  is the continuous path with nonnegative slope from the tip of the nose to the shank defined in Figure 1 ([4]). Although mass is lost from the nose of the projectile, which changes the shape of the nose, we will treat  $N$  and  $M$  in (4) and (5) as approximately constant in this paper.

Integrals for (3) are easy to obtain and one of them relates position,  $z$ , in the target to the current velocity,  $v$ . This relationship takes the form

$$z = \frac{m}{2\pi a^2 \rho_1 N} \ln \left[ \frac{\rho_1 N v_0^2 + R(1 + \mu M) + \tau_0 M}{\rho_1 N v^2 + R(1 + \mu M) + \tau_0 M} \right] \quad (6)$$

The work done by the tangential forces acting at the surface of the nose is given by

$$W_t = \pi a^2 \int_0^z (\mu \rho_1 N_1 v^2 + \mu R M + \tau_0 M) dz \quad (7)$$

where  $N = N_0 + \mu N_1$ . The definitions of  $N_0$  and  $N_1$  come from (4). We can transform the integral in (7) and evaluate it. This will only be done for one case,  $\mu = 0$ , and the result is

$$W_t = \pi a^2 \tau_0 M z \quad (8)$$

where the velocity  $v$  has been algebraically eliminated in favor of the penetration depth  $z$ . This expression will be combined with the results of the next section to produce an estimate for mass loss by the projectile.

To estimate target shear we find the work done by the tangential forces, we must find a way to estimate  $\mu$  and  $\tau_0$ . The pressures and rates involved in the penetration process presently preclude the possibility of accomplishing this with any simple laboratory test. Penetration tests have often been used for this purpose because the appropriate pressures and rates are obviously achieved and penetration depths are easy to measure. A direct approach to the problem is to use (6) to correlate the post-test data. At the conclusion of penetration  $v=0$  and (6) becomes

$$Z = \frac{m}{2\pi a^2 \rho_1 N} \ln \left[ 1 + \frac{\rho_1 N v_0^2}{R(1 + \mu M) + \tau_0 M} \right] \quad (9)$$

where  $Z$  is the total depth of penetration.

With test data from a series of penetration experiments, we can look for the best fit by varying  $R$ ,  $\mu$ , and  $\tau_0$ . However, the physical parameters  $R$  and  $\tau_0$  only appear in (9) as a sum and cannot be separated unless more than one ogive is used, which gives us two different values of  $M$ . If penetration data for two different ogive-nose projectiles of the same steel into the same target material can be found, then  $R$  and  $\tau_0$  can be determined as the solution of a pair of simultaneous linear equations. A series of high velocity penetration tests were performed at Eglin AFB, FL [5]. The projectiles were hard 4340 steel with 3.0 and 4.25 CRH ogive noses. The targets were aged concrete.  $R=737\text{ MPa}$ ,  $\tau_0=13.8\text{ MPa}$ , and  $\mu=0.0$  gives the best fit to the data. The shear strength is only 1.87% of the normal compressive target strength.

The mass loss is calculated based on thermodynamic considerations. Steel penetrators impacting geological targets "wear" by melting. The melted material flows backward over the penetrator coating it with rapidly solidified material. A brief heat flux from the liquid steel transforms a thin layer on the surface to austenite and, upon cooling, to untempered martensite. The *Peclet Number* [6],  $Pe = VL_c/h$ , where  $V$  is the velocity of the penetrator,  $L_c$  is a characteristic length, and  $h$  is the thermal diffusivity of the penetrator, is on the order of  $10^{-3}$  for the penetration events. Thus, the heat shared by the target due to frictional heating is less than one part in a thousand. We will assume that all of the heat generated is accepted by the penetrator.

The mechanical work done by the forces acting on the nose of the projectile was estimated. As work is done by friction (shear) acting on the surface of the penetrator nose, heat is generated. The relationship between the heat generated  $Q$  and the work done by shear  $W_t$  is given by

$$W_t = kQ \quad (10)$$

where  $k=4.18$  joules/calorie is the *mechanical equivalent of heat* [7].

The first law of thermodynamics defines the relationship between heat and other thermodynamic

state variables. The heat capacity of metals is only weakly dependent on pressure below 10 GPa [7] which is well below the pressure levels at the penetrator/target interface as estimated by either analytical models [1] or continuum code calculations [8]. Also, in this pressure regime, the solid-solid and solid-liquid phase transitions in steel have little pressure dependence [9]. The path dependence in the integration is for the most part reflected by the temperature dependence in the heat capacity. Therefore, the enthalpy is evaluated in the integration to assess the end state assuming no change in pressure. This means that

$$dH = \rho \Delta V c_p dT \equiv dQ \quad (11)$$

where  $H$  is the enthalpy,  $T$  is the temperature,  $c_p$  is the heat capacity,  $\rho$  is the penetrator density, and  $\Delta V$  is the volume of the heat affected zone.

The change in enthalpy is estimated directly from heat capacities and the latent heats for the three allotropic phase transitions experienced by iron during melting. The temperature dependence in the heat capacity and enthalpy of the phase transitions are available from several sources [10]. When this data is used to perform the integration in (11), we can show that  $k \int C_p dT = 1032 \text{ J/g}$ . The calculated change in enthalpy is then combined with the work done by tangential forces in the penetration process to arrive at an estimate for the mass loss of the penetrator due to heating,  $\Delta m$ , given below

$$\Delta m = \frac{W_t}{k \int C_p dT} = \frac{\pi a^2 \tau_0 M z}{k \int C_p dT} \quad (12)$$

Equation (8) was used to estimate the mechanical work. Equation (12) indicates that the mass loss due to surface heating is directly proportional to the tunnel length  $z$ , the cross-sectional area of the projectile  $\pi a^2$ , and the target shear strength  $\tau_0$ . This result also indicates that increment of mass loss  $\Delta m$  is inversely proportional to the heat required to melt the steel.

## RESULTS

As mentioned earlier, for these targets  $\tau_0 = 13.8$  MPa. Figure 2 shows the estimated mass loss for 65g, CRH=3.0 and 4.25 ogive-nose projectiles against aged concrete targets. At this point, only one CRH=4.25 projectile has been recovered and weighed. The mass loss was 2.1g, which agrees very well with the estimate.

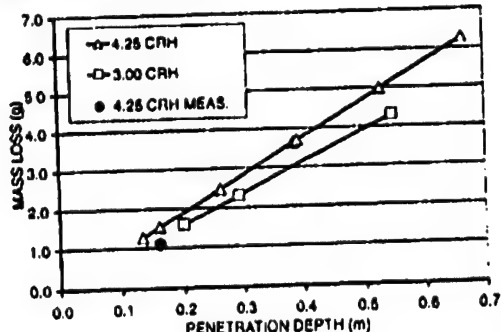


Figure 2. Predicted mass loss versus penetration depth based on tests by Wilson and Christopher. [5]

Another source of mass loss data is contained in [3]. Figure 3 gives comparisons between experiment and (12) for two different cases. The "small" projectiles were 478g, 20.1mm diameter, hard 4340 and AerMet 100 steel projectiles. The "large" projectiles were 1.62kg, 30.5mm diameter, AerMet 100 steel. The targets were high strength concrete ( $f'_c = 58.4$  MPa). All of the projectiles had CRH=3.0 ogive noses. The impact velocities ranged from 442m/s to 1225m/s and the mass losses were reported. Because only one nose shape was used, we could not estimate the target shear strength using the method employed for the Eglin targets discussed earlier. In order to make the estimate, we took the same fraction of normal dynamic strength (1.87%) as concluded earlier for the Eglin targets. In this case,  $\tau_0 = 8.22$  MPa. The agreement between (12) and the experiments is very good.

The target shear characteristics have been estimated from a series of high velocity penetration tests performed at Eglin AFB, FL [5].

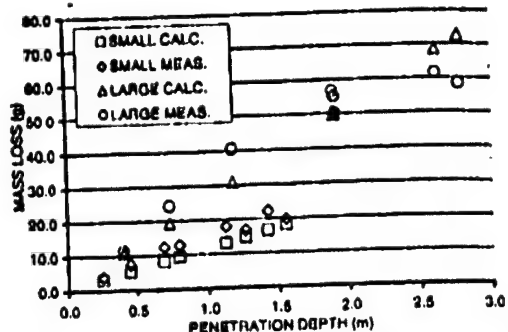


Figure 3. Comparison of calculated and measured (Frew et al., [3]) mass loss versus penetration depth.

## CONCLUSIONS

In this paper, we have presented an analytical estimate for mass loss from high velocity projectiles due to surface melting. A method for estimating the target shear stress is introduced and applied to a set of penetration experiments at Eglin AFB. The results correlate very well to experimental mass loss measurements from recovered projectiles.

## REFERENCES

1. Luk, V. K. and Forrestal, *Int. J. Impact Engng.*, 6, 291-301 (1987).
2. Forrestal, M. J., Norwood, F. R., and Longcope, D. B., *Int. J. Solids Structures*, 17, 915-924 (1981).
3. Frew, D. J., Hanchuk, S. J., Green, M. L., and Forrestal, M. J., *Int. J. Impact Engng.*, 21, 489-497 (1998).
4. Jones, S. E. and Rule, W. K., *Int. J. Impact Engng.* (to appear).
5. Wilson, L. L. and Christopher, F. R., *private Communication*.
6. Cowan, R. S. and Winer, W. O., in *Friction, Lubrication and Wear Technology*, ASM Handbook, Vol.18, 39-40 (1998).
7. Zemansky, M. W., *Heat and Thermodynamics*, McGraw-Hill, N. Y. (1968).
8. Johnson, G. R., and Holmquist, T. J., in *Shock Wave and High-Strain-Rate Phenomena in Materials*, (1992).
9. Leslie, W. C., *The Physical Metallurgy of Steels*, McGraw-Hill, N. Y. (1981).
10. Kubaschewski, O and Evans, E. L., *Metallurgical Thermochemistry*, 3<sup>rd</sup> ed., Pergamon Press, London, England (1958).

## **APPENDIX R**

# An Estimate for Mass Loss from High Velocity Steel Penetrators

by

**S. E. Jones<sup>1</sup>, J. C. Foster, Jr., O. A. Toness, R. J. DeAngelis<sup>2</sup>**

**Air Force Research Laboratory**

**Armament Directorate**

**Eglin AFB, FL 32542**

**And**

**W. K. Rule**

**SCP Global Technologies**

**Boise, ID 83704**

## ABSTRACT

Analytical models of the penetration process focus on estimating depth of penetration based on target density, target strength (sometimes associated with the unconfined compressive strength of the target for geological targets), the areal density of the penetrator (W/A), and the impact velocity. In this paper, an expression for work is used in conjunction with thermodynamic considerations to devise a simple estimate for mass lost by a high velocity projectile during the penetration process. The result shows that the mass loss is directly proportional to the tunnel length and the target shear strength. The constant of proportionality is not easy to deduce, however, in that it contains an unusual factor from the work analysis. A method for estimating target shear under high pressure from penetration experiments is introduced.

## INTRODUCTION

Traditionally, researchers interested in the terminal ballistics of rigid bodies have tried to connect depth of penetration to target density, target strength, weight per unit of cross-sectional area, and impact velocity. Absent are any references to penetrator strength, toughness, hardness, or resistance to wear. The first two, strength and toughness, are accounted for by assuming that the projectile has sufficient strength and toughness to remain a rigid body, though dynamically these quantities remain guesses. Hardness and resistance to wear have not been considered, despite the fact that carefully chosen nose geometries change as wear occurs. However, these parameters must somehow be included now because higher impact velocities are now producing longer tunnels that are promoting substantial wear. This is additionally significant because early wear may establish asymmetry in the nose that can result in unstable motion of the projectile. This has been observed in sub-scale tests of ogive-nose steel projectiles (Wilson and Christopher, 1997).

In this paper, we introduce a simple estimate for mass loss in steel penetrators. This estimate is based on surface melting of the nose of the projectile which we regard as the primary

---

<sup>1</sup> On leave from the Department of Aerospace Engineering and Mechanics, University of Alabama, Tuscaloosa, AL 35487

<sup>2</sup> On leave from the Department of Mechanical Engineering, University of Nebraska-Lincoln, Lincoln, NE

cause of wear. Surface melting of the nose blunts the projectile which increases the nose factor. This, in turn, degrades the performance of the penetrator. Based on elementary thermodynamic considerations, a one-dimensional estimate for mass loss from high speed steel projectiles is presented. It is shown that mass loss is directly proportional to the target shear strength and inversely proportional to the energy required to melt the steel. An additional fallout of this work is a practical estimate for dynamic target shear under high pressure.

## MOTION OF THE PROJECTILE

Consider the normal impact of an axisymmetric rigid rod projectile. A cross-section of the nose of the projectile is shown in Figure 1. Even if some other form of symmetry exists, this rectangular coordinate system attached to the nose is adequate to perform the analysis in this paper. For those nose geometries that are admissible to this study, the tip passes through zero at  $x=0$  and must join with the shank of radius  $a$  at  $x=b$ . Additionally, all admissible paths between  $x=0$  and  $x=b$  are continuous with nonnegative slope. A more detailed discussion of this nose geometry is given in Jones, et al (1998) or Jones and Rule (1999).

Assume that pressure sensitive friction per unit area  $f$  of the form

$$f = \mu p + \tau_0 \quad (1)$$

acts on the nose of the projectile, where  $\mu$  and  $\tau_0$  are constants and  $p$  is the normal pressure acting on the nose. This form for the friction has proved to be very useful in the study of the penetration of geological targets (e.g., Forrestal, et al, 1981). Now, the axial force,  $F$ , resisting the motion of the projectile has the form

$$F = \int_A (p \sin \theta + f \cos \theta) dA \quad (2)$$

where  $A$  is the surface area of the projectile nose and  $\theta$  is the tangent angle to the surface of the nose. We take the pressure  $p$  to have the form

$$p = \rho_t \sin^2 \theta v^2 + R \quad (3)$$

where  $\rho_t$  is the target density,  $R$  is the dynamic, compressive target strength under high confining pressure, and  $v$  is the axial velocity of the projectile. This form of velocity dependent pressure has been suggested by cavity expansion methods (e.g., Luk and Forrestal, 1987).

For a given nose shape  $y=y(x)$ ,  $\sin \theta = y' / \sqrt{1+y'^2}$  and  $\cos \theta = 1 / \sqrt{1+y'^2}$ . The integral in Equation (2) can be arranged for the pressure distribution given in Equation (3) and the result is

$$F = \pi a^2 (\rho_t N v^2 + R(1 + \mu M) + \tau_0 M) \quad (4)$$

where

$$N = \frac{2}{a^2} \int_0^b y \frac{y'^3 + \mu y'^2}{1 + y'^2} dx \quad (5)$$

and

$$M = \frac{2}{a^2} \int_0^b y dx. \quad (6)$$

For any given continuous nose shape, the integrals in Equations (5) and (6) can be evaluated and are constants. Note that the definition of the constant  $M$  has been changed from that which was given earlier by Jones and Rule (1999). This constant basically represents the dimensionless longitudinal cross-sectional area of the penetrator nose.

Using the force in Equation (4) and ignoring any mass loss for this application, the equation of motion of the rigid projectile is given by

$$m\dot{v} = -\pi a^2 (\rho_t N v^2 + R(1 + \mu M) + \tau_0 M). \quad (7)$$

This equation may be easily integrated to produce the relationship

$$z = \frac{m}{2\pi a^2 \rho_t N} \ln \left( \frac{\rho_t N v_0^2 + R(1 + \mu M) + \tau_0 M}{\rho_t N v^2 + R(1 + \mu M) + \tau_0 M} \right). \quad (8)$$

In Equations (7) and (8),  $m$  is the mass of the projectile,  $z$  is the current depth of penetration,  $v$  is the current velocity of the projectile, and  $v_0$  is the impact velocity. The constant of integration has been evaluated with the initial condition  $z = 0$  when  $v = v_0$ . At the end of the event,  $v = 0$  and the total depth of penetration  $Z$  can be found

$$Z = \frac{m}{2\pi a^2 \rho_t N} \ln \left( 1 + \frac{\rho_t N v_0^2}{R(1 + \mu M) + \tau_0 M} \right). \quad (9)$$

When  $\tau_0 = \mu = 0$ , we recover the classic rigid body penetration equation (e.g., see Luk and Forrestal, 1987).

Another independent integral of motion involving the time of penetration  $t$  can also be found by direct separation of the variables of Equation (7). This integral takes the form

$$t = \frac{m}{\pi a^2 \rho_t N} \sqrt{\frac{\rho_t N}{R(1 + \mu M) + \tau_0 M}} \left[ \tan^{-1} \left( \sqrt{\frac{\rho_t N}{R(1 + \mu M) + \tau_0 M}} v_0 \right) - \tan^{-1} \left( \sqrt{\frac{\rho_t N}{R(1 + \mu M) + \tau_0 M}} v \right) \right] \quad (10)$$

where the constant of integration was evaluated with the initial condition  $t = 0$  when  $v = v_0$ . When Equation (10) is carried to the end of the event, an estimate for the terminal time  $T$  can be found

$$T = \frac{m}{\pi a^2 \rho_t N} \sqrt{\frac{\rho_t N}{R(1 + \mu M) + \tau_0 M}} \tan^{-1} \left( \sqrt{\frac{\rho_t N}{R(1 + \mu M) + \tau_0 M}} v_0 \right). \quad (11)$$

Equations (8) and (10) are the only independent integrals of motion of Equation (7). What complicates their use, is the fact that  $R$  and  $\tau_0$  are not independent for the same nose shape. These two stresses are combined in the sum  $R(1 + \mu M) + \tau_0 M$  wherever they appear in Equations (8)-(11).

### ESTIMATES FOR $R$ , $\tau_0$ , AND $\mu$

There are several strategies for using combinations of Equations (8)-(11) to find the combination of compressive target strength under high confining pressure  $R$ , shear strength under high confining pressure  $\tau_0$ , and the friction coefficient  $\mu$ . Certainly, the most attractive would be to have measured values for the penetration depths and the terminal times. However, we rarely have reliable estimates for the terminal time. Finite thickness targets could be used in connection with Equations (8) and (10). However, the front crater and rear spall regions may occupy a large percentage of the tunnel, unless the target is very thick. The results presented in the previous section only apply when the tunnel is the dominant penetration mode.

This leaves us with Equation (9) as the only viable option. Suppose that we have test data from a series of  $n$  penetration experiments into semi-infinite targets of the same material with sufficiently high impact velocities that the tunnels are very long relative to the crater region at the surface of the target. Let the impact velocities for these tests be  $v_i$  ( $i = 1, 2, \dots, n$ ) and the measured penetration depths for these tests be  $Z_i$  ( $i = 1, 2, \dots, n$ ), respectively. Let us further assume that the impact velocities are sufficiently high to produce strain-rates in the target material that are high enough that the strength does not vary significantly between the tests. In all respects, we assume that the projectiles and targets are identical. This means that Equation (9) can be used to find

$$Z_i = \frac{m}{2\pi a^2 \rho_t N} \ln \left( 1 + \frac{\rho_t N v_i^2}{R(1 + \mu M) + \tau_0 M} \right) \quad (12)$$

where  $i = 1, 2, \dots, n$ . These equations are a system of nonlinear, transcendental equations for  $R(1 + \mu M) + \tau_0 M$  and  $\mu$ . They are complicated by the fact that  $N$  also depends on  $\mu$ , as observed in Equation (5). If we take any pair of data points, say the  $i$ -th and the  $j$ -th, and combine them, we can eliminate the dependence on  $\tau_0$ . This leaves us with a single equation in which the only unknown is  $\mu$ . This equation is given below

$$\frac{\exp\left\{\frac{2\pi a^2 \rho_i N Z_i}{m}\right\} - 1}{\exp\left\{\frac{2\pi a^2 \rho_j N Z_j}{m}\right\} - 1} = \left(\frac{v_i}{v_j}\right)^2. \quad (13)$$

Although equation (13) is transcendental in  $\mu$ , but can still be solved fairly easily.

Equations (12) and (13) apply to any nose shape. Later in this paper,  $N$  and  $M$  will be given for some of the common shapes. But, this does not answer the question of how to separate  $R$  and  $\tau_0$ . To do this, we make the observation that regardless of the shape of the nose, these quantities should remain the same. If we have penetration data for two distinct nose shapes into the same target, then  $M$  (and  $N$ ) will be different for these two projectiles. This means that we can take the results of the best fits to the data in Equation (12) and have two linear equations in two unknowns from which to determine  $R$  and  $\tau_0$ .

## PENETRATION INTO CONCRETE

A series of penetration experiments involving hard steel penetrators normally impacted into hardened concrete targets were performed at Eglin AFB, FL (Wilson and Christopher, 1997). The targets contained large aggregate limestone and had an unconfined compressive strength of 51 MPa (Jerome, 1998). The projectiles were ogive-nose cylindrical rods 12.7mm in diameter with a mass of 65 g. Two different ogives were used. They were of *Caliber Radius Head* (CRH) 3.0 and 4.25. Each class of projectile was impacted at increasing velocity until failure of the projectile occurred. The data from these experiments were shared with us by the project engineers (Wilson and Christopher, 1997) and are summarized in Tables 1 and 2. When the data from Tables 1 and 2 is used in a least squares fit to Equation (12), it follows that  $\mu = 0$ . This conclusion may be verified by taking any pair of data points within each data set and applying Equation (13).

Table 1. Observed penetration depths of 4.25 CRH hard 4340 ( $R_c=45$ ) steel penetrators ( $m = 0.065$  kg,  $a = 6.46$  mm) into concrete targets ( $f_c' = 51$  MPa,  $\rho = 2336$  kg/m<sup>3</sup> containing large limestone aggregates [Wilson and Christopher, 1997].

Eglin Experiment Number	Impact Velocity $v_0$ (m/s)	Observed Penetration Depth (m)
17	1431	0.528
20	1213	0.392
22	1636	0.665
24	1202	0.386
25	758	0.162
26	688	0.134
27	975	0.262

Table 2. Observed penetration depths of 3.0 CRH hard 4340 ( $R_c=45$ ) steel penetrators ( $m = 0.065$  kg,  $a = 6.46$  mm) into concrete targets ( $f_c' = 51$  MPa,  $\rho = 2336$  kg/m<sup>3</sup>) containing large limestone aggregates [Wilson and Christopher, 1997].

Eglin Experiment Number	Impact Velocity $v_0$ (m/s)	Observed Penetration Depth (m)
16	1505	0.548
33	1051	0.293
34	856	0.201

The least squares fit for the data in Tables 1 and 2 described above produced the parameter estimates  $R = 737$  MPa and  $\tau_0 = 13.8$  MPa. These strengths come from the solution of the simultaneous linear equations  $R + 5.399\tau_0 = 811.51$  MPa and  $R + 4.502\tau_0 = 799.13$  MPa. Measured and calculated penetration depths are compared in Fig. 2. The agreement is excellent. For the purpose of illustration, plots of penetration depth versus impact velocity, and penetration depth versus time for this system are included in Figures 3 and 4, respectively. The agreement with the observed penetration depths in Figure 3 is very good, with very slight deviations noted only for the highest impact velocities.

Table 3. Observed penetration depths of 3.0 CRH steel penetrators into concrete ( $f'_c = 58.4$  MPa,  $\rho = 2320$  kg/m<sup>3</sup>) targets [Frew et al., 1998].

Test ID	a (m) shank radius	b (m) nose length	Mass (kg)	Observed Penetration Depth (m)
1-0354	1.015E-02	3.370E-02	4.780E-01	2.870E-01
1-0355	1.015E-02	3.370E-02	4.780E-01	4.910E-01
1-0356	1.015E-02	3.370E-02	4.780E-01	8.400E-01
1-0357	1.015E-02	3.370E-02	4.780E-01	1.300E+00
1-0358	1.015E-02	3.370E-02	4.780E-01	1.590E+00
1-0390	1.015E-02	3.370E-02	4.780E-01	7.300E-01
1-0391	1.015E-02	3.370E-02	4.780E-01	1.160E+00
1-0392	1.015E-02	3.370E-02	4.780E-01	1.460E+00
LROD95-1	1.525E-02	5.050E-02	1.620E+00	4.600E-01
LROD95-2	1.525E-02	5.050E-02	1.620E+00	7.900E-01
LROD95-3	1.525E-02	5.050E-02	1.620E+00	1.230E+00
LROD96-0	1.525E-02	5.050E-02	1.620E+00	1.950E+00
LROD95-4	1.525E-02	5.050E-02	1.620E+00	1.960E+00
LROD95-6	1.525E-02	5.050E-02	1.620E+00	2.670E+00
LROD96-1	1.525E-02	5.050E-02	1.620E+00	1.960E+00
LROD96-4	1.525E-02	5.050E-02	1.620E+00	2.830E+00

An additional set of impact data reported by Frew et al. (1998) was also considered, see Table 3. A plot of observed versus calculated penetration depths for this data set with parameters  $R+M\tau_0 = 478$  MPa and  $\mu = 0$  (obtained from a least squares fit as before) is shown in Figure 5.

Figure 5 shows that the agreement between observed and calculated penetration depths is excellent in this case. It is interesting that again  $\mu$  was forced to zero by the least squares fit.  $\tau$  could not be separated from  $R$  in this data set since there is only one CRH in this case. Thus, the quantity  $R+M\tau_0 = 478$  MPa obtained for this case is actually an estimate for the dynamic, compressive target strength under the influence of high confining pressure. This target strength obviously compares very well with that obtained by Frew et al. (1998) for this data set, which was 485 Mpa, because their equation and Equation (9) are virtually the same when the shear combines in this manner.

## WORK DONE BY THE TANGENTIAL FORCES

We are now in a position to find an expression for the work done by the tangential components of force in bringing the projectile to rest. The tangential components of force consist of

$$F_t = \pi a^2 (\mu \rho_t N_1 v^2 + \mu R M + \tau_0 M) \quad (14)$$

where  $N = N_0 + \mu N_1$ . The work done by this force,  $W_i$ , is given by

$$W_i = \pi a^2 \int_0^z (\mu \rho_i N_1 v^2 + \mu R M + \tau_0 M) dz \quad (15)$$

where the integration is taken along the rectilinear tunnel length  $z$ . Using the equation of motion of the projectile, Equation (7), we can transform the integral in Equation (15) to

$$W_i = m \int_v^{v_0} \frac{(\mu \rho_i N_1 v^2 + \mu R M + \tau_0 M) v dv}{\rho_i N v^2 + R(1 + \mu M) + \tau_0 M} \quad (16)$$

which can be integrated to give

$$W_i = \frac{\mu m N_1}{2N} (v_0^2 - v^2) + \frac{m [\mu R(MN_0 - N_1) + \tau_0 M N_0]}{2 \rho_i N^2} \ln \left[ \frac{\rho_i N v_0^2 + R(1 + \mu M) + \tau_0 M}{\rho_i N v^2 + R(1 + \mu M) + \tau_0 M} \right]. \quad (17)$$

This equation expresses the work done in terms of the current velocity,  $v$ . Work is usually expressed in terms of distance, or arc length, along the trajectory. It is not difficult to find such a relationship. We can use the integral given in Equation (8) to eliminate the velocity in terms of the distance  $z$ . This will only be done for one case, because the results are particularly interesting. When  $\mu = 0$ , Equation (17) becomes

$$W_i = \frac{m \tau_0 M}{2 \rho_i N_0} \ln \left[ \frac{\rho_i N_0 v_0^2 + R + \tau_0 M}{\rho_i N_0 v^2 + R + \tau_0 M} \right] \quad (18)$$

and Equation (8) becomes

$$z = \frac{m}{2 \pi a^2 \rho_i N_0} \ln \left[ \frac{\rho_i N_0 v_0^2 + R + \tau_0 M}{\rho_i N_0 v^2 + R + \tau_0 M} \right]. \quad (19)$$

By eliminating the velocity between these two equations, we find

$$W_i = \pi a^2 \tau_0 M z \quad (20)$$

is the work done by the pressure independent target shear force acting on the projectile. This is a particularly simple result. It shows that the work done by shear is proportional to the cross-sectional area of the shank of the projectile, the normalized cross-sectional area of the nose, and the penetration depth. However, in spite of its simplicity, this result is not easy to anticipate because it involves the constant  $M$ .

It is interesting to compare the work done by shear to the total work done by all of the forces in bringing the projectile to rest. The total work done is equal to the available energy,  $mv_0^2/2$ , which means that  $2\pi r_0^2 \tau_0 M Z / mv_0^2$  is the fraction of work done by shear. For the Eglin experiments (Tables 1 and 2),  $\tau_0 = 13.8$  MPa. The highest impact velocity in the data set is  $v_0 = 1636$  m/s for a CRH = 4.25 ogive nose projectile. In this case,  $M = 5.399$ ,  $m = 65$ g,  $a = 6.46$ mm, and  $Z = 0.665$ m. With this data, we can see that the fraction of work done by shear is only 7.5% of the total work. While this is small, it is very significant to problems involving projectile heating and erosion. This topic will be discussed now.

## THERMODYNAMIC CONSIDERATIONS

The process driving the mass loss during the penetration process has been attributed to friction and shear by various investigators. The microscopic analysis of recovered penetrators serves as clear evidence of the thermal effects of these processes. For high velocity penetration problems, the heat generated by tangential forces between the penetrator and the stationary target goes into heating the surface of the penetrator. This fact is fairly easy to establish. The *Peclet Number* is a dimensionless heat transfer grouping that governs the heat partitioned between sliding bodies (e.g., Cowan and Winer, 1998). For our purpose, the *Peclet Number*,  $Pe$ , is defined by  $Pe = VL_c/h$ , where  $V$  is the velocity of the penetrator,  $L_c$  is a characteristic length, and  $h$  is the thermal diffusivity of the penetrator. For a steel penetrator,  $h = 0.127 \times 10^{-4} \text{ m}^2/\text{sec}$ . For example, take the velocity of the projectile  $V = 1000 \text{ m/sec}$  and the characteristic length to be a penetrator nose length, say  $2 \times 10^{-2} \text{ m}$ . In this case,  $Pe = 1.57 \times 10^6$ . For such an event, the heat partition factor is smaller than  $10^{-3}$ , indicating that less than one part in a thousand of the heat generated is shared by the target. Even for substantially larger characteristic lengths, the *Peclet Numbers* are still very large. Thus, we may ignore the target and assume that all of the heat generated by frictional heating is accepted by the penetrator.

In the previous section, the mechanical work done by the forces acting on the nose of the projectile was estimated. As work is done by friction (shear) acting on the surface of the penetrator nose, heat is generated. The relationship between the heat generated  $Q$  and the work done by the tangential forces  $W$ , is given by

$$Q = kW \quad (21)$$

where  $k = 4.18$  calories/joule is the *mechanical equivalent of heat* (e.g., see Zemansky, 1968).

The first law of thermodynamics defines the relationship between heat and other thermodynamic state variables,

$$du = dQ - dW \quad (22)$$

where the inexact differentials in  $dQ$  and  $dW$  indicate path dependent functions. The standard thermodynamic functions: internal energy, enthalpy, Gibb's free energy, and Helmholtz free energy

provide a means to select the most suitable integration path to calculate the end state which results from the addition of the heat. The heat capacity of metals is only weakly dependent on pressure below 10 Gpa (Zemansky, 1968) which is well below the pressure levels at the penetrator/target interface as estimated by either analytical models (e.g., Luk and Forrestal, 1987) or continuum code calculations (e.g., Johnson and Holmquist, 1992). Also, in this pressure regime, the solid-solid and solid-liquid phase transitions in steel have little pressure dependence (e.g., Leslie, 1981). The path dependence in the integration is for the most part reflected by the temperature dependence in the heat capacity. Therefore, the enthalpy is used to do the integration to assess the end state assuming  $dp=0$ . This means that

$$dH = \rho \Delta V c_p dT \equiv dQ. \quad (23)$$

where  $H$  is the enthalpy,  $\Delta V$  is the volume of the heat affected zone,  $\rho$  is the penetrator density, and  $c_p$  is the temperature dependent heat capacity of the penetrator material. Equation (23) can now be integrated to produce an estimate for  $Q$ . This result is

$$Q \equiv \rho \Delta V \int_T^T c_p dT \quad (24)$$

where the integration is taken from the ambient temperature to the melt temperature. A complete discussion of the evaluation of the integral in Equation (24) is given in the next section. For the moment, Equations (21) and (24) can be combined to arrive at the estimate for mass loss from the penetrator due to surface heating,  $\Delta m$ , given below

$$\rho \Delta V = \Delta m = \frac{W_t}{k \int_T^T c_p dT}. \quad (25)$$

When this equation is combined with Equation (20), we get

$$\Delta m = \frac{\pi a^2 \tau_0 M z}{k \int_T^T c_p dT} \quad (26)$$

which indicates that the mass loss due to surface heating when  $\mu = 0$  is directly proportional to the tunnel length  $z$ , the cross-sectional area of the projectile  $\pi a^2$ , and the target shear strength  $\tau_0$ . This result appeared earlier in Foster, et al, 1999. This result also indicates that increment of mass loss  $\Delta m$  is inversely proportional to the heat required to melt the steel.

## EVALUATION OF HEAT REQUIRED TO MELT

The heat required for melting the steel penetrator can be found once the integral in Equation (24) has been evaluated. In this paper, we approximate the properties of the steel

penetrator by the properties of its major constituent, iron. In this case, the temperature-dependent heat capacity  $c_p$  takes the form

$$c_p = C_1 + C_2 T \text{ (cal./gram}\cdot K\text{)} \quad (27)$$

where the constants  $C_1$  and  $C_2$  are given in Table 4 (see Kubaschewski and Evans, 1958). In Equation (27),  $K$  indicates temperature in degrees Kelvin. Iron goes through three distinct phases prior to melting. The first phase is the ferrite or  $\alpha$ -phase. The second is the austenitic or  $\gamma$ -phase. The last phase is called the  $\delta$ -phase. Table 4 gives the values of  $C_1$  and  $C_2$  during each of these three phases and the temperature range for each phase (Kubaschewski and Evans, 1958).

Now, using Equation (27), we can evaluate the integral in Equation (24) and get

$$\int_T c_p dT = \int_{T_a}^{T_\gamma} c_{p_\alpha} dT + \Delta H_\gamma + \int_{T_\gamma}^{T_\delta} c_{p_\gamma} dT + \Delta H_\delta + \int_{T_\delta}^{T_m} c_{p_\delta} dT + \Delta H_L \quad (28)$$

where  $T_a$  is the ambient temperature,  $T_\gamma$  is the temperature of transition from ferrite to austenite,  $T_\delta$  is the temperature of transition from austenite to  $\delta$ -phase, and  $T_m$  is the melt temperature of iron. In Equation (28),  $\Delta H_\gamma$ ,  $\Delta H_\delta$ ,  $\Delta H_L$  are the latent heats required for each of the three phase changes experienced by iron during heating through the melting point. The heat capacities in the integrands of the integrals in Equation (28) apply in the temperature range indicated by the limits of integration. The latent heats of transformation for iron are taken to be  $\Delta H_\gamma = 2.87$  cal/gram,  $\Delta H_\delta = 3.60$  cal/gram, and  $\Delta H_L = 58.98$  cal/gram (see Kubaschewski and Evans, 1958 and Kubaschewski and Alcock, 1979).

Table 4. Heat Capacity Coefficients

	$C_1$ (cal/gram $\cdot K$ )	$C_2$ (cal/gram $\cdot K^2$ )	$T$ (K)
$\alpha$ -phase	$7.49 \times 10^{-2}$	$1.06 \times 10^{-4}$	$273 < T < 1185$
$\gamma$ -phase	$3.30 \times 10^{-2}$	$8.35 \times 10^{-5}$	$1185 < T < 1674$
$\delta$ -phase	$1.88 \times 10^{-1}$	0.00	$1674 < T < 1812$

With the information provided in the previous paragraph, we can use Equation (28) to evaluate the heat capacity integral in Equation (27). After perfectly straightforward integrations and additions, we find that  $\int_T c_p dT = 302.58$  cal/gram. This means that  $k \int_T c_p dT = 1264.78$

J/gram for iron. This number will be used in the denominator of Equation (26) to estimate mass loss in steel penetrators.

## RESULTS

As indicated, mass loss can be estimated by Equation (26) using the heat required to melt iron given in the previous section. This will be accomplished for the experiments into concrete reported in Tables 1-3. Although there is mass loss and wear on the nose of the projectiles, we will use the value of  $M$  in Equation (6) for the initial ogive in this application.

In the first case, experimental data for two different ogives was provided by Wilson and Christopher, 1997 (Tables 1 and 2). This enables us to find  $\tau_0$ . In this case,  $\mu = 0$  and Equation (26) applies. The estimated mass loss for the two different ogives is shown in Figure 6. Unfortunately, only one of the penetrators has been removed from the target and weighed. However, the single data point shows very good agreement with the estimate. It must be pointed out that there is much uncertainty in experimental determinations of mass loss from the nose of a penetrator. Simply weighing the projectile usually underestimates the mass loss because molten penetrator material is reattached to the shank (see Toness, et al, 1999).

The second set of penetration data (Table 3) from Frew, et al, 1998, is for 3.0 CRH ogive nose projectiles. The estimate for  $\tau_0$  is based on the same fraction of  $R$  that was found for the previous data set. The mass loss estimates are shown in Figure 7 for two different classes of penetrators. The ‘small’ penetrators have a mass of 0.478kg and the ‘large’ penetrators have a mass of 1.62kg. The target material is the same. The agreement between Equation (26) and the experiments is good considering the nature of penetration testing. The agreement is excellent at the lowest impact velocity where the tunnel is shortest. This is expected because mass loss and wear are the least there. Obviously, we have used data to characterize the target and the penetrator that is influenced by mass loss and wear. It is evident that the more mass loss and wear that occurs, the greater this influence should be.

## METALLURGICAL OBSERVATIONS

In this section, we present the metallurgical observations that support the case for wear by surface melting of the nose. As indicated in the introduction of this paper, the analysis of experiments performed by WES of hard 4340 steel penetrators into weathered granite was the seed for the theory. For this reason, it is appropriate to present the supporting metallurgy in terms of the recovered penetrators from these experiments. Further details are contained in Toness, et al, 1999. In this context, the questions that must be answered are: 1) How much wear took place? 2) How much metal is removed? and 3) What is the wear mechanism? Each of these questions will be addressed separately in the paragraphs that follow.

First, let us address the question of how much wear took place. The parameters for two of the six experiments performed are given in Table 5. At first glance, it appears that very little wear took place. For example, the greatest weight lost, 2.29 lbs, is a mere 2%, more or less, of its gross weight. However, this grossly understates the wear process. When the 54.5kg penetrator hits the

rock, it carries from 5.2 to 23.5 megajoules of energy with it. Only approximately 10% of the work done by this energy is devoted to shear. Nevertheless, the rate of metal removal from the nose is respectably large (see Table 2). Compare this with what the American Society for Metals, International (ASM) calls "high removal rate machining" which achieves removal rates of  $370 \text{ in}^3 / \text{min}$  (for steel this is 104 lbs/min, see ASM Metals Handbook, Vol 16, Machining, p. 607). Thus, the wear process can be characterized as high energy, high rate. The resulting surface of the nose of the penetrator is very smooth and true to its original form, as illustrated in Figure 8. The smooth horizontal surface is the result of the high energy, high rate penetration wear. The rough vertical surface is saw cut.

Table 5. Material Loss From Two 4340 Steel Penetrators

Penetrator	Penetration Time (sec)	Lbs Lost	Lbs/sec	Lbs/minute
A	$1.12 \times 10^{-2}$	2.29	204	12,267
D	$8 \times 10^{-3}$	0.57	70	4,226

We will now address the questions of what is the wear mechanism and how much metal is removed. Pressures and velocities are such that the nose is melted. This is evident from the scabrous deposits on the shank of the projectile, see Figure 9. The small humps in the surface are a cast of the cavity in which the projectile came to rest. It is difficult to estimate the amount of re-deposited material. It is unevenly distributed both in location and thickness and, in addition, the re-deposited metal contains inclusions of geological materials.

Microstructural observations of surface layers of nose material indicate that the material had been heated to the austenite transformation temperature. This transformed layer is shown in Figure 10. This layer in the austenitic state is very plastic and is easily removed by abrasion. This removal process further raises the temperature to the melting point and the melted material flows backward onto the shank. Alternatively, the thin layers could be melted directly and the molten material wiped backward. Extensive metallurgical observations provided no evidence of shear banding or other indications of deformation of the nose.

The melted material forms layers on the shank. The heat from the melted material and friction raises the temperature of a thin layer on the surface of the shank to past that required for the formation of austenite. Thus, the shanks have three layers: melt, heat effected zone (HAZ), and bulk material. Microhardness measurements converted to Rockwell C ( $R_C$ ) are as follows: melt- $R_C=49.5$ , HAZ- $R_C=56.1$ , bulk  $R_C=40.4$ . A sample cut from the shank and polished through the surface reveals sufficient melt and HAZ surfaces for X-ray diffraction analysis. The results indicate that the structures are all ferrite with no retained austenite. Analysis of x-ray diffraction peaks in the transverse direction across the surface show a distinct broadening of the peaks in the melt and HAZ, indicating the presence of untempered martensite. The diffracting particle size was determined to be 11.1nm. The cooling rate associated with this particle size is greater than

1000C/sec (see Weins, et al, 1999). This is a reasonable estimate of the cooling rate experienced by a hot projectile entering into and stopping in ambient temperature granite

## CONCLUSIONS

In this paper, we have presented a simple one-dimensional estimate for mass loss from a high-speed steel projectile. Required for its use is an estimate for dynamic target shear stress under very high pressure. A method for estimating this stress is included in the paper. Another constant that is required is related to the longitudinal cross-sectional area of the ogival nose. A complete discussion of this constant is given in the Appendix of this paper.

The agreement between the one-dimensional theory and experimental observations is reasonable, considering the nature and reproducibility of penetration experiments and some of the fundamental assumptions in the development. Some of the shortcomings of this analysis are the subject of future work and work in progress. Because these are important considerations, we will mention a few of them. Penetrator wear is a time-dependent process. As mass is lost from the nose, the penetrator is blunted and the nose factor  $N$  increases. This can have a considerable influence on high-speed penetration. Because mass is primarily lost from the nose, even modest projectile mass loss can result in fairly substantial change in the nose. If regular wear is assumed, some of these changes can be modeled and a simple strategy for blunting and longitudinal area change in the nose produced. These topics will be addressed in future work.

## ACKNOWLEDGEMENT

S. E. Jones and R. J. DeAngelis gratefully acknowledge the support of the Air Force Office of Scientific Research and Eglin Air Force Base for University Resident Research Professor Grants.

## REFERENCES

Cowan, R. S. and Winer, W. O., 1998, "Frictional Heating Calculations," in *Friction, Lubrication, and Wear Technology*, ASM Handbook, Vol. 18, 39-40.

Davis, Joseph R., ed, 1989, Metals Handbook, Vol. 16, 9<sup>th</sup> edition, *Machining*, ASM International, Metals Park, OH.

Forrestal, M. J., Longcope, D. B., and Norwood, F. R., 1981a, "A Model to Estimate Forces on Conical Penetrators Into Dry Porous Rock," *Journal of Applied Mechanics, Trans. ASME*, **48**, 25-29.

Forrestal, M. J., Norwood, F. R., and Longcope, D. B., 1981b, "Penetration into Targets Described by Locked Hydrostats and Shear Strength," *Int. J. Solids Structures*, **17**, 915-924.

Forrestal, M. J. and Grady, D. E., 1982, "Penetration Experiments For Normal Impact Into Geological Targets," *Int. J. Solids Structures*, **13**, No. 3, 229-234.

Forrestal, M. J., 1986, "Penetration Into Dry Porous Rock," *Int. J. Solids Structures*, **22**, No. 12, 1485-1500.

Forrestal, M. J., Altman, B. S., Cargile, J. D., and Hanchak, S. J., 1994, "An Empirical Equation For Penetration Depth Of Ogive-Nose Projectiles Into Concrete Targets," *Int. J. Impact Engng.*, **15**, No. 4, 395-405.

Forrestal, M. J., Frew, D. J., Hanchak, S. J., and Brar, N. S., 1996, "Penetration of Grout and Concrete Targets with Ogive-Nose Steel Projectiles," *Int. J. Impact Engng.*, **18**, 5, 465-476.

Foster, J. C., Jr., Jones, S. E., Toness, O., DeAngelis, R. J., and Rule, William K., 1999, "An Analytical Estimate for Mass Loss from a High Velocity Rigid Penetrator," Proceedings of the 1999 APS Topical Conference on Shock Compression of Condensed Matter, Snowbird, UT.

Frew, D. J., Hanchak, S. J., Green, M. L., and Forrestal, M. J., 1998, "Penetration of Concrete Targets with Ogive-Nose Steel Rods," *Int. J. Impact Engng.*, **21**, No. 6, 489-497.

Jerome, D. M., 1998, private communication.

Johnson, G. R. and Holmquist, T. J., 1992, in *Shock Wave and High-Strain-Rate Phenomena in Materials*.

Jones, S. E., Rule, W. K., Jerome, D. M., and Klug, R. T., 1998, "On the Optimal Nose Geometry for a Rigid Penetrator," *Computational Mechanics* (to appear). A six page summary paper may be found in *Modeling and Simulation Based Engineering*, Volume II, S. N. Atluri and P. E. O'Donoghue, eds., Tech Science Press, Palmdale, CA, 1120-1125.

Jones, S. E. and Rule, W. K., 1999, "On the Optimal Nose Geometry for a Rigid Penetrator, Including the Effects of Pressure-Dependent Friction," *Int. J. Impact Engng.* (to appear).

Kubaschewski, O. and Evans, E. L., 1958, *Metallurgical Thermochemistry*, 3<sup>rd</sup> ed., Pergamon Press, London, England.

Kubaschewski, O. and Alcock, C. B., 1979, *Metallurgical Thermochemistry*, 5<sup>th</sup> ed., Pergamon Press, Oxford, England.

Leslie, W. C., 1981, *The Physical Metallurgy of Steels*, McGraw-Hill, N. Y.

Luk, V. K. and Forrestal, M. J., 1987, "Penetration Into Semi-Infinite Reinforced Concrete Targets With Spherical And Ogival Nose Projectiles," *Int. J. Impact Engng.*, **6**, No. 4, 291-301.

Luk, V. K. and Forrestal, M. J., 1989, "Comment on 'Penetration into Semi-Infinite Re-inforced - Concrete Targets with Spherical and Ogive Nose Projectiles'," *Int. J. Impact Engng.*, **8**, No. 1, 83-84.

Piekutowski, A. J., Forrestal, M. J., Poorman, K. L., and Warren, T. L., 1999, "Penetration of 6061-T6511 Aluminum Targets by Ogive-Nose Projectiles with Striking Velocities between 0.5 and 3.0 Km/s," *Int. J. Impact Engng.*, **23**,

Rule, W. K. and Jones, S. E., 1999, "Some Remarks on the Optimal Nose Geometry of a Rigid Penetrator in the Presence of Friction," *Structures Under Extreme Loading Conditions-1999*, ASME Pressure Vessels and Piping Conference, Boston, MA, August 1-5, 1999.

Toness, O., Jones, S. E., and Rule, W. K., 1999, "Some Remarks on Mass Loss in 4340 Steel Penetrators," submitted for publication.

Weins, W. N., Makinson, J. D., Xu, Y., and DeAngelis, R. J., 1999, "Diffracting Particle Size Analysis of Martensite-Retained Austenite Microstructures," *Adv. In X-Ray Anal.*, **43**, to appear

Wilson, L. L. and Christopher, F. R., 1997, private communication.

Zemansky, M. W., 1968, *Heat and Thermodynamics*, McGraw-Hill, New York.

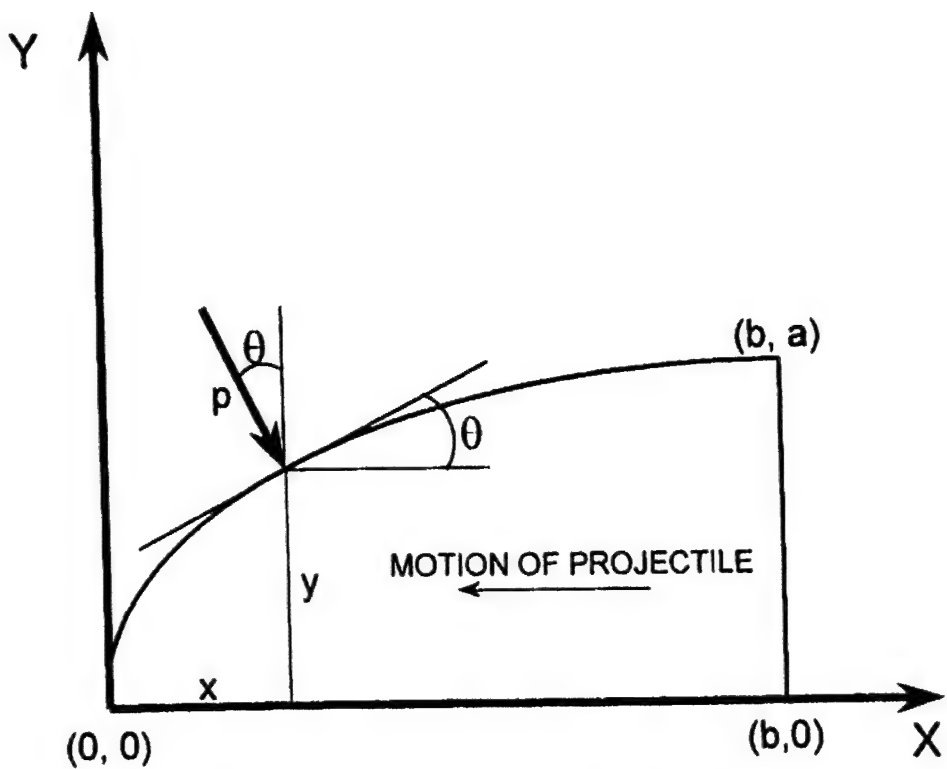


Figure 1. Cross section of projectile nose.

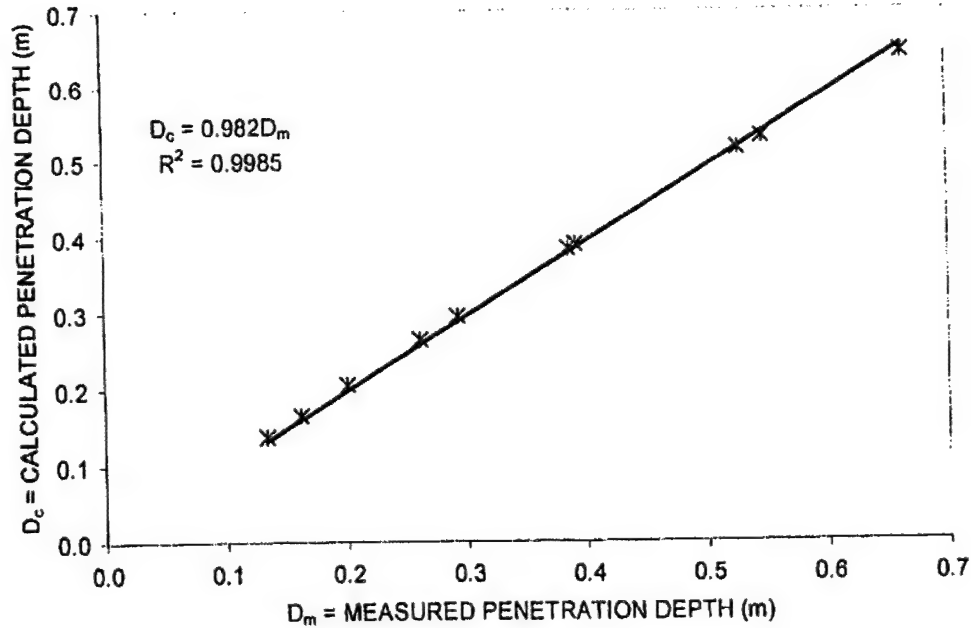


Figure 2. Plot of measured versus calculated penetration depths obtained by applying Equation (9) to the data of Tables 1 and 2 with the parameters  $R = 737$  MPa,  $\tau_0 = 13.8$  MPa, and  $\mu = 0.0$ . The parameters were obtained by a least squares fitting process.

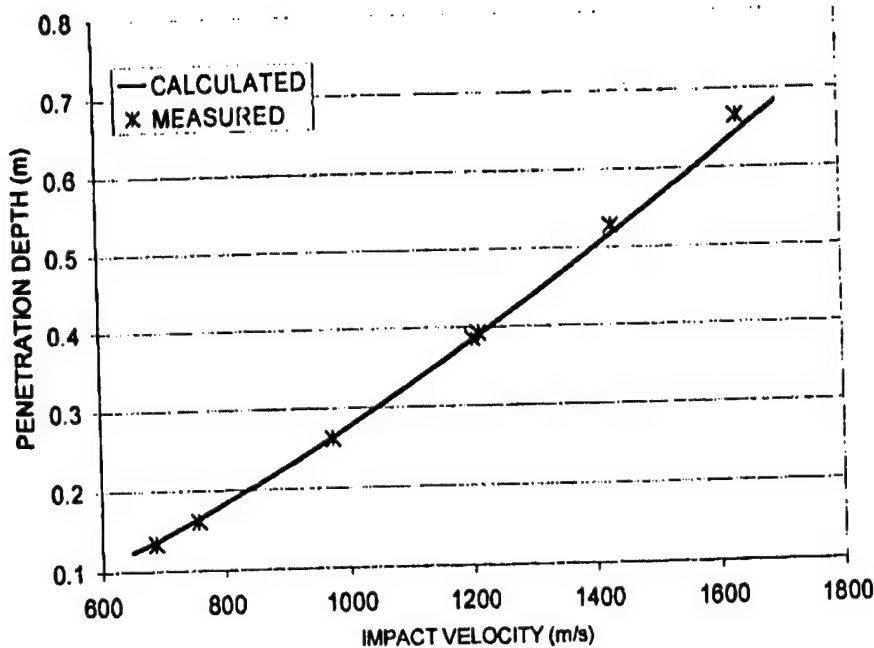


Figure 3. Plot of penetration depth versus impact velocity for the impact system of Table 1 with parameters  $R = 737$  MPa,  $\tau_0 = 13.8$  MPa, and  $\mu = 0.0$ .

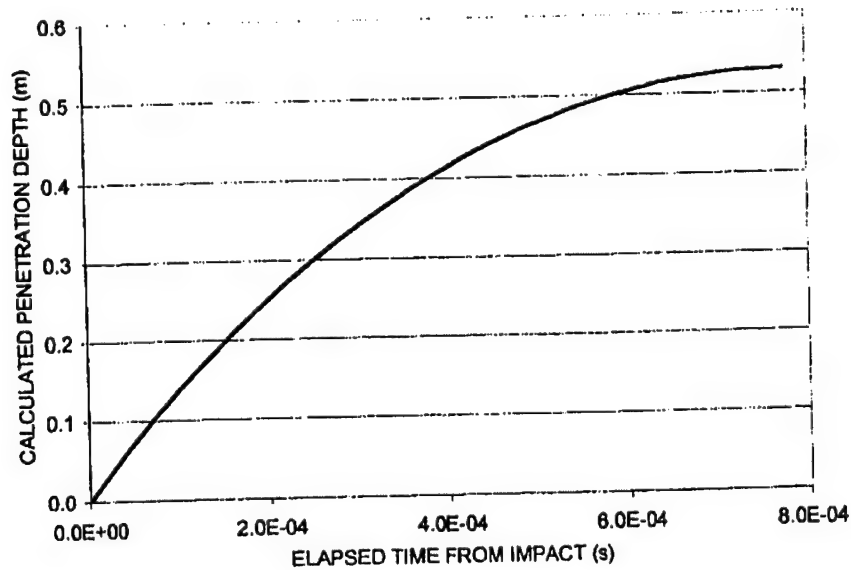


Figure 4. Plot of penetration depth versus time for the impact system of Table 2 (with parameters  $R = 737$  MPa,  $\tau_0 = 13.8$  MPa, and  $\mu = 0.0$ ) for the case of a projectile with an impact velocity of 1500 m/s.

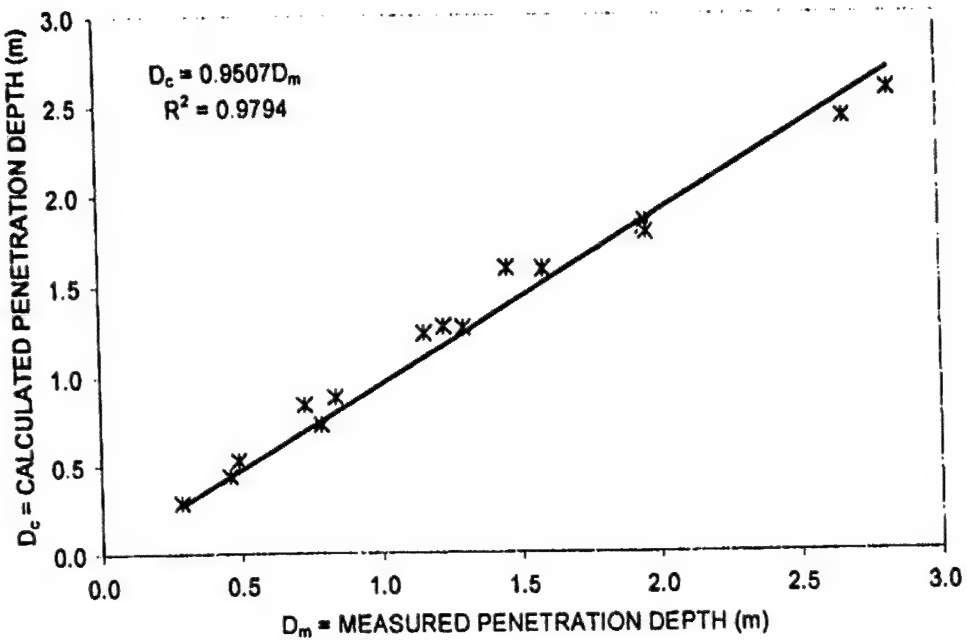


Figure 5. Plot of measured versus calculated penetration depths obtained by applying Equation (9) to the data of Table 3 with the parameters  $R+M\tau_0 = 478$  MPa and  $\mu = 0.0$ . The parameters were obtained by a least squares fitting process.

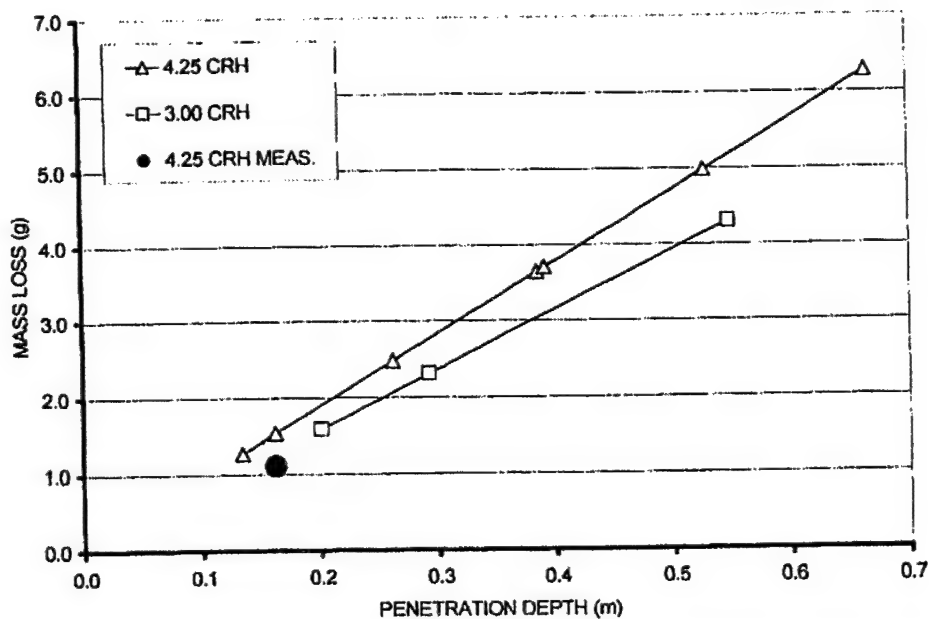


Figure 6. Predicted mass loss versus penetration depth based on tests by Wilson and Christopher (1997).

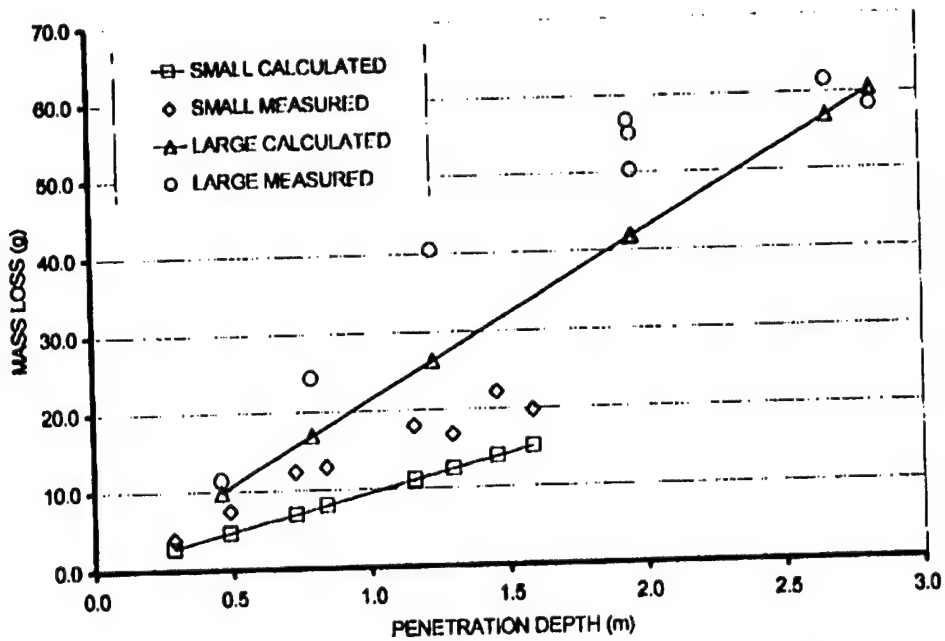


Figure 7. Comparison of calculated and measured (Frew et al., 1998) mass loss versus penetration depth.

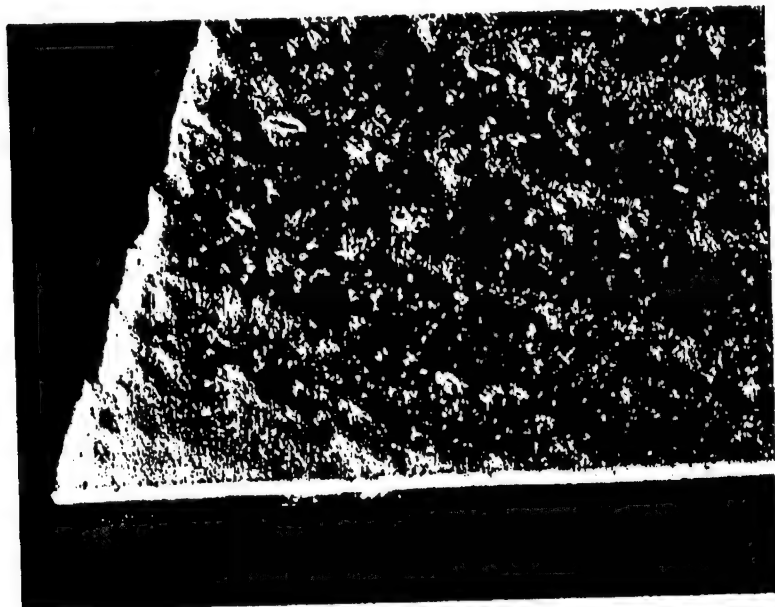


Figure 8. Micrograph of the surface of a 4340 penetrator. This longitudinal section shows the nonetched HAZ (heat affected zone) formed by friction along the horizontal surface at the bottom. The rougher edge rising at about 1 o'clock is a saw cut surface. (50x)



Figure 9. Nose of a 4340 penetrator showing HAZ and melted material, captured in solidified rock. (400x)



Figure 10. Cast of molten steel on the shank of a 4340 penetrator. Also visible is the non-staining HAZ (heat affected zone). (53x)

## APPENDIX

In this appendix, the integrals in Equations (5) and (6) are evaluated for some common and useful nose geometries. This enables us to easily employ the results in the previous section.

### The Conical Nose

There is a particular nose geometry that offers considerable simplification. In terms of the geometry noted in Figure 1, the conical nose has the equation

$$y = \frac{a}{b}x. \quad (\text{A-1})$$

By substituting Equation (A-1) into equations (5) and (6), we find

$$N = \frac{\alpha^2}{1+\alpha^2} + \mu \frac{\alpha}{1+\alpha^2} \quad (\text{A-2})$$

and

$$M = \frac{1}{\alpha}. \quad (\text{A-3})$$

### The Ogive Nose

Much of the penetration data that has been reported is for ogive-nose projectiles. This nose geometry is very significant. In this section, we detail the technique presented in the previous section for conical-nose projectiles with the ogive-nose. The results will certainly lack the simplicity of the conical-nose projectile, but are nevertheless very useful.

The ogival geometry is shown in Figure 6. It is easy to see that the equation for the ogive is given by

$$y = \sqrt{s^2 - (b - x)^2} - (s - a) \quad (\text{A-4})$$

where  $s$  is the radius of the ogive. The ogive is a circular arc of radius  $s$  tangent to the shank at  $x=b$ . In terms of the notation in Figure A-1, the ogive radius is given by

$$s = \frac{a^2 + b^2}{2a}. \quad (\text{A-5})$$

This means that the *Caliber Radius Head* (CRH) (e.g., see Luk and Forrestal, 1987),  $\psi = s/2a$ , can be expressed as

$$\psi = \frac{a^2 + b^2}{4a^2} = \frac{1 + \alpha^2}{4\alpha^2} \quad (A-6)$$

where  $\alpha = a/b$  is the dimensionless nose ratio (see Jones, et al. 1998).

The obstacle to Equation (A-4), in Equations (5) and (6), is the evaluation of the integrals. After some very tedious manipulations, we can show that

$$N = \frac{2\alpha^2(\alpha^2 + 2)}{3(1 + \alpha^2)^2} + \mu \left[ \frac{(1 + \alpha^2)^2}{16\alpha^4} \sin^{-1} \left( \frac{2\alpha}{1 + \alpha^2} \right) + \frac{1 - \alpha^2}{8\alpha^3} - \frac{(1 - \alpha^2)^3}{4\alpha^3(1 + \alpha^2)^2} - \frac{4(1 - \alpha^2)}{3\alpha(1 + \alpha^2)^2} \right] \quad (A-7)$$

and

$$M = \frac{(1 + \alpha^2)^2}{4\alpha^4} \sin^{-1} \left( \frac{2\alpha}{1 + \alpha^2} \right) - \frac{1 - \alpha^2}{2\alpha^3}. \quad (A-8)$$

These equations have been presented in a different form by Luk and Forrestal, 1989. They are included here for convenience.

Equations (A-7) and (A-8) are fairly complicated. However, there is one shape for which they reduce to something particularly simple. The spherical (hemispherical) nose is a degenerate case of the ogive for which the ogive radius is equal to the shank radius and the center of curvature moves to the axis of the specimen. In this case,  $\alpha = 1$  and Equations (A-7) and (A-8) become

$$N = \frac{1}{2} + \frac{\pi\mu}{8} \quad (A-9)$$

and

$$M = \frac{\pi}{2}. \quad (A-10)$$

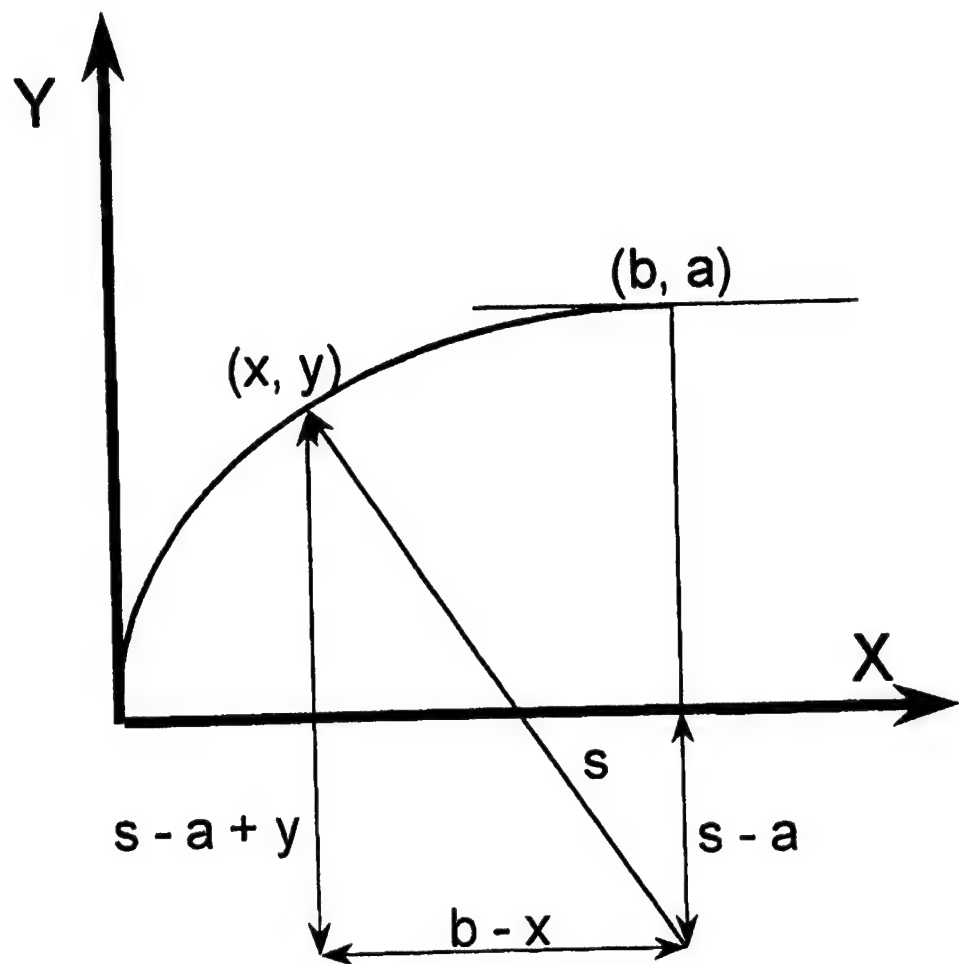


Figure A-1. Cross section of projectile with ogive nose

---

## **APPENDIX S**

# NORMAL PENETRATION OF SEMI-INFINITE TARGETS BY OGIVE-NOSE PROJECTILES, INCLUDING THE EFFECTS OF BLUNTING AND EROSION

**S. E. Jones**  
University of Alabama  
Tuscaloosa, AL 35487-0280

**D. M. Jerome**  
Armament Directorate, Air Force Research  
Laboratory  
Eglin Air Force Base, FL 32542

**O. Toness**  
Armament Directorate, Air Force Research  
Laboratory  
Eglin Air Force Base, FL 32542

**William K. Rule**  
Adjunct Professor of Mechanical Engineering  
Boise State University  
Boise, ID 83725

## ABSTRACT

Analytical modeling of high velocity penetration by rigid projectiles has generally ignored modest erosion with reasonable success. However, even modest mass loss from a high velocity penetrator can result in fairly significant change in performance due to blunting and volume change in the nose. Recent observations of mass loss in high velocity steel projectiles has lead to the conclusion that surface melting of the nose is the primary contributor to the total mass loss. This has motivated the formulation of a one-dimensional mathematical model to explain this process. This model uses data from post-test measurements of penetration tests, but neglects the time-dependent changes in the nose geometry produced by erosion.

This paper is devoted to a one-dimensional analysis of penetration that includes the effects of blunting and erosion. These effects are important because the nose factor can increase significantly for very little mass loss from the penetrator nose. The nose usually contains a small fraction of the total mass and small changes in total mass result in fairly large changes in the nose mass. These effects and their impact on penetration performance are investigated. Especially interesting is the impact that they have on the mechanical properties of the target material when the one-dimensional mathematical model is used to deduce these properties from penetration data. The results confirm that mass loss and blunting are important considerations in high velocity penetration analysis.

## INTRODUCTION

Analytical modeling of high velocity penetration by rigid projectiles has generally ignored modest erosion with reasonable success. However, the direction taken by some important hard target weapons programs has demanded substantial increases in impact velocity. Under these conditions, mass loss and blunting in recovered projectiles has been observed. Under some circumstances, this has lead to substantial reduction in performance at the higher velocities. Mathematical models that ignore blunting and erosion have failed to

produce reasonable correlations with experimental observations. This has lead to recent investigations where the effects of surface melting and wear have been used to explain the loss of penetrator performance (e.g., see Foster, et al. [1], Jones, et al. [2], and Beissel and Johnson [3]).

In order to correlate wear and penetrator mass loss with penetrator performance, a new one-dimensional penetration model is proposed in this paper. This model includes the effects of time-dependent mass loss and blunting (increases in the nose factor). Naturally, this complicates the analysis and an explicit solution is no longer possible. The equation of motion is nonlinear with time-dependent coefficients. The solution to this equation is shown to be implicit when the time-dependent coefficients are expressed in terms of the penetration depth. A blunting parameter is introduced and a simple erosion schedule is used to reduce the nose length in the penetrator. A two-parameter solution is shown to produce substantial agreement with experimental results.

## AN ERODING AND BLUNTING PROJECTILE MODEL

Consider an ogival nose rod projectile impacting a semi-infinite target, as shown in Figure 1. The projectile is acted upon by a net resistive force  $F$  at time  $t$  and has velocity  $v$  directed to the left. At some later time  $t + \Delta t$ , the projectile has lost an increment of mass  $\Delta m$  and has a new velocity  $v + \Delta v$ . An internal force  $F_I$  acts between the main body of the projectile and the mass increment. The mass increment is moving with velocity  $u$ . The change in linear momentum between time  $t$  and time  $t + \Delta t$  is equal to the impulse of the forces acting on the system, which leads us to

$$m\Delta v + \Delta m(v - u) = I = F\Delta t \quad (1)$$

where the linear impulse integral,  $I$ , has been evaluated using the mean value theorem. The force  $F = F(\xi)$  is evaluated at an intermediate time  $\xi$ , where  $t < \xi < t + \Delta t$ . Taking the limit as  $\Delta t \rightarrow 0$ , we find the equation of motion of the projectile

$$m\dot{v} + \dot{m}(v - u) = F \quad (2)$$

This equation, which accounts for the mass loss during penetration, was presented earlier by Jones, et al [4] and used in connection with projectile motion in which mass loss and mushrooming occurs. In the present context, mass loss will be permitted, but mushrooming of the nose will not. Blunting of the ogival nose will be accounted for in the time-dependent description of the force  $F$ . In general, we will assume that mass loss occurs at the nose and is the result of surface melting (Foster, et al. [1]). Thus, it is appropriate to assume that  $u \approx 0$  because the melted projectile material will be stripped from the nose by the longitudinally stationary target.

### THE FORCE $F$

The pressure  $P$  acting on the surface of the nose of the projectile is assumed to have velocity-squared dependence and have the form

$$P = \gamma v^2 \sin^2 \theta + R \quad (3)$$

where  $\gamma$  is a constant with the dimension of density,  $v$  is the current speed of the penetrator,  $R$  is a constant with the dimension strength, and  $\theta$  is the local tangent angle of the nose. The pressure in Equation (3) is of the Poncelet type. Cavity expansion methods suggest that  $\gamma = \rho_t$ , where  $\rho_t$  is the mass density of the target (e.g., see Luk and Forrestal [5]). This is not the only interpretation for  $\gamma$ . For example, the eroding penetrating rod model of Tate [6,7] employs the *Modified Bernoulli Equation* and rigid body penetration in this theory is a limiting case. The pressure acting on the face of the rod penetrator is also of the Poncelet type, but in this case,  $\gamma = \rho_t/2$ .

Assume that friction  $f$  acts on the surface of the nose of the projectile. This frictional resistance acts tangent to the surface and has the units of force per unit area (see Figure 2). Integrating over the surface of the nose leads to

$$F = 2\pi \int_0^b yy'Pdx + 2\pi \int_0^b yf dx. \quad (4)$$

Before proceeding further, we should mention the friction force that we will employ for this analysis. High speed friction is a subject that has very little history, in spite of the fact that references dating as early as 1785 can be found. However, Kragelskii [8] reports the results of several early investigations and some trends can be noted. Pressure dependence at low velocities serves to increase the maximum sliding friction attainable. As the velocity increases, friction decreases and appears to approach an asymptotic limit, as shown in Figure 3. The results reported by the early investigators, indicate that this asymptotic limit is approached for velocities that are much lower than those experienced in high speed penetration problems. With these observations, it is appropriate for a fundamentally one-dimensional analysis to assume that the friction

acting on the nose of the penetrator is constant. This friction will be denoted by  $f_0$ .

The nose of the projectile is assumed to be ogival. The ogival geometry is shown in Figure 4. Now, integrating over the surface of the ogive, we find that the component of force resisting the motion of the projectile is

$$F = \pi a^2 (\gamma N v^2 + R + f_0 M) \quad (5)$$

where

$$N = \frac{2}{a^2} \int_0^b y \frac{y'^3}{1+y'^2} dx \quad (6)$$

and

$$M = \frac{2}{a^2} \int_0^b y dx. \quad (7)$$

In general, the coefficients  $N$  and  $M$  in Equations (6) and (7) are time-dependent. From Figure 4, we can find the equation for the ogive

$$y = \sqrt{S^2 - (b-x)^2} - (S-a). \quad (8)$$

In this equation,  $S$  is the ogive radius,  $b$  is the nose length, and  $a$  is the radius of the shank of the penetrator. These quantities are all related to the nose ratio  $\alpha = a/b$  and the shank radius  $a$  through the ogive geometry in Figure 2. It is easy to show that  $S = a(1+\alpha^2)/2\alpha^2$ .

Evaluation of the integrals in Equations (6) and (7) is fairly tedious when Equation (8) is used. However, after many manipulations, we can show that

$$N = \frac{2\alpha^2(2+\alpha^2)}{3(1+\alpha^2)^2} \quad (9)$$

and

$$M = \frac{(1+\alpha^2)^2}{4\alpha^4} \sin^{-1} \left( \frac{2\alpha}{1+\alpha^2} \right) - \frac{1-\alpha^2}{2\alpha^3}. \quad (10)$$

These results have been presented in a slightly different form by Luk and Forrestal [9]. In the analysis that follows, both of these quantities will be time dependent because  $\alpha$ , the nose ratio, will be changing with time. This means that the equation of motion for the projectile, Equation (2), is not only nonlinear, but has time-dependent coefficients,  $m, N, M$ .

### MOTION OF THE PROJECTILE

Combining the results of the previous sections and the observation that  $u \approx 0$ , we get

$$m\dot{v} + \dot{m}v = -\pi a^2 (\gamma N v^2 + R + f_0 M) \quad (11)$$

as the equation of motion for the projectile. This differential equation appears to be complicated, but can be easily integrated. Let  $v = \phi/m$  and now  $\phi$  satisfies

$$\dot{\phi} + \pi a^2 \gamma m^{-2} N \phi^2 + \pi a^2 R \left[ 1 + \frac{f_0}{R} M \right] = 0. \quad (12)$$

However, the change of variables

$$\dot{\phi} = \frac{d\phi}{dz} \dot{z} = v \frac{d\phi}{dz} = \frac{\phi}{m} \frac{d\phi}{dz} \quad (13)$$

permits us to write Equation (12) in the form

$$\frac{dw}{dz} + 2\pi a^2 \gamma m^{-1} N w + 2\pi a^2 m R \left[ 1 + \frac{f_0}{R} M \right] = 0 \quad (14)$$

where  $w = \phi^2$ . This equation is linear and may be easily integrated after multiplying by the integrating factor  $E = \exp \left\{ 2\pi a^2 \gamma \int_0^z m^{-1} N dz \right\}$ . The result is

$$\phi^2 = E^{-1} \left[ v_0^2 m_0^2 - 2\pi a^2 R \int_0^z m \left[ 1 + \frac{f_0}{R} M \right] Edz \right]. \quad (15)$$

where  $m_0 = m(0)$  and  $\phi(0) = m_0 v_0$  ( $v(0) = v_0$ ) were used to evaluate the constant of integration. Now, reverting to the original dependent variable, we see that

$$v^2 = m^{-2} E^{-1} \left[ v_0^2 m_0^2 - 2\pi a^2 R \int_0^z m \left[ 1 + \frac{f_0}{R} M \right] Edz \right] \quad (16)$$

is an integral of motion of Equation (11). This integral can be used to find the maximum penetration depth achieved by the projectile,  $z = Z$ . Maximum penetration occurs when  $v = 0$ , which means that

$$\int_0^Z m \left[ 1 + \frac{f_0}{R} M \right] Edz = \frac{m_0^2 v_0^2}{2\pi a^2 R} \quad (17)$$

is the equation that determines  $Z$ .

Equation (17) is generally nonlinear and implicit in  $Z$ . As such, it is difficult to find  $Z$  as a function of the parameters in the problem. However, there is a simple example that can be used to test Equation (17). Suppose that  $m$ ,  $M$ , and  $N$  are all constants, say  $m = m_0$ ,  $M = M_0$ , and  $N = N_0$ . Then, all of the integrals in Equation (17) can be directly evaluated and it is easy to show that

$$Z = \frac{m_0}{2\pi a^2 \gamma N_0} \ln \left[ 1 + \frac{N_0 \gamma v_0^2}{R \left[ 1 + \frac{f_0}{R} M_0 \right]} \right]. \quad (18)$$

This is the estimate for penetration depth introduced by Jones, et al. [10] and used to estimate  $R$  and  $f_0$  from penetration data. When  $f_0 = 0$ , Equation (18) reduces to the classic rigid body penetration estimate obtained by cavity expansion methods, e.g., Luk and Forrestal [5].

A second integral of motion can now be found from Equation (16)

$$v = \frac{dz}{dt} = m^{-1} E^{-\frac{1}{2}} \sqrt{v_0^2 m_0^2 - 2\pi a^2 R \int_0^z m \left[ 1 + \frac{f_0}{R} M \right] Edz} \quad (19)$$

by separation of variables. The result is

$$t = \int_0^T \frac{m \sqrt{E} dz}{\sqrt{v_0^2 m_0^2 - 2\pi a^2 R \int_0^z m \left[ 1 + \frac{f_0}{R} M \right] Edz}} \quad (20)$$

and this naturally leads to the estimate for terminal time,  $t_f$ ,

$$t_f = \int_0^Z \frac{m \sqrt{E} dz}{\sqrt{v_0^2 m_0^2 - 2\pi a^2 R \int_0^z m \left[ 1 + \frac{f_0}{R} M \right] Edz}}. \quad (21)$$

Now, all that remains to use these results is to find suitable  $z$ -dependent estimates for  $m$ ,  $M$ , and  $N$ . This issue will be addressed in the next section.

#### ANALYSIS OF CHANGE IN OGIVAL PENETRATOR NOSES

Based on some earlier reasoning (Foster, et al. [1]), mass is lost from the surface of the nose through surface heating due to interaction with the target. Mass loss due to surface melting has been discussed by Foster, et al. [1] and Jones, et al. [10]. For ogive-nose projectiles  $N$  and  $M$  are expressed in terms of the nose ratio  $\alpha = a/b$  in Equations (9) and (10). The mass in the nose can also be expressed in terms of  $\alpha$ . For an ogive, the volume of the solid nose, expressed in the nomenclature of Figure 2, is given by

$$V = \pi \int_0^b y^2 dx \\ = \pi a^3 \left[ \frac{3 + 2\alpha^2 + 3\alpha^4}{12\alpha^5} - \frac{(1 - \alpha^2)(1 + \alpha^2)^2}{8\alpha^6} \sin^{-1} \left( \frac{2\alpha}{1 + \alpha^2} \right) \right]. \quad (22)$$

This means that the mass of the projectile material contained in the nose is  $m_n = \rho V$ , where  $\rho$  is the mass density of the projectile material. Notice that the mass of the nose is directly a function of the nose ratio  $\alpha$ .

Mass loss in high speed penetrators is largely due to surface melting of the nose (Foster, et al. [1] and Jones, et al. [10]). For this reason, it is safe to assume that the shank radius  $a$  remains constant. This means that the time-dependence in  $m_n$  is approximately restricted to changes in the nose length  $b=b(t)$ . This observation allows us to estimate the rate of mass loss in the nose by differentiating Equation (23)

$$\dot{m}_n = \rho \dot{V} \\ = \pi \rho a^2 b \left[ \frac{3+\alpha^2}{2\alpha^4} - \frac{(3-\alpha^2)(1+\alpha^2)}{4\alpha^5} \sin^{-1} \left( \frac{2\alpha}{1+\alpha^2} \right) \right]. \quad (23)$$

Evidently,  $\dot{m}_n < 0$  because  $\dot{b} < 0$ . For any prescribed erosion schedule, we can find the rate of change in the nose length from Equation (23) and the time-dependent nose length  $b=b(t)$  from Equation (22). However, penetration depth is time-dependent, which means that  $b$  is implicitly depth-dependent. Suppose that the initial length of the nose is  $b = b_0$  and erosion takes the nose length to a final length of  $b_f$ . Suppose that this process is roughly linear in the depth, which means that

$$b = b_0 - (b_0 - b_f) \frac{z}{Z}. \quad (24)$$

This is the simplest approximation to shortening of the nose. There are others, some of which are more complicated. These will be considered in later reports.

For the moment, Equation (24) allows us to express  $\alpha = a/b$  approximately as a function of  $z$ . This means that  $N$ ,  $M$ , and  $m$  can all be expressed in terms of  $z$  by Equations (6), (7), and (22). The mass of the projectile,  $m$ , can be written as the sum of  $m_n$  and the mass of the material in the shank, which is assumed to remain constant, so that any erosion only affects  $m_n$ . As indicated, we can use Equation (24) to express  $\alpha$  in terms of  $z$

$$\alpha = \frac{\alpha_0}{1 - \lambda \frac{z}{Z}} \quad (25)$$

where  $\alpha_0 = a/b_0$  is the initial nose ratio and  $\lambda = 1 - b_f/b_0$  is a dimensionless blunting parameter expressing the change in nose length. If no blunting occurs, then  $\lambda = 0$ . For significant blunting,  $\lambda$  is close to 1. However,  $\lambda$  is always between 0 and 1.

Each of the functions of  $\alpha$  that express the time-dependence of  $N$ ,  $M$ , and  $m$  is very complicated when Equation (25) is used. In spite of the simplicity of Equation (25), Equations (6), (7), and (22) are generally too difficult to perform the operations required by the theory. However, in this case some of the analysis can continue if a few more

assumptions that apply to high velocity penetration are made. Small changes in  $m$  and  $M$  do not significantly influence penetration results. So, we will neglect changes in these quantities and treat them as constants  $m_0$  and  $M_0$ , their initial values. This enables us to evaluate the integral in

$$E = \exp \left\{ 2\pi a^2 \gamma \int_0^Z m^{-1} N dz \right\} \\ = \exp \left\{ \frac{2\pi a^2 \gamma}{m_0} \int_0^Z \frac{2\alpha^2 (2+\alpha^2)}{3(1+\alpha^2)^2} dz \right\}. \quad (26)$$

After some tedious manipulations, we can show that

$$\int_0^Z \frac{2\alpha^2 (2+\alpha^2)}{3(1+\alpha^2)^2} dz = \frac{Z\alpha_0^2}{3\lambda} \left[ \frac{1 - \lambda \frac{z}{Z}}{\alpha_0^2 + (1 - \lambda \frac{z}{Z})^2} - \frac{1}{1 + \alpha_0^2} \right] \\ + \frac{Z}{\lambda} \left[ \tan^{-1} \left( \frac{1}{\alpha_0^2} \right) - \tan^{-1} \left( \frac{1 - \lambda \frac{z}{Z}}{\alpha_0^2} \right) \right]. \quad (27)$$

For a penetrator with no blunting,  $\lambda = 0$ . To recover this limiting case from Equation (27), we compute the limit as  $\lambda \rightarrow 0$  and we can show that the right hand side of Equation (27) tends to  $2\alpha_0^2 (2+\alpha_0^2)z / 3(1+\alpha_0^2)^2$  as it should. Now, we can use this result in Equation (26) and then substitute the result into Equation (17) to find  $Z$  for a specific erosion situation. If no erosion occurs, or the effect of blunting can be neglected, the right hand side of Equation (26) is replaced by the limit as  $\lambda \rightarrow 0$ .

## EXPERIMENTS

A series of penetration experiments were performed on the test range at Eglin AFB, FL. These 50-caliber depth of penetration experiments were conducted with steel projectiles striking grout and concrete targets at 800-1800 m/sec (2624-5904 ft/sec). The targets had nominal unconfined compressive strength of 56.3 MPa (8160 psi), and a mass density of 2300 kg/m<sup>3</sup> (143 lb/ft<sup>3</sup>). The projectiles were fabricated from several different types of high strength steel alloys, which ranged in yield strength from 1.24-1.76 GPa (180-255 ksi). All projectiles were machined with a 3.0 caliber-radius-head tangent ogive nose, a shank diameter of 12.7 mm (0.5 in), and length-to-diameter ratio of 7.0. The projectiles had a mass of 65g (0.143 lb), and also contained an internal cavity. Depths of penetration were recorded, which increased as striking velocity increased. An innovative projectile recovery technique was developed in order to study the in-situ projectile trajectories. This technique utilizes a fluorescent dye-impregnated two-part epoxy to stabilize the penetration channel and surrounding crack systems. Large diameter (25.4 cm/10.0 in) cores including the impact crater, penetration channel, and projectile were removed from the target, allowing the sectioning, visualization, and analysis of the in-situ trajectories. Subsequent projectile recovery revealed moderate nose erosion and blunting, and mass losses up to

8% of the total projectile mass. An 8% mass loss can be very significant if the volume of the nose is only a small fraction of the total volume of the projectile itself.

## RESULTS

For each set of experimental data, the blunting parameter is evaluated and a best fit to the experimental data is achieved by varying  $R$  and  $f_0$ . The results of these correlations are given in Figures 5-10. The most effective penetrator, Experimental Steel 2 (Figure 5), has the minimum frictional coefficient  $f_0 = 6.69 \text{ MPa}$ . The penetrator that performed worst, 4340 Steel (Figure 10), had the highest value of  $f_0 = 11.6 \text{ MPa}$ . All of the other materials were somewhere between. The values of  $R$  also varied from material to material, but not as much on a percentage basis. The range in  $R$  values is from 446 MPa to 625 MPa.

## CONCLUSIONS

The correlation between the theory and the experimentally measured penetration depths is excellent as expected because the parameters  $R$  and  $f_0$  were chosen to minimize the error. Nevertheless, important trends may be noted. The best performing projectile material was that for which the friction between target and the projectile nose was least. This correlation is consistent with mass loss observations. Instinctively, we would think that  $R$  would remain constant for the different penetrator materials because the normal pressure on the projectiles should be a target property, rather than a target/penetrator property.

There were several assumptions made to simplify the analysis that could account for the discrepancies. A more accurate friction law that reflects the velocity-dependence along the profile of the nose could account for the difference. Also, the assumption regarding the shortening of the nose in Equation (24) may be too crude. In any event, there are several points to address in future work.

## REFERENCES

1. Foster, J. C., Jr., Jones, S. E., Toness, O., DeAngelis, R. J., and Rule, W. K., 1999, "An Analytical Estimate for Mass Loss from a High Velocity Rigid Penetrator," Proceedings of the 1999 APS Topical Conference on Shock Compression of Condensed Matter, Snowbird, UT.
2. Jones, S. E., Foster, J. C., Jr., Toness, O. A., DeAngelis, R. J., and Rule, W. K., 2001, "An Estimate for Mass Loss from High Velocity Steel Penetrators," submitted for publication.
3. Beissel, S. R. and Johnson, G. R., 2000, "An Abrasion Algorithm for Projectile Mass Loss During Penetration," Int. J. Impact Engng., Vol. 24, No. 2, pp. 103-116.
4. Jones, S. E., Gillis, P. P., and Foster, J. C., Jr., 1987, "On the Penetration of Semi-Infinite Targets by Long Rods," J. Mech. Phys. Solids, Vol. 35, No. 1, pp. 121-131.
5. Luk, V. K. and Forrestal, M. J., 1987, "Penetration into Semi-Infinite Reinforced Concrete Targets With Spherical And Ogive Nose Projectiles," Int. J. Impact Engng., Vol. 6, No. 4, pp. 291-301.
6. Tait, A., 1967, "A Theory for the deceleration of long rods after impact," J. Mech. Phys. Solids, Vol. 15, p. 387.
7. Tait, A., 1969, "Further results in the theory of long rod penetration," J. Mech. Phys. Solids, Vol. 17, p. 141.
8. Krueger, J. V., 1965, *Friction and Wear*, Butterworths, Inc., Washington, DC.
9. Luk, V. K. and Forrestal, M. J., 1989, "Comment on 'Penetration into Semi-Infinite Reinforced Concrete Targets with Spherical and Ogive Nose Projectiles,'" Int. J. Impact Engng., Vol. 8, No. 1, pp. 83-84.
10. Jones, S. E., Foster, J. C., Jr., Toness, O. A., DeAngelis, R. J., and Rule, W. K., 2001, "An Estimate for Mass Loss from High Velocity Steel Penetrators," submitted for publication

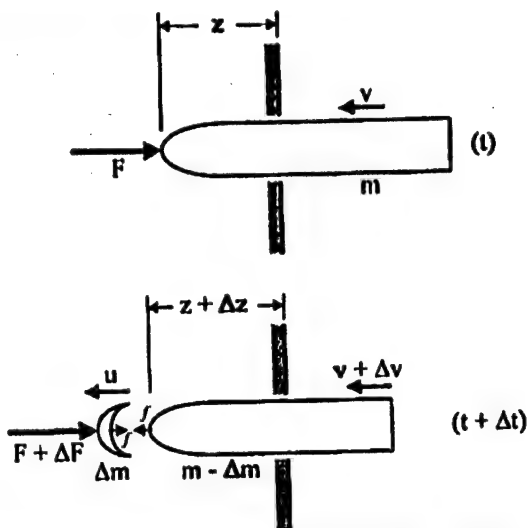


Figure 1. An ogive-nose projectile impacts a target. At time  $t$ , the projectile has mass  $m$  and velocity  $v$  at a depth of penetration  $z$ . At time  $t + \Delta t$ , the projectile has lost an increment of mass  $\Delta m$ . The mass increment  $\Delta m$  has velocity  $u$ , while the projectile has velocity  $v + \Delta v$  and the depth is  $z + \Delta z$ .

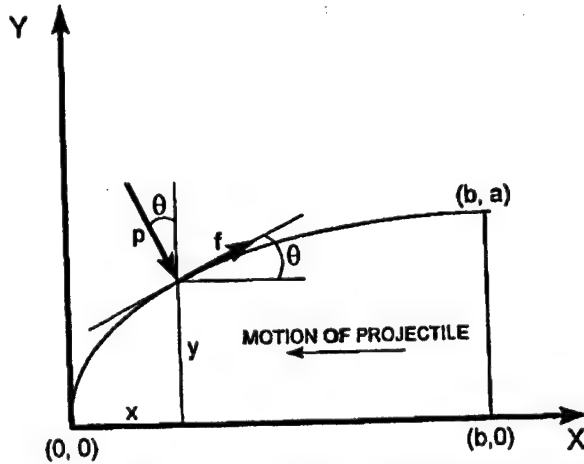


Figure 2. Pressure  $P$  and friction  $f$  acting on the surface of the nose of an axisymmetric projectile during penetration.

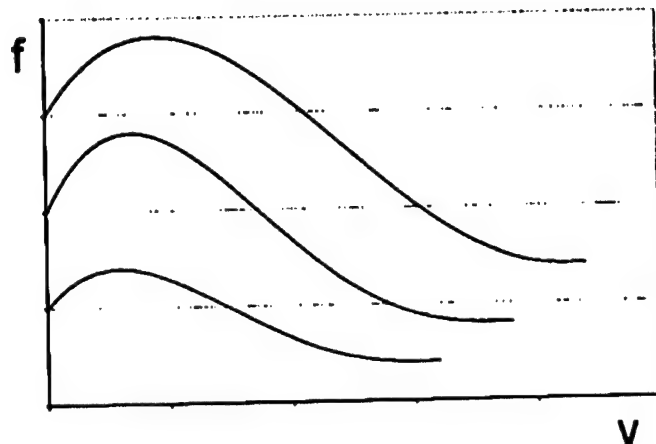


Figure 3. Typical sliding friction/velocity profiles. The shape of these curves depends on the materials in contact and the normal pressure. But, they all share one thing in common in the asymptotic limit.

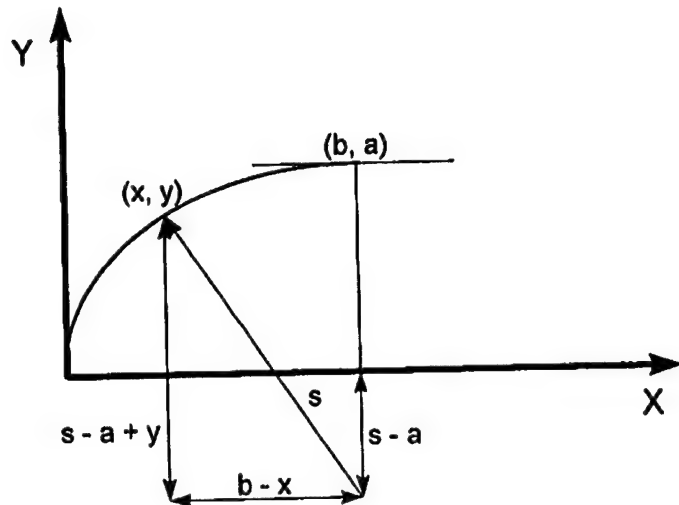


Figure 4. The ogival nose geometry. The tip passes through zero at  $x=0$  and the tangent is zero at  $x=b$ . The remainder of the projectile is a cylinder of length  $L$ .

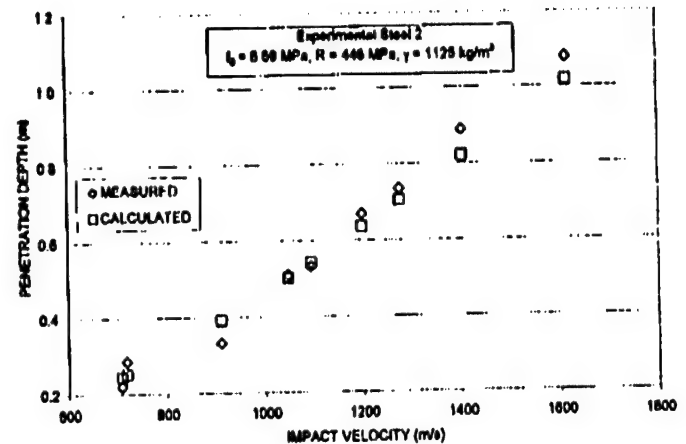


Figure 5. Plot of penetration depth versus impact velocity for experimental steel\_2.

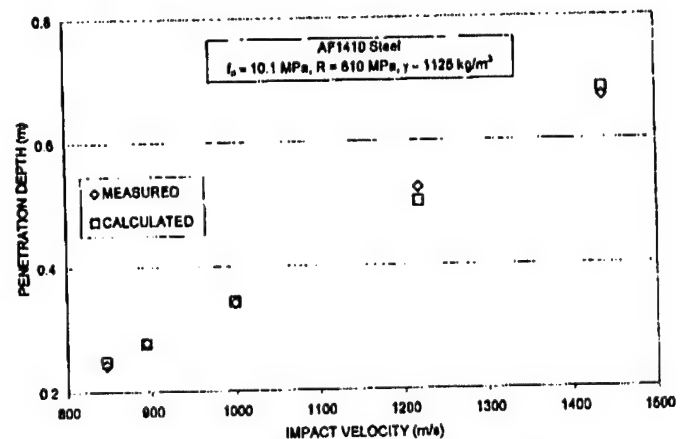


Figure 6. Plot of penetration depth versus impact velocity for AF1410 steel.

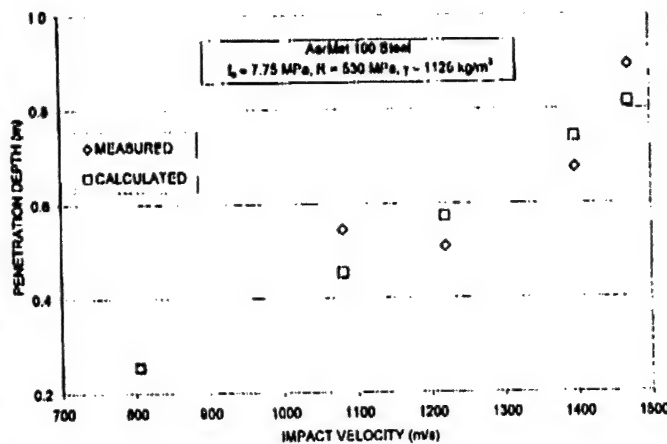


Figure 7. Plot of penetration depth versus impact velocity for AerMet100 steel.

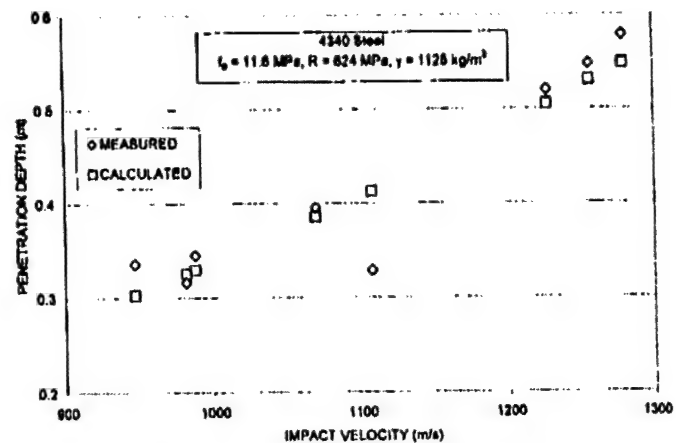


Figure 10. Plot of penetration depth versus impact velocity for 4340 steel.

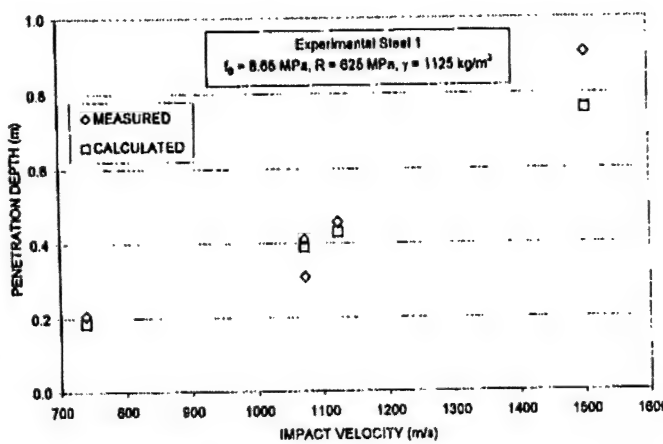


Figure 8. Plot of penetration depth versus impact velocity for Experimental Steel\_1.

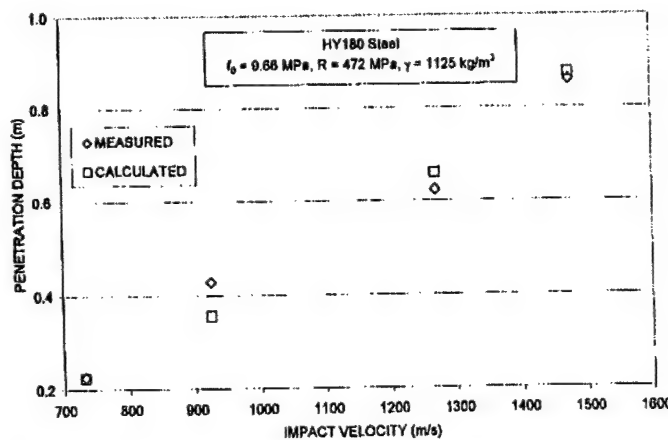


Figure 9. Plot of penetration depth versus impact velocity for HY180 steel.

---

## **APPENDIX T**

AN ANALYSIS OF ROD PENETRATION OF SEMI-INFINITE TARGETS  
USING AN AVERAGE PRESSURE ESTIMATE

John D. Cinnamon, Captain, US Air Force  
Department of Astronautics, US Air Force Academy Colorado

S. E. Jones, Senior Scientist  
Air Force Research Laboratory/MNMW, Eglin Air Force Base, Florida  
(on leave from the University of Alabama)

**ABSTRACT**  
A new one-dimensional analysis of long-rod penetration of semi-infinite targets is presented. Models in this field attempt to accurately describe the penetration process of a uniform long rod into a uniform semi-infinite target. This one-dimensional analysis predicts profile hole diameters and penetration depths over a wide range of material combinations and extends the previous analyses in this area to include hypervelocity impacts. This approach utilizes values of material dynamic yield strengths, known impact conditions, and the well-established crater volume/kinetic energy relationship to predict crater hole characteristics over an impact velocity range of 1 to 6 km/s.

The analysis presented here includes an initial transient phase and modifies previous estimates for pressure on the penetrator tip at steady state. The average pressure at steady state was found to be a constant value over the range of impact velocities for a particular shot combination. The specific value for the average pressure was found to be a direct function of target strength. The resulting equations retain computational simplicity by remaining completely algebraic in nature. Correlation with a majority of the readily available experimental data is given. The results are very reasonable for a one-dimensional model.

LIST OF SYMBOLS AND ABBREVIATIONS

$a$	slope of the crater volume/kinetic energy relationship
$A$	cross-sectional area of the mushroom of the rigid-plastic penetrator
$A_0$	initial cross-sectional area of the undeformed penetrator
$A_1$	cross-sectional area of the penetrator at impact
$A_2$	cross-sectional area of the penetrator at steady state
$b$	intercept of the crater volume/kinetic energy relationship
$D$	original diameter of the undeformed penetrator
$e$	engineering strain in the mushroom of the penetrator
$e_0$	engineering strain in the mushroom at impact
$e_1$	engineering strain in the mushroom at steady state
$E_0$	kinetic energy of the penetrator at impact
$l$	current undeformed section length
$L$	original length of the undeformed penetrator
$P_a$	pressure on the axis of the penetrator tip
$P_0$	pressure on the axis of the penetrator tip at impact
$P_1$	pressure on the axis of the penetrator tip at steady state

$P$	average pressure on the penetrator tip
$P_0$	average pressure on the penetrator tip at impact
$P_1$	average pressure on the penetrator tip at steady state
$Q$	average pressure on the penetrator tip at steady state, independent of $v_0$
$r$	radial distance from the axis of the penetrator
$R$	original undeformed penetrator rod radius
$R_t$	dynamic yield strength of target
$u$	current penetration velocity
$u_0$	penetration velocity at impact
$v$	current velocity of the undeformed section
$v_0$	impact velocity
$V_c$	crater volume of the recovered target
$Y_p$	dynamic yield strength of penetrator
$z$	penetration depth
$\rho$	penetrator density
$\mu^2$	ratio of target density to penetrator density

## INTRODUCTION

Tate (1967) and simultaneously Alekseevskii (1966), published a one-dimensional theory for the penetration of semi-infinite targets by long rods. Tate (1969) later published a second paper. These papers form the basis upon which the accepted theory of one-dimensional rod penetration rests. This theory attempts to accurately describe the penetration process of a uniform long rod into a uniform semi-infinite construct of target. A prediction of the resulting penetration hole characteristics is available from this analysis. By comparing the theoretical predictions to experimental data, we can evaluate the accuracy of these one-dimensional models.

Jones, *et al.* (1987) modified the equations of motion for the undeformed rod section by employing a balance of linear impulse and momentum. In subsequent papers, Wilson, *et al.* (1989) and Gillis, *et al.* (1989) offered some improvements and better agreement between the theory and experimental data was observed. However, this approach relied upon post-test measurements for estimates of the engineering strain in the mushroom of the penetrator tip. The strain was assumed to be constant throughout the process and equal to that measured from the profile hole diameter. By using the modified Bernoulli Equation proposed by Tate, the pressure, penetration velocity, and undeformed section velocity were coupled with the modified equation of motion and an equation for the conservation of mass passing from the undeformed section of the penetrator. This system was integrated and the resulting predictions for penetration depth were compared to experimentally observed values from the recovered targets. The penetrator and target dynamic yield strengths were taken to be constant during the event and estimated from laboratory values for yield strengths at the highest available strain-rates.

These results were satisfying and showed promise, but based analysis of key parameters on post-experiment measurement. Kerber, *et al.* (1990) utilized a well-established crater volume - kinetic energy relationship, e.g. Murphy (1987), to remove some of the dependence on post-test measurements. The aim was to produce engineering strain as a by-product of the solution of the model. However, because the penetration process was treated as being dominated by the steady state, the results did not correlate well over a large range of impact velocities and rod lengths. The correlations with experiments were satisfactory for longer rods and higher impact velocities where steady state penetration can be presumed to dominate the event. The initial and terminal transients were neglected in this and previous analysis. The initial transient would appear to become more important in shorter rods and lower impact velocities.

Cinnamon, *et al.* (1992a,b) reported a significant increase in accuracy by incorporating an initial transient phase to the penetration process. This analysis was based on observations by Ravid, *et al.* (1990), Gillis, *et al.* (1990), and Jones, *et al.* (1991). This latest approach yielded good accuracy for a one-dimensional model in the 1 to 3 km/s velocity range. The results depended only on physical parameters determined before testing and the well-established crater volume/kinetic energy relationship. The terminal transient was neglected in this model. The resulting equations were completely algebraic in nature. Of some concern in this approach was that the trends in the predicted penetration depth curves were tending toward significantly high values for impact velocities above 3 km/s. When experimental data for 3 - 6 km/s were evaluated, the model's accuracy indeed deteriorated. In examining the model, it became obvious that the predictions of pressure available from the modified Bernoulli Equation were simply too high. In fact, the correlation discovered by Cinnamon, *et al.* (1992a,b), indicated that the pressure profile could be successfully modified in such a way that the average pressure at steady-state predicted by the Bernoulli Equation was *reduced* by a specific factor (which depended exclusively on target strength) to match experimental penetration depths. The parabolic nature in which the modified Bernoulli Equation predicts the interface pressure at steady state as impact velocity increases was somewhat minimized by this technique.

In Jones, *et al.* (1993), the pressure distribution on the penetrator tip was modified to attempt to correct for the deteriorating results above 2.3 km/s. With a judicious choice of two dimensionless parameters, slight improvement was observed. However, a physical relationship between these parameters and the model was not discovered. The pressures predicted by the modified Bernoulli Equation were once again reduced to achieve acceptable results. However, this new pressure distribution contained the same parabolic component as the previous approach.

In this paper, several approaches to the choice of pressure at steady state were evaluated. It became clear that past successful solution forms for the pressure distribution were those that cancelled out the parabolic nature of the modified Bernoulli Equation. As a consequence, when the average pressure at steady state is taken to be a particular value for a specific material combination over all impact velocities and directly related to target strength, a significant increase in model accuracy resulted. The model was successfully extended up to 6 km/s. This paper includes results reflecting analysis of all readily available experimental data in this field of research, a great majority of which has been compiled by Anderson, *et al.* (1992).

## THEORY

The general concepts of the rod penetration process are detailed in Figure 1. The undeformed penetrator is a cylinder of known length and diameter, which impacts the target at a nominal normal incidence at a known velocity. The penetrator enters the target and experiences mushrooming in the tip. When the event has concluded a crater with a measurable diameter and depth remains.

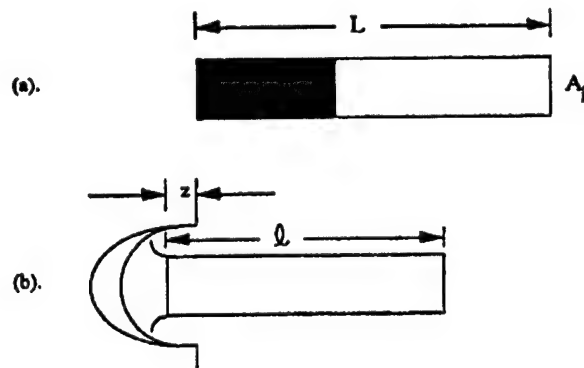


Figure 1. Schematic of Rod and Penetration Process.  
 (a) undeformed rod of length L and initial cross-sectional area A<sub>i</sub>. The shaded portion will be lost to erosion. (b) penetration event. l is the undeformed section length and z is the penetration depth.

### Primary Governing Equations

Jones, *et al.* (1987) proposed a modification to the equation of motion of the undeformed section of a rod penetrator. This equation is

$$\ell \dot{v} + \dot{\ell} (v - u) = \frac{-P}{\rho(1+e)} \quad (1)$$

where  $\ell$  is the undeformed section length,  $v$  is the current undeformed section velocity,  $u$  is the penetration velocity,  $P$  is the average pressure on the penetrator tip,  $\rho$  is the penetrator density, and  $e$  is the engineering strain in the penetrator mushroom. The details behind the development of this equation are contained in Jones, et al (1987).

Wilson, et al. (1989) added another key equation to the analysis. The conservation of mass across the plastic interface between the mushroom and the undeformed section of the penetrator was given in the form

$$\dot{e} \ell = v - u \quad (2)$$

The penetrator is assumed to be rigid-plastic during the event. In both (1) and (2), dots over the symbols represent differentiation with respect to time. The engineering strain in the mushroom is compressive and therefore negative. The current value of the engineering strain in the mushroom is defined to be

$$e = \frac{A_i}{A} - 1 \quad (3)$$

where  $A_i$  is the initial cross-sectional area of the undeformed penetrator and  $A$  is the current cross-sectional area of the mushroom.

#### Previous Pressure Analysis

The average pressure on the penetrator tip,  $P$ , can be varied by considering various pressure profiles. In Jones, et al (1987) and Wilson, et al (1989), the pressure was assumed to be uniform across the mushroom face. The intensity of the pressure was assumed to be the solution of the modified Bernoulli equation. This equation, from Tate (1967, 1969) and Alekscevskii (1966), is applied at steady state and relates pressure on the axis of the specimen at the penetrator tip,  $p_a$ , to the undeformed section speed  $v$ , the penetration velocity  $u$ , and material properties of the target and penetrator. The modified Bernoulli equation is

$$p_a = \frac{1}{2} \mu^2 \rho u^2 + R_t = \frac{1}{2} \rho (v - u)^2 + Y_p \quad (4)$$

where  $R_t$  and  $Y_p$  are dynamic yield strengths of the target and penetrator at suitably high strain rates respectively, and  $\mu^2$  is the ratio of the target to penetrator density.

Gillis, et al. (1990) suggested that the uniform pressure profile was not realistic and proposed a parabolic form, which was symmetric about the axis of the specimen and zero on the edge of the mushroom. In this case, the pressure  $p$  had the form

$$p = p_a (1 - \frac{r^2}{R^2}) \quad (5)$$

where  $p_a$  is the current pressure on the rod axis,  $R$  is the original rod radius, and  $r$  is the radial distance from the axis. The factor  $(1+e)$  in the denominator of the pressure term in (1) forces the pressure to act over the deformed mushroom face with area  $A$ , even though (5) refers to the original rod configuration.

The average pressure  $P$  can be computed, in general, by

$$P = \frac{1}{A_i A_i} \int p dA_i \quad (6)$$

When  $P$  was calculated for (5), the result was  $\frac{p_a}{2}$ . The predictions for penetration depths were somewhat improved over the previously assumed uniform pressure distribution. The results still suffered from ignoring the initial and final transients in the penetration event. This parabolic pressure distribution effectively reduced the parabolic nature of (4) by a factor of two. Although this improved the model by reducing the effect of (4), the addition of at least an initial transient seemed warranted.

In Cinnamon, et al. (1992a,b), the pressure distribution was generalized to the form

$$p = p_a (1 - \frac{r^2}{R^2})^n \quad (7)$$

which made the average pressure term become

$$P = \frac{p_a}{(n+1)} \quad (8)$$

This new pressure distribution was successfully employed with an initial transient phase to correlate to a large number of experimental cases. The pressure exponent  $n$  was found to be a direct function of target strength. Although this approach provided improved results over previous approaches, the analysis could not be successfully extended beyond 3 km/s.

Jones, et al. (1993) attempted to correct the problem by adding a uniform component to the pressure profile. The distribution had the form

$$p = q + (p_a - q)(1 - \frac{r^2}{R^2})^n \quad (9)$$

and the average pressure became

$$P = \frac{nq}{(n+1)} + \frac{p_a}{(n+1)} \quad (10)$$

This new pressure profile improved results slightly and extended them into the hypervelocity range (3 - 6 km/s). However,  $q$  and  $n$  were not successfully correlated to any physical parameters.

In this paper, another approach to the determination of the average pressure will be explored and a successful correlation to target strength will be presented. In addition, the widest possible body of available data will be used in the correlation.

#### Transient Penetration Analysis

In Cinnamon, et al. (1992a,b), an initial transient phase of penetration was added to the model. The transient phase is characterized by impact shock effects and complete mushroom growth which occurs between impact and the beginning of steady state penetration. We assume that the penetrator impacts the target at a known velocity,  $v_0$ , of sufficient magnitude (i.e.  $v_0 > 1$  km/s) such that the undeformed section cannot sustain any appreciable deceleration (i.e.  $\dot{v} \equiv 0$ ) during the initial transient. This means

that  $v = v_0$  throughout the transient or mushrooming phase of penetration. During the initial transient, the mushroom develops from a cross-sectional area  $A_0$  at impact to  $A_1$ , when steady state begins. The mushroom retains an area of  $A_1$  throughout the steady state portion of the penetration process until the end of the event.

Ravid, *et al.* (1990) reported that there was little change in penetration velocity  $u$  during the shock/impact stage of the initial transient phase. Motivated by this observation, we assumed that the penetration velocity was approximately constant (i.e.  $u = u_0$ ) throughout the initial transient. Hence, (1) becomes

$$\dot{\ell}(v_0 - u_0) = \frac{-P}{\rho(1+\epsilon)} \quad (11)$$

and (2) is modified to

$$\epsilon \dot{\ell} = v_0 - u_0 \quad (12)$$

These two equations, (11) and (12), govern the mushrooming of the rod during the initial transient phase of the penetration event - which precedes the steady state. At impact, the engineering strain in the mushroom is  $\epsilon_0$ . When steady state is reached, the strain becomes  $\epsilon_1$ .

By eliminating  $\dot{\ell}$  between (11) and (12) and solving for  $\epsilon$ , we arrive at an expression for the engineering strain.

$$\epsilon = \frac{-(v_0 - u_0)^2}{(v_0 - u_0)^2 + \frac{P}{\rho}} \quad (13)$$

This relationship provides us with an explicit formula for the strain in the mushroom as it develops during the transient phase. This equation governs the behavior until the beginning of the steady state penetration phase. The pressure on the axis,  $p_a$ , is changing rapidly during mushroom formation. It has a large value,  $p_0$ , at impact and a reduced value,  $p_1$ , at steady state.

When steady state is reached, we assume that the modified Bernoulli Equation, (4), is valid. At the transition point between the transient and steady state portions of the event, (4) can be expressed as

$$p_1 = \frac{1}{2} \mu^2 \rho u_0^2 + R_t = \frac{1}{2} \rho (v_0 - u_0)^2 + Y_p \quad (14)$$

and (13) can be written as

$$\epsilon_1 = \frac{-(v_0 - u_0)^2}{(v_0 - u_0)^2 + \frac{P_1}{\rho}} \quad (15)$$

where  $P_1$  is the average pressure on the penetrator tip at the beginning of steady state.

Equation (14) can then be used to solve for  $u_0$  in terms of the known quantities  $v_0$ ,  $\rho$ ,  $\mu^2$ ,  $R_t$  and  $Y_p$ . The remaining variable in the system of equations is  $P_1$ . The determination of  $P_1$  is the primary focus of this paper.

The penetration velocity  $u_0$  can be found algebraically from (14). The three primary cases are outlined below. For equal penetrator and target dynamic yield strength (i.e.  $R_t = Y_p$ ) and equal densities (i.e.  $\mu^2 = 1$ ),  $u_0$  reduces to

$$u_0 = \frac{1}{2} v_0 \quad (16)$$

For unequal penetrator and target dynamic yield strength (i.e.  $R_t \neq Y_p$ ) and equal densities (i.e.  $\mu^2 = 1$ ),  $u_0$  becomes

$$u_0 = \frac{\rho v_0^2 + 2(Y_p - R_t)}{2 \rho v_0} \quad (17)$$

In the general case,  $u_0$  is given by

$$u_0 = \frac{-v_0}{\mu^2 - 1} + \frac{1}{\rho(\mu^2 - 1)} \left[ \rho^2 v_0^2 - 2\rho(\mu^2 - 1)(R_t - Y_p - \frac{1}{2} \rho v_0^2) \right]^{\frac{1}{2}} \quad (18)$$

In each of these cases, then,  $u_0$  can be determined algebraically from known material properties and impact conditions. This leaves  $\epsilon_1$  in (15) as a function of known parameters and the average pressure on the penetrator tip at steady state.

#### Impact Conditions

The model outlined above also provides some information about conditions at impact. The strain on impact  $\epsilon_0$  can be calculated from (13) if we know the average pressure on the penetrator tip at impact,  $P_0$ .

$$\epsilon_0 = \frac{-(v_0 - u_0)^2}{(v_0 - u_0)^2 + \frac{P_0}{\rho}} \quad (19)$$

The impact pressure can be estimated from elementary shock physics, using

$$p_0 = \rho u_s u_0 \quad (20)$$

where  $u_s$  is the shock speed in the target. Values for  $u_s$  as a function of  $u_0$  can be found in shock Hugoniot tables, e.g. [16]. Calculation of  $P_0$  from a known value of  $p_0$  can typically be accomplished using the same approach as the calculation of  $P_1$  from  $p_a$ .

#### Cratering Analysis

The mathematical model for the behavior of the penetrator is a rigid-plastic, instantaneously eroding rod model. As a result, the penetrator enters the target with some impact engineering strain  $\epsilon_0$  that expands to  $\epsilon_1$  during the transient. The impact pressure  $p_0$  is usually very high relative to the steady state pressure  $p_1$ . Although

this pressure decreases rapidly during mushroom formation in the transient phase, the values for  $p_0$  can be significant. The mushroom diameter grows from the time of impact through the transient phase, and ceases at the beginning of the steady state portion of the event. The shock/impact stage takes place in a period of a few microseconds (Ravid, et al (1990)).

The instantaneous erosion assumption prevents the model from accounting for any additional erosion of the target - which occurs in actual practice. There is typically appreciable change in target geometry due to penetrator and target material ejection from the crater. As a consequence, the recovered targets will appear to have more cylindrical-type craters than the model would predict. Figure 2 illustrates the crater predicted by the mathematical model, and Figure 3 indicates how the actual geometry frequently appears.

#### Penetration Analysis

Predicting penetration depths from the above model is made possible through the use of a somewhat empirical approach. For a number of years, researchers have observed a significant correlation between crater volume in the recovered targets and impact kinetic energy, e.g. Murphy (1987). This relationship appears to be linear for impact cases of sufficient, but not excessively, high energy and can be expressed in the form

$$V_c = a E_0 + b \quad (21)$$

where  $V_c$  is the crater volume,  $E_0$  is the impact kinetic energy and is equal to  $\frac{1}{2} \rho A_i L v_0^2$ , and the variables  $a$  and  $b$  are regression constants determined from the available experimental data. The linear fit is performed for each shot combination.

These crater volume/kinetic energy relationships are computed from data points for a particular shot combination. The reliability of the linear fit is, of course, a function of the number of data points available. Since most experimental tests are quite expensive, frequently the data is sparse and/or somewhat scattered. When the linear fit predicts cratering at zero impact kinetic energy, or in some other way reflects erroneous trends, the usefulness of the

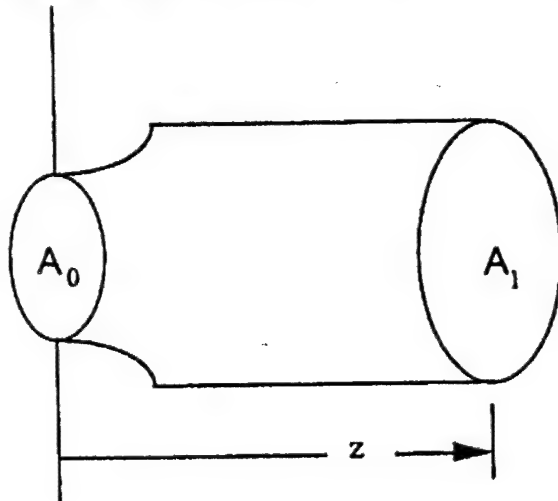


Figure 2. Idealized Crater Geometry  
 $A_0$  and  $A_1$  are the cross-sectional areas at impact and at steady state respectively.  $z$  is the penetration depth.

particular case is significantly reduced. This phenomenon is typically avoided by a sufficient number of experimental points. The accuracy of the penetration prediction is extremely dependent on the crater volume/kinetic energy relationship arrived at using this technique.

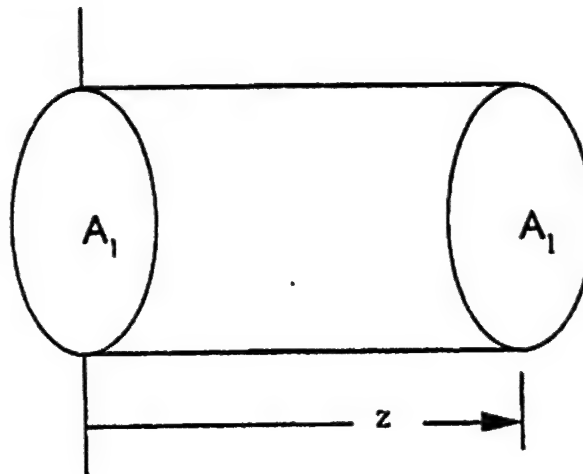


Figure 3. Actual Crater Geometry  
 $A_1$  is the observed crater cross-sectional area. The crater is assumed cylindrical with altitude  $z$ .

By adopting the cylindrical approximation for the crater geometry discussed above, we can generate predictions for the penetration depths. Because of the ejection of material from the crater, the cross-sectional area of the recovered target hole,  $A_1$ , will be

$$A_1 = \frac{A_1}{(1 + e_1)} \quad (22)$$

The crater volume can be expressed as

$$V_c = A_1 z \quad (23)$$

where  $z$  is the penetration depth. The penetration depth can be predicted by applying the crater volume/kinetic energy relationship to  $V_c$ . From (21) and (23),  $z$  is given by

$$z = \frac{1}{A_1} (1 + e_1) V_c = \frac{1}{A_1} (1 + e_1) (a E_0 + b) \quad (24)$$

Thus, the penetration depth can be expressed as an algebraic function of known material properties and impact conditions, and as a function of the average pressure on the penetrator tip at steady state.

#### CURRENT PRESSURE PROFILE ANALYSIS

In the previous work outlined above, it was noted that one of the primary difficulties in achieving good predictions for the crater characteristics was the manner in which the modified Bernoulli

Equation (4) predicted pressure as a function of  $u$  and  $v$ . The parabolic nature of (4) tended to over-predict penetration depths for the higher velocity cases (3 - 6 km/s). Earlier successes, particularly in the intermediate velocity range (1 - 3 km/s), were the result of pressure distributions that tended to reduce the effect of (4). In this paper, additional pressure distribution analysis is performed to address this problem.

#### Previous Pressure Distributions

An obvious departure point for the attempt to improve the one-dimensional analysis and extend it into the hypervelocity range was to begin with the previous pressure distributions. A great body of additional experimental data became available in Anderson, et al (1992) that expanded the range of materials, greatly increased the number of shot combinations accessible for analysis, and provided data in the hypervelocity range. The pressure profiles detailed in (7) and (9) were examined for possible application in these new cases.

The distribution in (7) was unable to compensate for the parabolic nature of (4) while maintaining accuracy in the intermediate velocity ranges if  $n$  was considered a constant as it was in Cinnamon, et al (1992a,b). Attempts to model  $n$  as a function of material properties or impact conditions were not successful. In general, it was observed that  $n$  needed to increase with impact velocity to essentially cancel the effects of the modified Bernoulli Equation. The distribution in (9) followed the same trend. Although the results improved, the net effect was to choose  $n$  and  $q$  to counter the dramatic pressure increase dictated by equation (4).

#### New Pressure Distribution

To attempt to find a solution to this dilemma, a new, more general, pressure distribution was proposed. The pressure profile takes the form

$$p = q + (p_s - q) \left(1 - \left(\frac{r}{R}\right)^m\right)^n \quad (25)$$

This profile is a more complex and versatile one. A great deal of additional control over the shape of the pressure distribution was provided by (25). The average pressure then is given by

$$P = q + 2(p_s - q) \frac{\Gamma(\frac{2}{m})\Gamma(1+n)}{m\Gamma(1+\frac{2}{m}+n)} \quad (26)$$

where  $\Gamma$  is the well known mathematical gamma function.

As a significant number of cases were examined, it became increasingly clear that in order to achieve the desired trends in the theoretical penetration curves,  $n$  and  $m$  were chosen in such a way as to essentially eliminate the effect of the second term in (26). That is, an average pressure comprised of a single value,  $q$ , which was unvarying over the range of impact velocities, achieved the best results. This discovery matched our previous experience with (7) and (9). Apparently, the magnitude and trends in the pressures predicted by the modified Bernoulli Equation were not leading to acceptable results. All previous successes were based on choices that reduced or eliminated the contribution of the velocity dependent axial pressure in (4) to the value of  $P_1$ .

#### Revised Average Pressure Approach

With the results described above, another approach was required. It became clear that the previous calculation of the average

pressure at steady state,  $P_1$ , was not acceptable. To simplify the analysis, the connection of  $P_1$  to a particular pressure distribution is ignored.

The problem is further simplified by the fact that the desired trends in the penetration depths result from a constant value for  $P_1$  over the entire velocity range.

This approach does not imply that the pressure distributions have the same shape for differing velocities, or that  $p_a$  is equivalent for all velocities, simply that the value of  $P_1$  is constant for a particular shot combination over all impact velocities.

#### **RESULTS**

When  $P_1$  was assumed to be some constant average pressure on the penetrator tip independent of  $v_0$ , defined here to be  $Q$ , for all impact velocities in a particular shot combination, the results of this model improved tremendously. The penetration depth theoretical curves adopted the trends present in the experimental data (i.e. penetration depths leveling off as velocity increases toward 6 km/s). In addition, the values for  $Q$  that yielded the best results correlated strongly to target strength.

In order to establish the most credible and most complete correlation possible, all available data were employed. As a consequence, this paper includes a large number of representative figures. In order for this theory to be applied effectively, experimental data sets must have included crater diameters. A number of the cases in Anderson, et al (1992) did not provide this information. In addition, a minimum of two data points was required to construct the crater-volume/kinetic energy relationship. Hence, some other cases could not be evaluated. With those limitations in mind, the author applied all readily available cases to this model and reports the results.

Table 1 summarizes all the cases and provides essential data about each shot combination. The figure numbers referred to can be found in this paper. The figures shown are representative of the entire body of data. One figure number is assigned to each shot combination shown. The crater volume/kinetic energy relationship used to generate the penetration depths appears in Table 2. In some cases (as indicated in Table 2), the relationship was modified by removing certain data points that appear erroneous or that skewed the general trend. When these points are removed, the relationship changes - which modifies the resulting penetration curve. Of course this does not alter the strain curve in any way. The entire data set, with both modified and unmodified curves for all cases, appears in Cinnamon (1992 a,b).

The figures show theoretical curves superimposed on discrete experimental points. The upper curve in the strain vs. impact velocity figures represents the estimate for  $v_0$ .

When these cases were evaluated, a certain value for  $Q$  could be chosen to match the experimental data. This  $Q$  was found to strongly correlate to target strength. Table 3 reports each of the different targets present in the data and their corresponding  $Q$  value.

With this information, it was immediately evident that some strong relationship existed between  $Q$  and target strength. Figure 4 depicts the values for  $Q$  chosen to allow the model to predict penetration depths and crater diameters accurately against  $R_t$ . A curve is fit through the data to both illustrate the correlation and provide a functional relationship between  $Q$  and  $R_t$ . The best fit is

$$Q = 3.8 (1 - e^{(-0.00135 R_t)}) - 0.8 \quad (27)$$

With  $Q$  as a direct function of target strength, this one-dimensional penetration model can be expressed in terms of known material properties and impact conditions. The crater volume/kinetic energy curve is still needed to allow for the calculation of penetration depths, however.

To place this revised model into context with regard to those used previously, Figures 5 and 6 are presented. These figures

illustrate the comparative results between these three different approaches to the calculation of the average pressure at steady state.

Table 1. Experimental Data Summary

Fig. #	Penetrator	$\gamma_p$ (MPa)	$\rho_q$ $\frac{\text{kg}}{\text{m}^3}$	L (mm)	$\frac{L}{D}$	Target	$R_t$ (MPa)	$\mu^2 \rho$ $\frac{\text{kg}}{\text{m}^3}$	Ref.
7	Alum Alloy	200	2700	63.5	10	Lead	200	11200	Tale
	1100-O Al	250	2720	9.525	3	1100-O Al	250	2720	Christ. & Gehr.
	2024-T3 Al	675	2770	9.525	3	1100-O Al	230	2720	Christ. & Gehr.
	7075-T6 Al	600	2804	9.525	3	1100-O Al	230	2720	Christ. & Gehr.
	CT015 St.	600	7600	9.525	3	1100-O Al	250	2720	Christ. & Gehr.
8	Soft 4340	1263	7850	31.75	5	2024-T4 Al	400	2770	Wilson, et al
	7075-T6 Al	600	2804	31.75	5	2024-T4 Al	400	2770	Wilson, et al
	Hard 4340	1826	7850	31.75	5	7075-T6 Al	600	2804	Wilson, et al
	Soft 4340	1263	7850	31.75	5	7075-T6 Al	600	2804	Wilson, et al
	7075-T6 Al	600	2804	31.75	5	7075-T6 Al	600	2804	Wilson, et al
	1100-O Al	250	2720	9.525	3	CT015 St.	600	7600	Christ. & Gehr.
	2024-T3 Al	675	2770	9.525	3	CT015 St.	600	7600	Christ. & Gehr.
	7075-T6 Al	600	2804	9.525	3	CT015 St.	600	7600	Christ. & Gehr.
	CT015 St.	600	7600	9.525	3	CT015 St.	600	7600	Christ. & Gehr.
	4340 Steel	1600	7810	68.58	18	6061-T651 Al	600	2710	Luk & Piekurowski
	1100-O Al	250	2720	9.525	3	2024-T3 Al	675	2770	Christ. & Gehr.
	1100-O Al	250	2720	9.525	3	304 St. St.	675	7900	Christ. & Gehr.
	2024-T3 Al	675	2770	9.525	3	2024-T3 Al	675	2770	Christ. & Gehr.
	2024-T3 Al	675	2770	9.525	3	304 St. St.	675	7900	Christ. & Gehr.
	CT015 St.	600	7600	9.525	3	2024-T3 Al	675	2770	Christ. & Gehr.
	CT015 St.	600	7600	9.525	3	304 St. St.	675	7900	Christ. & Gehr.
9	304 St. St.	675	7900	9.525	3	2024-T3 Al	675	2770	Christ. & Gehr.
	304 St. St.	675	7900	9.525	3	304 St. St.	675	7900	Christ. & Gehr.
	C110W1	1200	7850	25	10	St37	750	7850	Hohler, et al
10	C110W1	1200	7850	43	10	St37	750	7850	Hohler, et al
	C110W1	1200	7850	54	10	St37	750	7850	Hohler, et al
	C110W1	1200	7850	25	10	St52	850	7850	Hohler, et al
	C110W1	1200	7850	43	10	St52	850	7850	Hohler, et al
	C110W1	1200	7850	54	10	St52	850	7850	Hohler, et al
11	DI7	2500	17000	28	10	St52	850	7850	Hohler, et al
	DI7	2500	17000	60	10	St52	850	7850	Hohler, et al
	C110W2	1100	7850	58	10	H2B,A	850	7850	Hohler, et al
	Marag St	1000	7850	58	10	H2B,A	850	7850	Hohler, et al
	Marag St	1000	7850	116	20	H2B,A	850	7850	Hohler, et al
	35CrNiMo	2200	7850	54	10	H2B,A	850	7850	Hohler, et al
	Elmet	2000	15500	58	10	H2B,A	850	7850	Hohler, et al
	DI7K	2500	17300	58	10	H2B,A	850	7850	Hohler, et al
	DI7	2500	17000	58	10	H2B,A	850	7850	Hohler, et al
	W	2500	19300	60	10	H2B,A	850	7850	Hohler, et al
	W75	2500	15500	58	10	H2B,A	850	7850	Hohler, et al
	W90	2500	17000	58	10	H2B,A	850	7850	Hohler, et al
	DI8	2500	18000	58	10	H2B,A	850	7850	Hohler, et al
	H011	2000	14500	58	10	H2B,A	850	7850	Hohler, et al
	DI7.6	2000	17600	41.7	10	H2B,A	850	7850	Hohler, et al
	DI7.6	2000	17600	58	10	H2B,A	850	7850	Hohler, et al
12	Steel	1600	7850	58	10	H2B,A	850	7850	Hohler, et al
	DI7	2500	17000	116	20	H2B,A	850	7850	Hohler, et al
	DI8.5	2500	18500	58	10	H2B,A	850	7850	Hohler, et al
	H011	2000	14500	58	10	H2B,A	850	7850	Hohler, et al
	H601	1600	13500	60	10	H2B,A	850	7850	Hohler, et al

	11601	1600	13500	38	10	H2B,A	850	7850	Hohler, et al
	H701	1400	13500	60	10	H2B,A	850	7850	Hohler, et al
	11701	1400	13500	58	10	H2B,A	850	7850	Hohler, et al
	DT7.6	2000	17600	101.5	17.5	H2B,A	850	7850	Hohler, et al
	DT7.6	2000	17600	107.8	22	H2B,A	850	7850	Hohler, et al
	DT7.6	2000	17600	110.25	22.5	H2B,A	850	7850	Hohler, et al
	DT7.6	2000	17600	136.8	32	H2B,A	850	7850	Hohler, et al
13	DT7.6	2000	17600	163.2	32	H2B,A	850	7850	Hohler, et al
	Hard 4340	1826	7850	60	6	RHA	1000	7850	Wilson, exp. data
	OFHC Cu	300	8900	60	6	RHA	1000	7850	Cinnamon, et al
	Tantalum	500	16600	60	6	RHA	1000	7850	Cinnamon, et al
	Hard 4340	1826	7850	95.25	7.5	RHA	1000	7850	Cinnamon, et al
	Kenn W10	2300	17300	135.8	23	RHA	1000	7850	Silaby
	Kenn W10	2300	17300	121.75	23	RHA	1000	7850	Silaby
	DT7	2300	17000	28	10	WB	1000	7850	Hohler, et al
	U-3/411	7000	18600	266.7	20	RHA	1000	7850	Keald, et al
	W92.5	2500	17590	75	10	Ger RHA	1000	7850	Wilkins, et al
	Kenn W10	2300	17200	50	10	Ger RHA	1000	7850	Wilkins, et al
14	Teledy X27	2300	17330	78.74	10	RHA	1000	7850	Woolsey, et al
15	CT110W1	1200	7850	25	10	Ger Arm St	1100	7850	Hohler, et al
	CT110W1	1200	7850	43	10	Ger Arm St	1100	7850	Hohler, et al
	CT110W1	1200	7850	54	10	Ger Arm St	1100	7850	Hohler, et al
	DT7	2300	17000	28	10	Ger Arm St	1100	7850	Hohler, et al
	DT7	2300	17000	60	10	Ger Arm St	1200	7850	Hohler, et al
	DT7.6	2000	17600	17.4	3	Ger St	1200	7850	Hohler, et al
	DT7.6	2000	17600	29	3	Ger St	1200	7850	Hohler, et al
	DT7.6	2000	17600	42	10	Ger St	1200	7850	Hohler, et al
	Soft 4340	1263	7850	31.75	5	Soft 4340	1263	7850	Wilson, et al
16	7075-16 Al	600	2804	31.75	5	Soft 4340	1263	7850	Wilson, et al
17	Hard 4340	1826	7850	31.75	5	Soft 4340	1263	7850	Wilson, et al
	X21C	3500	17650	45.7	10	4340 Steel	1600	7810	Luk&Piekutowski
18	Teledy X27C	2300	17400	81.6	10	4340 Steel	1600	7810	Morris&Anderson
	Teledy X27C	2500	17400	81.6	15	4340 Steel	1600	7810	Morris&Anderson
	Hard 4340	1826	7850	63.5	10	Hard 4340	1826	7850	Wilson, et al
	Hard 4340	1826	7850	47.63	7.5	Hard 4340	1826	7850	Wilson, et al
	Hard 4340	1826	7850	47.63	5	Hard 4340	1826	7850	Wilson, et al
19	Hard 4340	1826	7850	31.75	5	Hard 4340	1826	7850	Wilson, et al
	Hard 4340	1826	7850	63.5	5	Hard 4340	1826	7850	Wilson, et al
	Hard 4340	1826	7850	31.75	3.33	Hard 4340	1826	7850	Wilson, et al
	Hard 4340	1826	7850	31.75	2.5	Hard 4340	1826	7850	Wilson, et al
	Soft 4340	1263	7850	31.75	5	Hard 4340	1826	7850	Wilson, et al
	OFHC Cu	300	8900	60	6	Hard 4340	1826	7850	Cinnamon, et al
	Tantalum	500	16600	60	6	Hard 4340	1826	7850	Cinnamon, et al
20	DT7	2300	17000	28	10	DT7	2500	17000	Hohler, et al

Table 2. Crater Volume/Kinetic Energy  
Relationship Used in Figures

Fig. #	a	b	Modified?
7	1.28233	-1405	Y
8	3.02053	-3545	N
9	1.91916	-240	N
10	0.39881	-850	Y
11	0.73457	-291	Y
12	0.17109	-538	N
13	0.90932	-19938	N
14	0.50125	-5403	Y
15	0.22431	-94	Y
16	0.12627	-764	N
17	0.30299	-884	N
18	0.39147	-2525	N
19	0.22845	-730	N
20	0.22239	-190	N

Table 3. Correlation of Q to Target Strength

Target Material	K <sub>t</sub> (MPa)	Q (GPa)
Lead	200	0.128
1100-O Al	250	0.28
2024-T4 Al	400	0.6
7075-T6 Al	600	1.05
CT015 Si	600	1.05
6061-T651 Al	600	1.05
2024-T3 Al	675	1.3
304 SL SL	675	1.3
Si37	750	1.4
Si32	850	1.7
H2B,A	850	1.7
RHA	1000	2.2
W8	1000	2.2
Ger RHA	1000	2.2
Ger Arm St	1100	2.275
Ger St	1200	2.35
Solt 4340	1263	2.4
4340 Steel	1600	2.5
Hard 4340	1826	2.6
DI7	2500	2.9

It is clear from the comparative figures (i.e. 5 & 6) that each subsequent theory lowered the average pressure in such a way as to lower the penetration and strain curves. This particular case that appears in Figures 5 and 6 was chosen for its higher velocity data and its presentation in Jones, et al (1993).

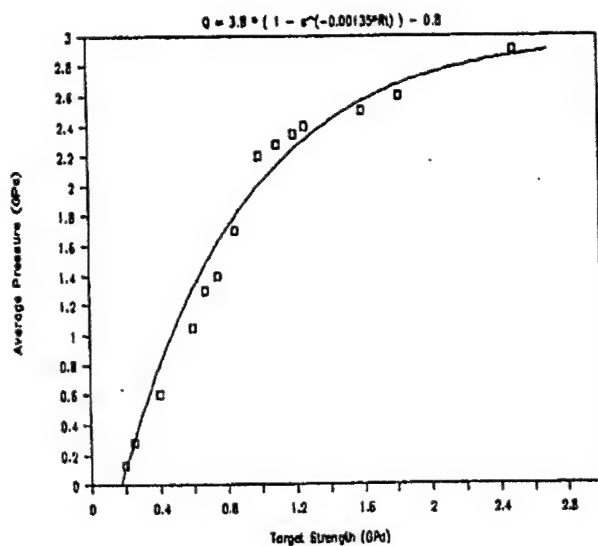


Figure 4. Average Pressure vs. Target Strength  
Q is the average pressure.

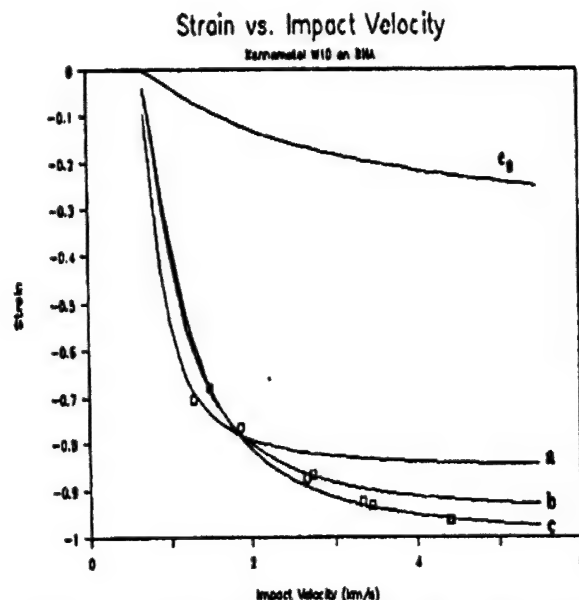


Figure 5. Comparative Case: Strain vs. Impact Velocity (km/s)  
(a) indicates results from Cinnamon, et al (1992a,b).  
(b) indicates results from Jones, et al (1993).  
(c) indicates current model.

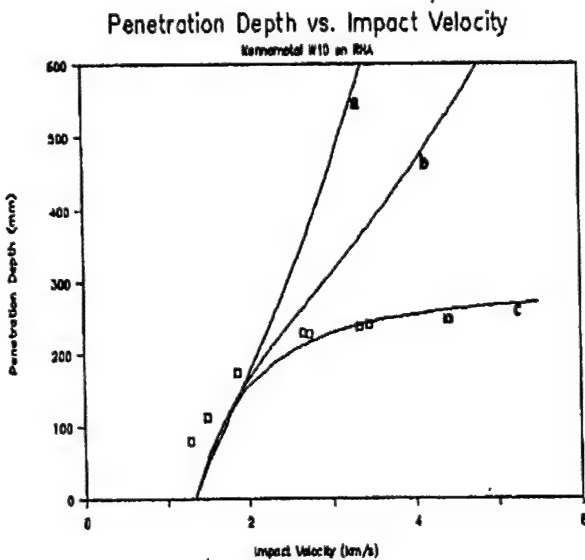
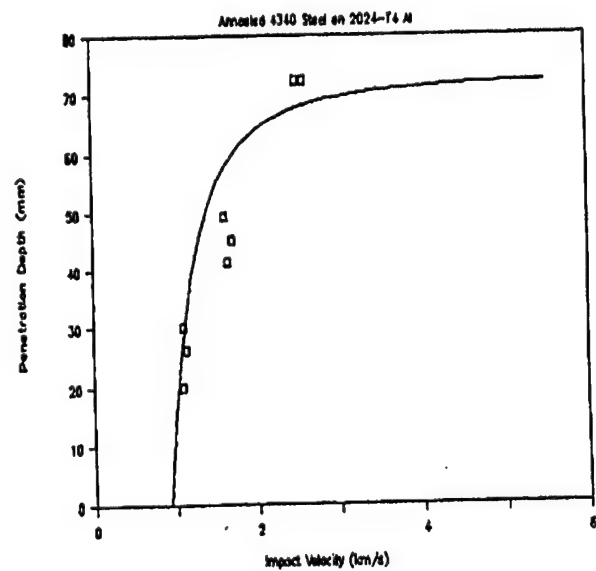
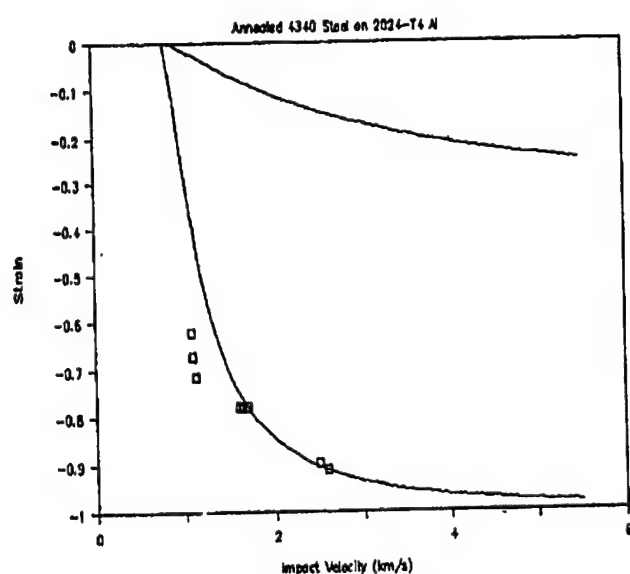
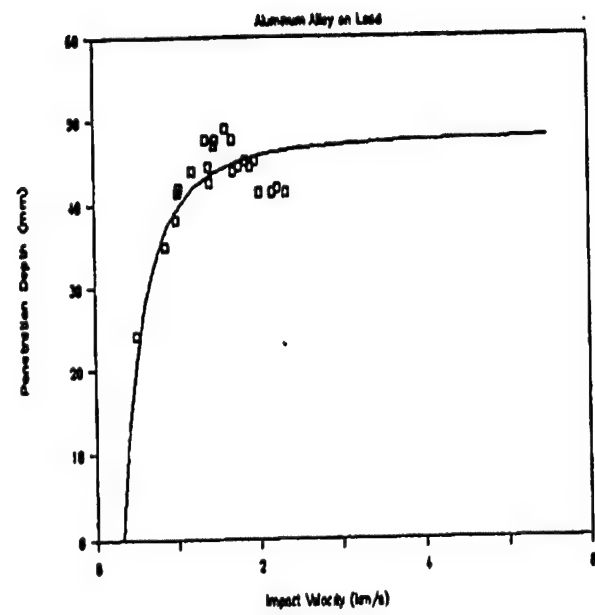
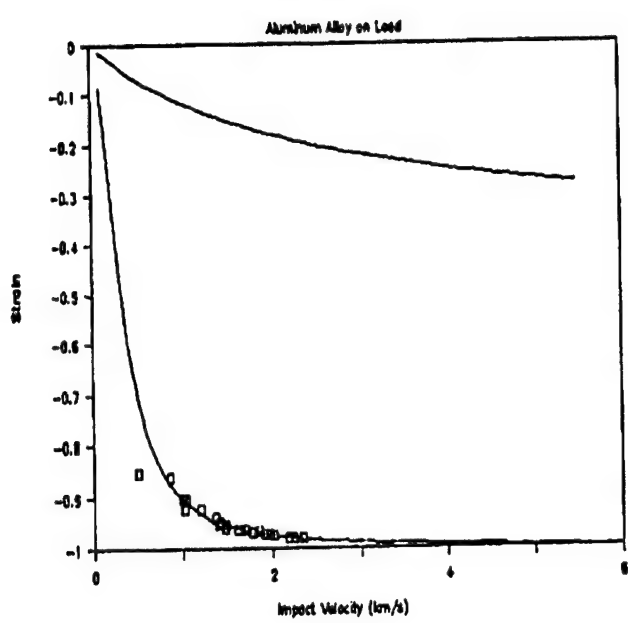


Figure 6. Comparative Case: Penetration Depth (mm) vs. Impact Velocity (km/s)  
(a) indicates results from [Cinnamon, et al (1992a,b)].  
(b) indicates results from Jones, et al (1993). (c) indicates current model



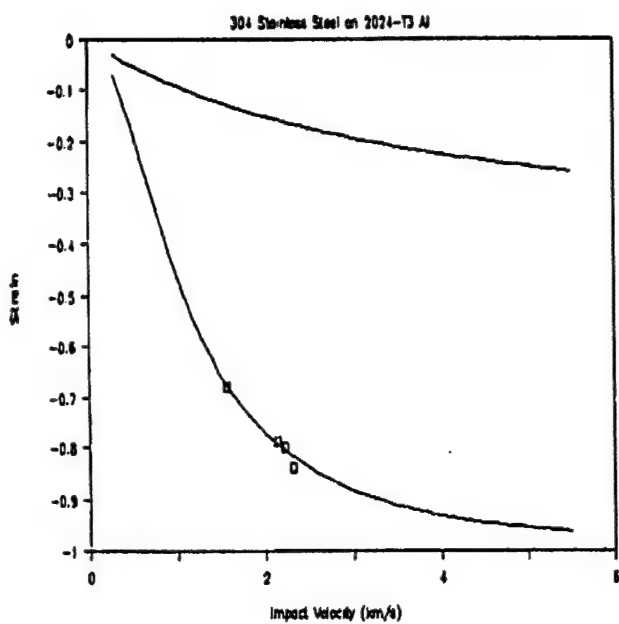


Figure 9a. Strain vs Impact Velocity (km/s)

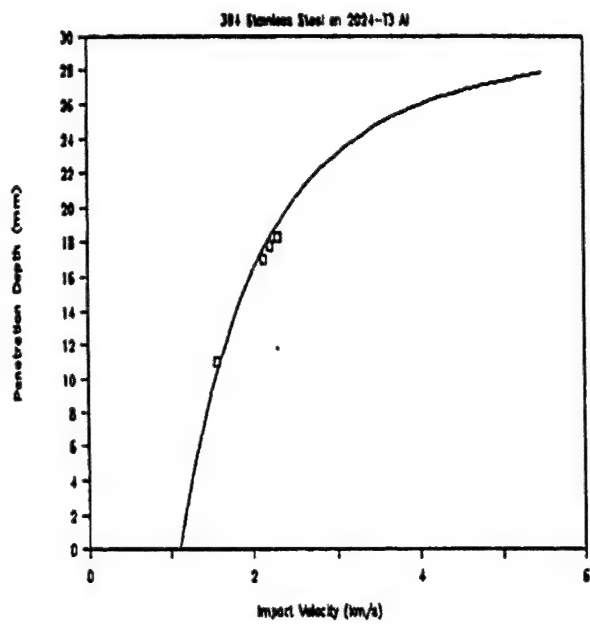


Figure 9b. Penetration Depth (mm) vs Impact Vel. (km/s)

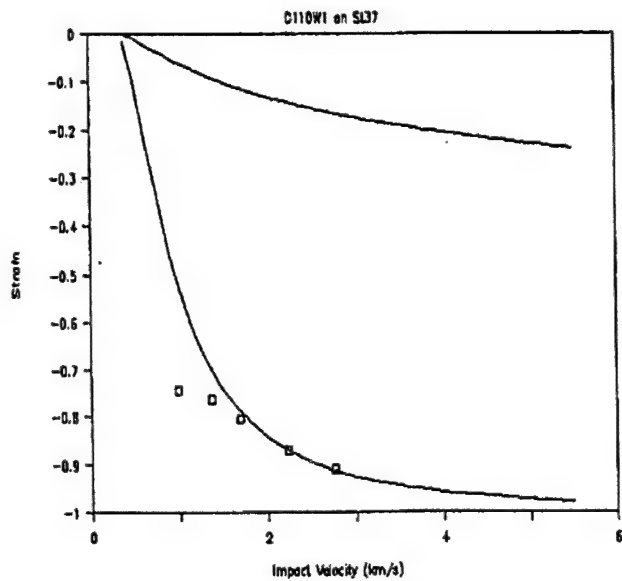


Figure 10a. Strain vs Impact Velocity (km/s)

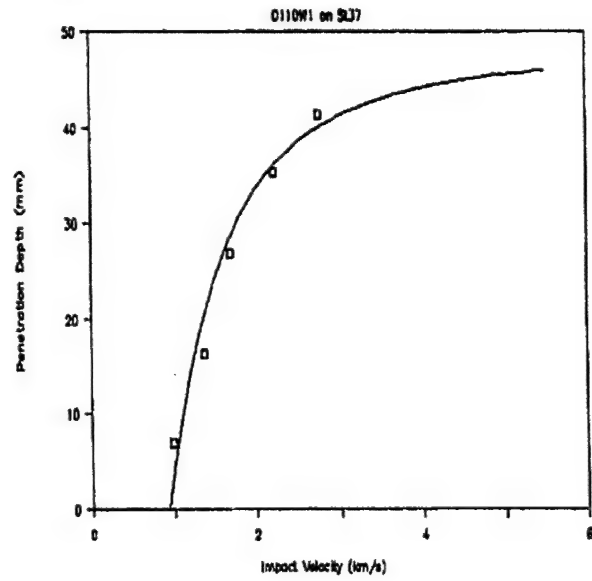


Figure 10b. Penetration Depth (mm) vs Impact Vel.(km/s)

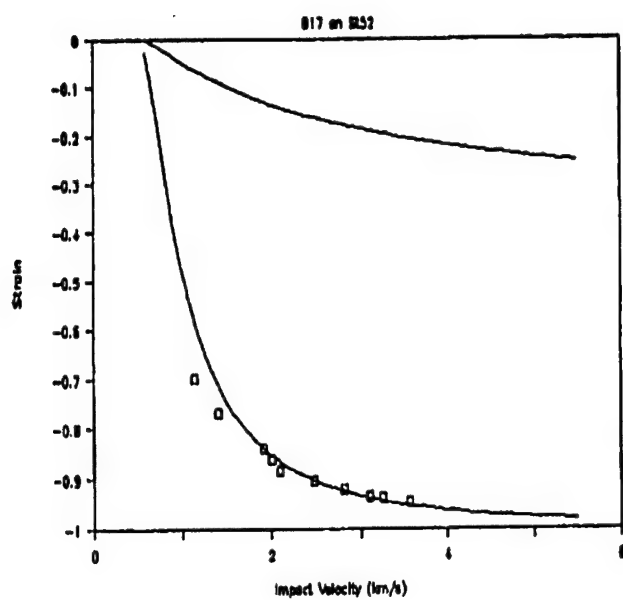


Figure 11a. Strain vs Impact Velocity (km/s)

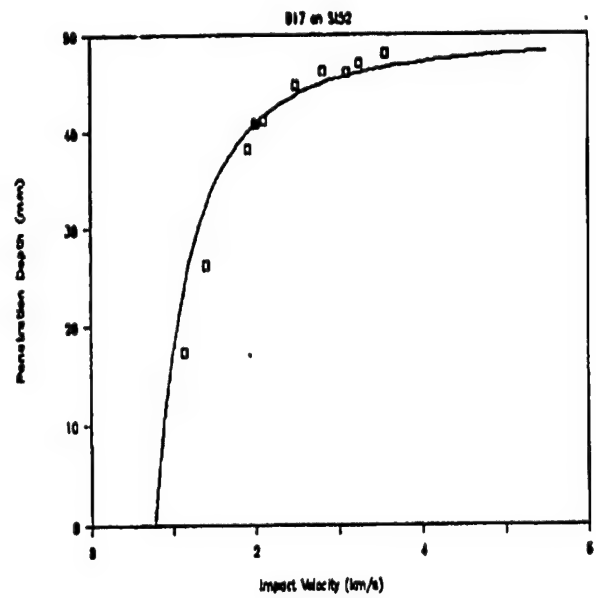


Figure 11b. Penetration Depth (mm) vs Impact Vel.(km/s)

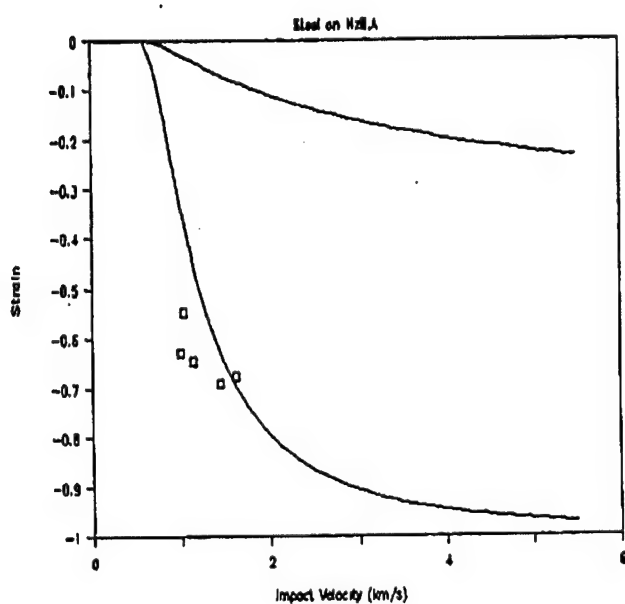


Figure 12a. Strain vs Impact Velocity (km/s)

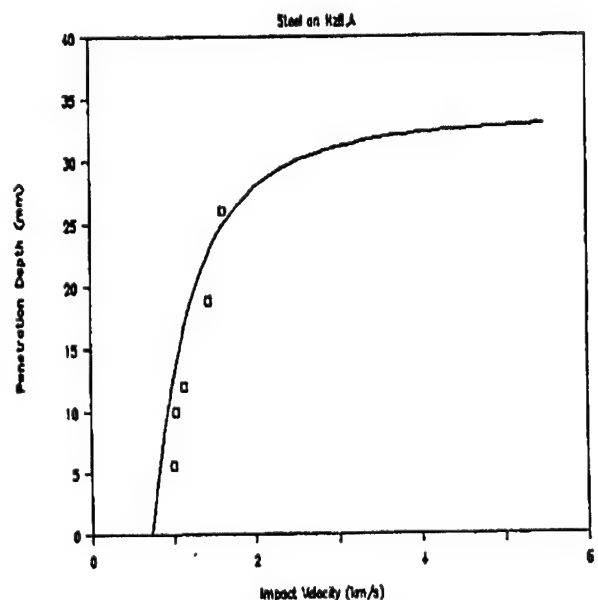


Figure 12b. Penetration Depth (mm) vs Impact Vel.(km/s)

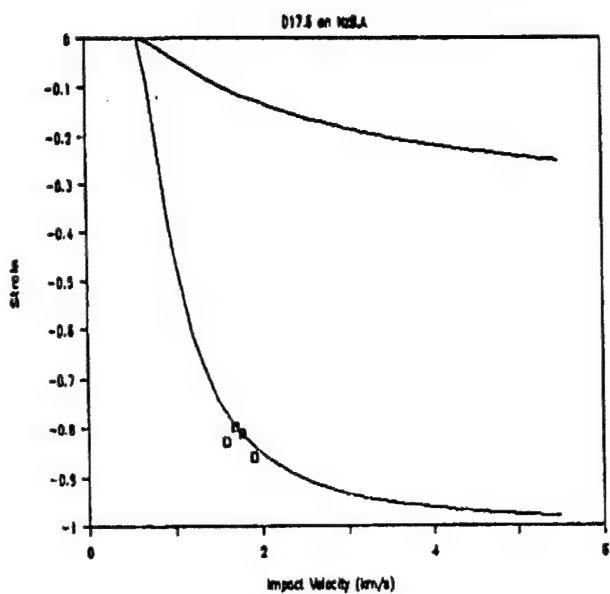


Figure 13a. Strain vs Impact Velocity (km/s)

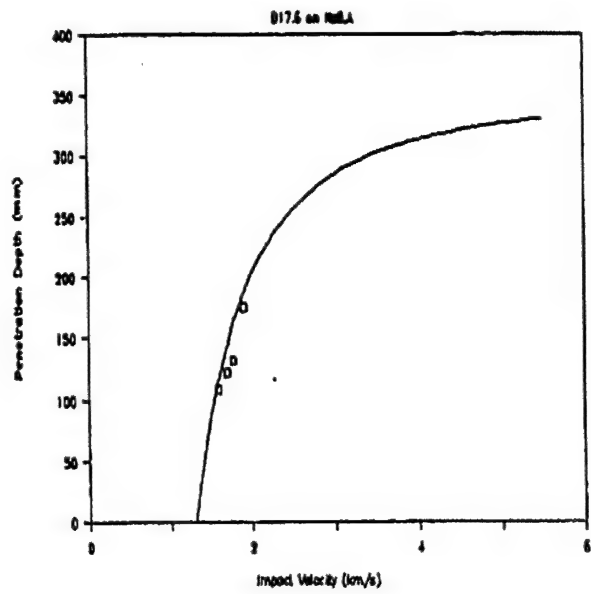


Figure 13b. Penetration Depth (mm) vs Impact Vel (km/s)

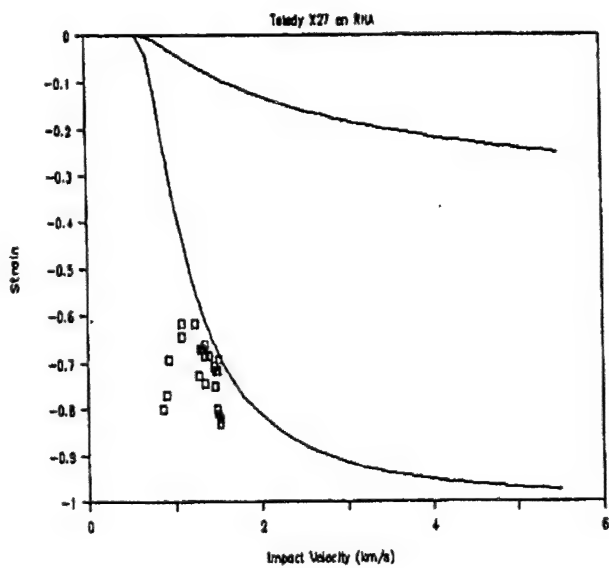


Figure 14a. Strain vs Impact Velocity (km/s)

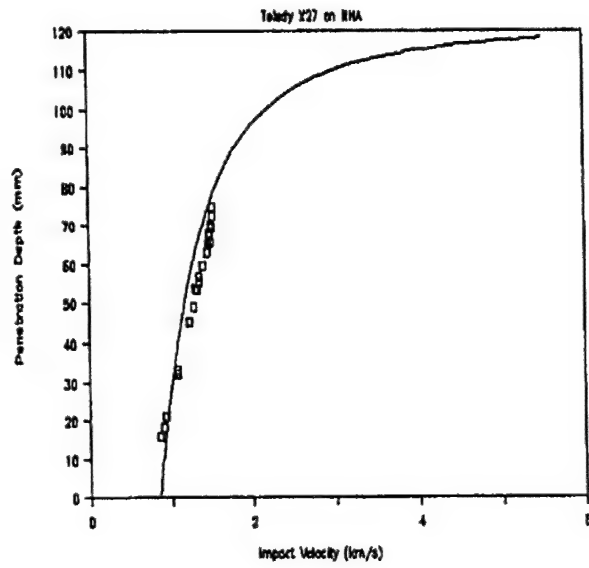
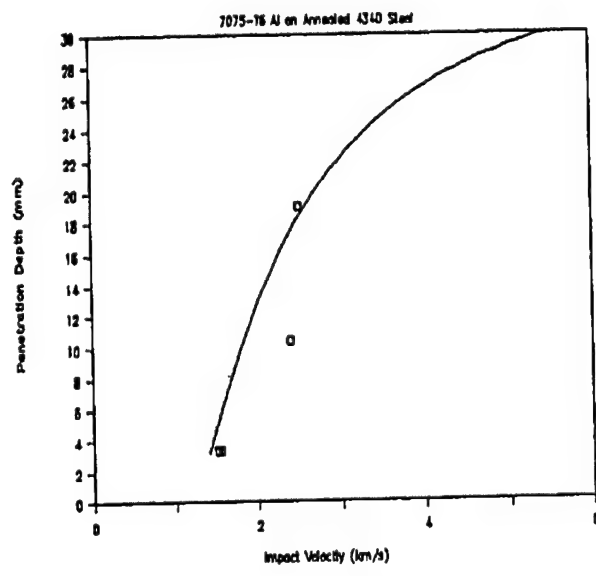
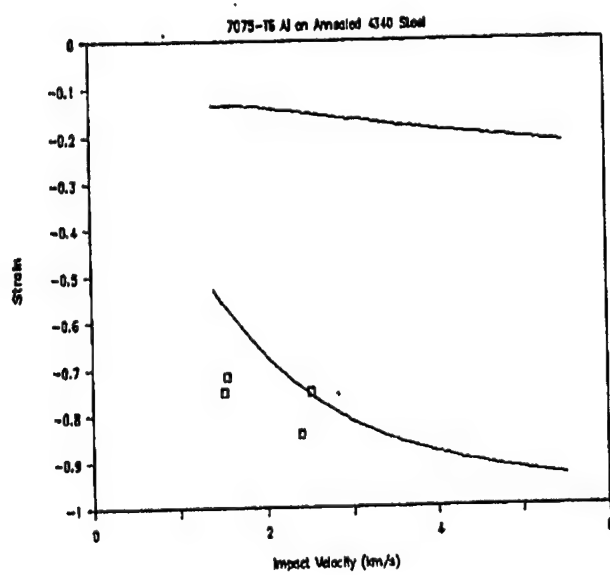
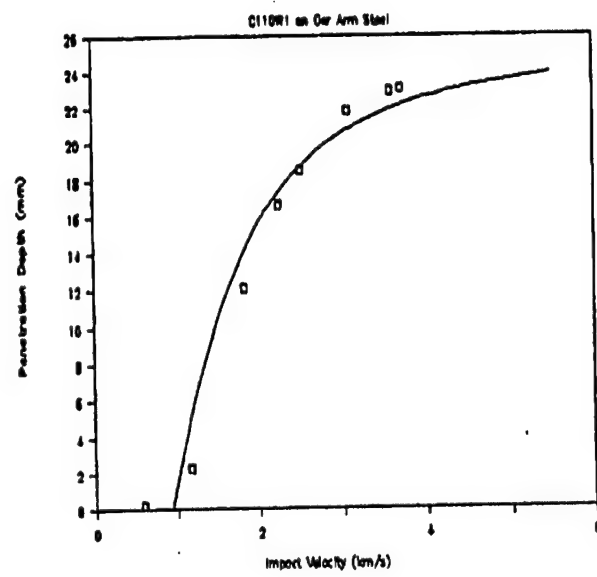
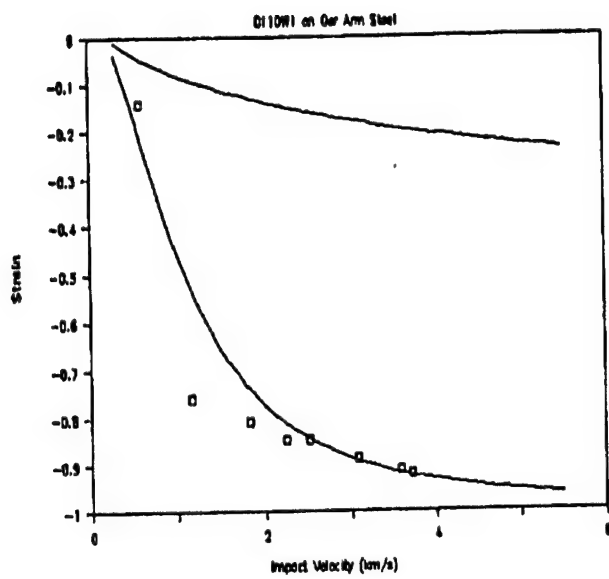


Figure 14b. Penetration Depth(mm) vs Impact Vel.(km/s)



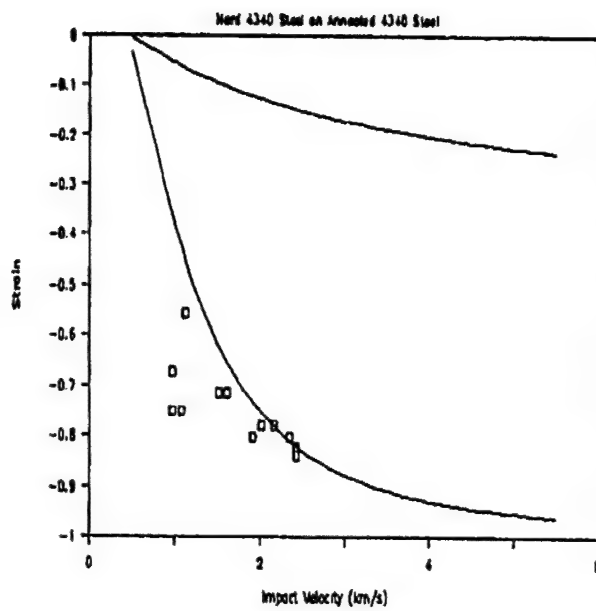


Figure 17a. Strain vs Impact Velocity (km/s)

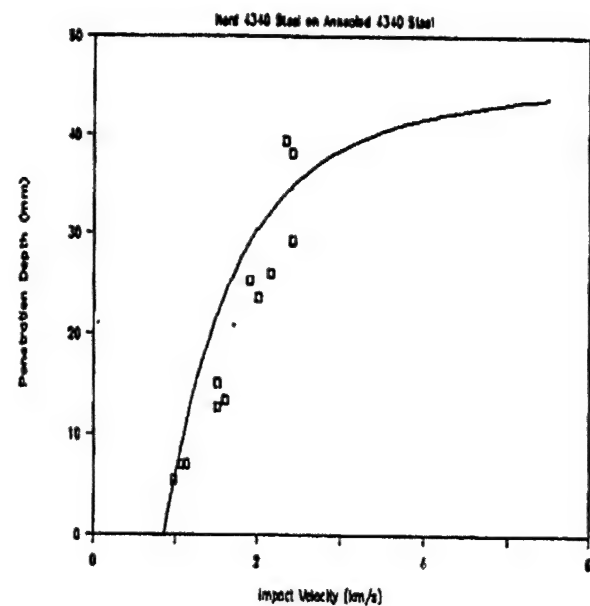


Figure 17b. Penetration Depth (mm) vs Impact Vel.(km/s)

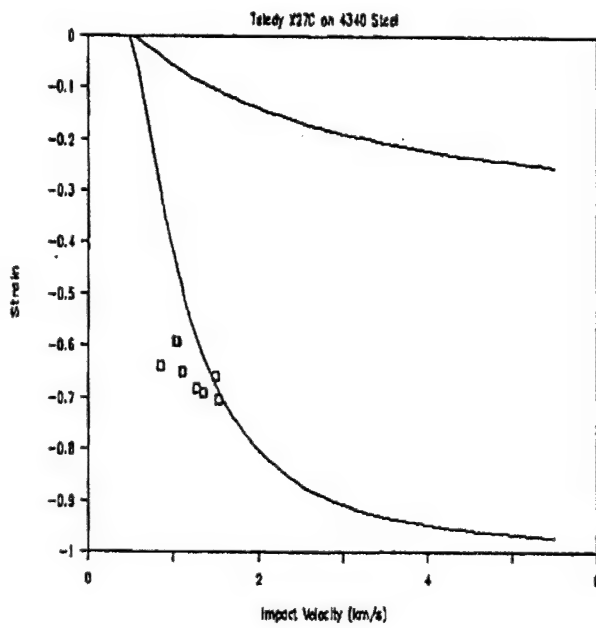


Figure 18a. Strain vs Impact Velocity (km/s)

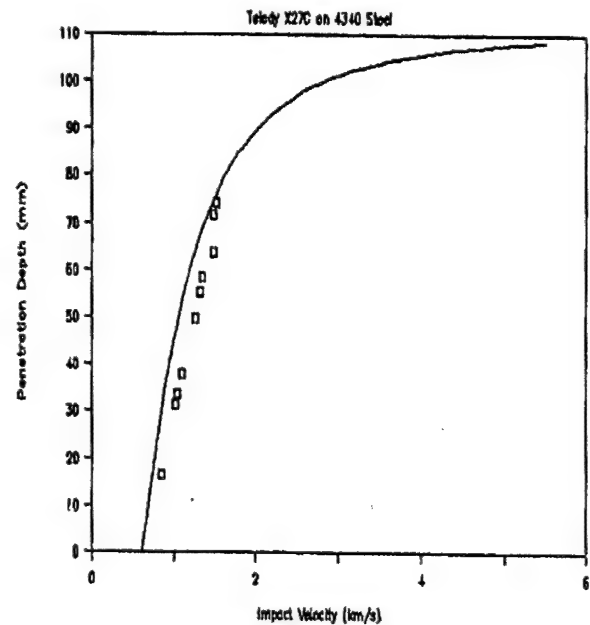


Figure 18b. Penetration Depth (mm) vs Impact Vel.(km/s)

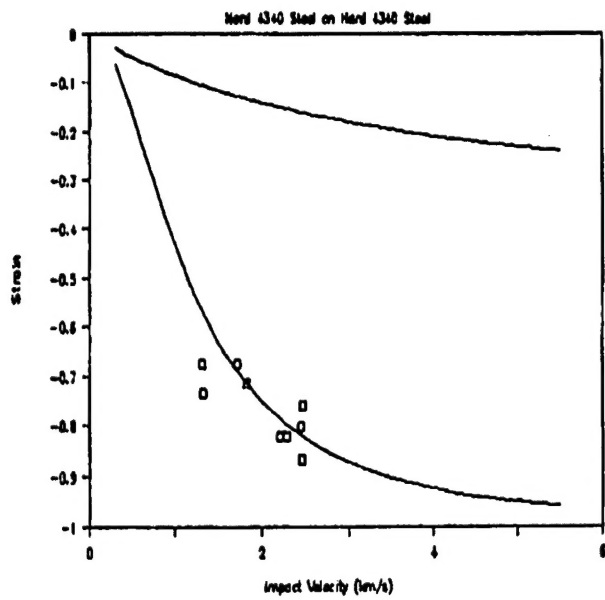


Figure 19a. Strain vs Impact Velocity (km/s)

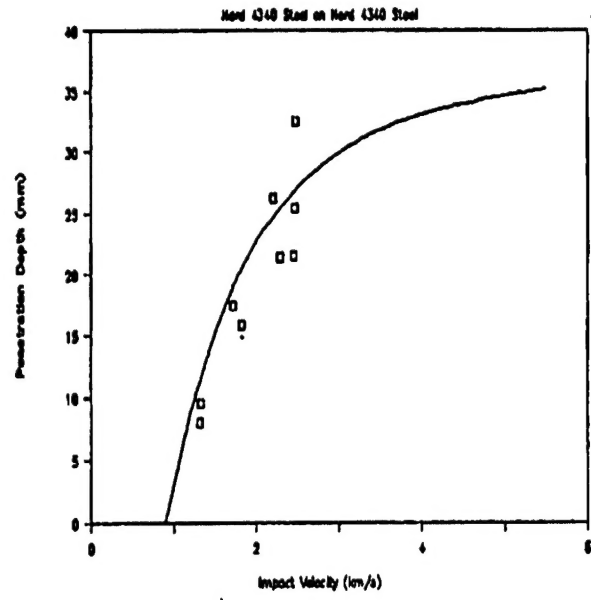


Figure 19b. Penetration Depth (mm) vs Impact Vel.(km/s)

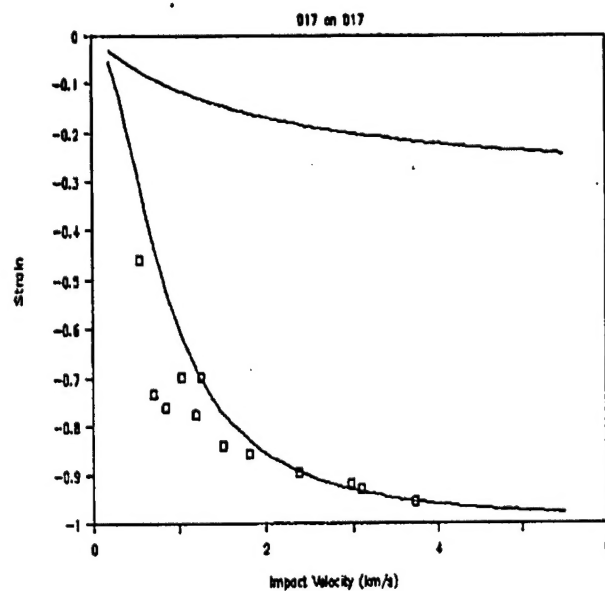


Figure 20a. Strain vs Impact Velocity (km/s)

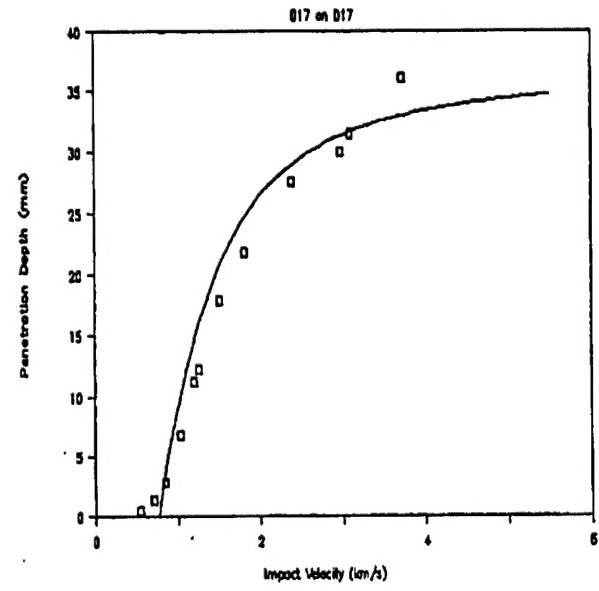


Figure 20b. Penetration Depth (mm) vs Impact Vel.(km/s)

## CONCLUSION

In this paper, a new one-dimensional model for the penetration of semi-infinite targets by long rods was developed. Its basis was the revision of the previous techniques employed to calculate the average pressure at steady state. The modified Bernoulli Equation appears to result in values for  $P_1$  that are simply too high for the impact cases in the hypervelocity range.

By correlating a new approach to a great body of data, it was discovered that a single value for the average pressure on the penetrator tip at steady state,  $Q$ , could successfully represent the pressure at steady state over the impact velocity range of 1 to 6 km/s. This formulation for  $Q$  allowed the model to improve its accuracy and its trends at higher velocities. In addition, this value  $Q$  was shown to have a strong correlation to target strength. This approach has resulted in a completely algebraic solution that relies only on known test parameters and the well-established crater volume/kinetic energy relationship.

Future work will involve an effort to revise or replace the modified Bernoulli Equation's estimate for pressure at steady state. Additional analysis also needs to be conducted to ascertain the form of the pressure distribution that leads to a constant  $Q$  over all impact velocities.

The aim of this paper was to extend the one-dimensional penetration analysis into the hypervelocity range. The resulting model offers reasonable accuracy for a one-dimensional description of the penetration event.

## REFERENCES

Alekscevskii, V. D., 1967, "Penetration of a Rod into a Target at High Velocity," in *Combustion, Explosion, and Shock Waves*.

Anderson, C. E., Morris, B. L., and Littlefield, D. L., 1992, "A Penetration Mechanics Database," Southwest Research Institute, SwRI Report 3593/001.

Christman, D. R. and Gehring, J. W., 1963, Semiannual Report on Penetration Mechanisms of High-Velocity Projectile," Report No. TR63-250 prepared for Ballistic Research Laboratories.

Cinnamon, J. D., Jones, S. E., Wilson, L. L., and House, J. W., 1992a, "Further Results in the One-Dimensional Analysis of Rod Penetration," in the Proceedings of SECTAM XVI, Nashville, TN.

Cinnamon, J. D., Jones, S. E., House, J. W., and Wilson, L. L., 1992b, "A One-Dimensional Analysis of Rod Penetration," *Int. J. Impact Engng.*, 12, 2, 145-166.

Cinnamon, J. D., 1992a, "Further One-Dimensional Analysis of Long-Rod Penetration of Semi-Infinite Targets," Masters Report, Department of Aerospace Engineering, University of Texas at Austin.

Cinnamon, J. D., 1992b, "Further One-Dimensional Analysis of Long-Rod Penetration of Semi-Infinite Targets," Air Force Institute of Technology Technical Report, AFIT/CI/CIA-92-086.

Gillis, P. P., Jones, S. E., Wilson, L. L., and Foster, J. C., Jr., 1989, "An Analytical and Experimental Approach to the Penetration of Semi-Infinite Targets by Long Rods," in *Recent Advances in Impact Dynamics of Engineering Structures*, D. Hui and N. Jones, eds., ASME-AMD-Vol.105.

Gillis, P. P., Jones, S. E., Wilson, L. L., Foster, J. C., Jr., 1990, "Parabolic Penetration Pressures," Proceedings of the 19th Yugoslav Congress on Applied Mechanics.

Hohler, V. and Stilp, A. J., 1977, "Penetration of Steel and High Density Rods in Semi-Infinite Targets," Proceedings of the 3rd International Symposium on Ballistics, Karlsruhe, FRG.

Hohler, V., Schneider, E., Stilp, A. J., and Tham, R., 1978, "Length and Velocity Reduction of High Density Rods Perforating Mild Steel and Armor Steel Plates," Proceedings of the 4th International Symposium on Ballistics, Monterey, CA.

Hohler, V. and Stilp, A., 1984, "Influence of the Length-to-Diameter Ratio in the Range from 1 to 32 on the Penetration Performance of Rod Projectiles," Proceedings of the 8th International Symposium on Ballistics, Orlando, FL.

Hohler, V. and Stilp, A., 1987, "Hypervelocity Impact of Rod Projectiles with L/D from 1 to 32," *Int. J. Impact Engng.*, 5, 1-4, 323-331.

Hohler, V. and Stilp, A., 1990, "Penetration Performance of Segmented Rods at Different Spacing-Comparison with Homogeneous Rods at 2.5-3.5 km/s," Proceedings of the 12th International Symposium on Ballistics, San Antonio, TX.

Jones, S. E., Gillis, P. P., and Foster, J. C., Jr., 1987, "On the Penetration of Semi-Infinite Targets by Long Rods," *J. Mech. Phys. Solids*, 35, 121.

Jones, S. E., Gillis, P. P., Foster, J. C., Jr., and Wilson, L. L., 1991, "A One-Dimensional, Two-Phase Flow Model for Taylor Impact Specimens," *J. Engng. Materials Tech.*, *Trans ASME*, 113, 228 (see also *Recent Advances in Impact Dynamics of Engineering Structures*, D. Hui and N. Jones, eds., ASME-AMD-Vol. 105).

Jones, S. E., Marlow, R. B., House, J. W., and Wilson, L. L., 1993, "A One-Dimensional Analysis of the Penetration of Semi-Infinite 1100-0 Aluminum Targets by Rods," *Int. J. Impact Engng.*, 14, 401.

Keele, M., Rapacki, E., Jr., and Bruchey, W., Jr., 1990, "High Velocity Ballistic Performance of a Uranium Alloy Long Rod Penetrator," Proceedings of the 12th International Symposium on Ballistics, San Antonio, TX.

Kerber, M. W., Jones, S. E., Fisher, C. A., and Wilson, L. L., 1990, "Penetration and Cratering of Semi-Infinite Targets by Long Rods," Proceedings of the 12th International Symposium on Ballistics, San Antonio, TX.

Luk, V. K. and Pickutowski, A. J., 1991, "An Analytical Model on Penetration of Eroding Long Rods into Metallic Targets," *Int. J. Impact Engng.*, 11, 3.

Marsh, S. P., 1980, *LASL Shock Hugoniot Data*, Univ. California Press, Berkeley and Los Angeles, CA.

Morris, B. L. and Anderson, C. E., Jr., 1991, "The Ballistic Performance of Confined Ceramic Tiles," Proceedings of the 1991 TACOM Combat Vehicle Survivability Symposium.

Murphy, M. J., 1987, "Survey of the Influence of Velocity and Material on the Projectile Energy /Hole Volume Relationship," Proceedings of the 10th International Symposium on Ballistics, San Diego, CA.

Ravid, M., Bodner, S. R., and Holoman, I., 1990, "Analytical Investigation of the Initial Stages of Impact of Rods on Metallic and Ceramic Targets at Velocities of 1 to 9 km/s," Proceedings of the 12th International Symposium on Ballistics, San Antonio, TX.

Silsby, G. F., 1984, "Penetration of Semi-Infinite Steel Targets by Tungsten Long Rods at 1.3 to 4.5 km/s," Proceedings of the 8th International Symposium on Ballistics, Orlando, FL.

Tate, A., 1967, "A Theory for the Deceleration of Long Rods after Impact," *J. Mech. Phys. Solids*, 15, 387.

Tate, A., 1969, "Further Results in the Theory of Long Rod Penetration," *J. Mech. Phys. Solids*, 17, 141.

Wilkins, M., Gibbons, J., Hohler, V., Stilp, A. J., and Cozzi, M., "Ballistic Performance of AlN, SiC, and Al2O3 Ceramic Tiles Impacted by Tungsten Alloy Long Rod Projectiles," Proceedings of the U. S. Army TACOM Combat Survivability Symposium, Vol. II, 75-95.

Wilson, L. L., Foster, J. C., Jr., Jones, S. E., and Gillis, P. P., 1989, "Experimental Rod Impact Results," *Int. J. Impact Engng.*, 8, 15.

Woolsey, P., Mariano, S., and Kokidko, D., 1989a, "Alternative Test Methodology for Ballistic Performance Ranking of Armor Ceramics," Proceedings of the 5th Annual TACOM Armor Coordinating Conference.

## CONCLUSION

In this paper, a new one-dimensional model for the penetration of semi-infinite targets by long rods was developed. Its basis was the revision of the previous techniques employed to calculate the average pressure at steady state. The modified Bernoulli Equation appears to result in values for  $P_1$  that are simply too high for the impact cases in the hypervelocity range.

By correlating a new approach to a great body of data, it was discovered that a single value for the average pressure on the penetrator tip at steady state,  $Q$ , could successfully represent the pressure at steady state over the impact velocity range of 1 to 6 km/s. This formulation for  $Q$  allowed the model to improve its accuracy and its trends at higher velocities. In addition, this value  $Q$  was shown to have a strong correlation to target strength. This approach has resulted in a completely algebraic solution that relies only on known test parameters and the well-established crater volume/kinetic energy relationship.

Future work will involve an effort to revise or replace the modified Bernoulli Equation's estimate for pressure at steady state. Additional analysis also needs to be conducted to ascertain the form of the pressure distribution that leads to a constant  $Q$  over all impact velocities.

The aim of this paper was to extend the one-dimensional penetration analysis into the hypervelocity range. The resulting model offers reasonable accuracy for a one-dimensional description of the penetration event.

## REFERENCES

Alekscevskii, V. D., 1967, "Penetration of a Rod into a Target at High Velocity," in *Combustion, Explosion, and Shock Waves*.

Anderson, C. E., Morris, B. L., and Littlefield, D. L., 1992, "A Penetration Mechanics Database," Southwest Research Institute, SwRI Report 3393/001.

Christman, D. R. and Gehring, J. W., 1963, Semiannual Report on Penetration Mechanisms of High-Velocity Projectile, Report No. TR63-250 prepared for Ballistic Research Laboratories.

Cinnamon, J. D., Jones, S. E., Wilson, L. L., and House, J. W., 1992a, "Further Results in the One-Dimensional Analysis of Rod Penetration," in the Proceedings of SECTAM XVI, Nashville, TN.

Cinnamon, J. D., Jones, S. E., House, J. W., and Wilson, L. L., 1992b, "A One-Dimensional Analysis of Rod Penetration," *Int. J. Impact Engng.*, 12, 2, 145-166.

Cinnamon, J. D., 1992a, "Further One-Dimensional Analysis of Long-Rod Penetration of Semi-Infinite Targets," Masters Report, Department of Aerospace Engineering, University of Texas at Austin.

Cinnamon, J. D., 1992b, "Further One-Dimensional Analysis of Long-Rod Penetration of Semi-Infinite Targets," Air Force Institute of Technology Technical Report, AFIT/CI/CIA-92-086.

Gillis, P. P., Jones, S. E., Wilson, L. L., and Foster, J. C., Jr., 1989, "An Analytical and Experimental Approach to the Penetration of Semi-Infinite Targets by Long Rods," in *Recent Advances in Impact Dynamics of Engineering Structures*, D. Hui and N. Jones, eds., ASME-AMD-Vol.105.

Gillis, P. P., Jones, S. E., Wilson, L. L., Foster, J. C., Jr., 1990, "Parabolic Penetration Pressures," Proceedings of the 19th Yugoslav Congress on Applied Mechanics.

Hohler, V. and Stilp, A. J., 1977, "Penetration of Steel and High Density Rods in Semi-Infinite Targets," Proceedings of the 3rd International Symposium on Ballistics, Karlsruhe, FRG.

Hohler, V., Schneider, E., Stilp, A. J., and Tham, R., 1978, "Length and Velocity Reduction of High Density Rods Perforating Mild Steel and Armor Steel Plates," Proceedings of the 4th International Symposium on Ballistics, Monterey, CA.

Hohler, V. and Stilp, A., 1984, "Influence of the Length-to-Diameter Ratio in the Range from 1 to 32 on the Penetration Performance of Rod Projectiles," Proceedings of the 8th International Symposium on Ballistics, Orlando, FL.

Hohler, V. and Stilp, A., 1987, "Hypervelocity Impact of Rod Projectiles with L/D from 1 to 32," *Int. J. Impact Engng.*, 5, 1-4, 323-331.

Hohler, V. and Stilp, A., 1990, "Penetration Performance of Segmented Rods at Different Spacing-Comparison with Homogeneous Rods at 2.5-3.5 km/s," Proceedings of the 12th International Symposium on Ballistics, San Antonio, TX.

Jones, S. E., Gillis, P. P., and Foster, J. C., Jr., 1987, "On the Penetration of Semi-Infinite Targets by Long Rods," *J. Mech. Phys. Solids*, 35, 121.

Jones, S. E., Gillis, P. P., Foster, J. C., Jr., and Wilson, L., 1991, "A One-Dimensional, Two-Phase Flow Model for Taylor Impact Specimens," *J. Engng. Materials Tech.*, *Trans ASME*, 113, 228 (see also *Recent Advances in Impact Dynamics of Engineering Structures*, D. Hui and N. Jones, eds., ASME-AMD-Vol. 105).

Jones, S. E., Marlow, R. B., House, J. W., and Wilson, L., 1993, "A One-Dimensional Analysis of the Penetration of Semi-Infinite 1100-0 Aluminum Targets by Rods," *Int. J. Impact Engng.*, 14, 401.

Keele, M., Rapacki, E., Jr., and Bruchey, W., Jr., 1990, "High Velocity Ballistic Performance of a Uranium Alloy Long Rod Penetrator," Proceedings of the 12th International Symposium on Ballistics, San Antonio, TX.

Kerber, M. W., Jones, S. E., Fisher, C. A., and Wilson, L., 1990, "Penetration and Cratering of Semi-Infinite Targets by Long Rods," Proceedings of the 12th International Symposium on Ballistics, San Antonio, TX.

Luk, V. K. and Pieikutowski, A. J., 1991, "An Analytical Model on Penetration of Eroding Long Rods into Metallic Targets," *Int. J. Impact Engng.*, 11, 3.

Marsh, S. P., 1980, *LASL Shock Hugoniot Data*, Univ. California Press, Berkeley and Los Angeles, CA.

Morris, B. L. and Anderson, C. E., Jr., 1991, "The Ballistic Performance of Confined Ceramic Tiles," Proceedings of the 1991 TACOM Combat Vehicle Survivability Symposium.

Murphy, M. J., 1987, "Survey of the Influence of Velocity and Material on the Projectile Energy /Hole Volume Relationship," Proceedings of the 10th International Symposium on Ballistics, San Diego, CA.

Ravid, M., Bodner, S. R., and Holoman, I., 1990, "Analytical Investigation of the Initial Stages of Impact of Rods on Metallic and Ceramic Targets at Velocities of 1 to 9 km/s," Proceedings of the 12th International Symposium on Ballistics, San Antonio, TX.

Silsby, G. F., 1984, "Penetration of Semi-Infinite Steel Targets by Tungsten Long Rods at 1.3 to 4.5 km/s," Proceedings of the 8th International Symposium on Ballistics, Orlando, FL.

Tate, A., 1967, "A Theory for the Deceleration of Long Rods after Impact," *J. Mech. Phys. Solids*, 15, 387.

Tate, A., 1969, "Further Results in the Theory of Long Rod Penetration," *J. Mech. Phys. Solids*, 17, 141.

Wilkins, M., Gibbons, J., Hohler, V., Stilp, A. J., and Cozzi, M., "Ballistic Performance of AlN, SiC, and Al2O3 Ceramic Tiles Impacted by Tungsten Alloy Long Rod Projectiles," Proceedings of the U. S. Army TACOM Combat Survivability Symposium, Vol. II, 75-95.

Wilson, L. L., Foster, J. C., Jr., Jones, S. E., and Gillis, P. P., 1989, "Experimental Rod Impact Results," *Int. J. Impact Engng.*, 8, 15.

Woolsey, P., Mariano, S., and Kokidko, D., 1989a, "Alternative Test Methodology for Ballistic Performance Ranking of Armor Ceramics," Proceedings of the 5th Annual TACOM Armor Coordinating Conference.

**DISTRIBUTION LIST**  
**AFRL-MN-EG-TR-2002-7001**

Defense Technical Information Center  
8725 John J. Kingman Road, Ste 0944  
Ft Belvoir, VA 22060-6218

1

**EGLIN AFB OFFICES:**

AFRL/MN CA-N	1
AFRL/MNOC-1 (STINFO Office)	1
AFRL/MNM	1
AFRL/MNMW	5

Prof. S. E. Jones	2
Dept of Aerospace Engineering and Mechanics	
University of Alabama	
Tuscaloosa, Alabama 35487-0276	

Prof. P. P. Gillis	2
Dept of Chemical and Material Science Engineering	
University of Kentucky	
Lexington, Kentucky 40506-0046	